MODELLING CLIMATE CHANGE IMPACTS ON GROUNDWATER RECHARGE IN A SEMI-ARID REGION, SOUTHERN OKANAGAN, BRITISH COLUMBIA

by

Michael W. Toews

B.Sc., University of Calgary, 2003

A THESIS SUBMITTED IN PARTIAL FULFILLMENT
OF THE REQUIREMENTS FOR THE DEGREE OF

MASTER OF SCIENCE

In the Department
of
Earth Sciences

APPROVAL

Name: **Michael W. Toews**

Degree: **Master of Science**

Title of thesis: **Modelling climate change impacts on groundwater recharge in a semi-arid region, southern Okanagan, British Columbia**

Examining Committee:

Chair: **Dr. Andrew Calvert**

Dr. Diana Allen, Associate Professor
Department of Earth Sciences, SFU
Senior Supervisor

Dr. Paul Whitfield, Adjunct Professor
Environment Canada
Committee Member

Dr. Doug Stead, Professor
Department of Earth Sciences, SFU
Committee Member

Mr. Mike Wei, Senior Hydrogeologist
BC Ministry of Environment
External Examiner

Date Defended: _____

Abstract

The impacts of future predicted climate change on groundwater recharge resources are modelled for the arid to semi-arid south Okanagan region, British Columbia. The hydrostratigraphy of the region consists of Pleistocene-aged glaciolacustrine silt overlain by glaciofluvial sand and gravel. Spatial recharge is modelled using available soil and climate data with the HELP 3.80D hydrology model. Climate change effects on recharge are investigated using stochastically-generated climate from three GCMs. Recharge is estimated to be $\sim$45 mm/year, with minor increases expected with climate change. However, growing season and crop water demands will increase, posing additional stresses on water use in the region. A transient MODFLOW groundwater model simulates increases of water table in future time periods, which is largely driven by irrigation application increases. Spatial recharge is also used in a groundwater model to define capture zones around eight municipal water wells. These capture zones will be used for community planning.

Keywords: groundwater; recharge; irrigation return flow; climate change; capture zone; Oliver; Okanagan

Subject terms: Water table – Climatic factors – British Columbia
Groundwater – Flow Computer Simulation – Southern Okanagan

For my friends and family

And anyone else that have reported me
as "missing" for the past several years

Acknowledgments

I would like to gratefully acknowledge Diana for her continued support, motivation to attend conferences and publish my research, and allowing me the freedom to explore new methods. Paul for exposing me to climatology, and many unique statistical and graphical techniques. Doug for very thorough revisions and comments of this thesis. Alex Cannon for his support through our discussions regarding downscaling methods. The support and company from former and current lab-mates Sarah McArthur, Megan Surrette, Jacek Scibek, Hendrik Voeckler, Brian Smerdon, and notably Jessica Liggett for her enthusiasm, GIS expertise and coordination between our projects. Jerome Lesemann and Tracy for allowing me to tag along a field trip and offering their incite to the interpretation of the Cordilleran Quaternary geology.

I would also like to thank various people and organizations for providing funding, data, and other resources, including the BC Ministry of Environment, the Canadian Water Network, Terry Underwood from TRUE Consulting, NCEP/NCAR, the Canadian Institute for Climate Studies, and the Canadian Centre for Climate Modelling and Analysis.

And lastly, people I've never met, but provided me with either data or support. Thanks to Lynne Campo and Tom Mathews from Environment Canada; Steve Carle for providing source code for T-PROGS; Klaus Berger for providing specific details concerning the HELP model; members of the Open Source Geospatial Foundation for providing assistance and with GDAL; and the R Core Team, particularly Brian Ripley, for help with many aspects of the R system.

Contents

List of Figures

List of Tables

Glossary

AGCM*n*	*n*th Generation Atmospheric General Circulation Model
CDED1	Canadian Digital Elevation Data, Level 1
CSSC	Canadian Soil Survey Committee
CCCma	Canadian Centre for Climate Modelling and Analysis
CFR	Calculated fixed radius
CGCM*n*	*n*th Generation Coupled Global Climate Model
CICS	Canadian Institute for Climate Studies
CIS	Cordilleran Ice Sheet
CLASS	Canadian Land Surface Scheme
ENSO	El Niño-Southern Oscillation
GCM	Global Climate Model *or* General Circulation Model
GLP	Glacial Lake Penticton
GMS	Groundwater Modelling System
HadCM*n*	*n*th Generation Coupled Model from the Hadley Centre
HELP	Hydrologic Evaluation of Landfill Performance
LAI	Leaf area index
LARS-WG	A modern weather generating program
MODFLOW	Modular Groundwater Flow Model
NCAR	National Center for Atmospheric Research
NCEP	National Centers for Environmental Prediction
PDO	Pacific Decadal Oscillation
RMSE	Root mean squared error
SDSM	Statistical Downscaling Model
SRES	Special Report on Emissions Scenarios
SOLID	South Okanagan Land Irrigation District
T-PROGS	Transition Probability Geostatistical Software
WTN	Well Tag Number

Chapter 1

Project Introduction and Overview

1.1 Background

Climate change poses uncertainties to the supply and management of water resources (Wolock et al., 1993; Green et al., 1997; Winter, 2000; Holman, 2006). The Intergovernmental Panel on Climate Change (IPCC) estimates that the global mean surface temperature has increased 0.6 ± 0.2°C since 1861, and predicts an increase of 2 to 4°C over the next 100 years (Solomon et al., 2007). Temperature increases also affect the hydrologic cycle by directly increasing evaporation of available surface water and vegetation transpiration. Consequently, these changes can influence precipitation amounts, timings and intensity rates, and indirectly impact the flux and storage of water in surface and subsurface reservoirs (i.e., lakes, soil moisture, groundwater). In addition, there may be other associated impacts, such as sea water intrusion, water quality deterioration, potable water shortage, etc. (Mearns et al., 2001).

Although the most noticeable impacts of climate change could be fluctuations in surface water levels and quality (Winter, 1983), the greatest concern of water managers and government is the potential decrease and quality of groundwater supplies, as it is the main available potable water supply source for human consumption and irrigation of agriculture produce worldwide (Bear et al., 1999). Because groundwater aquifers are recharged

mainly by precipitation or through interaction with surface water bodies, the direct influence of climate change on precipitation and surface water ultimately affects groundwater systems.

Aside from the influence of climate, recharge to aquifers is very much dependent on the characteristics of the aquifer media and the properties of the overlying soils. Several physical, chemical, and numerical modelling approaches can be used to estimate recharge based on surface water, unsaturated zone and groundwater data (Scanlon et al., 2002). Among these approaches, numerical modelling is the only tool that can predict recharge. Modelling is also extremely useful for identifying the relative importance of different controls on recharge, provided that the model realistically accounts for the all process involved. However, the accuracy of recharge estimates depends largely on the availability of high quality hydrogeologic and climatic data. Determining the potential impact of climate change on groundwater resources, in particular, is difficult due to the complexity of the recharge process, and the variation of recharge within and between different climatic zones.

1.2 Previous research

1.2.1 Climate change impacts on groundwater

The scientific understanding of an aquifer's response to climate change has been studied in several locations within the past decade (e.g., Vaccaro, 1992; York et al., 2002; Croley and Luukkonen, 2003; Allen et al., 2004; Brouyère et al., 2004; Jyrkama and Sykes, 2007; Scibek et al., 2006; Scibek and Allen, 2006a,b). These studies link atmospheric models to unsaturated soil models, which, in some cases, were further linked into a groundwater model. The groundwater models used were calibrated to current groundwater conditions and stressed under different predicted climate change scenarios.

Allen et al. (2004) used a simplified approach to quantifying impacts of climate change on groundwater. In that study, mean annual recharge to the Grand Forks aquifer in the semi-arid region of south central British Columbia (BC), Canada was modelled using

HELP (Schroeder et al., 1994) for current and future climate change. Extreme conditions for precipitation and temperature, based on projections from global climate models (GCMs),[1] were used to adjust the climate parameters in a stochastic weather generator.

Scibek and Allen (2006b) revisited the Grand Forks climate change study by conducting enhanced recharge modelling and investigating the use of different downscaling methods. That study highlighted the value of using spatially distributed recharge modelling for climate change impacts assessments, and indicated that there is much uncertainty in the downscaling of precipitation. Scibek and Allen (2006a) compared the responses of two aquifers in BC and Washington State: the Grand Forks aquifer (semi-arid region) and the Abbotsford/Sumas aquifer (humid region). Results suggested observable, but small, changes in groundwater levels, forced by changes in recharge. At the Grand Forks site, significant river-aquifer interactions occur, thus water levels within the floodplain respond significantly and more directly to shifts in the river hydrograph under scenarios of climate change. Scibek et al. (2006) described in detail the methodology for incorporating the predicted change in stream flow in the Grand Forks aquifer model.

Vaccaro (1992) undertook a similar study that explored the sensitivity of recharge estimates for the Columbia Plateau, Washington, to historical climate variability and to projected climate change. In his study, WGEN (Richardson and Wright, 1984) was used to produce synthetic climate data. Historic climate data and data from three GCMs were to model recharge using a deep percolation model (Bauer and Vaccaro, 1987).

1.2.2 Climate change in Okanagan Basin

Cohen et al. (2004) investigated climate change impacts to Okanagan Basin, focusing on regional water demand and sustainability. They used a variety of GCMs to investigate future predicted climate change trends for the region, and to forecast their impact on surface watershed yields and crop water demands. They concluded that the present rates

[1] Global climate change can be simulated using GCMs. These complex models attempt to simulate atmospheric circulation with greenhouse gas forcing scenarios. GCMs are physically based and usually coupled with ocean circulation, sea ice and land hydrology models (Washington and Parkinson, 2005).

of water consumption in Okanagan Valley may become unsustainable within decades if current population, water demands and climate change trends persist.

Merritt et al. (2006) investigated the hydraulic response in sub-watersheds to climate change, including Vaseux Creek, located in the southern Okanagan region near Oliver. Their investigation used the UBC Watershed Model (Quick, 1995), which was driven by output from CGCM2, CSIROMk2 and HadCM3 climate models. Temperature data from the GCMs were downscaled using SDSM (Wilby et al., 2002), and precipitation changes were calculated directly from the GCMs. They found that the hydrology of the sub-watersheds was influenced most by snowpacks at high elevations, and that most of the stream discharge occurs during spring snowmelts. Simulations using future-predicted GCM scenarios forecast that the peak discharge occurs sooner, and has less volume throughout the year. Furthermore, their downscaling results indicate that summer precipitation may decrease by 0 to 35% relative to present normals.

Crop water demands were investigated by Neilsen et al. (2006) using the same downscaled data as Merritt et al. (2006). Crop water demands were modelled for several crop types found in the region. Projected water demand increases were determined to be 12–20% for the 2020s, and up to 40–61% by the 2080s. These increases may extend the water demand beyond the capabilities of the present water supply infrastructure. The growing season, as determined from growing degree days, are estimated to lengthen up to 20–35% by the 2080s.

1.3 Purpose and objectives

The purpose of this research is to quantify the impacts of climate change on recharge and groundwater resources in an arid region of British Columbia. The study site, referred to as the Oliver region, is situated in the southern Okanagan Basin, along the valley between Vaseux Lake and Osoyoos Lake (Figure 1.1). The region is highly dependent on groundwater from unconfined, unconsolidated sand and gravel aquifers for both water supply and irrigation.

Figure 1.1 Map of southern Okanagan Basin, highlighting the Oliver study region, bounded by Vaseux Lake and Osoyoos Lake.

The region is ideally situated for a study of this type due the availability of geologic information (from well logs and geological studies), and because it is an arid region with high water use demands. This region also encompasses the Town of Oliver, which was a focus area of a larger research project supported by the Canadian Water Network (CWN) to develop decision support tools for groundwater management in Okanagan Basin. In the Oliver area, aquifer vulnerability maps have been developed and incorporated into a land use allocation model (LUAM) (Liggett et al., 2006). The LUAM will incorporate the well capture zones for Oliver region water supply wells based on the results of this study. Furthermore, this research lends itself to the overall objectives of the CWN project to contribute to knowledge on groundwater recharge in the Okanagan Basin.

The research objectives are:

1. To develop a conceptual model of the hydrogeology of the Oliver study region;

2. To investigate how regional and local weather events affect recharge;
3. To refine the recharge modelling procedure used previously by Scibek and Allen (2006a,b) such that more detailed information on soil properties can be incorporated in to the HELP model;
4. To determine potential impacts of climate change on recharge for the study area, and to assess the sensitivity of the results to different global climate models;
5. To develop and calibrate a regional-scale three-dimensional groundwater flow model of the Oliver region of the southern Okanagan and to use that model to assess the impacts of climate change on groundwater resources; and,
6. To develop and calibrate a local-scale three-dimensional groundwater flow model, and to undertake a well capture zone analysis for the local community water supply wells for the Oliver region.

1.4 Scope of work

The methods used in this study are similar to those employed by Scibek and Allen (2006a,b). In keeping the methodologies similar to previous work in BC, it will be ultimately possible to undertake a comparison of the impacts of climate change on groundwater for arid, semi-arid and humid climate zones in southern BC.

The main tasks that are involved in this study are:

1. Review Quaternary geology, borehole data and hydrogeologic data, and develop a hydrostratigraphic model for the Oliver region;
2. Build and calibrate a 3D regional-scale groundwater flow model;
3. Undertake a statistical analysis to separate climate into regional and local events and determine the role of each in contributing to groundwater recharge;
4. Analyze climate data from weather stations and modelled GCM, and build future predicted climate change datasets with temperature, precipitation and solar radiation variables;

5. Quantify the spatially distributed recharge rates using the climate data and spatial soil survey data;
6. Simulate groundwater flow using each recharge data set, and evaluate the changes in groundwater flow and levels through time;
7. Undertake a sensitivity analysis of the groundwater and recharge models; and,
8. Develop a local scale groundwater model for the Oliver area and conduct a well capture zone analysis.

The various aspects of the project are shown in Figure 1.2. The figure shows the connection from the climate analysis, to recharge simulation, and finally to a groundwater model. Recharge is applied to a three-dimensional groundwater flow model, which is calibrated to historical water levels. Transient simulations are undertaken to investigate the temporal response of the aquifer system to historic and future climate periods.

1.5 Thesis outline

Chapter 1: Project Introduction and Overview

Introduction and rationale for the research. The purpose and objectives, along with the scope of work are presented.

Chapter 2: Oliver Region Physical Setting, Geology and Hydrogeology

Geology and hydrostratigraphy of the Oliver region, including detailed maps of geologic units and geologic interpretations, are presented. This chapter is included in a report submitted to the BC Ministry of Environment (Toews and Allen, submitted).

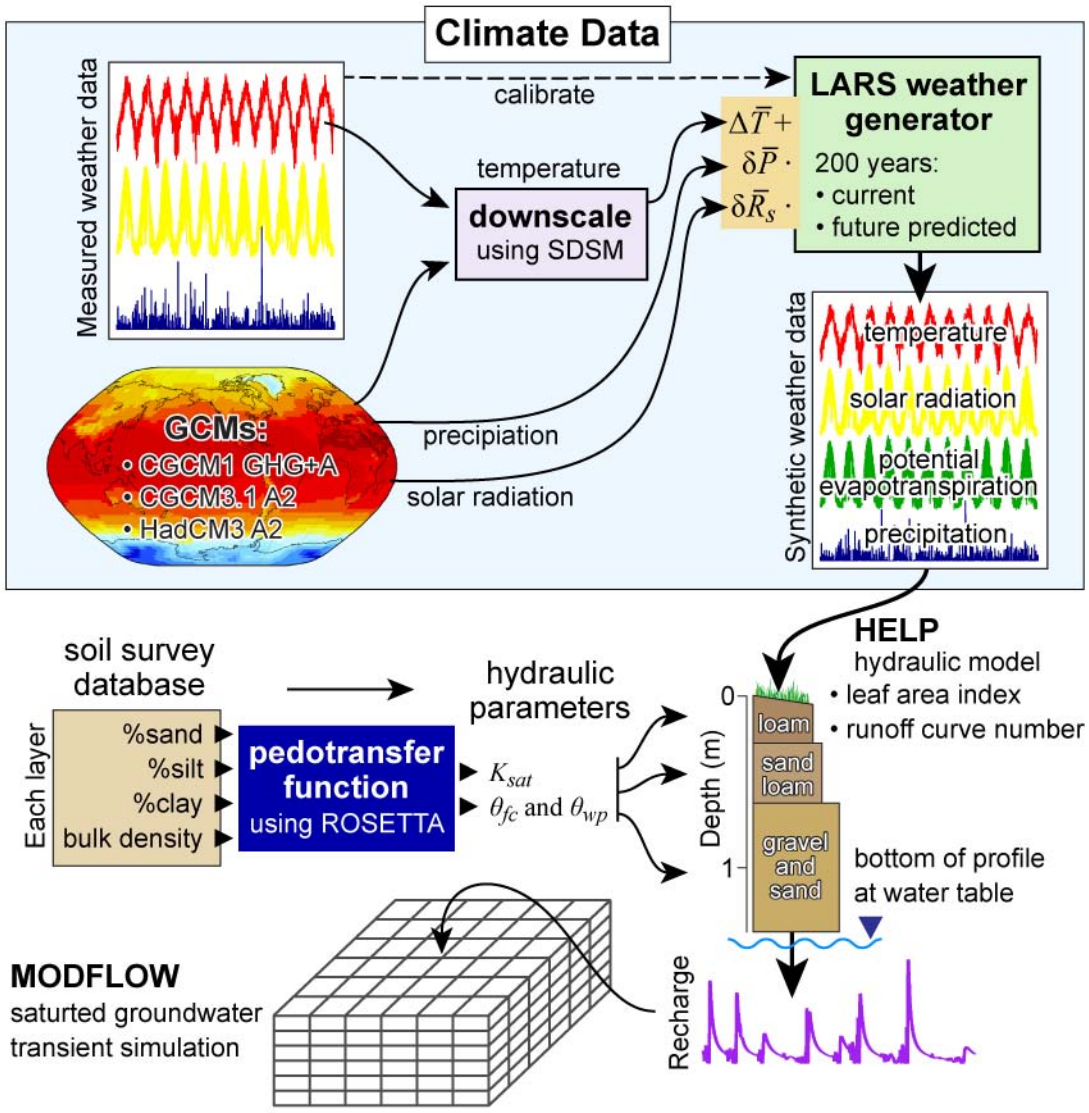

Figure 1.2 Flow chart of tasks in the thesis project. Tasks in the upper part of the chart assemble several climate data sets for current and future predicted conditions, which are used to simulate recharge using HELP. The soil layers are parameterized using a pedotransfer function program, which utilizes detailed soil survey measurements. Mapped monthly recharge from HELP is then used in a three-dimensional MODFLOW model to simulate transient saturated groundwater flow.

Chapter 3 *(paper)*: Recharge Sensitivity to Local and Regional Precipitation in the Southern Okanagan Basin, British Columbia

This paper is based on a poster[2] presented at the Geological Society of America annual meeting in Salt Lake City, October 2005 (Toews et al., 2005). The poster attempted to show the influence of reduced effective precipitation on groundwater recharge as a result of runoff increase during intense rainstorms associated with local convective precipitation. The results showed that there is a limited recharge response from the adjustments of precipitation during the summer months, and that winter precipitation associated with regional precipitation is the dominant control on recharge. This paper details the sensitivity of recharge to the local and regional components of precipitation, and how these influence recharge on different soils encountered in Okanagan Basin.

Chapter 4 *(paper)*: Spatial Recharge in the Arid Southern Okanagan Basin and the Influence of Future Predicted Climate Changes

This chapter details the groundwater recharge modelling methodology, as well as the impacts from climate change on recharge. This paper is an improvement and extension of a paper[3] and oral presentation at the International Association of Hydrogeologists meeting in Vancouver, September 2006 (Toews et al., 2006). The methodology is refined to include: (1) a more sophisticated method of estimating soil hydraulic properties using pedotransfer functions; (2) more spatially-varying input parameters, such as LAI and land use; (3) three GCMs for comparison; and (4) estimation of irrigation through crop water demand modelling, which is used to simulate irrigation return flow.

[2]Located on the CD at `print/GSA05_poster.pdf`

[3]Located on the CD at `print/recharge_IAH06.pdf`

Chapter 5: Hydrogeology and Groundwater Flow Model of the Oliver Region

This chapter describes the conceptual model for groundwater flow in the Oliver region, including quantitative descriptions of aquifer hydraulic properties, and boundary conditions. A transient three-dimensional MODFLOW model is constructed, which is calibrated to current conditions. Impacts of future-predicted climate changes are simulated using spatial recharge with irrigation return flow, simulated in Chapter 4 using the CGCM3.1 A2 GCM. The regional-scale model was used to assess changes in water levels, and the balance of water from lakes, river and recharge with future-predicted climate change and conditions.

Chapter 6: Well Capture Zone Analysis for Oliver, British Columbia

This chapter is based on a poster[4] presented at a Canadian Water Network conference in November, 2006 (Toews and Allen, 2006). The numeric model used was constructed using stochastic simulations of aquifer materials, using geostatistical methods. Spatial recharge rates, as determined in Chapter 4 using precipitation and irrigation return flow, are applied to the groundwater model. Groundwater capture zones were established for 60-days, 1- and 10-years.

Chapter 7: Conclusions and Recommendations

This chapter presents the conclusions from each chapter and recommendations for future research and monitoring.

Appendix A: Climate Data and Methods

Supplementary analyses of climate data between climate stations around Okanagan Basin; including the differences of climatology between Summerland and Oliver, and an analysis of precipitation lapse rates using various stations from a range of elevations around Oliver.

[4]Located on the CD at `print/CWN06Montreal_poster.pdf`

Appendix B: GCM Downscaling

Additional tables and figures from the work for Chapter 4 including: supplementary data and methods used to downscale GCMs, additional figures of changes between raw GCM values, and tables of shift factors (which have figures in Chapter 4).

Appendix C: Recharge Modelling

Another supplement to Chapter 4, which contains details of particular methods used for recharge modelling, such as determining runoff curve numbers, operation of the Python module for HELP, and the analysis of netCDF files.

Appendix D: Supplementary CD Contents

Contents listing for CD-ROM, including programs, some GIS data, papers and posters presented over the course of the thesis work. A brief description is provided for each file.

Chapter 2

Oliver Region Physical Setting, Geology and Hydrogeology

2.1 Study location

The Oliver study region is located between Lake Vaseux and Lake Osoyoos (see Figure 1.1), in Okanagan Basin of the southern interior of British Columbia (BC). The Town of Oliver in the center of the region has a population of about 4300. The rural area surrounding Oliver adds an additional 4500 people, which includes the Osoyoos Indian Band #1 Reserve on the Eastern side of the study region. Domestic water is obtained through several municipal and other public water supply wells, and several hundred private domestic wells. The main industries of the region are agriculture (orchard and vineyards) and tourism, both of which have a strong dependence on fresh water resources. The region is popularly known as the "Wine Capital of Canada", and also hosts two world-class golf courses.

2.1.1 Physiography and climatology

The Okanagan Valley is a narrow, north–south trending valley that is deeply incised in the Interior Plateau of the North American Cordillera. It has a topographic relief of $\sim$1100 m

from the valley bottom to the surrounding plateau level. Within the study region, the topography varies from 375 to 1862 m at Mt. Kobau, 7 km east of Oliver. The valley width ranges from less than 2 km at McIntyre Bluff at the north end of the study region, to 5 km near Oliver. The valley bottom is generally flat, with the exception of a few minor raised 'bars' along the valley center, and other small isolated topographic depressions. The sides of the valley have at least four terraces (also called benches).

The southern Okanagan is the only populated arid region in Canada, with typical 'wet' seasonal patterns occurring in the winter and summer periods. The annual precipitation in the valley bottom is about 300 mm, and nearly twice that amount at higher elevations, with a regional precipitation gradient decreasing toward the southwest. Winter precipitation is typically in the form of snowfall, derived from frontal systems, while rainfall from May to June is from cold lows, and from August to September from convective precipitation systems (B. Taylor, pers. comm. 2007; Environment Canada, 2006).

Natural climate variability in southern BC is influenced by the El Niño-Southern Oscillation (ENSO) (Trenberth, 1997), and the Pacific Decadal Oscillation (PDO) (Mantua and Hare, 2002). El Niño episodes generally result in decreased winter precipitation anomalies with warmer temperatures, while La Niña episodes result in increased winter precipitation with lower temperatures (Shabbar et al., 1997). During positive phases of the PDO, southern BC has higher temperature anomalies and slightly lower precipitation anomalies. The ENSO and PDO climate patterns have different time-scales, and can have coupled influences on the climatology (Wang et al., 2003; Fleming et al., in press).

2.1.2 Surface water

Okanagan River is the main surface water body in the region flowing from Vaseux Lake, southward to Lake Osoyoos (Figure 2.1). The river is controlled near the outlet of Vaseux Lake by McIntyre Dam, which also diverts water into the SOLID[1] irrigation channel. While the upper reach of the river is natural (unaltered channels), the remaining 2/3 is

[1]South Okanagan Land Irrigation District

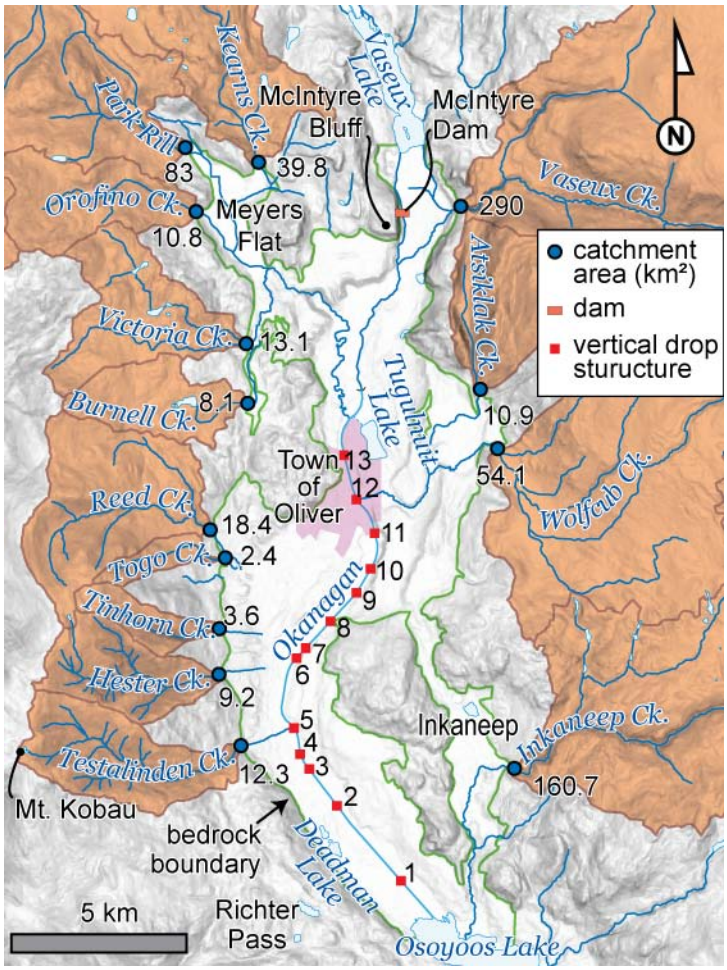

Figure 2.1 Surface hydrology, showing tributary basins and catchment area to the bedrock–fill boundary (in km^2). Okanagan River flows southward into Osoyoos Lake, and passes through 13 vertical drop structures along the channelized portion.

channelized, from 1 km north of Oliver to Osoyoos Lake. The river was channelized in the 1950s to prevent flooding (Nichols, 1993), and has thirteen vertical drop structures to slow and control the river flow (Schubert, 1983).

The majority of the streams entering the Oliver region are ephemeral, and do not extend far down into the valley. It is assumed that some of these small streams directly recharge to groundwater at the bedrock–fill boundary, since they disappear partway down the valley over unconsolidated material. The stream catchment areas to the bedrock–fill boundary are shown in Figure 2.1.

There are many small ($\leq$ 1 km^2) lakes along the valley bottom and valley sides, such as Tugulnuit Lake,[2] Gallagher Lake, and Deadman Lake. These water bodies do not have any major streams flowing in or out of their perimeter (with the exception of Tugulnuit Lake, which has a gravity-fed pipe down to Okanagan River). It is interpreted that all of these lakes are sustained through groundwater, and represent the water table surface.

2.1.3 Ecology, agriculture, irrigation and land-use

The valley-bottom of the Oliver region is in both *bunchgrass* and *ponderosa pine* biogeoclimatic zones (Pojar et al., 1987), which are indicative of hot, arid climates. The Oliver region has some of the most extensive irrigated agriculture in Okanagan Basin, including vineyards and fruit tree orchards (apple, plum, peach, etc.). Each crop generally has unique irrigation demands (see Neilsen et al., 2004), which is met during the growing season from water abstracted from Okanagan River (or connected irrigation channels), or from groundwater wells.

Other land use and land coverage includes gravel pits, golf courses, and natural riparian regions along reaches of Okanagan River. The upper valley sides are predominantly undeveloped, and consist of native bunchgrass, ponderosa pine and related vegetation. Natural vegetation is sparse, but is thicker and more prevalent on north-facing slopes (particularly in creek gullies), and at higher elevations.

2.2 Geologic background of Okanagan Basin

2.2.1 Quaternary geology

The Quaternary stratigraphy in the Okanagan Valley can be simplified as dominantly silt (by volume), with sand and gravel on the top and along sides of the valley. British Columbia has been glaciated multiple times throughout the past 1 Ma by the Cordilleran

[2]This is the official geographic name, however, *Tuc-el-Nuit Lake* is also very common

Ice Sheet (CIS), the most recent glaciation ending about 11 000 a (Clague, 1991). An extensive Glacial Lake Penticton (GLP) formed at the end of the last glaciation, into which fine-grained material was rapidly deposited. This fine-grained material comprises the characteristic silt bluffs, found in many valleys in the Interior of BC (Fulton, 1965).

The Quaternary stratigraphy of Okanagan Basin was first documented in detail by Flint (1935), who described both the character and distribution of the silt deposits, and the gradation of sands and gravels along the valley margins. Nasmith (1962) mapped and interpreted Quaternary deposits and landforms throughout the Okanagan, including the Oliver region (Figure 2.2). Nasmith identified several important depositional facies and landforms, including glaciofluvial deposits, kettled outwash, raised and present-day alluvial fans, and glaciolacustrine sediments. Fulton (1972) and Fulton and Smith (1978) constructed several stratigraphic sections across the BC Interior, and interpreted a record of multiple glaciations throughout the Cordilleran region, including in the valley-bottom of Okanagan Basin.

However, some of these initial interpretations for the Okanagan Valley have been questioned, in particular: (1) the presence or absence of large volumes of glacial till and preglacial sediments in the valley bottom; and (2) the timing and sequence of deglaciation, and distribution of deglacial ice and GLP. These interpretations influence the interpretation of further data, the theory behind depositional conceptual models, and interpolation of stratigraphy where there is limited or no available data.

Several stratigraphic conceptual models have been published that relate geologic evidence to possible modes of valley erosion and/or the stratification, and the distribution of the valley fill. These conceptual models are largely incompatible with each other, but nonetheless are supported (or denied) by geologic evidence. Much of the newer supporting evidence is from seismic surveys, listed in Table 2.1.

The traditional conceptual model of glaciation in the Okanagan Valley is of alpine valley glaciation, where a large tongue of ice occupies the valley, producing complex stratigraphy and preserving previous glacial and non-glacial deposits. This conceptual model is supported by earlier interpretations by Nasmith (1962), Fulton (1965, 1972, 1991), and

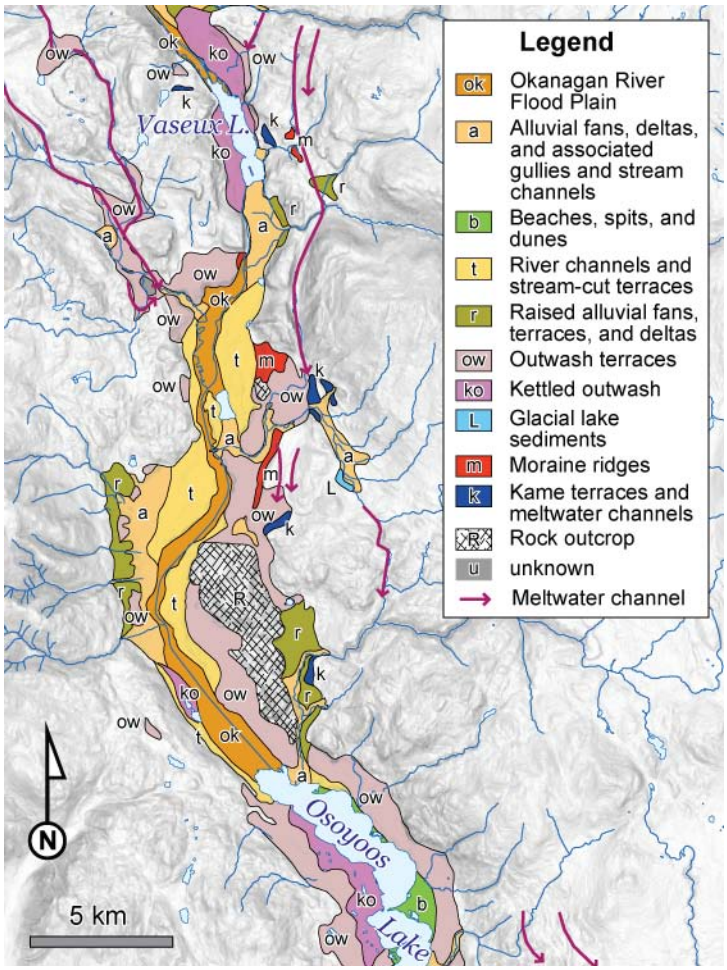

Figure 2.2 Surficial deposits of the Oliver region, as mapped and interpreted by Nasmith (1962). The legend order is from most recent to oldest.

Table 2.1 Seismic surveys undertaken in Okanagan Basin.

Reference	Location	Type	Source
MacAulay and Hobson, 1972	north Okanagan	refraction	dynamite
Mullins et al., 1990	Kalamalka Lake	reflection	air gun
Eyles et al., 1990	Okanagan Lake	reflection	air gun
Vanderburgh, 1993	north Okanagan	reflection	buffalo gun

Fulton and Smith (1978), and it is an analogue of present-day alpine glacial environments. However, few till deposits have been confirmed in the valley bottom (many of these diamicton deposits have alternate diageneses), and the stratigraphy, as interpreted in seismic profiles, is relatively simple (Eyles et al., 1990; Eyles and Mullins, 1991).

Eyles and Mullins (1991) proposed a supraglacial lake hypothesis, in an attempt to produce both simple stratigraphy and the silt bluffs. In this conceptual model, coarse material is deposited near the base of an active glacier from high-velocity subglacial drainage. Once the tongue of ice in the valley bottom is stagnant, fine lacustrine materials are rapidly deposited over the ice. The ice slowly melts, which lowers the lake bottom to produce silt bluffs.

Vanderburgh and Roberts (1996) developed a depositional systems framework, which is based on seismic profiles, borehole and sediment core lithologies. This empirically based conceptual model attempts to explain the seemingly complex stratigraphy as a result of the interactions of a few geologic processes, or depositional systems: (1) subglacial fluvial, (2) glaciolacustrine, (3) alluvial fan, and (4) channel systems (Figure 2.3).

Shaw et al. (1999) and Lesemann et al. (2005) proposed a revised depositional conceptual model, which is an extension of the work by Vanderburgh and Roberts (1996). They found lacustrine and related deposits at a higher elevation, which is evidence that the surface elevation and spatial extent of GLP was much greater than previously mapped by Fulton (1969). This glacial lake is interpreted to have a maximum elevation of at least 900 m (Lesemann and Brennand, 2007), which would have extended over many of the upper side valleys along the main valley, and covered a vast region, from northern Okanagan Basin to Okanogan Valley in Washington. Furthermore, Lesemann et al. (2005) postulate that this lake would have been beneath a thin cover of the Cordilleran Ice Sheet (as a subglacial lake), and would have had minimal ice-contact with the bedrock bottom of the valley. Other evidence suggests that this subglacial lake may have periodically and catastrophically drained, eroding smaller marginal valleys into bedrock, and over-deepening Okanagan Valley itself.

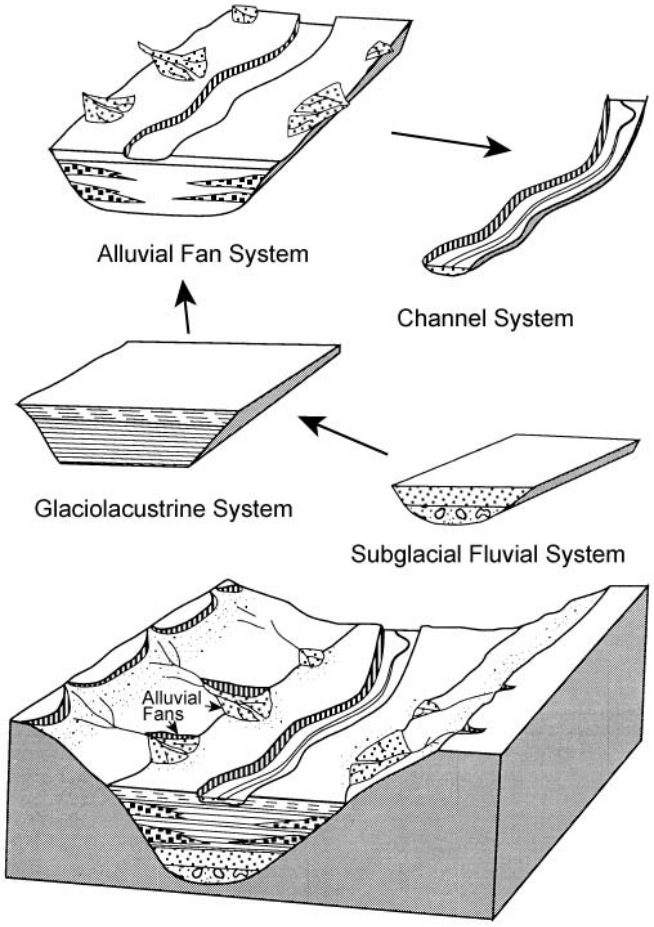

Figure 2.3 Depositional systems framework for the north Okanagan basin.

From the review of Quaternary geology literature, it is apparent that more work is required to understand the geologic history and timing of the CIS. However, the general distribution and character of the unconsolidated sediments in Okanagan Valley are, for the most part, well understood.

2.2.2 Bedrock geology

2.2.2.1 Bedrock composition and tectonics

The bedrock in the Oliver region consists primarily of metamorphic and intrusive igneous rocks (Figure 2.4), ranging in age from Proterozoic to Middle Jurassic (Massey et al., 2005). The Okanagan Valley fault system, which is a west-dipping crustal shear with 90 km of

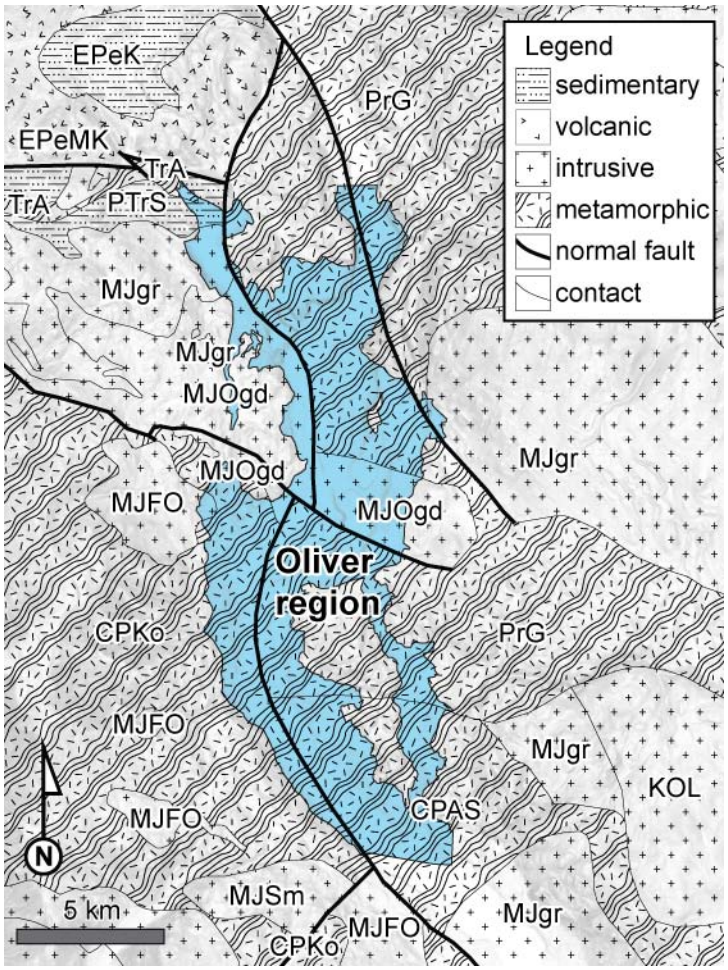

Figure 2.4 Bedrock geology and approximate locations of faults (Massey et al., 2005). The north–south trending Okanagan Valley fault system, which underlies the Oliver region (highlighted in the center), is beneath $\lesssim$280 m of unconsolidated Quaternary sediment.

offset, strikes southward through the valley and was active during the Middle Eocene (Tempelman-Kluit and Parkinson, 1986). The shear zone is approximately 1 to 2 km wide, and is characterized by mylonite and microbreccia.

2.2.2.2 Bedrock surface and modes of erosion

The bedrock surface in Okanagan Basin is highly variable, and has a similar spatial variability below the unconsolidated fill to where it is exposed—that is, the bedrock surface is very irregular, with many cliff-like drops. This is confirmed from large differences found

in the elevations of the bedrock contacts between two closely-spaced boreholes throughout many regions of Okanagan Basin.

The bedrock surface beneath the unconsolidated deposits, as revealed using seismic techniques (see Table 2.1), is very deep and irregular. MacAulay and Hobson (1972) mention the "extreme changes in bedrock slope" interpreted from their seismic survey. The deepest bedrock erosion is in Okanagan Lake at 650 m *below* sea level (Eyles et al., 1990), which makes Okanagan Valley possibly one of the deepest known erosional features within a continental landmass. The valley-axis bedrock elevation profile ranges upwards to 115 m above sea level (WTN[3] 82362, near Okanagan Falls), which indicates that the base of the bedrock surface along the valley ranges within an elevation range of 765 m.

Okanagan Valley is located along the fault system, as it provided a zone of weakness for erosion; however, there is no clear consensus regarding the erosional process(es) that created the present Okanagan Valley physiography (Tribe, 2005). Possible erosion processes are: (1) tectonic down-dropping during the Eocene; (2) river erosion; (3) glacier basal erosion; (4) subglacial fluvial erosion; and (5) erosional scouring from cataclysmic outburst flooding.

Erosion from rivers would have been early in the erosional history, and the extent of erosion would be limited to sea level elevation at that time (which would have been relatively higher than today); however, much of the bedrock valley is below present sea level (Fulton, 1972). Glacial erosion can potentially erode below sea level—Nasmith (1962) termed the Valley a "fiord-lake" to describe this phenomena found in Okanagan Basin. However, the down-valley bedrock profile is highly variable and is not graded.[4] Furthermore, the cross-valley widths and profiles are dramatically different along the valley (not a typical U-shape). A map-view of the main valleys reveals an anastomosing pattern, whereby the main valleys diverge and converge from north to south. These clues suggest that classic valley glacier erosion was not solely responsible for the over-deepening of the valley.

[3]Well Tag Numbers are unique well identifiers for the WELLS database (BC MoE, 2006, Report 7)

[4]A graded profile exponentially levels off to a vertical datum; an example is a river elevation profile

Eyles and Mullins (1991) and Vanderburgh and Roberts (1996) suggest that meltwater in subglacial drainage systems was actively flowing beneath the CIS. In addition, Shaw et al. (1999) and Lesemann et al. (2005) speculate that the subglacial meltwater drainage may have been periodically cataclysmic and responsible for the over-deepening of the valley. Subglacial fluvial systems are closed channel hydraulic systems, and have the ability to flow and potentially erode in any direction (including up and down). Tunnel valleys along the sides of the main valley (some of which "flow uphill") support an erosional mechanism. The deep and irregular bedrock profile of the main valley is also supported by this mechanism.

2.3 Geologic model of the Oliver area

2.3.1 Data and methods

Lithology data were obtained from the WELLS database (BC MoE, 2006), which has been corrected, standardized and modified under contract by Simon Fraser University under contract with the BC Ministry of Environment (BC MoE). A custom Microsoft Access database (Figure 2.5) was developed from the WELLS data[5] for use and interpretation as a standalone program, and within ArcGIS (ESRI, 2005). This database allows rapid correction and classification of the borehole data in a GIS. Additional routines, written in the Python programming language,[6] translate the lithology data for GMS version 6.0 (Owen et al., 1996; EMRL, 2005) for 3D interpretation and surface interpolation.

Within the study region, the WELLS database contains records from ~600 wells. The quality and detail vary from well to well, depending on the driller, depth and type of well. GMS can display borehole lithology data using two levels of interpretation: soil and hydrogeologic units. The former was used to classify the lithologic materials, while the later was used to group units into possible depositional facies.

[5]Located on the CD at `gisdata/wells_mt.mdb`

[6]Located on the CD at `programs/well2gms.py`

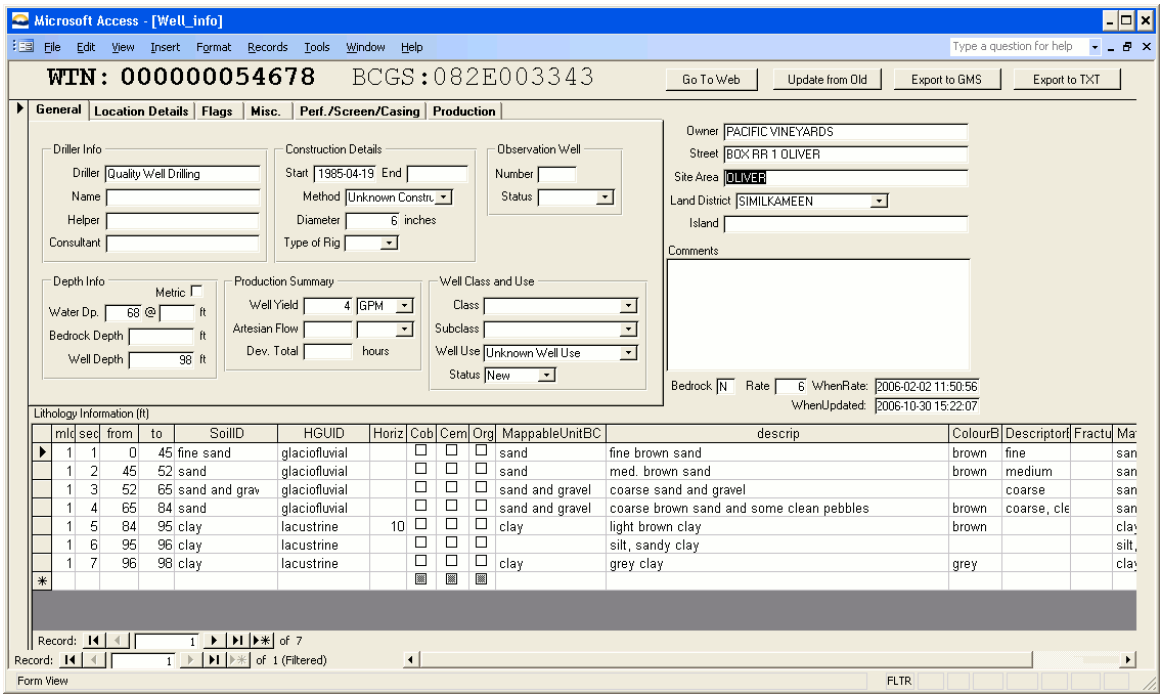

Figure 2.5 Well database interface used for lithology interpretation and classification. Lithologic units are classified using both a soil ID, and a geologic facies (in the 'HGU ID' field). Other data for each well can be viewed using the tabs near the top.

The lithologic descriptions were manually classified into 10 material types: (1) undifferentiated bedrock, (2) diamicton (clay mixed with gravel, cobbles or boulders), (3) boulder and gravel, (4) gravel, (5) sand and gravel, (6) sand, (7) fine sand, (8) silt, (9) clay, and (10) organic materials.

The depositional facies (described later) are: (1) bedrock, (2) till, (3) glaciolacustrine, (4) glaciofluvial, (5) boulder, (6) alluvial, and (7) recent fluvial channel.

The materials and depositional facies were determined from an interpretation of the text descriptions for each layer, and how the borehole relates with surrounding boreholes. Units with ambiguous or diagenetic descriptions, such as "till", "topsoil" or "hardpan" were classified with the assistance of surrounding boreholes, if available.

Digital elevation data were obtained from Natural Resources Canada (2005), which are unprojected 0.75-arc second, Level 1 DEM data.[7] Elevation data were projected on a Transverse Mercator, and interpolated onto 25 m resolution grid for ArcGIS, using bilinear interpolation; and ∼50 m resolution TIN (triangular irregular network) for GMS, using linear interpolation.

The 25 m ground elevation grid was used to determine surface slope, slope aspect, flow accumulation, hypsometric curves, and other GIS operations that are needed to determine the catchment hydrology of the region.

Point data (including bedrock contacts, silt tops and water table) were interpolated to ∼50 m resolution TIN surfaces, using either *kriging* (e.g., Deutsch and Journel, 1997) or *natural neighbour* methods (e.g., Sibson, 1981). Interpolated TIN surfaces were truncated using a custom Python routine; for example, an interpolated silt surface was "truncated" to be below the ground surface, and above the bedrock surface.[8]

Other geospatial data were obtained from the BC MoE, including: 0.5 m colour orthophoto data, locations of water wells (from WELLS database), and surface hydrology (lakes, rivers). Elevations of the wells were interpolated from the digital elevation data; however, the map position accuracy of the boreholes ranges from 1 to 100 m (the median is 20 m), which can propagate to the accuracy of interpolated maps derived from the WELLS database that are based on elevation. Surface hydrology map data were modified to honour the orthophoto imagery, such that streams terminated where they could no longer be identified along their stream course.[9]

It must be stressed that the interpretations of the Quaternary deposits presented in the following sections are predominantly based on information from the WELLS database, and need more supporting data and field work to gain more confidence. Furthermore,

[7] This is the 1:50 000 CDED1 series, which can be accessed at `http://geobase.ca`. At the latitude of the study region, 0.75-arc seconds projects to approximately 22 m north–south by 15 m east–west. Level 1 DEM data are typically generated through photogrammetric methods, using aerial photographs (USGS, 1997)

[8] GMS presently has a trunc($\mathbf{x}, a, b$) function, which truncates the TIN data values from $\mathbf{x}$ such that they are $\geq a$ and $\leq b$, where a and b are constant values. The `trunch5.py` custom Python routine extends the procedure to allow **a** and **b** to be TIN surfaces, compatible with $\mathbf{x}$

[9] The original stream data are linked and routed together, such that ephemeral and naturally discontinuous streams are connected through straight lines to the nearest water source, such as Okanagan River

interpretations of the timing of deglaciation and of depositional environments are subject to change with ongoing Quaternary research of the CIS.

2.3.2 Bedrock valley

In the Oliver region, there are only a limited number of valley-bottom boreholes that reached bedrock through the fill (Figure 2.6), and no seismic data are presently available. The term, "Oliver region", used in this study is defined by the area south of Vaseux Lake, and north of Osoyoos Lake, which is underlain by a significant thickness (generally >5 m) of unconsolidated material. The region also includes Meyers Flat, to the north-west, and Inkaneep[10] to the east. The spatial definition of the bedrock boundary was approximated from a GIS analysis of boreholes, digital elevation, slope, and orthophoto data.

The bedrock surface was kriged using a hybrid semivariogram model shown in Figure 2.7. Point sample data include: (1) available borehole bedrock contacts, (2) sampled ground elevation data, where bedrock is assumed to be exposed; and, (3) control points to extend bedrock contact below boreholes that did not reach bedrock, and below the ground surface.

From the available data, it appears the lowest bedrock surface elevation ranges from approximately 0 to 100 m above sea level (see Figure 2.6). There are no indications that the bedrock is eroded as deeply as in the northern Okanagan, where the bedrock contact is below sea level in many parts of the Valley. However, the bedrock depth can only be verified by deep mid-valley boreholes or from geophysical investigation.

2.3.3 Quaternary deposits

The first detailed map of surficial deposits in the southern Okanagan was produced by Nasmith (1962) (see Figure 2.2). In that study, Nasmith interprets a complex assemblage of outwash terraces, kame terraces, and moraines. The map and related interpretations

[10]This is the official geographic name; however, it is also popularly known as *Nk'Mip* or *Inkameep*

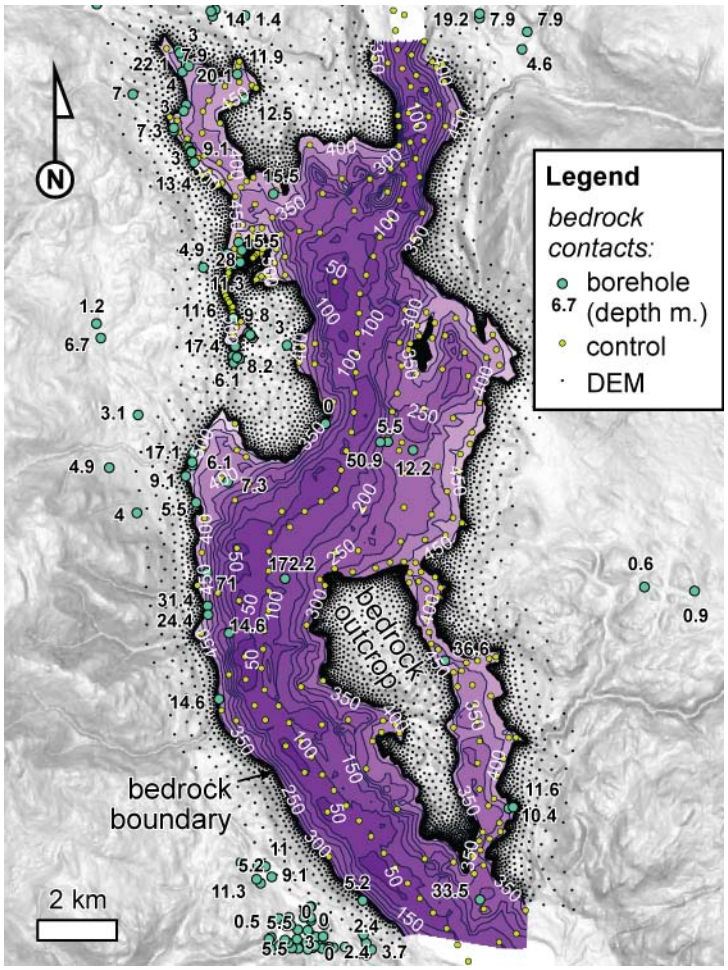

Figure 2.6 Bedrock surface elevation, kriged (see Figure 2.7) using 23 borehole contacts, 8917 sampled ground elevation points, and 327 control points. The bedrock boundary divides predominantly exposed bedrock from significant depths of unconsolidated material.

are perhaps too detailed—as it divides regions with similar deposits into multiple depositional environments, which have specific diagenetic contexts that are subject to multiple interpretations. Nasmith's map was used as a guide to further map the basic distributions of materials. The map in Figure 2.8 shows a simpler distribution of surficial deposits, as mapped from borehole, digital elevation and orthophoto data.

The stratigraphy and interpreted depositional facies in the Oliver region is best described using the depositional system framework (Vanderburgh and Roberts, 1996), with the exception of the subglacial fluvial system (in Figure 2.3), which appears to be absent

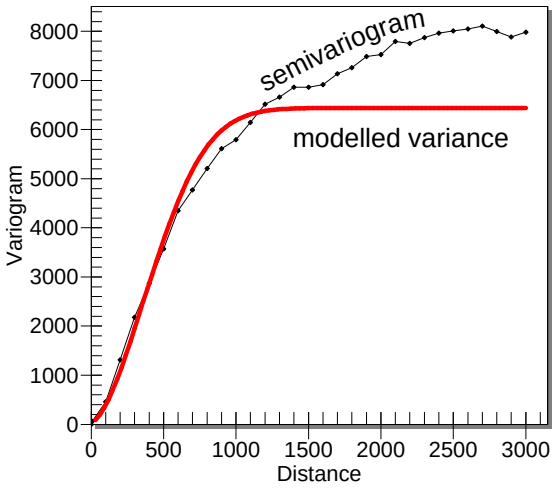

Figure 2.7 Semivariogram and geostatistical model for the bedrock surface. The hybrid model has: (1) nugget of 5; (2) Gaussian model with a contribution of 5926 and a sill of 975; and (3) a spherical model with a contribution of 505 and a range of 374.

in the Oliver region. However, all of the conceptual models fail to adequately describe all of the mapped geological materials unique to the Oliver region, so additional depositional environments are proposed here—specifically the boulder deposits and the drainage currents near McIntyre Bluff during deglaciation.

Geologic cross-sections through the Oliver region are shown in Figure 2.9, which show both the borehole materials with interpretations of their depositional facies, and the water table. The cross-sections were constructed from information in the WELLS database. Additional cross-sections and hydrostratigraphic descriptions are available from Wei (1985).

2.3.3.1 Glacial till deposits

Many lithologic units in the WELLS database are described by drillers as "till", "hardpan" or related terminology; however, many of these are, at most, a diamicton. Generally, these units are consolidated or semi-consolidated materials, often containing gravel. The deposits are usually located near the surface, and are either on alluvial fans or along steep valley margins, and many are interpreted here as debris flow deposits, which are part of an alluvial fan facies, described later.

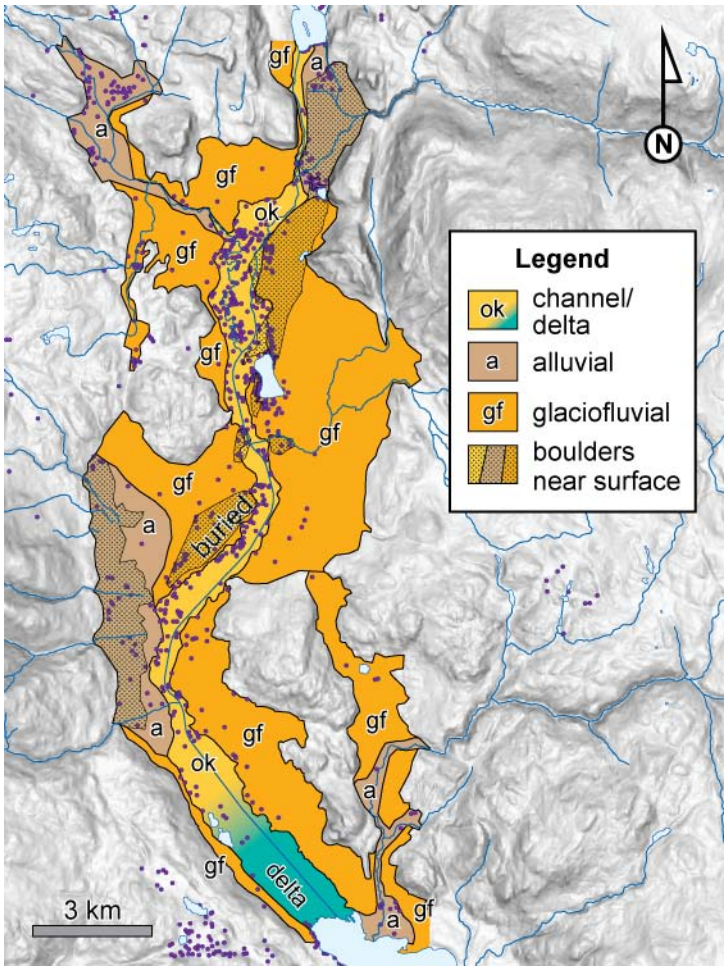

Figure 2.8 Surficial deposits of the Oliver region, showing three primary facies, with accessory boulder deposits. Glaciolacustrine silt and clay (not shown) generally underlie the relatively coarse-grained deposits in this map.

Glacial till appears to be rare in the Oliver area; however, this speculation is based on borehole descriptions, and is influenced by glacial conceptual models. Areas where till deposits are interpreted are at higher elevations, along the sides of the valley, near Meyers Flat and Inkaneep. The deposits are generally described as a "hard" mixture of clay and gravel, and overlie the bedrock surface. Till deposits appear to be spatially discontinuous, and are found below glaciofluvial and glaciolacustrine materials. To verify a glacial origin of diamicton deposits, detailed sedimentology and age dating (such as photoluminescence dating) are required.

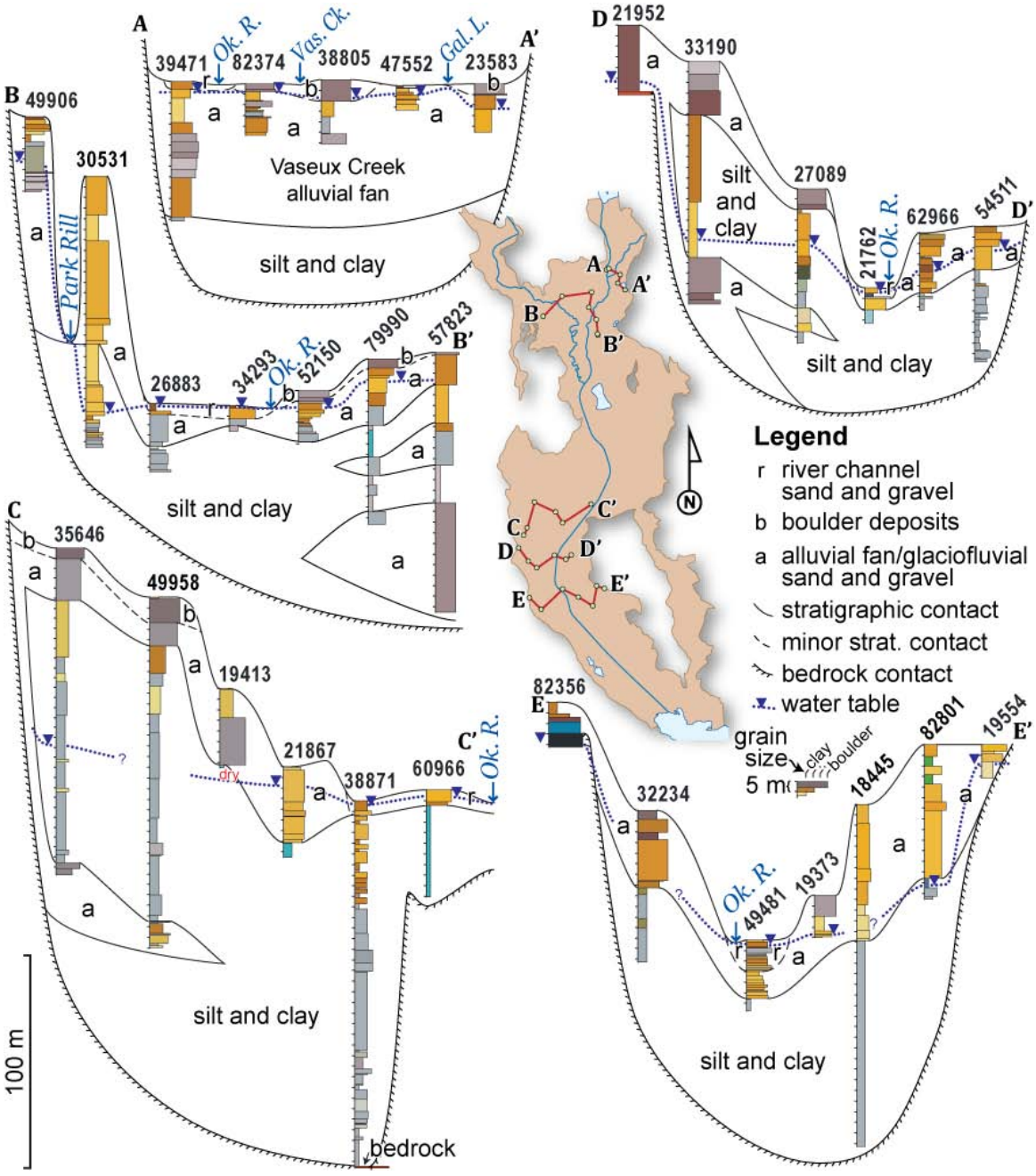

Figure 2.9 Cross-sections through the Oliver region showing textures from the WELLS database, identified by their well tag numbers (WTNs). The width of the columns are proportional to the grain size, and the shading is the colour either directly indicated or interpreted from the descriptions. Alluvial and glaciofluvial deposits are grouped together in this interpretation, as it is difficult to distinguish between the facies in some boreholes.

2.3.3.2 Glaciolacustrine deposits

Thick silt and clay deposits ($\lesssim$250 m) constitute the majority of unconsolidated valley fill sediment, and are found throughout the study area, up to 700 m above sea level near Richter Pass, and often onlap the bedrock surface (Figure 2.10). Fulton (1965) and Shaw (1977) describe these sediments as rhythmites of silt and clay, which have high-lateral continuity, and decrease upwards in sequence thickness, from several metres to several millimetres. The silt and clay can be interbedded with sand, usually near the valley margins and toward the northern end of the study area. Coarser sand and gravel are also found in discrete beds within the silt and clay unit, and are proximal to alluvial fans and creeks entering the valley. Rare wood and other organic material are found in isolated boreholes, which are usually suspended in fine-grained materials. Similar "white silt" deposits are found throughout Okanagan Valley, Thompson Valley, and similar valleys in the BC Interior (Flint, 1935).

The fine-grained deposits are interpreted to have been rapidly deposited from sediment suspension in a lacustrine environment in or near a glacier margin (Mullins et al., 1990; Eyles and Mullins, 1991). The coarser sand within this unit is interpreted to have been deposited from minor turbidity flows and slumps along the margins of the valley, while in the northern part of the study region, the sand is interpreted to have been derived from higher-energy water currents near McIntyre Bluff. Higher-energy currents may have occurred from water drainage diversions around possibly stagnant deglacial ice at McIntyre Bluff, where the Okanagan Valley narrows to less than 2 km wide. The diversion of drainage in this region would have changed as the water surface of GLP receded—in particular when the water surface reached the elevation threshold around the overflow channels in Figure 2.11.

The top of the silt and clay was interpolated using natural neighbours (Figure 2.10). The silt contacts in the boreholes were selected as the first significant thicknesses of silt or clay; however, this contact can overlie confined (or buried) sand and gravel aquifers. The silt contact depth is coincidently where many of the water well drillers stopped, as

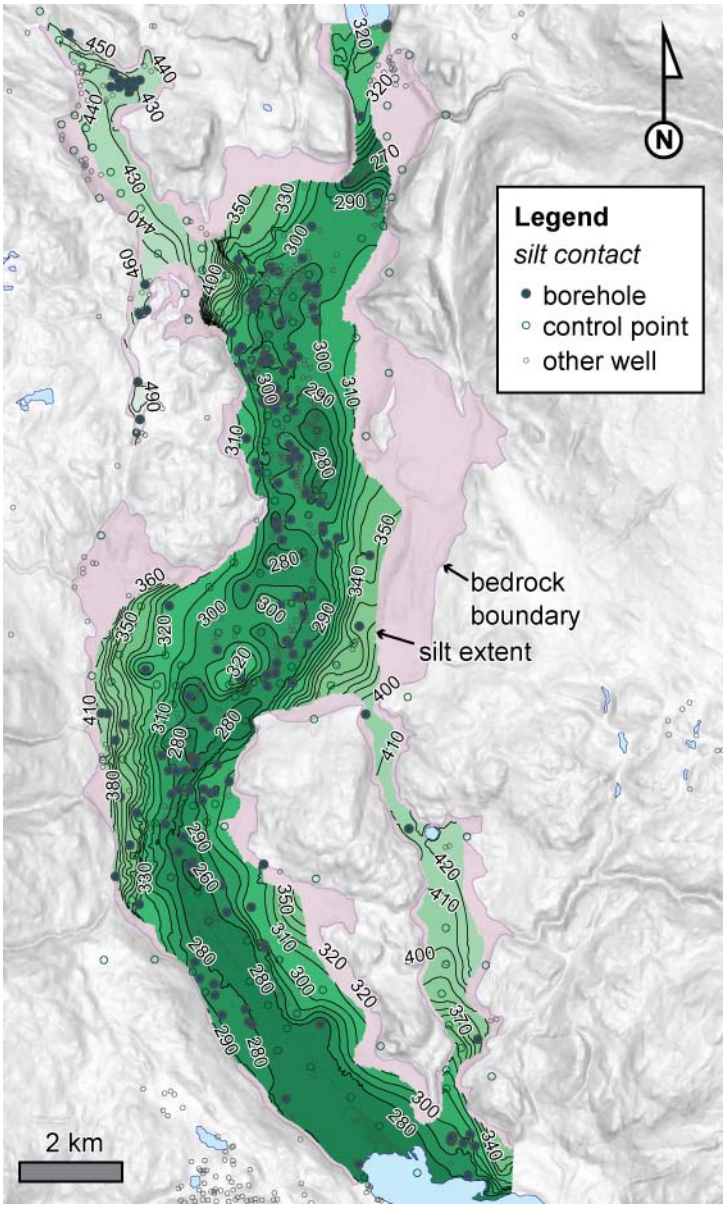

Figure 2.10 Elevation and extent of glaciolacustrine silt and clay, which is predominantly buried beneath glaciofluvial sand and gravel. This surface was interpolated using natural neighbours, using 187 borehole contacts and 146 control points. Control points were added to ensure a reasonable thickness of sand and gravel above the silt to the surface, and also to the interpolated water table surface, described later.

drillers are likely aware of this thick, poorly producing hydrogeologic unit. The silt top surface was trimmed between the bedrock and the ground surface, with an additional ~10 m depth surrounding Okanagan River and Park Rill. The depth adjustment in the interpolated surface around the rivers is to maintain continuity of the sand and gravel deposits above the silt top and adjacent to the rivers.

A possible influence of higher-energy currents is evidenced by alternations between sand, silt and clay units in boreholes to the north; some of which have shells (possibly from a lacustrine environment) in the finer material above coarser grained deposits (e.g., WTN 46717, Hodge and Lowen, 1980). The coarse deposits are also found at lower elevations in this area, which may have been a result of high-energy currents due to a drainage diversion during deglaciation.

The top of the silt and clay in Figure 2.10 identifies several isolated topographic lows in the center of the region (about 5–10 m magnitude), which could be interpreted as kettle holes (described later). The silt top appears to be deepest at the northern part of the study region, adjacent to Vaseux Creek.

2.3.3.3 Glaciofluvial deposits

Sand and gravel deposits are abundant along the sides of the valley, and usually consist of gravel and sand cross-beds with minor finer material present in some locations. The deposits are found throughout the region, and have formed large terraces on either side of the valley (Figure 2.11), and are above the Okanagan River floodplain. Terraces to the north-west with flatter surface slopes have finer-grained sediments, ranging between silt to medium-grained sand.

These glaciofluvial deposits are interpreted to have been deposited near glacial ice, which supplied large volumes of sediment and water. During the deglaciation of the CIS, very large volumes of water would have melted in Okanagan Basin and drained through the Oliver region over several hundred years. The four major terraces in Figure 2.11 were likely formed as the surface of GLP dropped. The current energy of the water would have also increased, as the water-column depth decreased, resulting in coarser sediments

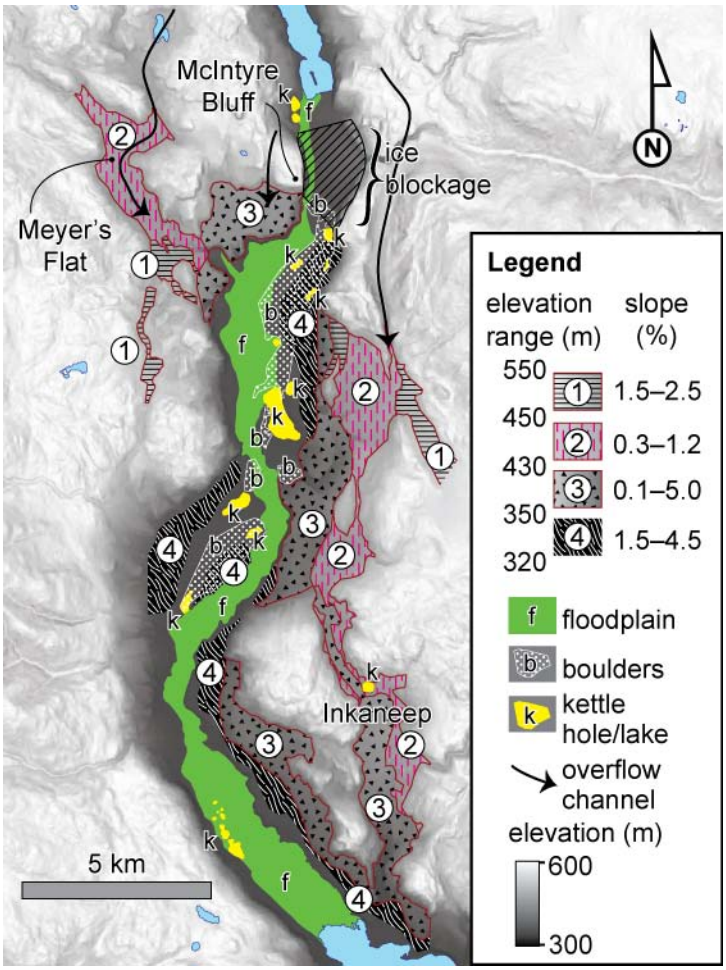

Figure 2.11 Map showing the stepped glaciofluvial terraces along the valley margins with their approximate elevation ranges and surface slopes. The terraces are interpreted to have been created due to the diversion of water flow around McIntyre Bluff, and the dropping glacial lake level. The distribution of boulders is possibly the result of a breached ice dam near McIntyre Bluff, which may have also redistributed large ice-blocks that would later melt to form kettle holes.

near the top. The terrace immediately south-west of McIntyre Bluff may have preserved backwash water from the main currents, as the sediment consists of sequences of fine- to medium-grained sand and silt.

Glaciofluvial deposits have buried the much finer glaciolacustrine deposits, and the contact between the two geologic facies is an unconformity, as some of the fine material has possibly been eroded by the strong currents that deposited the glaciofluvial deposits.

This important contact has been reached at least 187 boreholes in the region, and it has a moderately flat contact surface elevation, with local highs and lows (see Figure 2.10). The glaciofluvial deposits have since been removed or reworked in many regions, such as along the Okanagan River and other creeks.

2.3.3.4 Boulder deposits

An anomalous boulder deposit is found at or near the surface in several discrete locations of the Oliver study area (Figure 2.11). It is usually composed of boulders, cobbles, and gravel. Sand is also found in some deposits; however, finer material is generally absent. The boulder deposits appear to overlie either sand and gravel, or silt and clay. The deposit, south of Oliver, is buried beneath 6 to ∼20 m of sand and other deposits. Other discrete boulder deposits are found near the mouths of creeks along the margins of the valley, above sand and gravel alluvial fans.

These very coarse units can only be transported in a high energy environment. Many of these deposits form the upper sequences of alluvial fans, and are likely deposited through related alluvial processes; however, other discrete boulder deposits in the valley center are not proximal to alluvial fans or valley margin creeks, and require a different transportation process. One possibility is that coarse material accumulated near McIntyre Bluff, along with ice blockage, and was rapidly dispersed when the ice dam breached. In this event, the volume and flow of water would have been potentially very large, and could have transported the boulders, and washed out any finer materials. In addition, large blocks of ice could have been transported throughout the region south of McIntyre Bluff, and would have created kettle holes and lakes.

2.3.3.5 Alluvial fan deposits

Sand and gravel deposits are generally found near the mouths of creeks along the valley margins, and fan out a few kilometres toward the basin center. The deposits are generally thick, and are often associated with cobbles, and boulders in the upper parts. In isolated

sections, the deposits are either cemented or can be classified as a diamicton due the presence of clay, and are often termed by drillers as “hardpan” or “till”.

The deposits are interpreted to be part of an alluvial fan facies, which consists of coarse material deposited from streams and debris flows. Cemented or diamicton units are probably mass-debris flow deposits, which have calcite cements that may have formed shortly after the debris flow event. Calcite cement may have been available from freshly ground and volatile calcite-rich minerals from the parent rocks. Alluvial deposition was active from the time that glaciolacustrine deposition began, and has continued at a slower rate to the present day.

Alluvial deposition also occurred at the same time as glaciofluvial processes, and in many areas it is impossible to distinguish the two facies. As both the glaciofluvial and alluvial facies generally share similar sedimentological characteristics and timing, these can be mapped as a single unit. Nasmith (1962) recognized and mapped raised alluvial fan deposits, which appear to grade to the former GLP water surface. Although the distinction of two alluvial fan deposits is interesting from a Quaternary geologic perspective, they are treated and mapped as a single depositional facies and material for this study.

2.3.3.6 River channel deposits

These deposits consist of a range of grain-sizes from silt and clay to sand and gravel. Many vertical sections are fining upward sequences, which grade from gravel and cobbles at the base (called a channel lag) to silt and clay at the top (overbank deposits). In addition, silt and clay is found in discrete lenses, which are several metres thick. Peat and other vegetation are found in several boreholes, which extend up to 15 m below the ground surface, near the shores of Lake Vaseux, Lake Osoyoos, Gallagher Lake, Tugulnuit Lake, and near Park Rill. This facies is very continuous, and is adjacent to Park Rill and Okanagan River. Oxbow lakes are commonly found within 1 to 2 m elevation of the present river, and many other buried oxbow lakes are apparent in orthophotos (Figure 2.12). The southern 3 km of Okanagan River flows through a wetland, and has a very

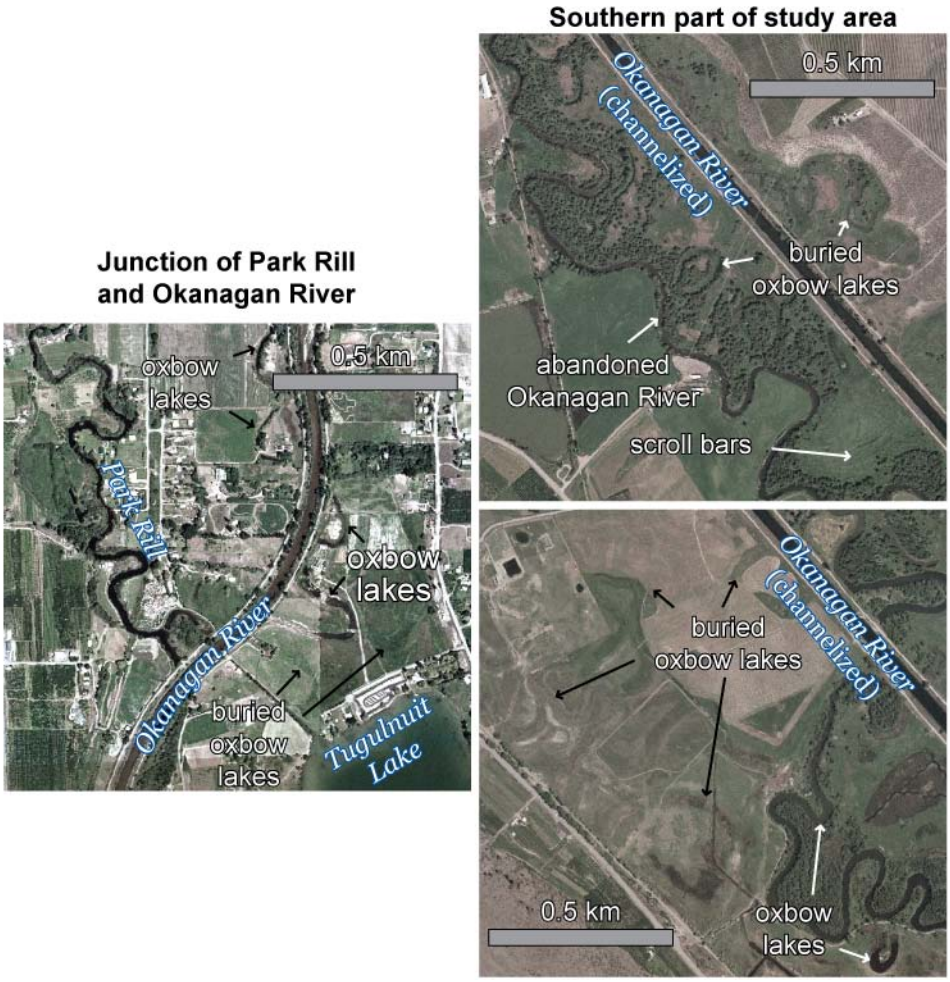

Figure 2.12 Examples of oxbow lakes in aerial photos, also showing buried oxbow lakes.

low gradient. Okanagan River has a deltaic morphology, as viewed in orthophotos, as it flows into Osoyoos Lake.

This fluvial channel facies was deposited from the Okanagan River and Park Rill, and consists of fluvially re-worked sediment derived from glaciofluvial and alluvial sediments. Deposition is interpreted to have begun when the hydrologic profile of Okanagan River had reached a minimum elevation—possibly after the discharge wained as the CIS melted.

Okanagan River has since aggraded as much as 15 m, as interpreted from the depth of peat deposits, which may represent former vegetation horizons. However, it is cautioned that these organic sediments may have been deposited in deeper water, giving a false horizon and aggradation estimate. Aggradation of this deposit is interpreted to be in

response to the accumulation of Vaseux Creek alluvial fan to the north, and Tonasket Creek alluvial fan to the south, near Oroville, Washington. In boreholes where coarse sediments appear to be deeper than 15 m, the deeper deposits may be older glaciofluvial sediments. A contact between the two facies is not easily identifiable due to their similar textures.

Sediment sequences in this facies are that of typical sand and gravel channel deposits, with over-bank silt and isolated oxbow-lake clay plugs. The contacts from channel deposits to glaciofluvial or alluvial deposits are not easily recognized, as they consist of similar materials. This facies is mapped with the assistance of digital elevation data, as it is no higher than perhaps a few metres above the present-day water surface of Okanagan River.

The southern ∼3 km of the study area is interpreted to be a delta, which is prograding into Osoyoos Lake. There are limited boreholes in this region (as the water table is very shallow); however, sediments in this region appear to be similar to the other river channel deposits, having gravel channel lag and silt flood plain deposits.

2.3.4 Kettle landforms

Several isolated depressions have been identified in both the ground surface topography (see Figure 2.11), and in the silt top surface (see Figure 2.10). The features in the silt top are not identified on the surficial river channel deposits, and they are filled above with sand and gravel deposits. Many of these features appear to be in the same regions where the anomalous boulder deposits are found.

These buried and surficial landforms are interpreted to be either kettle holes or kettle lakes (such as Tugulnuit Lake, Gallagher Lake, and multiple lakes near Deadman Lake). The landform would have developed from rapid sediment deposition on buried ice, which would have later melted to produce depressions in the surface. The depressions in the silt top indicate that stagnant ice blocks may have been present in the valley during glaciolacustrine deposition; however, the size and the distribution of the ice remains unknown due to the apparent absence of deglacial till deposits.

Kettle landforms are also found on the surface topography in the glaciofluvial deposits. Since these appear to be spatially independent from the kettle landforms in the silt, these may have been formed from ice blocks that were transported during glaciofluvial deposition. Due to their proximity to the anomalous boulder deposits, these may have been transported in a related event described previously. Kettle landforms are generally not identified on the Okanagan River flood plain, as they would have been filled in. One exception is Lake Tugulnuit, which had previously been influenced by Okanagan River (see Figure 2.12).

2.3.5 Chronology

An illustration of the possible timing and deposition of sediments during the Quaternary Period is shown in Figure 2.13. The timing of deposition and the volume of valley ice is poorly understood, although it is likely that the majority of sedimentation occurred during the Late Wisconsin glaciation, as the CIS was melting. Preservation of any prior glacial sediments in the Oliver region (e.g., Fulton and Smith, 1978) is inconclusive, since there are no seismic surveys that could indicate any possible unconformities, nor are there any reliable and direct stratigraphic age estimates (e.g., *in situ* organic material from interglaciations).

Two nearby radiocarbon date locations are selected for chronology of Holocene-aged sediments: (1) a wood fragment from Penticton at a depth of 51 m and an age of 9070 $\pm$ 80 years before present (BP) (GSC-3601; McNeely and Clague, 1996); and (2) a series of radiocarbon dates from organic material between 8.5 and 11.5 m below the bottom of Tugulnuit Lake, with dates ranging from 3780 $\pm$ 50 to 3860 $\pm$ 50 years BP (Rück et al., 1998). The radiocarbon date from Penticton is possibly a waterlogged wood fragment that was deposited in GLP, and represents one of the first signs of flora in Okanagan Basin after the last glaciation. The series of radiocarbon dates from the bottom of Tugulnuit Lake are likely timed with over-bank flooding of Okanagan River, which briefly flowed into the lake.

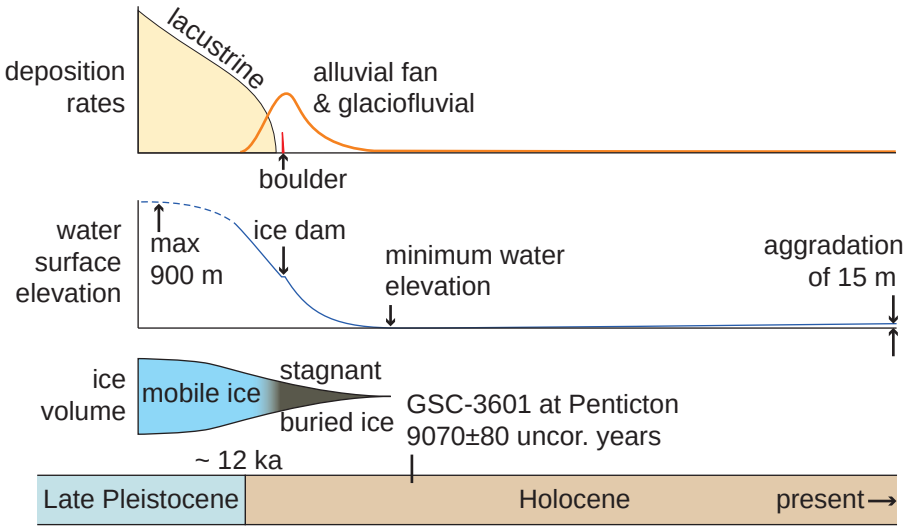

Figure 2.13 Conceptual diagram of deposition in the Oliver region during the Quaternary Period. Depositional rates have greatly diminished from their former rates, after the disappearance of the CIS. The transition of deposition from glaciolacustrine to glaciofluvial is partly due to the declining water surface elevation, which controlled the water energy. As stagnant and buried ice volume melted, kettle lakes and holes appeared on the surface. The selected radiocarbon date indicates the first sign of flora in the region after the last ice age.

2.4 Overview of groundwater

2.4.1 BC aquifer classification

In the study region, the BC MoE has mapped four aquifers using the WELLS database (Berardinucci and Ronneseth, 2002). In this region, two types of aquifers are mapped: highly-vulnerable unconfined and low-vulnerable confined aquifers (Figure 2.14). The mapped aquifers are described in "worksheets", available through the BC MoE, and are summarized below.

Aquifer 254 is located in the southern half of the study area, and is a shallow sand and gravel aquifer, which is underlain by thick silt and clay deposits. The median depth to water is 3.1 m, and the median production rates in the aquifer are 3.8×10^{-3} m^3/s

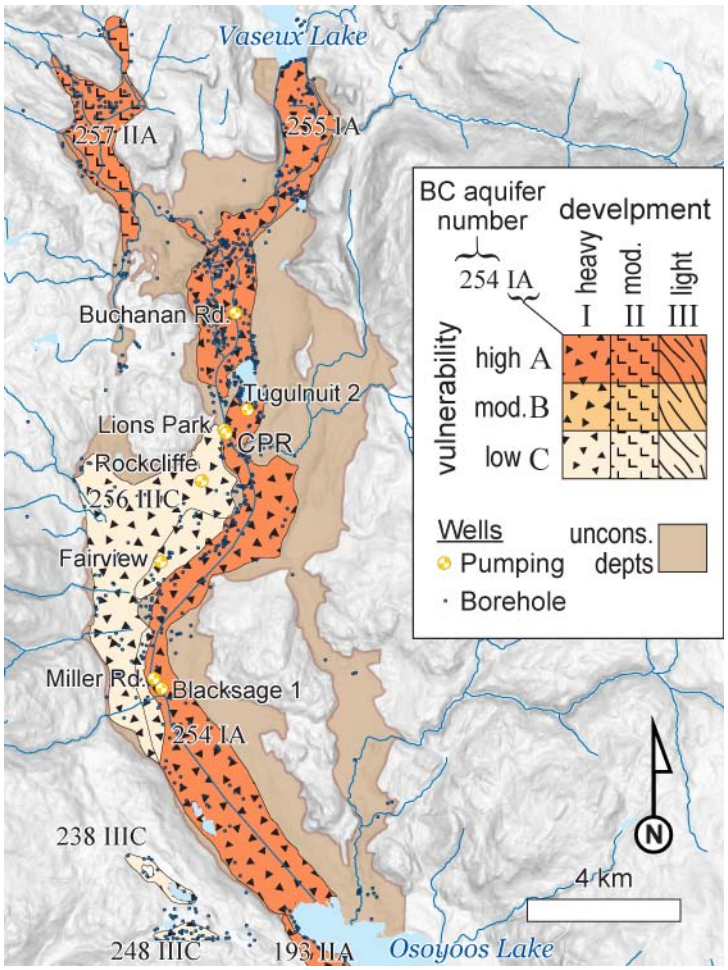

Figure 2.14 BC aquifer classification map, described by Berardinucci and Ronneseth (2002). The unconsolidated deposits surrounding the mapped aquifers are either dry or undeveloped (thus unrecognized).

(60 USgpm[11]). This aquifer is said to be recharged by the Okanagan River, irrigation and precipitation.

Aquifer 255 is in the northern half of the study area, and consists of sand and gravel with boulder deposits, and is also underlain by silt and clay. This aquifer is predominantly unconfined, although some deeper wells in this region are completed in confined sand and gravel aquifers below the silt and clay deposits. The median

[11] US liquid gallon per minute; 1 USgpm $\approx 6.31\times10^{-5}\,m^3/s \approx 5.45\,m^3/day$

depth to water is 11.6 m, and the median production rates are 9.5×10^{-4} m^3/s (15 USgpm). This aquifer is recharged from the Okanagan River and from precipitation.

Aquifer 256 is along the western side of the valley, and is a deep confined sand, gravel aquifer. It is the only aquifer in the Oliver region with a low vulnerability rating, due to the water depth and the presence of confining beds consisting of cemented and finer grained deposits. The median depth to water is 9 m (the maximum depth is 99 m), and the median well yield is 1.9×10^{-4} m^3/s (3 USgpm). It is recharged from precipitation, and the adjacent creeks.

Aquifer 257 is located at Meyers Flat, at higher elevations in the north-west part of the study region. This moderately developed unconfined aquifer consists of variably cemented sand and gravel deposits, and is underlain by silt, diamicton and bedrock at variable depths. The median depth to water is 8 m, and the median well yield is 2.5×10^{-3} m^3/s (40 USgpm). The aquifer is said to be recharged from precipitation, although Park Rill flows through the center of the mapped aquifer.

2.4.2 Hydrostratigraphy

Hydrostratigraphic units can be defined by combining several depositional facies having similar sediments with assumed hydrogeological properties. In particular, geologic units that are generally comprised of sand and gravel (river channel, glaciofluvial and alluvial facies) or silt and clay (glaciolacustrine facies) can be combined and treated as single hydrogeologic units.

The simplification of stratigraphy can help reduce the complexity of groundwater model construction; however, the heterogeneity of the materials can affect flow paths, and the delineation of capture zones to production wells. Heterogeneity is the degree of spatial variation of materials and their associated hydrogeologic properties within a region. All of the units express some degree of heterogeneity, such as: (1) rhythmites of silt and clay in the glaciolacustrine deposits, (2) cementation and presence of boulders in the alluvial fan deposits, and (3) presence of fine-grained buried oxbow lake sediments within the fluvial

channel deposits. These heterogeneities can be addressed in groundwater modelling by employing stochastic techniques of the material properties (see Chapter 6).

The important hydrogeologic units in the Oliver region are:

Silt and clay: consisting of the lacustrine deposits; this unit has poor groundwater production potential, due to the assumed low hydraulic conductivity and storage properties; it is interpreted as an aquitard;

Sand and gravel: consisting of the (1) river channel, (2) glaciofluvial, (3) and the alluvial deposits; this unit has high groundwater production potential; however, it is generally dry if it is far from a river or creek;

Boulder: these anomalous deposits can potentially have very high production potentials, and may provide buried conduits for water flow, if they are below the elevation of a nearby river.

2.4.3 Water table

A map of the water table elevation (Figure 2.15) was defined using the water depth as reported in the WELLS database, and calculated from the difference of well elevation and the water depth. However, this method of defining water table elevation can present problems, since the water depths in each well were obtained at different dates, between 1922–2004, and measured using different methods. Furthermore, some measurements are influenced from the development and purging of the well, while other measurements are in confined aquifers, which may not adequately represent the water table elevation.

From the water table elevation map, it can be observed that the water table is relatively flat in the valley bottom, and is close to the elevation of Okanagan River. Along the valley margins, near the bedrock outcrops, the water table is at a higher elevation; however, the exact profile of the water table from the valley bottom to the bedrock margin is difficult to define without detailed data. At higher elevations along the benches, it is assumed that both the depth of the bedrock and silt influence the depth of the water table, such that

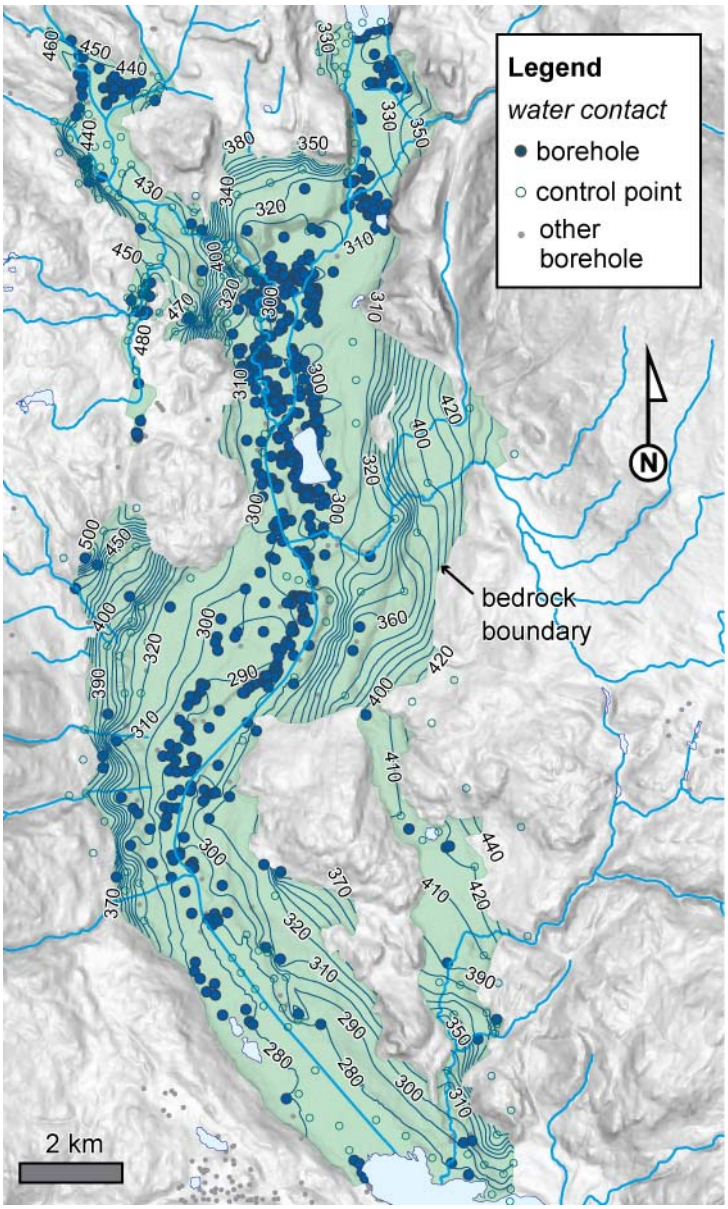

Figure 2.15 Map of water table elevation, interpolated with the natural neighbour interpolation method using 569 data points from the WELLS database, and an additional 202 control points. It should be cautioned that this map is technically a potentiometric head map, as some of the wells on the valley side are in confined aquifers.

if the water table is shallow, then the depth of the silt or bedrock contact is at a nearby depth (unless already defined in the borehole lithology).

2.4.4 Aquifer geometry and layers

Despite the abundance of highly-permeable sediments, locations of aquifers in the Oliver region are highly dependant on the groundwater table depth and the proximity to surface water features, such as Okanagan River. There are two forms of aquifers in the study area: (1) upper unconfined, and (2) lower or confined aquifers. The upper aquifer is adjacent to Okanagan River, and is the most productive and accessible aquifer in the study region. Much less is known about the lower confined aquifers, as they are disconnected from each other, and fewer boreholes have defined their geometry.

2.4.5 Upper unconfined aquifer

The main aquifer in the study region is the upper unconfined sand and gravel aquifer adjacent to Okanagan River. The upper aquifer is the same as Aquifers 254 and 255 in Figure 2.14. The majority of water wells (including all of the municipal wells) are completed in this aquifer, since it has a very high specific capacity. Many of the water well records in the WELLS database are dug wells (222 or 32% in the region), as this aquifer is at a shallow depth and is near surface water features.

Upper unconfined sand and gravel aquifers are also present at higher elevations in the study region, along the valley margins. This includes (but is not limited to) Aquifer 257 in Figure 2.14 at Meyers Flat. These aquifers have a much more limited total capacity, and are likely to be highly influenced by local streams. Aquifer tests from Meyers Flat (Kalyn, 1983) indicate that these sediments have similar hydraulic properties as the aquifer adjacent to Okanagan River.

The saturated thickness of the upper sand and gravel (Figure 2.16) is determined from the difference in the water table elevation (see Figure 2.15) and the top of the uppermost silt and clay contact (see Figure 2.10). The aquifer thickness, b, is directly proportional to the transmissivity, T, through the relation $T = K\,b$, where K is the hydraulic conductivity

of the aquifer. The saturated thickness is important for providing adequate horizontal groundwater flow through the unconfined upper aquifer; e.g., from a river to a pumping well. A thin saturated aquifer would have a limited ability for the well to access groundwater recharged through the river.

The map in Figure 2.16 should be consulted with discretion, as it is derived from two interpolated datasets; thus it may only be reliable in regions where data points from both sets are nearby. However, regions with sufficient data points show that the saturated thickness of the upper aquifer adjacent to Okanagan River varies from a few metres to 20 m or more—mostly due to variations in the silt top elevation. Some areas with isolated zones of high saturated thicknesses can be associated with kettle holes in the silt top, such as near Rockcliffe, Fairview, Miller Rd., and other production wells.

The presence of boulder deposits also appears to influence high specific capacities for many wells in the upper aquifer. These boulder deposits are mappable in several zones, and can potentially offer very high hydraulic conductivities (if saturated).

2.4.6 Lower confined aquifers

The upper glaciofluvial units in the northern valley bottom contain layers of fine sand, which make some of the wells partially confined (e.g., WTNs 53199, 46717). These finer-grained confining deposits appear to be discontinuous, and may have resulted from varying water currents in GLP during the Late Pleistocene.

Deep confined sand and gravel aquifers are found along the valley margins, which are in alluvial deposits. This includes Aquifer 256 in Figure 2.14. Many of these alluvial fan deposits interfinger the glaciolacustrine deposits at depth, and possibly extend less than several hundred metres toward the valley center. These aquifers are likely to be most influenced by ephemeral streams. As these streams have also deposited the alluvium, they are likely to be hydraulically connected.

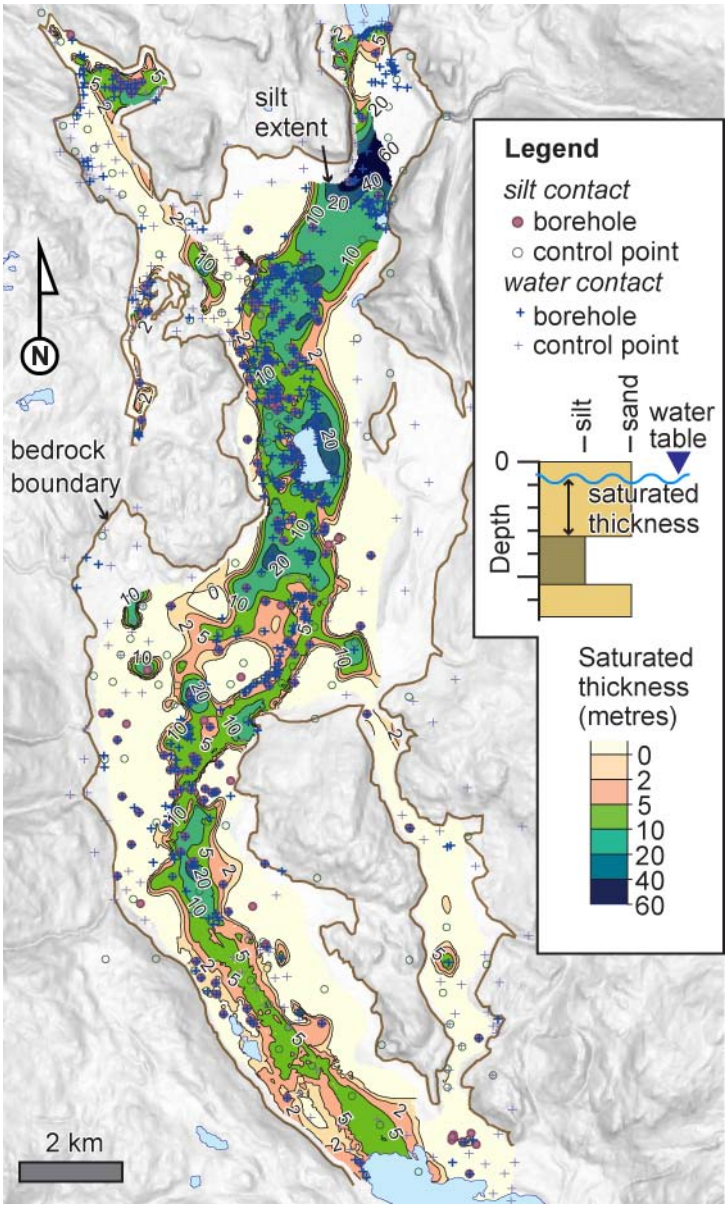

Figure 2.16 Saturated thickness of upper sand and gravel aquifer, b, as calculated from the difference of the water table (Figure 2.15; 569 contacts), and the uppermost silt top (Figure 2.10; 187 contacts). This map does not consider confined aquifers beneath the uppermost silt contact, which is why there are many producing wells found where $b = 0$. Interpretations to the reliability of this data are dependant on borehole data, and should only be considered most reliable where *both* silt and water table contacts are available (162 boreholes locations).

Chapter 3

Recharge Sensitivity to Local and Regional Precipitation in the Southern Okanagan Basin, British Columbia

By Michael W. Toews, Diana M. Allen and Paul H. Whitfield**

To be submitted as a Paper to Water Resources Research

Abstract

The influence of *regional*, *local* and *total* precipitation on recharge in an arid region is investigated using a technique of climate separation and recharge modelling. Daily precipitation data at two meteorological stations within Okanagan Basin, British Columbia, Canada, are compared using a cross-plot, and classified into regional and local precipitation events. Daily classed precipitation data are used as model inputs to a one-dimensional unsaturated recharge model, HELP 3.80D, and the recharge response is calculated at the base of the ∼1.2 m soil columns. Recharge is simulated using 86 soil profiles

*By permission

detailed from soil surveys from the region. Results suggest that regional precipitation events contribute significantly to recharge in comparison to local events.

Keywords: precipitation; climate separation; groundwater recharge; Okanagan

3.1 Introduction

Rates of groundwater recharge depend on the regional climatology, the physical properties of the upper soil layers, and land uses. Changes in any of these conditions will potentially modify recharge rates. The influences of climate on recharge, in general, are not well understood—and uncertainties in recharge prediction are confounded by climate change and natural climate variability. The analysis and graphical representation of observed daily climate data variables (maximum, mean and minimum temperature; rain, snow and total precipitation) can provide insight for understanding the dynamics of the climatology of a region, which has direct impact on the hydrologic cycle and, thus, groundwater recharge.

Local precipitation events can be regarded as being delivered from convective clouds, which may have high precipitation rates, but limited spatial and temporal scales (0.5–2 km, 5–100 minutes), and may derive much of their source water from local evapotranspiration. Regional precipitation events are regarded as being from frontal precipitation climate systems, which may have a lower precipitation rate, larger spatial and temporal scales (10–300 km, 0.5–5 days), and which derive their source water largely from the ocean.

Previous studies have used downscaled data from global climate models (GCMs) as input to recharge models (e.g., Scibek and Allen, 2006b). However, downscaled precipitation data may not calibrate adequately with observed data, particularly in the summer months. It is likely that this observed precipitation is from local convection, since synoptic-scale NCEP/NCAR reanalysis data (Kalnay et al., 1996) underestimate precipitation during summer months for this region. Scibek and Allen (2006b) demonstrated that precipitation series downscaled using Statistical Downscaling Model (SDSM) (Wilby

et al., 2002) were too low in the late spring to summer months, especially June, but fit the observed normals reasonably well in other months. They proposed that the problem lies in inability of the GCM used to adequately model summer precipitation in this region as a result of local convective precipitation and valley-mountain-rain-shadow effects, which have a strong influence on local precipitation. Precipitation was underestimated by roughly 40% compared to observed during the summer, even after downscaling with an adequately calibrated model.

In this study, the influence of *regional*, *local* and *total* precipitation on recharge is investigated using a technique of climate separation and recharge modelling. Specifically, the sensitivity of recharge to precipitation during the summer from regional and local-scale processes is investigated in southern Okanagan Basin, British Columbia (BC), Canada. Recharge is simulated in 86 soil profiles constructed from soil survey data, and hydraulic parameters estimated using pedotransfer functions.

3.1.1 Study area

Okanagan Valley is a narrow, north–south trending valley that is deeply incised in the Interior Plateau of the North American Cordillera. It has a topographic relief of ∼1100 m from the surrounding plateau level to the valley bottom. Okanagan Lake is the dominant surface water feature throughout much of the valley bottom (Figure 3.1), which drains southward through Okanagan River and two other connecting lakes. Summerland is situated next to Okanagan Lake, while the Oliver region has smaller lakes and Okanagan River. Most aquifers in the region are unconfined sand and gravel aquifers, which are underlain by silt and clay glaciolacustrine deposits (Vanderburgh and Roberts, 1996).

Soils in the region have developed from glacially derived sediments after the last glaciation. Soils types (using CSSC, 1978) that are well to rapidly drained typically include: Brown Chernozemic soils, which have formed in grasslands, and Brunisolic soils, which are found at higher forested elevations. Soils that are in poorly drained areas are typically Gleysolic soils, which are derived from clay to sand parent materials. Regosolic

Figure 3.1 Map of Oliver and Summerland in Okanagan Basin.

soils are the youngest, and are found in the river floodplains, and several other steeply sloping sites in the region (Wittneben, 1986).

The Okanagan Valley region has a semi-arid to arid climate due to the rain-shadow effect caused by the Coast and Cascade Mountains to the West. Temperature, precipitation and solar radiations normals for Summerland are shown in Figure 3.2. The diurnal variability of temperature in Figure 3.2a is greatest during the summer (as indicated by the span of thick vertical lines), while the largest variability in seasonal mean temperature is during the winter time (as indicated by the range of the boxplots, which are defined using quartiles). Outlier temperature minima between November and February are likely indicative of cool arctic climate systems. Precipitation normals (Figure 3.2b) are bimodal, with higher precipitation normals during summer and winter months. Winter precipitation is typically in the form of snowfall, derived from frontal systems, while rainfall from May to June is from cold lows, and from August to September from convective precipitation systems (B. Taylor, pers. comm. 2007; Environment Canada, 2006). The annual precipitation in the valley bottom is about 300 mm (median is 280 mm/year), and nearly twice that amount at higher elevations, with a regional precipitation gradient decreasing toward the southwest. Global solar radiation normals are shown in Figure 3.2c, which

shows variable amounts of daily total solar radiation throughout the year. This is influenced by cloud cover, and it is likely that summer days with low total solar radiation may be influenced by frontal (regional) climate systems, which have associated cloud cover with potential precipitation. In late July, median solar radiation is highest, with outlier minima also occurring around this time. The climatology of Oliver, ∼50 km south in Okanagan Valley, has nearly identical climatology, with notable differences in slightly higher temperatures and a median annual precipitation of 305 mm/year.

The valley-bottom is situated in both bunchgrass and ponderosa pine biogeoclimatic zones (Pojar et al., 1987), which are indicative of hot, arid climates. Both Summerland and Oliver regions have large developments of irrigated vineyards and fruit tree orchards (primarily apple, plum, and peach). The upper valley sides are predominantly undeveloped, and consist of native *Agropyron spicatum* (bluebunch wheatgrass), *Artemisia tridentata* (big sagebrush), and *Pinus ponderosa* (ponderosa pine) (Meidinger and Pojar, 1991). Natural vegetation is sparse, but is thicker and more prevalent on north-facing slopes (particularly in creek gullies), and at higher elevations.

3.2 Methods

3.2.1 Climate separation

There are many possible methods that can be used to separate regional precipitation events from local precipitation. Some advanced methods include using a K-index, which determines convective precipitation potential (McGinley et al., 1991). The method used in this study compares daily precipitation measured at two primary meteorologic stations within Okanagan Valley (Summerland and Oliver) which are separated by ∼50 km (Table 3.1). This method is perhaps the simplest, as daily climate data are readily available.

Climate data include daily temperature and precipitation data (Environment Canada, 2002), as well as hourly RF1 global solar radiation from Summerland CDA. Missing daily measurements from the primary stations were substituted using the secondary stations from the same region (see Table 3.1). Relative humidity and wind speed measurements

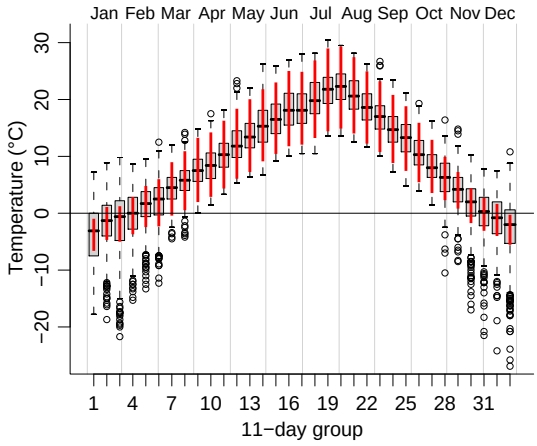

(a) Temperature; boxplots show distribution of daily T_{mean}, while thick vertical lines represent diurnal variability between daily T_{min} and T_{max}

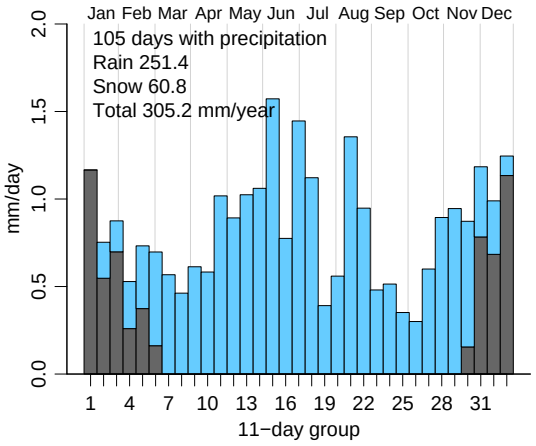

(b) Precipitation; showing rain (light bars) and snow (dark bars) fractions

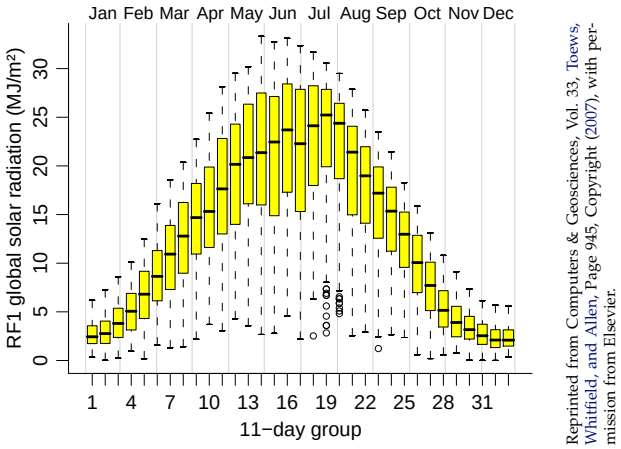

(c) Global solar radiation

Figure 3.2 Climatology normals for Summerland (1960–1994).

Table 3.1 Weather stations used in analysis.

Station name	ID	Location	Elev. (m)
Summerland CDA*	`1127800`	49°34′N, 119°39′W	455
Summerland CS	`112G8L1`	49°34′N, 119°39′W	434
Oliver*	`1125760`	49°10′N, 119°34′W	315
Oliver STP	`1125766`	49°11′N, 119°33′W	297

*Primary stations for daily temperature and precipitation

were determined from the median of hourly measurements at Summerland CS. The time range used in this study is limited to the period of available solar radiation measurements, between 1962 to 1994.

Daily precipitation data were classified as *local* through a logical analysis of daily total precipitation, P, and snowfall P^{snow} (where total precipitation is the sum of rainfall and snowfall amounts), at Summerland and Oliver, or locations $\mathcal{A}$ and $\mathcal{B}$, respectively. The daily ratio of precipitation between the two locations, $\eta = P_{\mathcal{A}}/P_{\mathcal{B}}$, was used to assess the likelihood of local precipitation on days with non-zero amounts at both locations. A cutoff envelope value, $\breve{\eta}$, was used to define the bounds of local or regional amounts, such that $\breve{\eta} > \eta > \breve{\eta}^{-1}$ is regarded as regional, since there are similar amounts at each location within reasonable limits. The following logical expression was used to select daily local precipitation events at Summerland:

$$\overbrace{\left\langle P_{\mathcal{A}}^{\text{snow}} = 0 \right\rangle}^{\text{no snow at } \mathcal{A}} \text{ AND } \left\langle \overbrace{\left[(P_{\mathcal{A}} > 0) \text{ AND} (P_{\mathcal{B}} = 0) \right]}^{\text{precip. at } \mathcal{A}\text{, but not } \mathcal{B}} \text{ OR } \overbrace{\left[(\eta > \breve{\eta}) \text{ OR} (\eta < \breve{\eta}^{-1}) \right]}^{\text{precip. at } \mathcal{A} \text{ not in } \breve{\eta}} \right\rangle \tag{3.1}$$

A cross-plot of daily precipitation between Summerland and Oliver is shown in Figure 3.3, which also shows the envelope cut-off value $\breve{\eta}$. The envelope cut-off was set at 2 to encompass most of the common points along the diagonal region of the plot, which are regarded as regional phenomena. A sensitivity analysis of different values of $\breve{\eta}$ and the corresponding fraction of local annual precipitation is shown in Figure 3.4. A value $\breve{\eta} = 2$ was ultimately used, which corresponds to ~54% of the annual precipitation regarded as local precipitation.

A problem with this analysis method is that it may not include regional phenomena recorded separately over two days; for example, noon precipitation that is recorded in the afternoon at one location, and recorded in the morning of the following day at the other location (Dingman, 2002, Ch. 4). Furthermore, the separation methodology may not exclude type I errors (i.e., "false positive"), where both locations record near-equal amounts of local precipitation from separate convective cells, which would be falsely interpreted as regional.

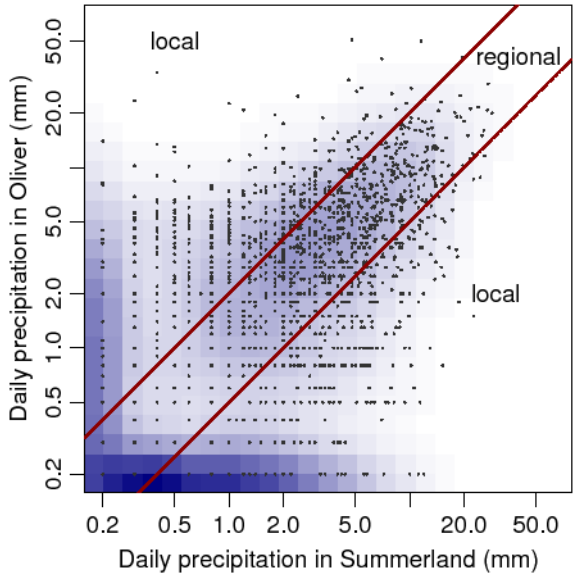

Figure 3.3 Cross-plot of daily precipitation between Summerland and Oliver using a log-log scale. Darker shading indicates higher density of log-transformed points, and lines represent a cut-off envelope, $\breve{\eta} = 2$ (or a line with slopes 2 and 0.5); points within the envelope are considered regional, while others are considered local.

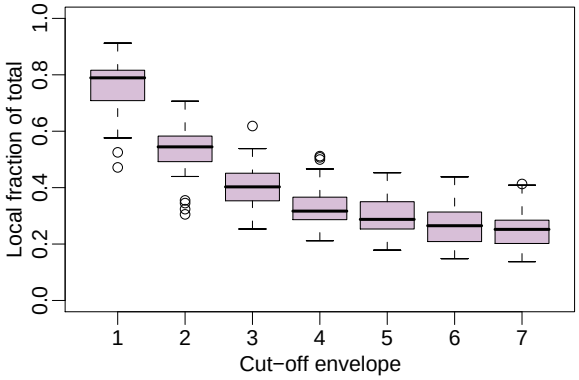

Figure 3.4 Sensitivity of the cut-off envelope for precipitation separation. Each boxplot shows the annual fraction of local precipitation selected from the total using different values of $\breve{\eta}$. A value of 2 was ultimately used in this study.

3.2.2 Recharge modelling

Rates of daily recharge and evapotranspiration were simulated using HELP 3.80D (Schroeder et al., 1994; Berger, 2004). This hydrology model uses daily precipitation, temperature and total global solar radiation to simulate water storage and flow on the ground surface and through the upper layers of a soil profile. Multiple surface and near surface hydrologic processes are simulated in the HELP numerical model, including: (1) accumulation of solid precipitation (snow and ice) on the surface; (2) surface runoff or infiltration; (3) estimated and potential evapotranspiration; (4) transpiration in relation to the growth and decay of vegetation; (5) soil freeze and thaw from air temperature; and (6) groundwater flow through discrete layers of variably saturated soil. The model uses vertical (1D) soil profiles, and simulates the leakage at the base of the profile. If the base of the soil column is set equal to the water table depth, the leakage across this boundary is effectively the groundwater recharge. HELP has been used extensively to estimate groundwater recharge (Gogolev, 2002; Scanlon et al., 2002; Scibek and Allen, 2006b; Jyrkama and Sykes, 2007).

Simulations were performed for a series of 86 soil columns using the three different precipitation time series (regional, local and total). Soil data for each column were derived from a detailed soil survey database[1] for the southern Okanagan and Similkameen regions of BC (Wittneben, 1986; Kenk and Sondheim, 1987). Each soil profile in the database has up to eight layers to a depth of ~1.2 m, which describe: proportions of sand, silt and clay, bulk density and available soil water capacity (water content between field capacity and wilting point). Other properties were available; however, these measured parameters could not be utilized as predictors by pedotrasfer function programs available at the time of writing (such as coarse fraction, organic carbon content, pH, CEC and others). Bulk soil texture properties for each soil column are shown in a USDA triangle plot in Figure 3.5 and are listed in Table 3.2.

[1]This soil database is available (not by the authors) in dBase format, at ftp://fshftp.env.gov.bc.ca/pub/outgoing/Soil_Data/CAPAMP/Okdsok/, uploaded 5 August 2005 and last accessed 13 September 2007.

Table 3.2 Bulk soil textures for each profile, from Figure 3.5. Full names and detailed descriptions of the soil profiles are available in Wittneben (1986). Thicknesses (cm) are for upper peat Th_{Pt} (if present) and silisiclastic portions Th_{Si} (in which the texture description is determined), and can be summed for the full depth of each profile.

Key	Txt*	Th_{Pt}	Th_{Si}	Key	Txt*	Th_{Pt}	Th_{Si}	Key	Txt*	Th_{Pt}	Th_{Si}
A	SiL	–	159	HA	S	–	133	PA	SL	4	116
AA	SL	–	136	HD	SL	3	123	PE	LS	4	85
AC	LS	–	157	HG	SiL	2	96	PL	SL	4	67
BE	SiCL	2	99	HN	L	3	140	PO	SL	–	120
BK	LS	3	91	IK	SiL	5	123	PR	SL	3	117
BL	LS	–	135	IL	LS	2	122	PT	SiL	4	130
CA	L	2	135	K	SiL	8	112	PY	S	5	95
CD	LS	2	112	KA	SL	–	119	R	LS	–	112
CH	SiL	–	110	KD	Pt	142	–	RH	L	55	65
CK	CL	2	111	KE	SL	–	164	RN	SL	–	137
CN	LS	3	105	KG	LS	2	110	RY	SL	3	115
CP	SL	–	133	KN	L	2	116	SA	SCL	4	113
CY	S	–	98	KR	SL	4	126	SK	LS	–	114
DE	LS	–	89	KY	SL	–	158	SM	L	–	120
DH	LS	–	127	LY	L	3	122	SN	SL	3	90
DL	Pt	165	–	MC	SiL	–	180	SO	S	–	140
DU	S	2	124	MD	L	4	105	SR	SiCL	–	125
EN	LS	2	109	MK	L	5	127	ST	L	–	100
ES	SL	–	88	ML	L	5	134	SU	LS	3	94
FR	L	–	95	MU	SiL	–	113	SW	SL	–	140
GF	LS	–	150	MY	S	2	94	TA	SL	–	125
GH	L	–	155	NG	S	2	62	TC	LS	3	135
GL	SiC	–	90	NK	SL	2	115	TL	SL	–	105
GM	S	5	125	NM	SiL	–	151	TM	LS	4	139
GN	SL	3	169	O	S	–	146	TR	L	3	160
GR	SL	2	114	OH	SL	–	131	VW	SiL	2	162
GS	SiCL	2	111	OL	L	–	114	WK	C	2	94
GT	L	–	123	OY	SL	–	147	WW	SL	3	115
GY	SiCL	2	122	P	SiL	–	130				

*S: sand; LS: loamy sand; SL: sandy loam; SCL: sandy clay loam; L: loam; SiL: silt loam; CL: clay loam; SiCL: silty clay loam; SiC: silty clay; C: clay; Pt: peat

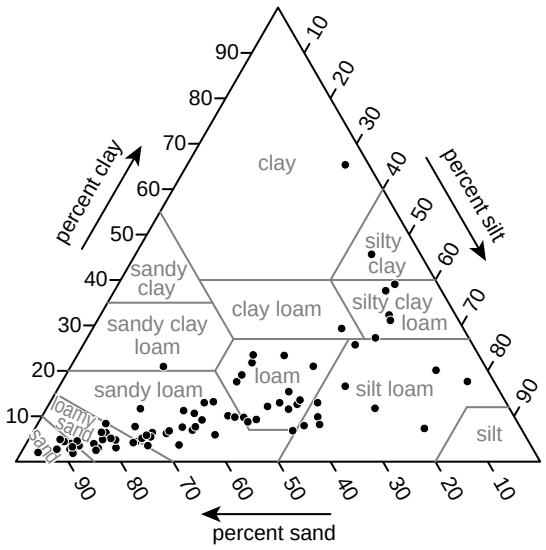

Figure 3.5 Bulk soil profile textures plotted on a USDA triangular plot (USDA, 2007). Percent sand, silt and clay are determined from a depth-weighted analysis from all the soil layers of each soil profile. Profile names for each group are listed in Table 3.2. All-peat soil profiles DL and KD are not plotted, since texture was not determined for peat horizons.

Soil hydraulic parameters were determined for each layer using the H3 hierarchical pedotransfer function in the ROSETTA model (Schaap et al., 2001, Version 1.2), which uses bulk density and proportions of sand silt and clay as input parameters. ROSETTA directly calculates saturated hydraulic conductivity, K_s, saturated and residual water contents, θ_s and θ_r, respectively, and van Genuchten (1980) water retention curve parameters α and n. Porosity, ϕ, was set equal to θ_s. Field capacity, θ_{fc} (where suction pressure, $|\psi| = 33$ kPa ≈ 337 cm of water) and wilting point, θ_{wp} (where $|\psi| = 1500$ kPa $\approx 15\,306$ cm) were calculated using:

$$\theta(\psi) = \theta_r + \frac{\theta_s - \theta_r}{[1 + (\alpha \cdot |\psi|)^n]^{1-1/n}} \tag{3.2}$$

Hydraulic properties for organic soil layers were determined independently using estimates from peat (Päivänen, 1973; Silins and Rothwell, 1998), as soil texture data were unavailable for these soil horizons. Saturated hydraulic conductivity for these layers was estimated using the linear relation (Päivänen, 1973):

$$\log_{10}(K_s) = 2.8 - 10\rho_b \tag{3.3}$$

Table 3.3 Input parameters used in HELP.

Parameter		Value
Runoff curve number		75
Leaf area index		2
Latitude		49.56°N
Evaporative depth zone		40 cm
Wind Speed		7 km/hr
Relative humidity	JFM:	79%
(Quarterly*)	AMJ:	53%
	JAS:	47%
	OND:	80%

*JFM = January, February, March, etc.

where K_s is saturated hydraulic conductivity (cm/day), and ρ_b is bulk density (Mg/m^3), which ranged between 0.22 and 0.36 Mg/m^3. The water retention parameters for peat were approximated by fixing $\theta_s \leftarrow 0.85$ (close to porosity), $\theta_r \leftarrow 0$, and $n \leftarrow 1.4$ (Silins and Rothwell, 1998). The α shape parameter was adjusted in equation 3.2 to obtain $\theta_{fc} - \theta_{wp} \approx \theta_a$, where θ_a is the available water content from the soil database.

All other HELP model parameters were held constant for each simulation (Table 3.3). Evaporative depth zone was set to a typical rooting depth for vegetation expected in the region. Percolation at the base of the soil column was regarded as groundwater recharge, although this typically varies depending on the depth to water table, and on the hydrogeology of deeper unsaturated horizons. All simulations were run using a scriptable Python module, which assembled and retrieved simulation data for HELP 3.80D.

3.3 Results

Precipitation images for Summerland for total, local and regional precipitation proportions are displayed in Figure 3.6. A precipitation image (Toews et al., 2007) can provide a detailed visual description of the seasonal distribution of any discontinuous variable (such as precipitation or recharge rates). The image shows precipitation rates for 11-day

groups for each year, which are sorted and contoured in the lower-left frames of each image to show the distribution of precipitation rates at any given time of the year. Annual totals, or row-wise sums are plotted on the right side. A seasonal 'normal' can be derived from the figure as the normally occurring rate across the span of the year, which is indicated with a horizontal line. Figure 3.6b shows the local separation of precipitation events from regional precipitation between approximately April to September (Figure 3.6c).

Separated precipitation data (local, regional) as well as total precipitation were used as inputs to the recharge model. Annual recharge (mm/year) results for all 86 soil profiles are shown as boxplots in Figure 3.7. Results are sorted from least to greatest total recharge. The general trend shown by the left-to-right ordering in this figure is from lower rates in the fine-grained clay soils, to larger recharge rates in the coarser soils.

Recharge simulated using the total precipitation series (Figure 3.6a) is represented best by recharge simulated using the regional precipitation time series (Figure 3.6c). Recharge rates using the local precipitation series (Figure 3.6b) are almost all zero, as shown in Figure 3.7. The simulation results suggest that the soil moisture during simulation was too dry for water to begin flowing, likely due to high rates of evapotranspiration during the summer than in winter. As the local precipitation events are associated with summer evapotranspiration (and local convection), establishing subsurface moisture essential for recharge flow is difficult to establish with a simulation with limited precipitation input.

Recharge images for each of the total, local and regional simulations for the CY soil profile (chosen as an example) are shown in Figure 3.8. Recharge simulated with the total precipitation (Figure 3.8a) has increasing rates from December to January, and decreased rates through the later part of the winter season (until March). Recharge increases again in late May, peaks in June, and decreases in July. Recharge simulated using regional precipitation (Figure 3.8c) has a very similar form. Recharge simulated using local precipitation (Figure 3.8b) has very weak recharge pulses with no seasonality.

As discussed above, summer precipitation is of particular interest in statistical downscaling of global climate data. Previous attempts in south-central BC have had limited success calibrating and perturbing mid-summer precipitation (Scibek and Allen, 2006b;

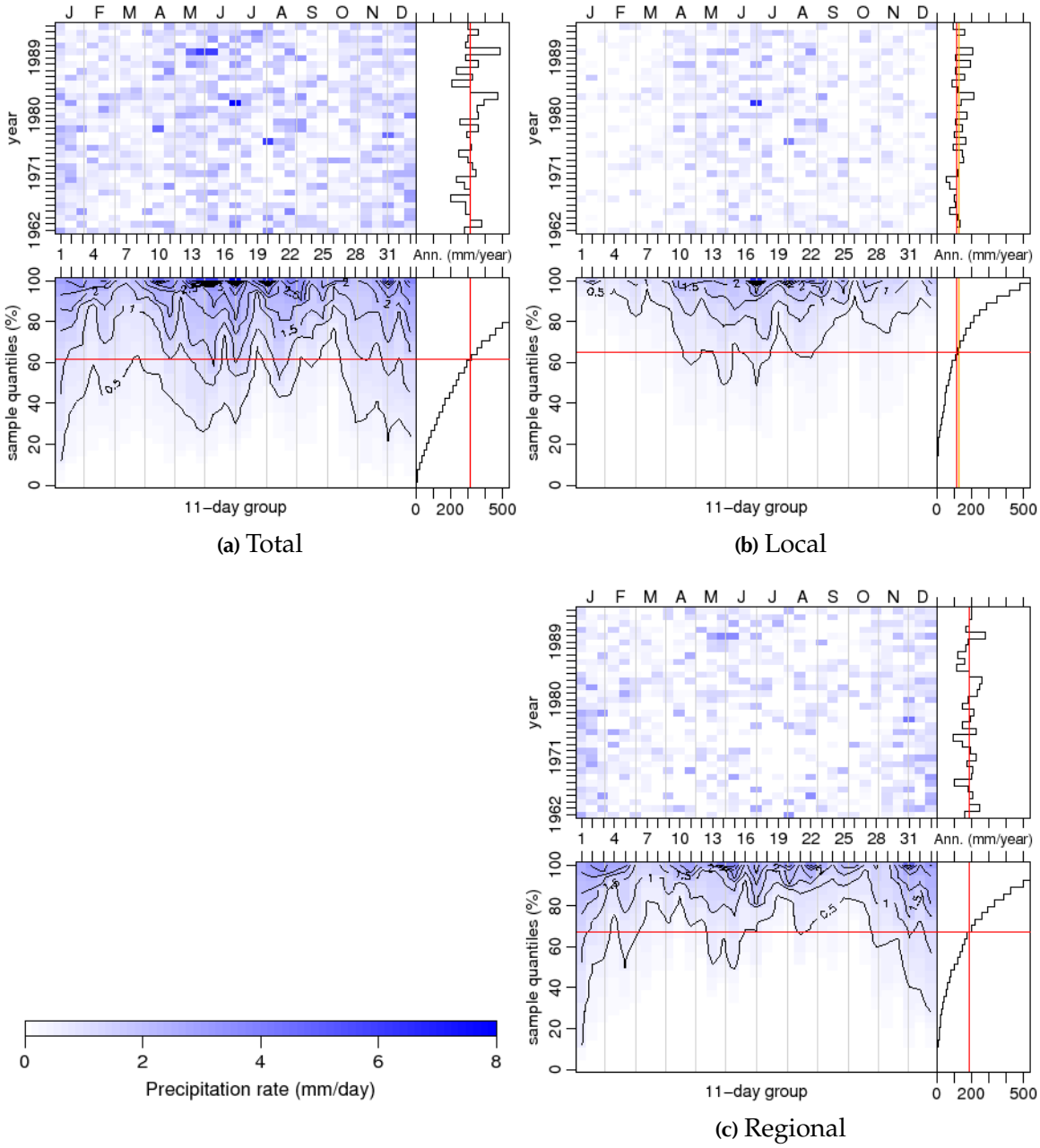

(a) Total

(b) Local

(c) Regional

Figure 3.6 Detailed images of separated precipitation from Summerland of (a) total, (b) local, and (c) regional amounts. Each image shows measured rates in the upper frame, and are sorted and contoured in the lower frame to show distributions of precipitation rates throughout the year; annual totals (row-wise sums) are shown in the right-side frames of each image.

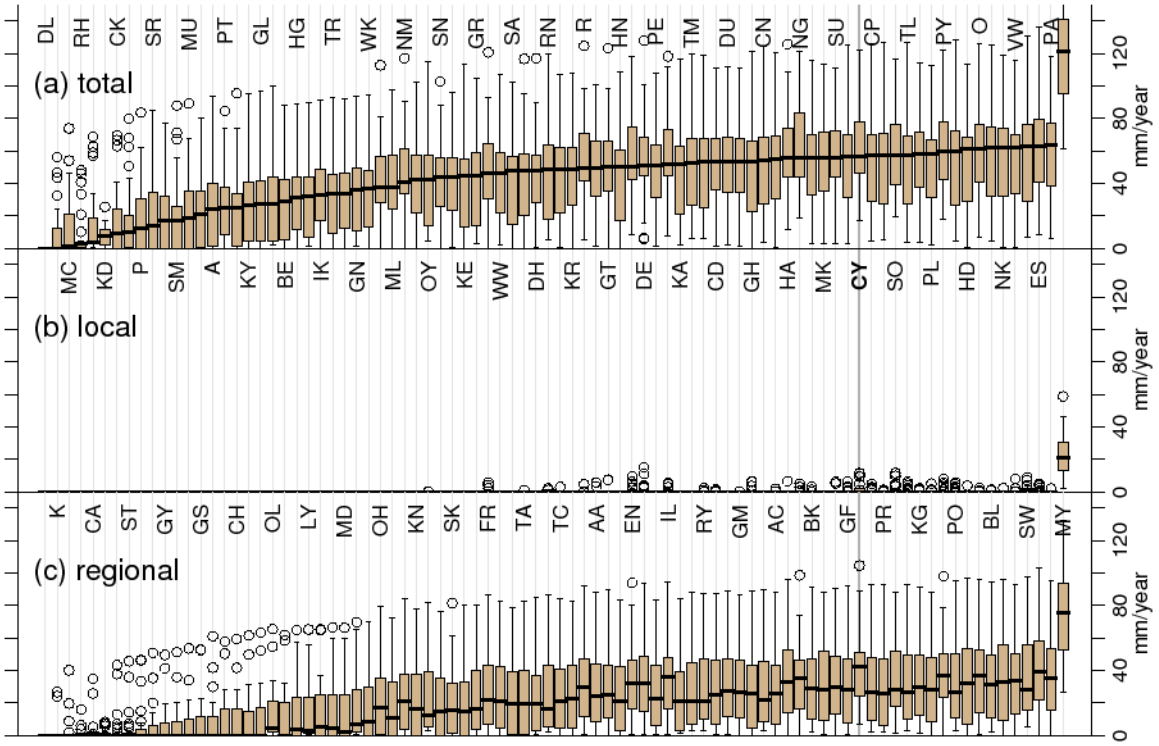

Figure 3.7 Boxplots of annual recharge using (a) total, (b) local, and (c) regional precipitation (mm/year). Results from each soil profile (indicated with letters from the database key) are sorted from least to greatest total recharge. An arbitrarily selected CY soil profile is detailed in Figure 3.8.

Merritt et al., 2006). It is likely that this observed precipitation is from local convection, as synoptic-scale NCEP/NCAR reanalysis data (Kalnay et al., 1996) underestimate precipitation during summer months for this region.

Although reliable downscaling of locally-derived convective precipitation is critical for surface runoff and streamflow (e.g. Salathé, 2003), this study suggests that the effects on both the timing and seasonal signal of modelled recharge response are limited. The limiting influence of summer time recharge is presumed to be controlled dominantly by the high evapotranspiration at that time of year.

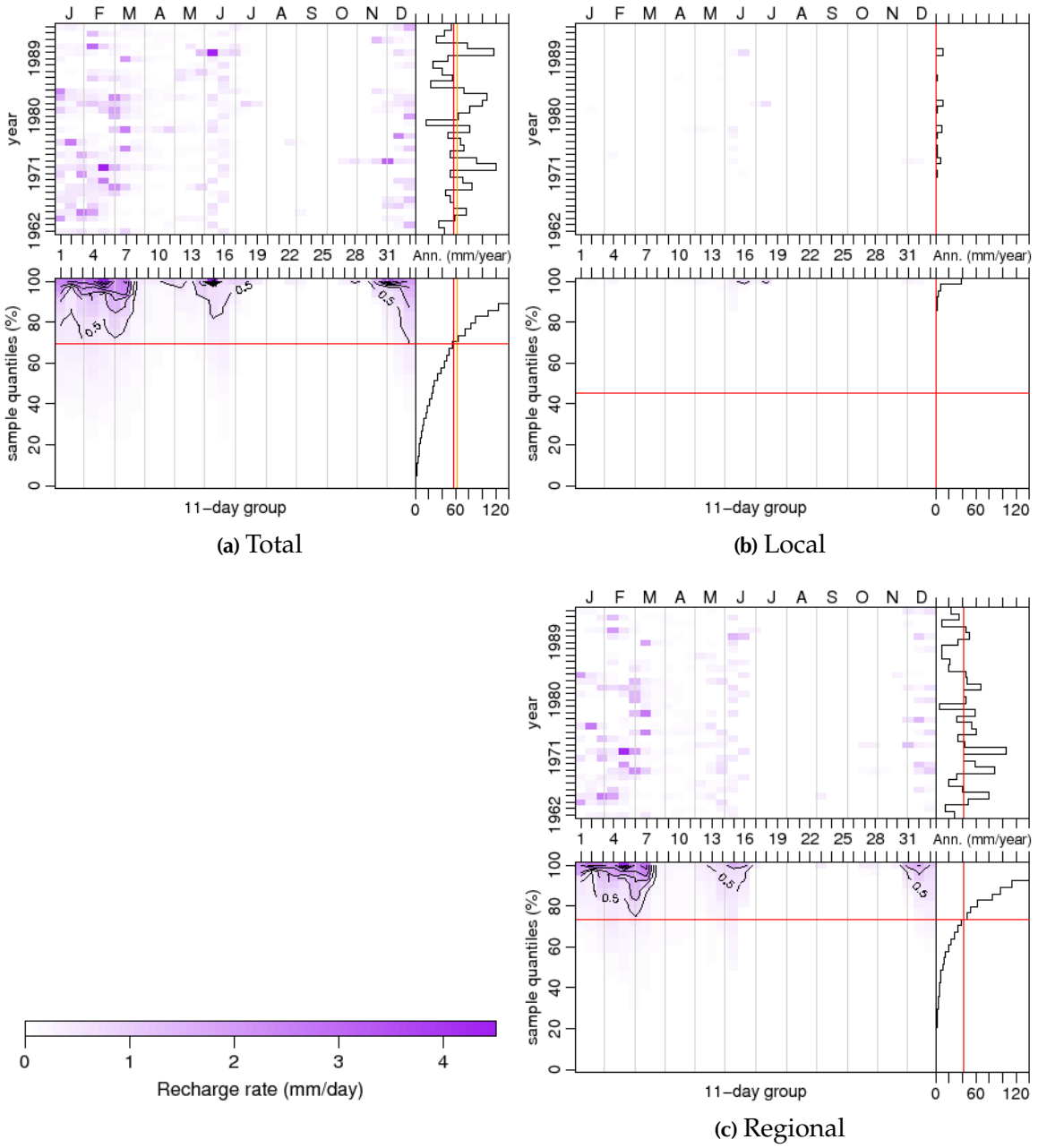

(a) Total

(b) Local

(c) Regional

Figure 3.8 Detailed images of recharge rates in the CY soil profile, using (a) total, (b) local, and (c) regional precipitation inputs.

3.4 Conclusions

Daily precipitation time series were separated into regionally and locally derived sources using a cross-plot of values from two regions in Okanagan Valley. The local, regional and total precipitation components were independently simulated in the HELP hydrology model to evaluate the recharge response through multiple soil columns from soil surveys from the region. Recharge results show that the majority of recharge is controlled from the regionally derived precipitation, while there is much less influence from locally derived precipitation. This contrast of recharge rates is influenced by the timing of regional precipitation during late winter and spring, when evapotranspiration is limited. Local precipitation, however, is typically associated with higher evapotranspiration rates during mid-summer, thus contributing little to recharge during this time. The implication of the research is that precipitation data from global climate models may provide reasonable estimates for groundwater recharge modeling, notwithstanding their poor ability predicting local precipitation.

Acknowledgments

The authors gratefully acknowledge Tom Mathews from Environment Canada for providing solar radiation data.

Chapter 4

Spatial Recharge in the Arid Southern Okanagan Basin and the Influence of Future Predicted Climate Changes

*By Michael W. Toews and Diana M. Allen**

To be submitted as a Paper to Journal of Hydrology

Abstract

Groundwater systems in arid regions will be particularly sensitive to climate change owing to the strong dependence of rates of evapotranspiration on temperature, and shifts in the precipitation regimes. Within high latitude countries, loss of winter snowpack and timing of snowmelt can potentially have significant impacts on the amount and timing of spring runoff, and these shifts may consequently influence groundwater recharge. In this study, future predicted climate change scenarios from three GCMs (CGCM1 GHG+A, CGCM3.1 A2, and HadCM3 A2) are used to evaluate the sensitivity of recharge in the

*By permission

Oliver region of the arid Okanagan Valley where annual precipitation is approximately 300 mm. Temperature data were downscaled using Statistical Downscaling Model (SDSM), while precipitation and solar radiation changes were estimated directly from the GCM data. Results for the region suggest that temperature will increase up to 4°C by the end of the century. Precipitation is expected to decrease in the spring, and increase in the fall. Solar radiation may decrease in the late summer. Shifts in climate, from present to future-predicted, were applied to a stochastic weather generator. A one-dimensional hydrologic model, HELP, was applied spatially over a 22.5 km by 8.6 km region around Oliver. A GIS soil-survey database was used to construct vertical soil profiles used in the modelling process. Other spatially distributed parameters, such as slope and vegetation, were incorporated into the model. Recharge results show a general increase of annual recharge, with the peak recharge shifting from March to February. Lower recharge rates and higher potential evapotranspiration rates are expected in the summer. The minor increase of annual recharge in future predicted climate states is due the shift of peak recharge from increased temperature. Irrigation application rates were also modified for each climate scenario to match present irrigation application rates. Recharge in these areas are significantly higher, with irrigation return flow between 25–58%. Growing season lengths, as determined from growing degree day accumulation, are expected to lengthen by 3–4 weeks by the 2080s.

Keywords: recharge modelling; climate change; GCM; Okanagan

4.1 Introduction

Rates of groundwater recharge depend on the regional climatology, the physical properties of the upper soil layers, and land uses. Changes in any of these conditions will potentially modify recharge rates and, ultimately, modify groundwater flow and the sustainability of the groundwater resource. Influences of climate on recharge, in general, are not well understood—and uncertainties in recharge prediction are confounded by climate

change and natural climate variability. Thus, understanding the link between climate and recharge processes is essential to investigating the sensitivity between the two systems.

Groundwater systems in arid regions will be particularly sensitive to climate change owing to the strong dependence of rates of evapotranspiration on temperature, and shifts in the precipitation regimes. Irrigation use is typically a large component of the water budget in such regions, which may increase due to changes in soil moisture resulting from higher temperatures and changes in the timing of precipitation events. Within high latitude countries, loss of winter snowpack and timing of snowmelt can potentially have significant impacts on the amount and timing of spring runoff (Whitfield and Cannon, 2000), and these shifts may consequently influence groundwater recharge (Scibek and Allen, 2006b).

Assessing the impact of climate change on groundwater resources requires a physically based approach for estimating groundwater recharge. The method must not only account for temporal variations in climatic variables and their impact on the hydrologic cycle, but also consider the spatial variation of surface and subsurface properties across the study area (Jyrkama and Sykes, 2007).

To date, a handful of studies have attempted to model temporal and spatial changes in groundwater recharge, each with varying degrees of sophistication. Jyrkama and Sykes (2007) used 40 years of past climate data to simulate groundwater recharge across the Grand River Basin in south-western Ontario, Canada. Digital spatial land use and land cover (LULC) data and soil data were used as input to the HELP hydrologic model (Schroeder et al., 1994). Climate change scenarios were based on the Intergovernmental Panel on Climate Change (IPCC) Third Assessment report (Houghton et al., 2001). Climate inputs to the stochastic weather generator in HELP were shifted according to a range of relative shifts in precipitation, and absolute shifts in temperature and solar radiation. However, the weather generator assumes that other statistics remain constant for dry/wet days. Results suggested an increase in groundwater recharge across the region, with higher intensity and higher frequency of precipitation contributing to greater surface runoff, and higher temperatures resulting in increased evapotranspiration. The increase

in annual recharge was due largely to warmer winter temperatures reducing the extent of ground frost and shifting spring melt to earlier in the year, thus permitting more infiltration.

Scibek and Allen (2006b) simulated the impacts of climate change on recharge in the semi-arid region of Grand Forks, British Columbia, Canada using a similar approach to Jyrkama and Sykes (2007). Scibek and Allen (2006b) downscaled predictions of absolute shifts in temperature and relative shifts in precipitation derived from CGCM1, along with absolute shifts in solar radiation (not downscaled) to generate stochastic weather series using LARS-WG (Semenov and Barrow, 1997) for current and two future time periods, which were used to drive the HELP hydrologic model. In the 2010–2039 climate period, recharge increased from between 2 to 7% (spatially-variable) relative to the historical mean annual recharge, while in the 2040–2069 climate period, recharge increased by 11 to 25% relative to the historical mean annual recharge. The contribution of irrigation was also considered to add to recharge as a fixed percentage (25%), but was not altered for future climate simulations. Spatially distributed recharge estimates were then used as a surface boundary condition (recharge flux) in a numerical model, and the impacts on the groundwater system were quantified. Because the aquifer is in close hydraulic connection to the Kettle River, which meanders through the Kettle Valley, the predicted hydrologic response of the river to climate shifts were incorporated in the model as shifts in river stage. Overall, the shifts in the river's hydrologic response had a much greater influence on groundwater levels (timing of peaks and lows) than shifts in direct recharge under the scenario of climate change considered.

Vaccaro (1992) investigated groundwater recharge in the arid to semiarid Ellensburg basin in the Columbia Plateau, Washington (approx. 250 km south-west of Oliver). In that study, the sensitivity of recharge was investigated using stochastic weather for historic and future-predicted climate changes simulated in GCMs. Synthetic weather data were generated using WGEN (Richardson and Wright, 1984), and recharge was modelled using a deep percolation model (Bauer and Vaccaro, 1987). Land use conditions and irrigation were also considered in that study. Mean annual precipitation was estimated at 230 mm,

Figure 4.1 Map of southern Okanagan Basin, highlighting the Oliver study region, which is bounded by Vaseux Lake and Osoyoos Lake.

and irrigation use (for current and future) was estimated to be 440 mm. Recharge estimates were found to be ∼60 mm for natural (sagebrush) coverages, and 230 mm for irrigated coverages. Their estimates for future scenarios with an "average GCM" showed significant decreases of recharge in irrigated coverages (25%), and modest decreases (16%) over the natural cover.

The current study builds on these studies by attempting to simulate the changes in groundwater recharge in an arid region of Canada using downscaled data from three different GCMs. The study site is situated in the southern Okanagan Basin, in southern Okanagan Valley, between Vaseux Lake and Osoyoos Lake, and passes through the Town of Oliver (Figure 4.1). The region is highly dependent on groundwater from unconfined aquifers for both water supply and irrigation. Global climate model (GCM) data from three GCMs (CGCM1, CGCM3.1 and HadCM3) are used to force a hydrologic model in

order to investigate the potential changes in recharge under scenarios of future-predicted climate change. Three different GCMs are selected to better reflect the range of scientific approaches used by the climate modelling community. All atmospheric models are synoptic-scale (spatial resolution on order of 2° to 4° or hundreds of kilometres between grid points), and couple ocean, sea-ice and land-surface processes with atmospheric processes.

The objectives of this paper are to estimate changes in future predicted climate change near Oliver using GCM data, and then to apply the synthetic climate data to a hydrologic model to simulate recharge. Recharge for each climate change scenario at future time periods is estimated. The methodology uses a combination of computer models including: (1) GCMs for future-predicted climate change periods; (2) Statistical Downscaling Model (SDSM) to statistically downscale temperature from GCMs; (3) LARS-WG to stochastically generate weather and evapotranspiration data; (4) ROSETTA to estimate the hydraulic properties of soils from given soil measurements; and (5) HELP for simulating surface and subsurface hydrology from climate and soil data. Results are obtained for a grid with 100 m resolution, using geospatial data from each location, including soil, land use, surface slope, groundwater depth, and leaf area index (LAI).

4.2 Background and data

4.2.1 Study area and climate

Okanagan Valley is a narrow, north–south trending valley that is deeply incised in the Interior Plateau of the North American Cordillera. It has a topographic relief of $\sim$1100 m from the valley bottom to the surrounding plateau level. Within the study region, the topography varies from 375 to 1862 m at Mt. Kobau, 7 km east of Oliver. The valley width ranges from less than 2 km at McIntyre Bluff at the north end of the study region, to 5 km near Oliver. The valley bottom is generally flat, with the exception of a few minor raised 'bars' along the valley center, and other small isolated topographic depressions. The sides

of the valley have at least four Pleistocene-aged terraces, consisting of mainly glaciofluvial sand and gravel deposits.

The southern Okanagan is the only populated arid region in Canada, with typical 'wet' seasonal patterns occurring in the winter and summer periods. The annual precipitation in the valley bottom is about 300 mm, and nearly twice that amount at higher elevations (such as Mt. Kobau), with a regional precipitation gradient decreasing toward the southwest. Winter precipitation is typically in the form of snowfall, derived from frontal systems, while rainfall from May to June is from cold lows, and from August to September from convective precipitation systems (B. Taylor, pers. comm. 2007; Environment Canada, 2006).

Precipitation regimes were analyzed by Toews et al. (see Chapter 3) and precipitation time series were separated as local and regional sources. These time series were simulated in HELP using data from soil profiles common to the region. Recharge results show that the majority of recharge is controlled from the regionally derived precipitation, while there is much less influence from locally derived precipitation. This contrast is influenced by the timing of regional precipitation during late winter and spring, when evapotranspiration is limited. Local precipitation, however, typically is associated with higher evapotranspiration rates during mid-summer, thus contributing little to recharge during this time. The inference from this sensitivity study is that recharge is not sensitive to summer precipitation, which GCMs are not able to resolve with through coarse resolutions.

4.2.2 Observed weather data

Daily measurements of precipitation and temperature are available throughout much of the Okanagan, and are provided by the Meteorological Service of Canada (Environment Canada, 2002). Station names and locations are listed in Table 4.1. Hourly global solar radiation data are available at Summerland and Mt. Kobau, west of Oliver, and hourly wind velocity and relative humidity data from Osoyoos, south of Oliver. These climate

Table 4.1 Weather stations used from Okanagan Basin. Multiple stations from regions were used to complete missing data.

Station name	ID	Location	Elev. (m)	Years
Oliver*	1125760	49°10′ N, 119°34′ W	315	1938–*present*
Oliver STP	1125766	49°11′ N, 119°33′ W	297	1924–2004
Mt Kobau Observatory†	1125223	49°07′ N, 119°41′ W	1862	1966–1980
Osoyoos CS	1125852	49°02′ N, 119°26′ W	283	1990–*present*
Summerland CDA*†	1127800	49°34′ N, 119°39′ W	455	1916–1995
Summerland CS	112G8L1	49°34′ N, 119°39′ W	434	1990–*present*

*Primary stations for daily temperature and precipitation
†Station with hourly solar radiation

variables are used to (1) calibrate the stochastic weather generator, (2) downscale GCM climate variables, and (3) provide meteorological data to estimate evapotranspiration.

Temperature and precipitation normals for Oliver are shown in Figure 4.2. The diurnal variability of temperature in Figure 4.2a is greatest during the summer (as indicated by the thick vertical lines), while the largest variability in seasonal mean temperature is during the winter time (as indicated by the heights of the 1st and 3rd quartiles of the boxplots). Outlier temperature minima between November and February are likely indicative of cool arctic climate systems. Maximum temperatures in the Oliver region peak near July 27. Precipitation normals (Figure 4.2b) are bimodal, with higher precipitation normals during summer and winter months. Precipitation normally occurs in the form of snow between December and January.

4.2.3 Global climate models

Coupled atmosphere-ocean global climate models (GCMs) are used to estimate changes in climate to the end of the 21st Century. These physically-based numerical models simulate synoptic-scale climate and hydrological processes (Washington and Parkinson, 2005), and are forced with greenhouse gas and aerosol emission scenarios (Solomon et al., 2007). A wide diversity of GCMs developed by leading climate centres are available for other researchers to evaluate potential impacts of climate change. Three GCMs were selected

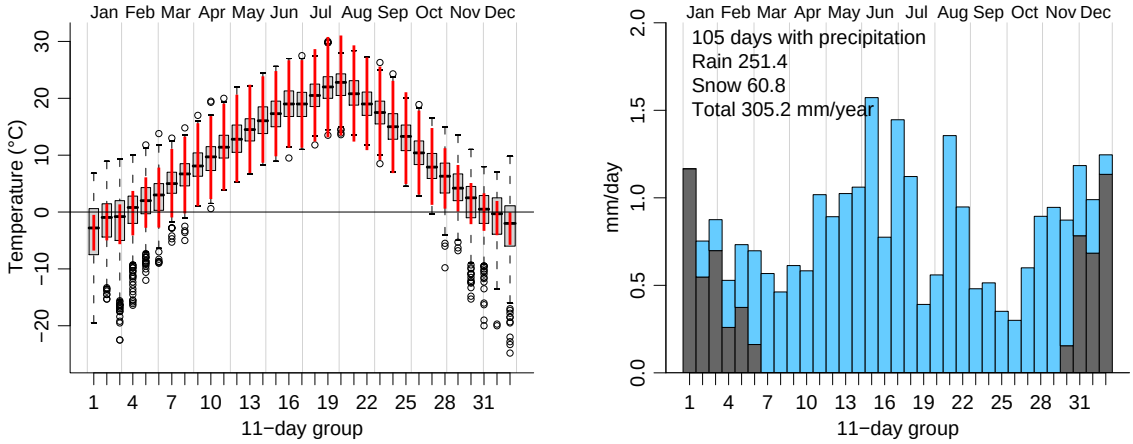

(a) Temperature boxplots; thick vertical lines represent diurnal variability between daily $T_{\min}$ and $T_{\max}$

(b) Precipitation; showing rain and snow fractions

Figure 4.2 Temperature and precipitation normals for Oliver (1961–2000).

for this analysis, which represent a range of possible outcomes of climate change for south-central BC. All models used in this study are the 'A'-series emission scenarios of greenhouse gas emissions and aerosols, which are generally referred to as the "business as usual" family of emission scenarios. The GHG+A scenario was first introduced by Houghton et al. (1992), and has further been refined to the A2 scenario (Nakicenovic and Swart, 2000), which is generally considered the current state of business. Data for CGCM1 and HadCM3 (including regridded NCEP/NCAR predictors) were provided by the Canadian Institute for Climate Studies (2005). CGCM3.1 predictor data sets for SDSM were not available at the time of analysis, and were manually constructed (see Appendix B.1.1.1, page 180) from available data and resources (NCAR, 2006; Zender, 2007). Climate data and recharge results were compared at several time-ranges, listed in Table 4.2.

CGCM1 and CGCM3.1 were developed at the Canadian Centre for Climate Modelling and Analysis (Flato et al., 2000). The older of the two, CGCM1/T32L10, is used to compare results with other similar studies (Scibek, 2005). It is forced with the GHG+A IPCC IS92a emission forcing scenario (Houghton et al., 1992), and is based on the AGCM2 atmospheric general circulation model (McFarlane et al., 1992).

Table 4.2 Time ranges used for climate state comparison, and their approximate decade name referred to in this paper. Differences between the ranges between GCMs are due to limited data availability of CGCM3.1

	CGCM1/HadCM3		CGCM3.1	
Name	Start	End	Start	End
base or current	1961	2000	1961	2000
2020s	2010	2039	*not available*	
2050s	2040	2069	2046	2065
2080s	2070	2099	2081	2100

The most recent model, CGCM3.1/T47L31, is based on the AGCM3 atmospheric general circulation model, which utilizes the CLASS module (Canadian Land Surface Scheme) for synoptic-scale interactions between soil, snow and canopy surfaces (Verseghy et al., 1993). The first run (of three) of the IPCC SRES A2 emission scenario (Nakicenovic and Swart, 2000) was selected from this GCM. Both GCMs from CCCma have the same spatial grid dimensions of 96×48 and use a 365-day year (no leap) calendar. GCM variables were selected at the grid point at $\sim$50.1° N, 120.0° W (Figure 4.3). Although CGCM3.1 was simulated between 1961–2100, only certain time periods were available for required climate variables (consequently, there is no "2020s" time period in this analysis).

The Hadley GCM models are considered to the most mature and popular of the GCMs, and have formed the basis for many of the conclusions in past IPCC reports (e.g., Houghton et al., 2001). HadCM3 with the A2 emissions scenario was selected (Gordon et al., 2000). This GCM is unique in that it does not require flux adjustments to produce a realistic scenario (Collins et al., 2001). The GCM uses a 360-day year, and has a fixed spatial grid with dimensions 96×73; data were selected from the grid point at 50.0° N, 120.0° W (Figure 4.3).

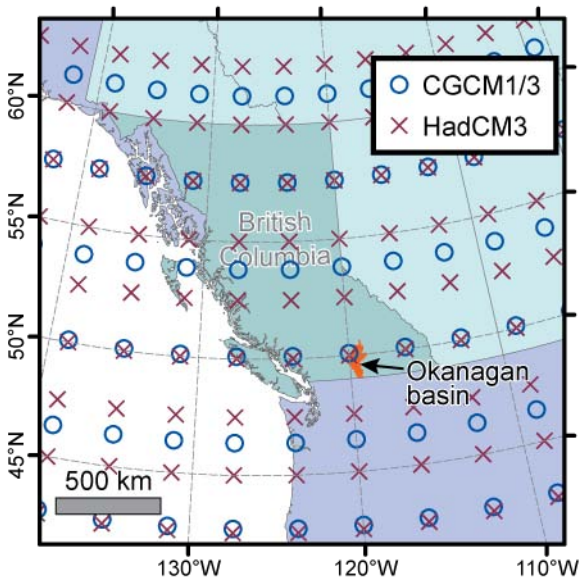

Figure 4.3 Map of western Canada, showing Okanagan basin, and GCMs grid points.

4.2.4 Spatial data

Input spatial data, used both directly and indirectly to model recharge, are shown in Figure 4.4. An extensive valley-bottom soil database was used to determine both the spatial variation and vertical assemblage of soil horizons in the Oliver region (Wittneben, 1986; Kenk and Sondheim, 1987). The database identifies 91 primary soil types from the valley-bottoms of the Okanagan and Similkameen regions. This GIS database represents soil coverages with polygons, which identify the dominance of up to three primary soil types in each polygon (Figure 4.4a), which are weighted by deciles. Physical and chemical measurements were recorded from type-section pits (~1.2 m deep) for each primary soil type. Each soil type is described with up to eight layers, and layer data include bulk density, available water content, soil chemistry measurements, and percentages of: coarse material (>2 mm), sand, silt, clay, and organic matter. Soil drainage was obtained from the bulk properties assigned to each soil type (Figure 4.4b).

Level 1, 1:50 000 series (0.75-arc second resolution) digital elevation data (Natural Resources Canada, 2005) were used to determine surface slope (Figure 4.4c). Leaf area index (LAI) was estimated from Landsat 5 TM imagery acquired on August 8, 2005 (Soffer et al.,

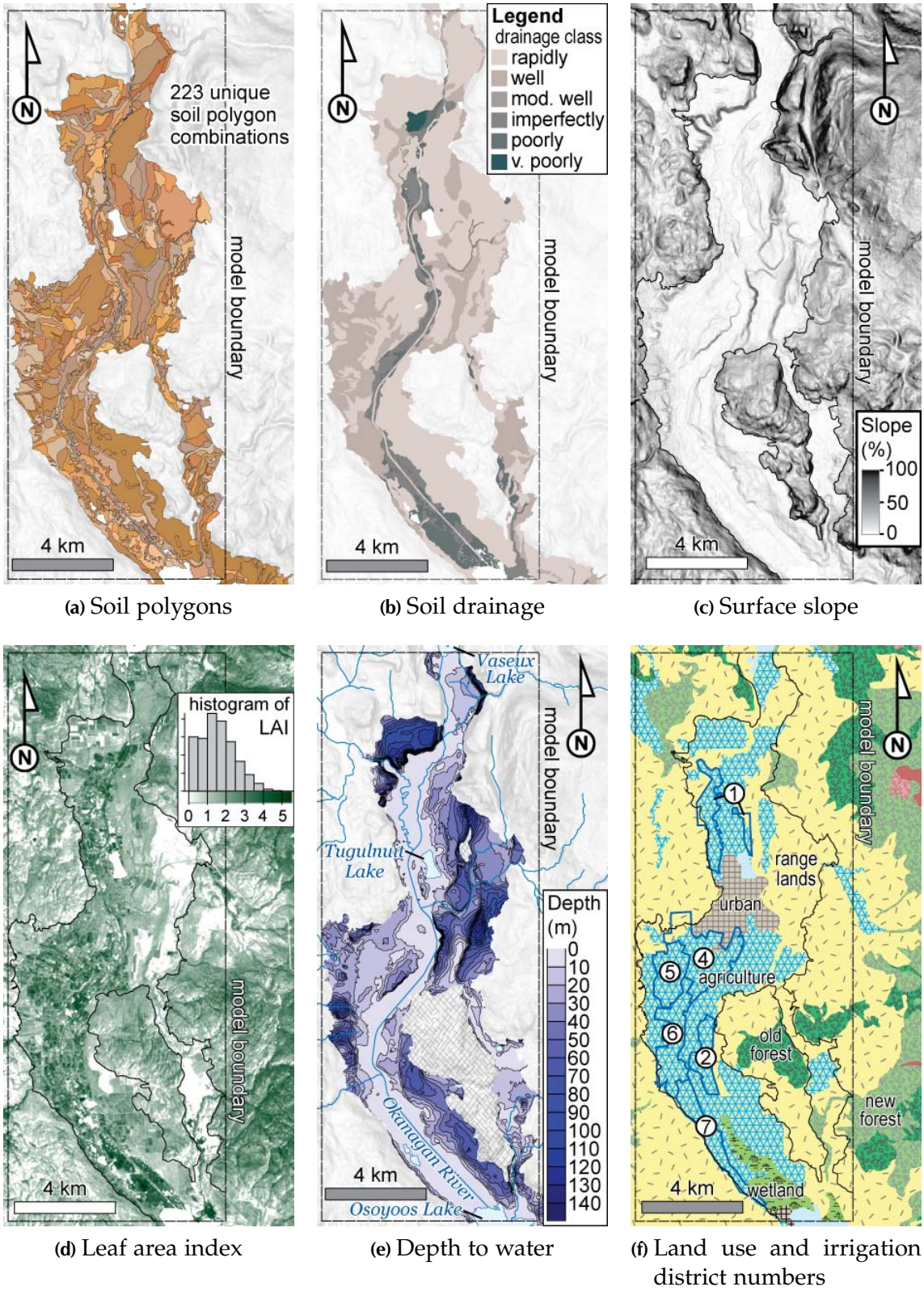

(a) Soil polygons **(b)** Soil drainage **(c)** Surface slope

(d) Leaf area index **(e)** Depth to water **(f)** Land use and irrigation district numbers

Figure 4.4 Spatial input variables for HELP model, described in the text.

2007), and algorithms were calibrated from ground measurements made in August of 2005 and 2006 (e.g., Fernandes, 2003; Leblanc et al., 2005). LAI data were originally gridded at 30 m resolution (Figure 4.4d), but were regridded to a coarser 100 m resolution. Depth to water table (Figure 4.4e) was determined using differences between ground elevation and interpolated water table elevation. Water table elevation data were interpolated using natural neighbours (e.g., Sibson, 1981) on a 100 m grid using water depth records in a water well database (BC MoE, 2006), and well elevations determined from digital elevation data using their coordinates. Vector-based 1:250 000 land use data (Yazdani et al., 1992), and locations of irrigation districts (T. Underwood, pers. comm. 2006) are shown in Figure 4.4f.

4.3 Methods

4.3.1 Statistical downscaling

To insure that the predictive elements from a GCM are realistic, a statistical downscaling technique should be employed to bridge the local- and synoptic-scale processes (Wilby and Wigley, 1997). Statistical downscaling uses a correlation between *predictands* (site measured variables, such as precipitation) and *predictors* (region-scale variables, such as GCM variables).

SDSM version 3.1 (14 May 2004 edition) was used to downscale temperature data (Wilby et al., 2002; Wilby and Dawson, 2004). SDSM uses a multi-linear regression approach, using one or more synoptic-scale predictors to build a correlation with the predictand variables (station measured data). This correlation is calibrated using NCEP/NCAR reanalysis data (Kalnay et al., 1996), which are gridded daily historic data that have been processed from the vast record of world-wide measured data. The reanalysis data are regridded to match the spatial resolution of each GCM, and the downscaling is calibrated from correlations between the measured data and the regridded NCEP/NCAR data.

Table 4.3 Synoptic-scale predictors used to downscale temperature.

SDSM label	Description	CGCM1/ CGCM3.1	HadCM3
`temp`	mean temperature	✓	✓
`p850`	850 hPa geopotential height	✓	✓
`r850`	850 hPa relative humidity		✓
`s850`	850 hPa specific humidity	✓	
`p5_z`	500 hPa vorticity*	✓	✓

*Derived from zonal and meridional wind components

Four predictors, shown in Table 4.3, were selected from the NCEP/NCAR variables, as they were found to have good monthly correlations with the station measured daily mean temperature in Oliver (see Table B.2). These predictors were used to calibrate SDSM for CGCM1/3.1 and HadCM3 for minimum temperature, maximum and mean temperatures (T_{min}, T_{max}, and T_{mean}, respectively). Variance inflation was adjusted to 12 to match observed distributions, and 20 ensembles were generated for each scenario. Details and additional data concerning temperature downscaling are provided in Appendix B.

Precipitation is commonly downscaled in climate change impact studies (e.g., Wilby and Wigley, 2000; Salathé, 2003); however, the reliability of the downscaled result is often poor or unreliable, as there is often little correlation between the predictors and the predictands (e.g., Scibek and Allen, 2006b; Merritt et al., 2006). A poor correlation is often attributed to mesoscale processes occurring at the site-scale that are not represented in regional models due to their representative spatial and temporal sizes in comparison to larger-scale regional precipitation (Kim et al., 1984). Mesoscale precipitation processes generally occur in the summer season in the form of convective clouds, which are a result of local-scale evapotranspiration from elevated temperatures and solar radiation magnitudes. As a result, global-scale models may underestimate the summer precipitation measured at a site.

Downscaling of solar radiation and precipitation using SDSM near Oliver was attempted; however, the correlations between predictors and predictands during calibration

were poor, and the attempts producing future scenarios appeared unrealistic and inconsistent with regional trends from the GCM. Merritt et al. (2006) independently arrived at the same conclusion for Okanagan Basin using similar data and downscaling methods. Instead, relative changes in solar radiation and precipitation were identified in the GCMs, and were applied directly to the stochastic weather generator. This methodology, although less sophisticated, avoids introducing potentially erroneous climate trends into future climate predictions.

4.3.2 Stochastic weather generation

Weather and evaporation data were generated stochastically generated using LARS-WG (Semenov and Barrow, 1997). This weather generator is calibrated using daily precipitation, maximum and minimum temperature, and global solar radiation. The calibration process uses conditional relationships between the observed parameters. For example, realistic temperature and solar radiation values are generated depending whether the day is considered rainy or dry. Recurrence of precipitation is determined using a first-order Markov chain.

LARS-WG can reproduce realistic climate data, which has similar climate normals to the original data. In addition, the climate output from LARS-WG can be adjusted using monthly shift terms. This is useful for creating realistic climate change scenarios, by adjusting, for example, the absolute maximum temperature in September by $+2.3^{\circ}$C, or the relative change of precipitation in December by -23.2%. The monthly shift terms can be viewed symbolically as:

$$\bar{T}_{\mathcal{S}2} = \bar{T}_{\mathcal{S}1} + \Delta\bar{T}_{\mathcal{S}1\rightarrow\mathcal{S}2} \tag{4.1a}$$

$$\bar{P}_{\mathcal{S}2} = \bar{P}_{\mathcal{S}1} \cdot \delta\bar{P}_{\mathcal{S}1\rightarrow\mathcal{S}2} \tag{4.1b}$$

where $\bar{T}$ and $\bar{P}$ are the monthly normals between climate states $\mathcal{S}1$ and $\mathcal{S}2$; Δ symbolizes an *absolute* change and δ for a *relative* change. The complete set of available shift terms

used in LARS-WG includes absolute changes to monthly maximum and minimum temperatures, and relative changes to monthly total precipitation, solar radiation, standard deviation of temperature, and the durations of wet- and dry-spells.

The shift terms are determined by comparing the monthly climate normals between two climate states, which generally have about 30 years of data. A climate state is the condition of a climate system at a time and/or location that produces a unique set of climate normals. The shift terms are simply a rearrangement of equations 4.1a and 4.1b, and can be calculated from two climate normals:

$$\Delta\bar{T}_{\mathcal{S}1\rightarrow\mathcal{S}2} = \bar{T}_{\mathcal{S}2} - \bar{T}_{\mathcal{S}1} \tag{4.2a}$$

$$\delta\bar{P}_{\mathcal{S}1\rightarrow\mathcal{S}2} = \frac{\bar{P}_{\mathcal{S}2}}{\bar{P}_{\mathcal{S}1}} \tag{4.2b}$$

Data from Summerland between 1962 and 1995 were used to calibrate LARS-WG, since all the required climate variables were available at this location. Although Summerland is 50 km to the north of Oliver, the two locations share a similar climatology, and are both in the valley-bottom of Okanagan Basin. The slight climate variability between the two locations is compensated by determining shift (equations 4.2a and 4.2b) from the climate normals calculated using concurrent historical data (see Appendix A.2, page 172). Solar radiation differences were determined using the data from Mt. Kobau to represent Oliver, which is on the mountain ridge 7 km to the west of the study region, at an elevation of 1862 m above sea level.

Shift terms were determined for each synthetic time period (Table 4.2) for: maximum and minimum temperatures ($\Delta\bar{T}_{\text{max}}$ and $\Delta\bar{T}_{\text{min}}$), standard deviation of mean temperatures ($\delta\,\text{stdev}\{\bar{T}\}$), global solar radiation ($\delta\bar{R}_s$), and monthly precipitation normals ($\delta\bar{P}$). Each shift term is a comparison of the relative or absolute changes from the *base* (or *current*; $\mathcal{S}1$ in equations 4.1–4.2) to *future* simulated climate periods ($\mathcal{S}2$) from either a GCM or downscaled output. Since only the monthly shifts are used (rather than the monthly absolute downscaled or GCM values), introducing the bias of the GCM or downscaling technique is avoided.

Relative change of wet- and dry-spell lengths (also known as interarrivals) were not used from GCMs, as this requires: (1) raw daily GCM data (not directly available for HadCM3), and (2) is subjective to the interpretation of a precipitation cut-off value for wet/dry days. A sensitivity analysis using CGCM1 revealed that recharge is relatively insensitive to interarrival lengths. Only relative changes of wet- and dry-spells between Summerland and Oliver were used for all simulations.

To combine both the spatial and temporal changes between the calibrated weather generator at Summerland to future climate in Oliver, the shift terms used in LARS-WG were calculated using:

$$\bar{T}_{\text{future}} = \bar{T}_{\text{Summ.}} + \Delta\bar{T}_{\text{Summ.}\rightarrow\text{Oliver}} + \Delta\bar{T}_{\text{past}\rightarrow\text{future}} \tag{4.3a}$$

$$\bar{P}_{\text{future}} = \bar{P}_{\text{Summ.}} \cdot \delta\bar{P}_{\text{Summ.}\rightarrow\text{Oliver}} \cdot \delta\bar{P}_{\text{past}\rightarrow\text{future}} \tag{4.3b}$$

Synthetic weather were generated for 200 years using equations 4.3 and a random seed of 677. Output synthetic data include daily maximum and minimum temperature, precipitation, solar radiation and potential evapotranspiration. Synthetic 'base' climate from LARS-WG is confirmed to reproduce the 1961–1990 normals from Oliver for measured temperature and precipitation normals (see Appendix A.3, page 173).

4.3.3 Irrigation

Irrigation was added to precipitation in irrigation districts (Table 4.4) located in the Oliver region using proportions of crop types, and daily climate and evapotranspiration data from LARS-WG. There are six irrigation districts in Oliver (identified in Figure 4.4f) with monitored irrigation uses. The two dominant crop types are orchard (including peaches, cherries and apples) and vineyards (grapes). The proportion of crop type in each irrigation district is identified in Table 4.4 and were generalized from maps by Neilsen et al. (2004).

Average rates of actual applied irrigation can be calculated for the various irrigation districts using estimates of the amount of water used, and the total area of the respective irrigation district. However, average rates do not provide a realistic measure of the actual

Table 4.4 Irrigation districts, coverage types, and average annual water use between 2000–2005. Irrigation efficiency, N_D, is determined from these averages.

Name	No.	Coverage fraction		Area	Avg. water use	Avg. rate	N_D
		orchard	vineyard	(m^2)	(m^3/yr)	(mm/yr)	–
Mud Lake	1	0.8	0.2	2 852 090	3 143 968	1102	1.8
Blacksage	2	0.8	0.2	1 849 150	2 570 480	1390	2.2
Rockcliffe	4	0.8	0.2	4 867 269	4 789 357	984	1.6
Fairview	5	0.8	0.2	2 559 064	2 347 473	917	1.5
Hester Ck.	6	0.5	0.5	3 636 838	2 340 087	643	1.2
Mt. Kobau	7	0.8	0.2	2 846 035	2 489 884	875	1.4

Source: T. Underwood, pers. comm. 2006

daily irrigation rates, because on some days it actually rains. Therefore, an approach was developed to calculate the daily applied irrigation based on the precipitation and evaporation data from LARS-WG. The approach relies on estimates of seasonal crop water demand.

Allen et al. (1998) describe *crop water demand* as the water that a given crop will require to compensate the evapotranspiration loss, while the *irrigation water requirement* is defined as the difference between the crop water demand and effective precipitation. Irrigation may also include additional water for leaching of salts. Seasonal crop water demand was estimated using crop water demand coefficients, K_c, from Neilsen et al. (2006):

$$K_c = 6.770\times10^{-8}\,d^3 - 6.466\times10^{-5}\,d^2 + 0.01407\,d - 0.1149 \qquad \text{for orchard trees} \tag{4.4a}$$

$$K_c = 2.161\times10^{-7}\,d^3 - 1.434\times10^{-4}\,d^2 + 0.02616\,d - 0.1602 \qquad \text{for grapes} \tag{4.4b}$$

where d is the day of the growing season, which begins at 1 and accumulates to the end of the growing season. The polynomial K_c ranges from 0 to 1.29 (at $d = 129$) in equation 4.4a, and 0 to 0.77 (at $d = 139$) in equation 4.4b. The start of the growing season in the spring is established after 5 consecutive days where $T_{\text{mean}} > 10°\text{C}$, and ends in the fall after 5 consecutive days where $T_{\text{mean}} < 10°\text{C}$ (Neilsen et al., 2006). In addition, the growing season was limited to begin at earliest mid-March and at latest late-October, as plant growth is limited by the photoperiod, regardless of temperature.

Daily irrigation rates, I_r (in mm/day), were calculated using:

$$I_r = N_D \, K_c \, E_p - P \tag{4.5}$$

where N_D is an efficiency factor for each irrigation district, E_p is daily potential evapotranspiration, and P is daily precipitation; the last two variables are from LARS-WG and have units mm/day. If I_r is negative (e.g., from excessive precipitation), it was reset to zero for that day. K_c coefficients were weighted by relative proportions of vineyard and orchard tree crops in each irrigation district. N_D was determined from trial and error to obtain similar measured average irrigation rates in Table 4.4 using the base synthetic climate data. The values of N_D (above 1.0) indicate that most crops are likely over irrigated for their respective crop water demand. The average crop water demand for orchard trees is 717 mm/yr and for vineyards it is 408 mm/yr using the same synthetic base climate data set. N_D values were not modified for future simulations, despite the need for possible irrigation efficiency improvements.

4.3.4 Recharge modelling

4.3.4.1 HELP model

Version 3.80D of the HELP model (Berger, 2004), which is a revised and updated version of the original HELP model by Schroeder et al. (1994), was used to estimate recharge. HELP simulates surface and near surface hydrologic processes critical for estimating recharge, including: accumulation of solid precipitation (snow and ice) on the surface; surface runoff/infiltration; estimated and potential evapotranspiration; transpiration in relation to the growth and decay of vegetation; soil freeze/thaw from air temperature, and; water flow through discrete layers of variably saturated soil. The model uses vertical (1D) soil profiles, and simulates the leakage at the base of the profile. If the base of the soil column is set equal to the water table depth, the leakage across this boundary is effectively the groundwater recharge. HELP has been used in many groundwater recharge studies (e.g., Gogolev, 2002; Allen et al., 2004; Jyrkama and Sykes, 2005, 2007; Scibek and Allen, 2006a,b).

It is recognized that the HELP hydrologic model is not the best-available model for simulating recharge processes. Scanlon et al. (2002) compared several similar hydrologic codes, and rated HELP poorer than others, such as UNSAT-H (Fayer, 2000), and SHAW (Flerchinger, 2000). The main drawback of HELP is that it employs a storage-routing unsaturated flow process. Other codes generally solve Richards' equation through finite-differences, where water may move up or down, depending on the matric potential gradient. The HELP model uses the following critical assumptions: (1) water may only escape upwards (as evapotranspiration) if it is within the evaporative depth zone, which is a non-physically-based depth parameter of the model, but often specified by the user to coincide with the rooting depth; and (2) water drained from the base of the evaporative depth zone will eventually be routed to the base of the model. Furthermore, the timings and threshold of freeze/thaw of the soil layers in HELP are calculated based on an empirical dataset from a limited number of studies from the United States and Germany. It is unknown how well these empirical relationships hold for the soils and climate in the Okanagan region.

Despite these limitations, the HELP model was selected for several reasons: (1) its simplicity and speed—a soil profile with 200 years of climate data can be simulated in seconds, rather than hours; (2) it utilizes daily climate data needed for climate change simulations; (3) it simultaneously models multiple hydrologic processes, including soil freeze/thaw; and (4) it allows comparison with other similar investigations that have used the same model in different climate regimes (e.g., Scibek and Allen, 2006a).

As part of this study, a program module was developed in Python (e.g., Lutz and Ascher, 2004) as a programming interface to the HELP model.[1] The programming interface can be adapted to any task through a script, particularly where the task is repetitive. The module was coded in a Python script[2] to effectively run the HELP model at each unique location over a region, and store the results as a raster with a time dimension.

[1] Located on the CD at `programs/HELP.py`

[2] Located on the CD at `programs/model_HELP.py`

Because HELP is a 1D model, spatially-distributed recharge estimates require simulations for each unique combination of physical parameters that might influence recharge. These include soil (and its depth layering), vegetation, slope and water table depth. Consequently, the study area was discretized into 100 m grid cells for recharge analysis, which covered a 2100 m by 1100 m region, with 10 102 active cells (and unique HELP simulations) for each climate state simulation. LAI and water depth were used directly, as they were gridded to match the modelling domain. Polygon coverages of soil and land use data were interpreted through a weighted approach. Each grid location (i, j) can have $k \in \{1, 2, \ldots\}$ categories, which are weighted by the surface area occupied by each category, A_k, using:

$$W_k = \frac{A_k}{\sum A_k} \quad \text{where } \sum W_k = 1 \tag{4.6}$$

which is multiplied with each k parameter value, and summed to arrive at a single value for each grid location.

One of the major limitations of using a 1D recharge model is that surface (and subsurface, if important) water routing from one grid cell to the next is not accounted for by the model. Thus, this excess water will not be routed to adjacent down-gradient cells. For this reason, use of a 1D recharge model is not particularly well suited to areas with moderately steep to steep topography. However, in this particular study area, the valley bottom is generally flat, and the soils well drained, so that there will be little surface runoff, and little lateral flow within the vadose zone; only vertical flow.

HELP uses daily mean temperature, total daily precipitation and total solar radiation as weather inputs. In this study, weather time series and evapotranspiration input parameters (Table 4.5) were assumed to be constant throughout the modelling domain. However, unique precipitation time series were generated for each irrigation district, including the daily irrigation application (equation 4.5) as influenced by both the crop type and irrigation efficiency.

Table 4.5 Input parameters used in HELP.

Parameter	Value	
Latitude		49.15°N
Wind Speed		6 km/hr
Relative humidity	JFM:	72%
(Quarterly*)	AMJ:	52%
	JAS:	51%
	OND:	80%

*JFM = January, February, March, etc.

4.3.4.2 Vegetation and runoff

Runoff curve numbers (USDA, 1986) were calculated for each grid location based on vegetation and soil texture, as arbitrarily quantified by Schroeder et al. (1994). A vegetation number, V_n, can range from 1.0 for bare ground to 5.0 for an "excellent" stand of grass; and a soil texture number, T_n, can range from 1.0 for coarse sand to 15.0 for clay. Values for V_n were interpreted from land use through Table 4.6, while T_n was first approximated from soil drainage (Figure 4.4b), then modified by adding values of $T_n^{\pm}$ in Table 4.6. The intention of these adjustments is to increase the potential for runoff in regions with more development. Finally, runoff curve numbers were adjusted according to surface slope (Figure 4.4c). The runoff curve number calculation method used in this study is similar to the "computed curve number" from the HELP 3.07 code; however, it was modified to support fractional input values of T_n and V_n, and to improve interpolation of internally coded polynomial coefficients. See Appendix C.2.1, page 192 for more details.

Values for the evaporative depth zone, E_Z, were obtained from land use, using Table 4.6. These values are typically set to the vegetation rooting depths of vegetation. In the study area, this may consist of orchards, vineyards, or native *Agropyron spicatum* (bluebunch wheatgrass), *Artemisia tridentata* (big sagebrush), and *Pinus ponderosa* (ponderosa pine) (Meidinger and Pojar, 1991).

Table 4.6 Influence of land use on vegetation cover, V_n, soil texture number modifier, $T_n^{\pm}$, and evaporative depth zone, E_Z (cm).

Land use	V_n	$T_n^{\pm}$	E_Z
Agriculture	3.2	+1	100
Old Forest	4.5	0	200
Range Lands	1.8	0	35
Recreational	3.2	+2	40
Urban	2.2	+4	40
Wetlands	3.5	0	40
Young Forest	4.3	0	100

4.3.4.3 Soil layers

Soil columns were dynamically created across the site to represent the unique spatial soil data combinations. Each soil column was defined using 1 to 9 vertical percolation layers, because it is assumed that only vertical flow is present. Soil profiles were built for each grid square using weighted spatial and depth averages of hydraulic properties determined from the soil database (Figure 4.5).

Soil hydraulic properties for each soil horizon were estimated using the ROSETTA computer program (Version 1.2), which implements hierarchical pedotransfer functions (Schaap et al., 2001). The H3 artificial neural network model selected requires four input parameters: (1) measured bulk density, (2) % sand, (3) % silt, and (4) % clay. The model directly calculates saturated hydraulic conductivity, K_s, saturated and residual water contents, θ_s and θ_r, respectively, and van Genuchten (1980) water retention curve parameters α and n. Porosity, ϕ, was set equal to θ_s. Field capacity (θ_{fc}, where suction pressure, $|\psi|$, is 33 kPa $\approx$ 337 cm of water) and wilting point (θ_{wp}, where $|\psi| = 1500$ kPa $\approx$ 15 306 cm) were calculated using:

$$\theta(\psi) = \theta_r + \frac{\theta_s - \theta_r}{\left[1 + (\alpha\,|\psi|)^n\right]^{1-1/n}} \tag{4.7}$$

Hydraulic properties for organic soil layers were determined independently using estimates from peat (Päivänen, 1973; Silins and Rothwell, 1998), as soil texture data were unavailable for these soil horizons. Saturated hydraulic conductivity for organic layers

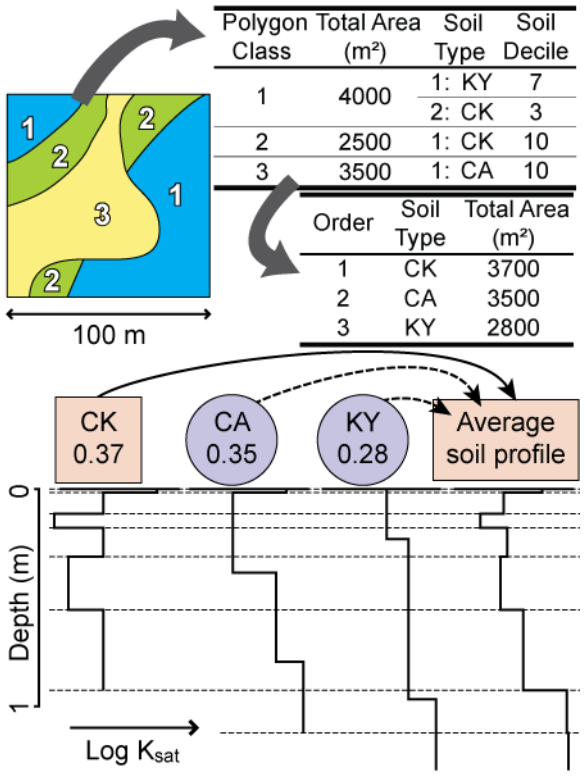

Figure 4.5 Illustration of the soil database for a 100 m grid cell. This example shows three-different soil coverages comprising varying proportions of soil types, which are combined using area-weighted means. The illustration at the bottom shows the depth-weighted average soil profile of log K that is used to represent the grid cell. Here, the dominant soil type 'CK' is used as a template, and "inherits" the properties of 'CA' and 'CK', depending on their relative abundance. The resulting soil profile has eight layers.

were estimated using the linear relation (Päivänen, 1973):

$$\log_{10}(K_s) = 2.8 - 10\rho_b \tag{4.8}$$

where K_s is saturated hydraulic conductivity (cm/day), and ρ_b is bulk density (Mg/m^3), which ranged between 0.22 and 0.36 Mg/m^3. The water retention parameters for peat were approximated by fixing $\theta_s \leftarrow 0.85$ (close to porosity), $\theta_r \leftarrow 0$, and $n \leftarrow 1.4$ (Silins and Rothwell, 1998). The α shape parameter was adjusted in equation 4.7 to obtain $\theta_{fc} - \theta_{wp} \approx \theta_a$, where θ_a is the available water content from the soil database.

Where the water table extends below the base of the soil profile ($\gtrsim$1.2 m), average aquifer values were used to append a bottom layer, which extends to the water table

(Figure 4.4e). This bottom layer, if appended, has a K_s of 0.1 cm/sec and ϕ of 0.25, as approximated from multiple pump tests in the regional sand and gravel aquifer (see Chapter 5). Water retention parameters θ_{fc} and θ_{wp} were approximated to be 0.045 and 0.018, respectively (Rawls et al., 1993).

Soil moisture was first initiated automatically[3] (1 year model spin-up), but model spin-up was extended by running 200 years of climate data, while only keeping the last 100 for analysis. A longer spin-up time was needed to initialize soil moisture, as simulations using tall soil columns generally underestimated recharge during the early time series.

4.4 Results

4.4.1 Climate change

4.4.1.1 Temperature

Figure 4.6 shows the downscaled temperature results, superimposed on boxplots of the measured parameters for Oliver. Ideally, the "current" GCM simulation should coincide with the middle of the boxplots (which indicates the median); however, each downscaled GCM has slight seasonal biases. Since this analysis only considers the change between the baseline to future time periods, these absolute biases do not directly influence the weather generator. The downscaled temperature shift factors (Figure 4.7) show that all of the future climates expect increased warming during summer months. Of notice are particularly high shifts predicted by CGCM3.1 and HadCM3 during late summer months.

Figure 4.8 shows the standard deviation of downscaled mean temperature, stdev$\{\bar{T}\}$, for each scenario. Minor changes in stdev$\{\bar{T}\}$ are expected (Figure 4.9), except for CGCM1 (Figure 4.9a). An analysis of 2 m screen temperature in CGCM1 (see Figure B.2) reveals unrealistic data, whereby temperatures during winter and early spring are at 0°C

[3]Soil moisture is initiated in HELP by setting the moisture content to θ_{fc}, then running the first year of data twice, ignoring the first year of results (Schroeder et al., 1994, Section 3.6)

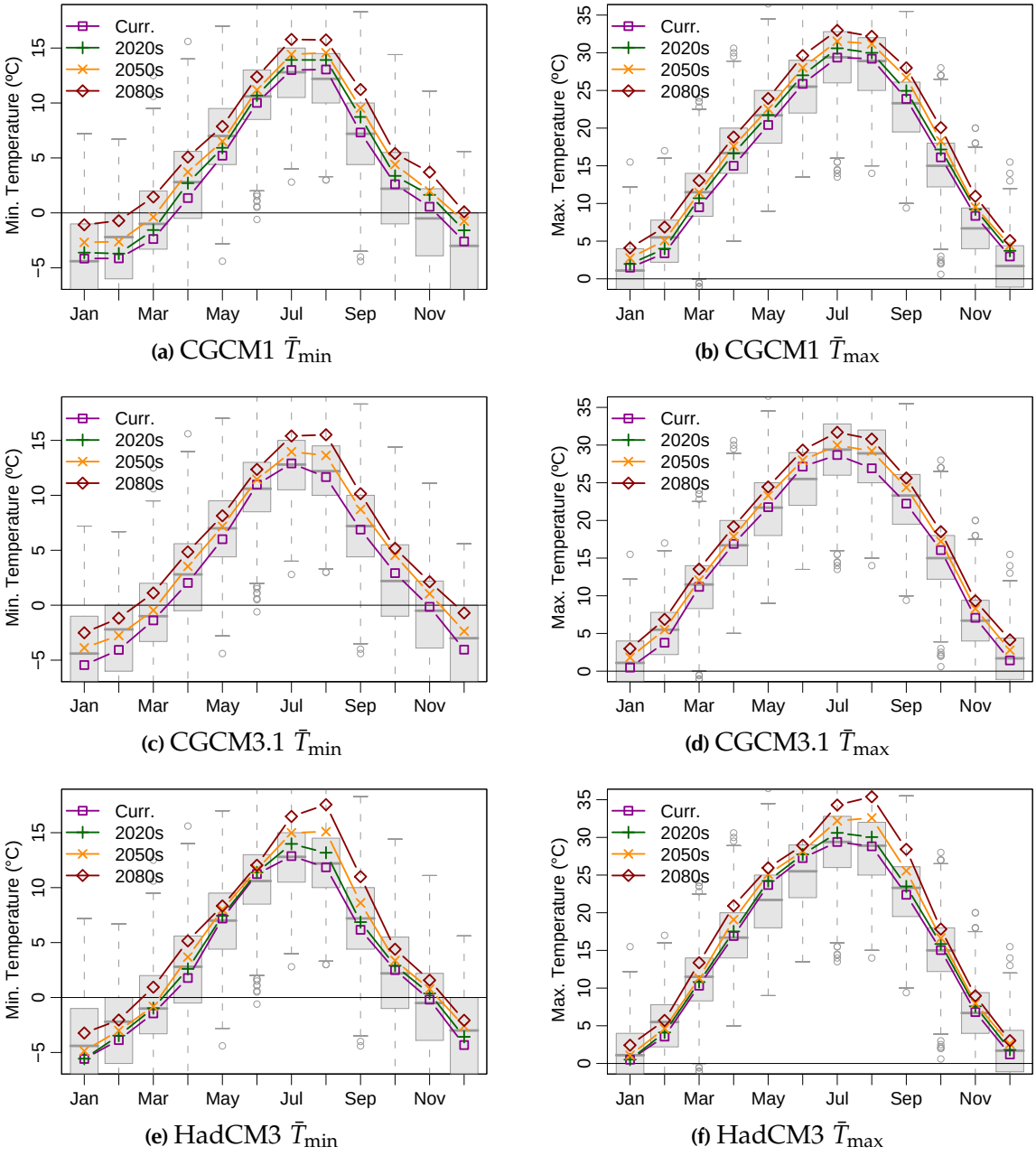

(a) CGCM1 $\bar{T}_{\min}$ **(b)** CGCM1 $\bar{T}_{\max}$

(c) CGCM3.1 $\bar{T}_{\min}$ **(d)** CGCM3.1 $\bar{T}_{\max}$

(e) HadCM3 $\bar{T}_{\min}$ **(f)** HadCM3 $\bar{T}_{\max}$

Figure 4.6 Downscaled temperature means from each GCM scenario, superimposed on boxplots of minimum and maximum temperatures measured at Oliver (1961–2000).

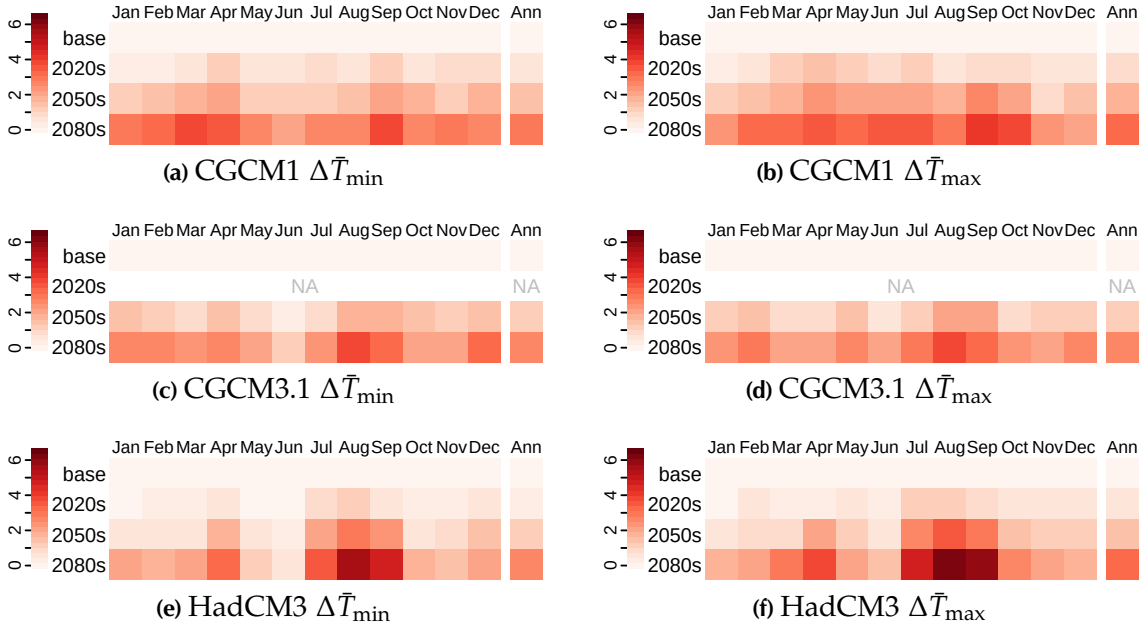

(a) CGCM1 $\Delta\bar{T}_{\text{min}}$ (b) CGCM1 $\Delta\bar{T}_{\text{max}}$

(c) CGCM3.1 $\Delta\bar{T}_{\text{min}}$ (d) CGCM3.1 $\Delta\bar{T}_{\text{max}}$

(e) HadCM3 $\Delta\bar{T}_{\text{min}}$ (f) HadCM3 $\Delta\bar{T}_{\text{max}}$

Figure 4.7 Absolute changes in downscaled minimum and maximum temperature. Tones in each grid indicate relative magnitude of change for each month and bulk year, for each time range.

or above, but seldom below freezing (in the 'current' climate, winter temperatures are almost all 0°C). This anomaly is not found in CGCM3.1, which uses a different atmospheric component. (More details are in Appendix B.3, page 184).

4.4.1.2 Precipitation

Plots of monthly precipitation normals of the GCM values are shown in Figure 4.10 along with monthly precipitation normals from Oliver, which are scaled for comparison. The observed precipitation normals have maxima in December and June. The increased precipitation during the summer (in Figure 4.2b, between May–mid-July) is not well produced by the GCMs due to difficulties in reproducing mesoscale climate phenomena from convective precipitation in synoptic scale GCMs (Kim et al., 1984). CGCM3.1 and HadCM3 (Figures 4.10b and 4.10c), however, show some ability to recreate these increases in mid-summer precipitation. Relative changes in precipitation are shown in Figures 4.11. All GCMs indicate potential reductions of precipitation during the summer at future time

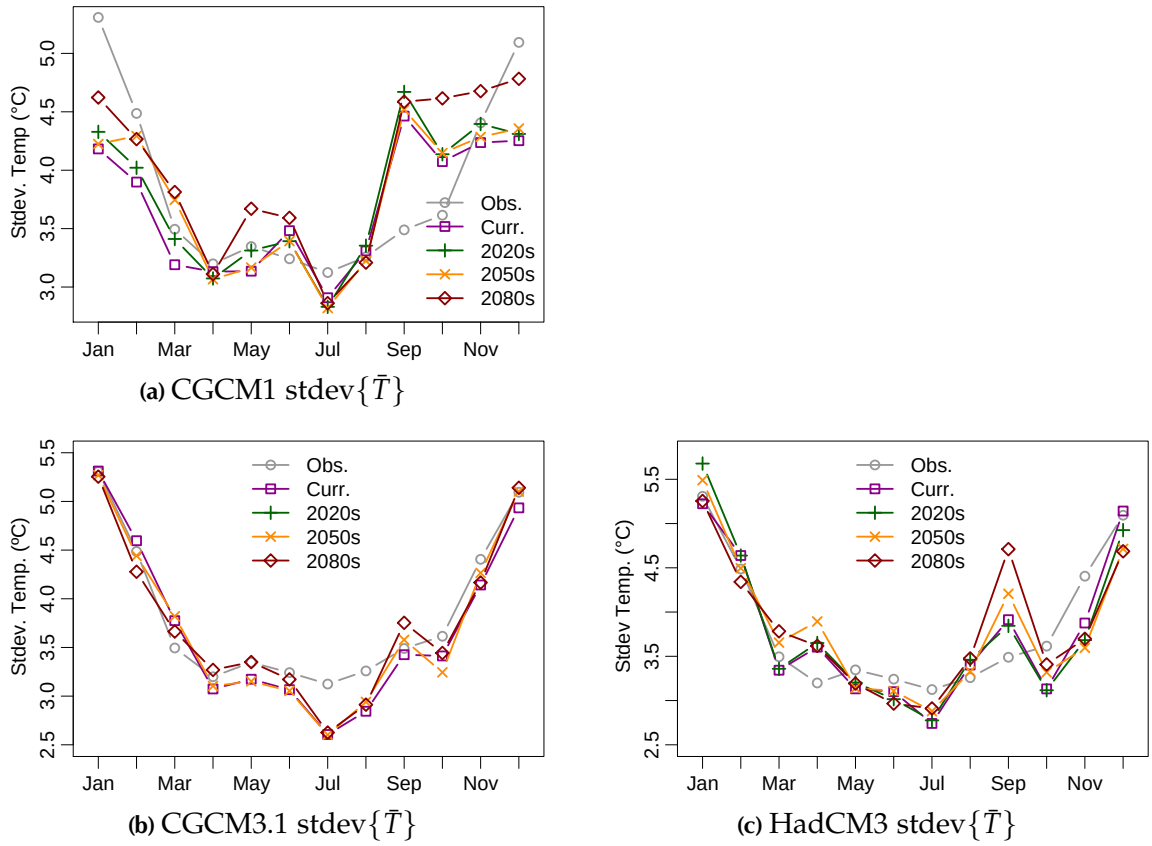

(a) CGCM1 stdev$\{\bar{T}\}$

(b) CGCM3.1 stdev$\{\bar{T}\}$

(c) HadCM3 stdev$\{\bar{T}\}$

Figure 4.8 Downscaled mean temperature standard deviations.

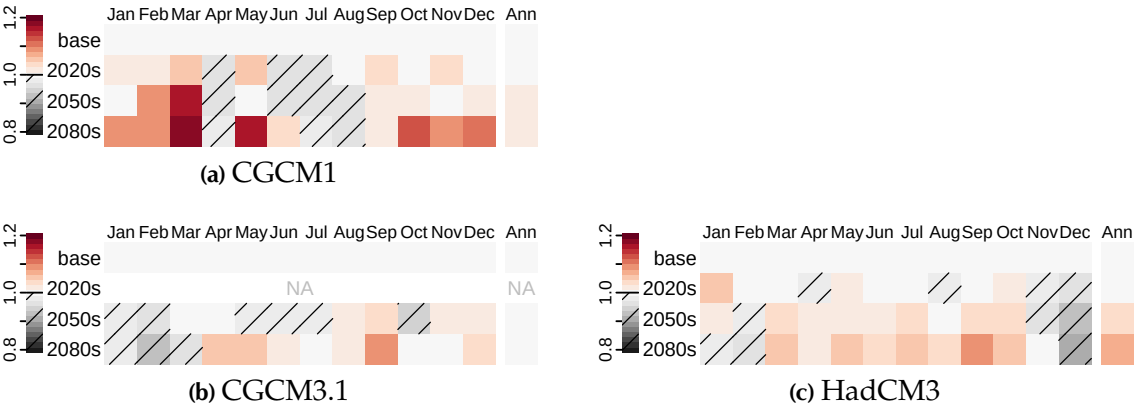

(a) CGCM1

(b) CGCM3.1

(c) HadCM3

Figure 4.9 Relative changes in standard deviation of downscaled temperature. Tones with hashmarks indicate negative changes.

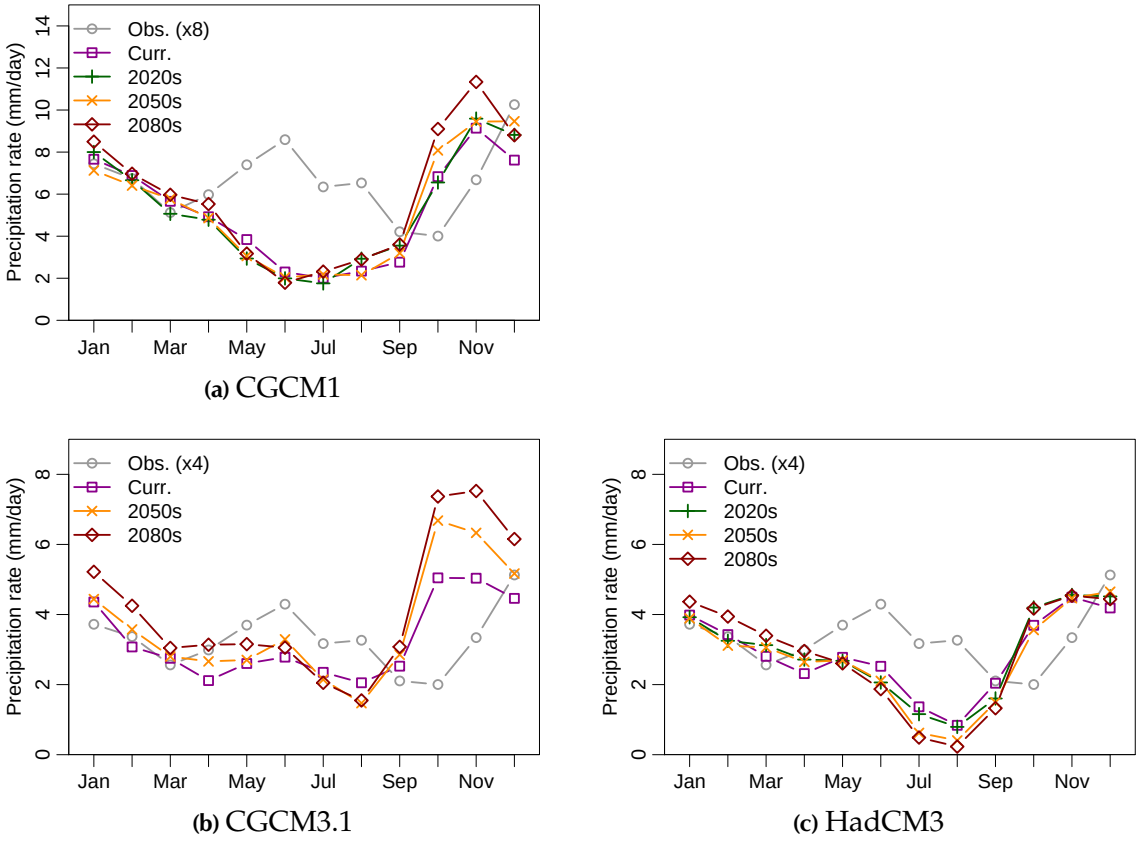

(a) CGCM1

(b) CGCM3.1

(c) HadCM3

Figure 4.10 Precipitation plots (not downscaled); the observed data precipitation normals are from Oliver (1961–2000), and are scaled to match the approximate values from the GCM to allow comparison of the seasonal signal.

periods. CGCM1 and CGCM3.1 (Figures 4.11a and 4.11b) show increases in precipitation from late summer to winter.

4.4.1.3 Solar radiation

Plots of monthly solar radiation are in Figure 4.12, superimposed on boxplots of measured solar radiation at Summerland. CGCM3.1 (Figure 4.12b) shows lower absolute values, and anomalously low early-summer values for the 'current' time period, particularly in June. Solar radiation changes are shown in Figure 4.13. Changes in precipitation appear to be inversely proportional to changes in precipitation normals (Figure 4.11). This coincidence is possibly due to atmospheric coupling in the GCMs, which may result in low solar

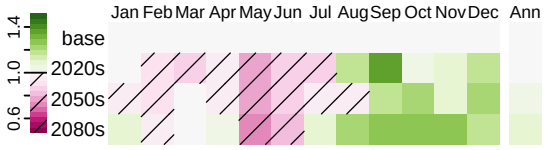

(a) CGCM1

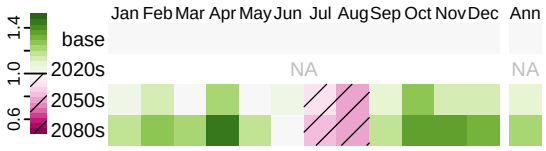

(b) CGCM3.1

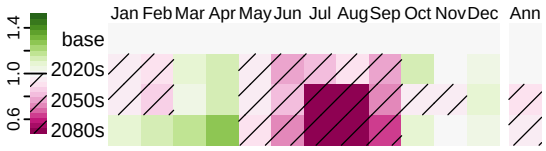

(c) HadCM3

Figure 4.11 Relative changes in precipitation (not downscaled).

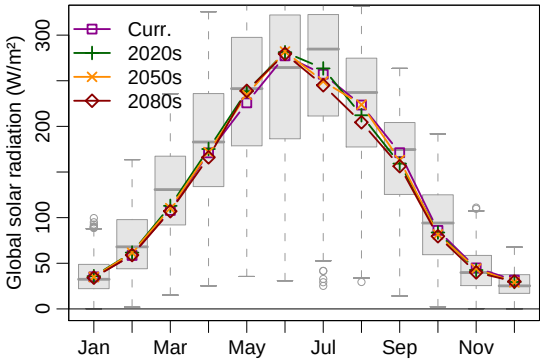

(a) CGCM1

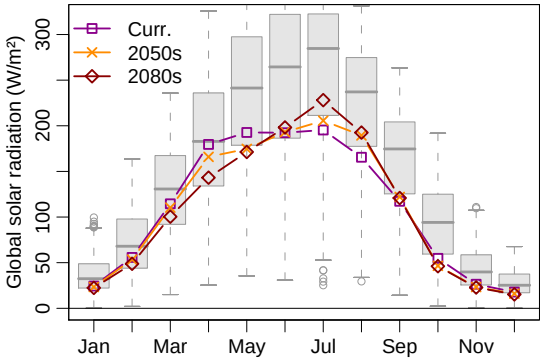

(b) CGCM3.1

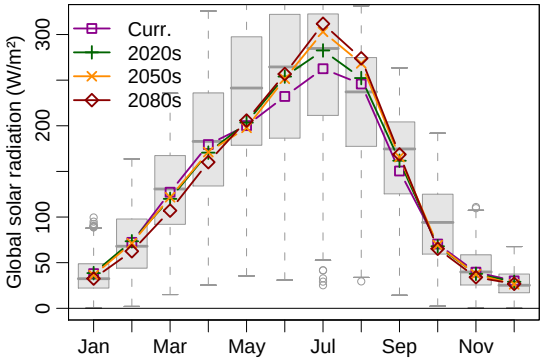

(c) HadCM3

Figure 4.12 Global solar radiation at the surface (not downscaled). Boxplots show measured solar radiation from Summerland (1962–1994).

radiation on days with precipitation. However, this signal is not evident in the observed solar radiation.

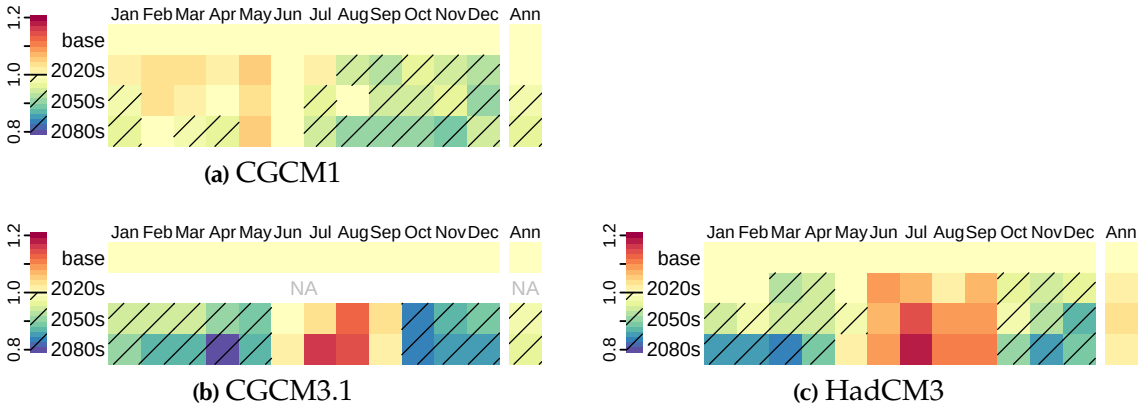

Figure 4.13 Relative changes in solar radiation at the surface (not downscaled).

4.4.2 Growing season and water demand

Typical growing season start and ending dates are summarized in Table 4.7, and Figure 4.14. All scenarios show that the growing season will increase between 3–4 weeks due to rise in temperature. The start and end periods were adjusted for each HELP simulation, as these are used by the model to restrict vegetation growth (and transpiration).

Crop water demands will inevitably increase in future time periods as a result of both increased growing season range and temperature increases. However, from the available data, it is apparent that most of the irrigation districts are presently over-irrigating. A constant irrigation efficiency for each district (N_D in equation 4.5 and listed in Table 4.4) was used for all simulations, as the irrigation application behaviour and technology cannot be predicted in future times. Optimistically, both irrigation technology and application practices will improve with time, such that the irrigation application rates will not have to increase at the same rate as crop water demand.

4.4.3 Recharge results

Maps showing the geometric mean of K_s for all soil layers and calculated runoff curve numbers are shown in Figure 4.15. Mean annual results using a 'base' synthetic climate without irrigation are shown in Figure 4.16. Mean annual recharge rates in Figure 4.16a

Table 4.7 Length of growing season and annual water demand (mm/yr); median and interquartile ranges (in parentheses) are displayed.

Case	Start	End	Length	Water demand
base	114 (17)	289 (13)	176 (18)	Orch.: 660 (110)
	April 24	October 16	25.1 weeks	Vin.: 366 (67)
CGCM1				
2020s	106 (16)	294 (8)	187 (18)	Orch.: 721 (94)
	April 16	October 21	26.7 weeks	Vin.: 404 (57)
2050s	95 (17)	295 (1)	196 (17)	Orch.: 764 (90)
	April 5	October 22	28.0 weeks	Vin.: 430 (54)
2080s	90 (15)	295 (0)	206 (13)	Orch.: 802 (86)
	March 31	October 22	29.4 weeks	Vin.: 455 (53)
CGCM3.1				
2050s	106 (16)	295 (4)	188 (17)	Orch.: 748 (92)
	April 16	October 22	26.9 weeks	Vin.: 419 (56)
2080s	96 (15)	295 (0)	199 (16)	Orch.: 817 (78)
	April 6	October 22	28.4 weeks	Vin.: 463 (51)
HadCM3				
2020s	109 (16)	293 (10)	181 (18)	Orch.: 728 (104)
	April 19	October 20	25.9 weeks	Vin.: 407 (64)
2050s	103 (15)	295 (5)	190 (17)	Orch.: 808 (84)
	April 13	October 22	27.1 weeks	Vin.: 455 (50)
2080s	92 (13)	295 (0)	203 (15)	Orch.: 896 (76)
	April 2	October 22	29.0 weeks	Vin.: 508 (50)

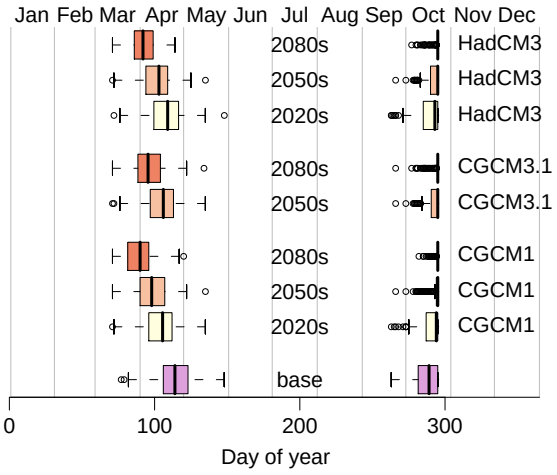

Figure 4.14 Boxplots of starting and ending dates of the growing season for each time range and GCM.

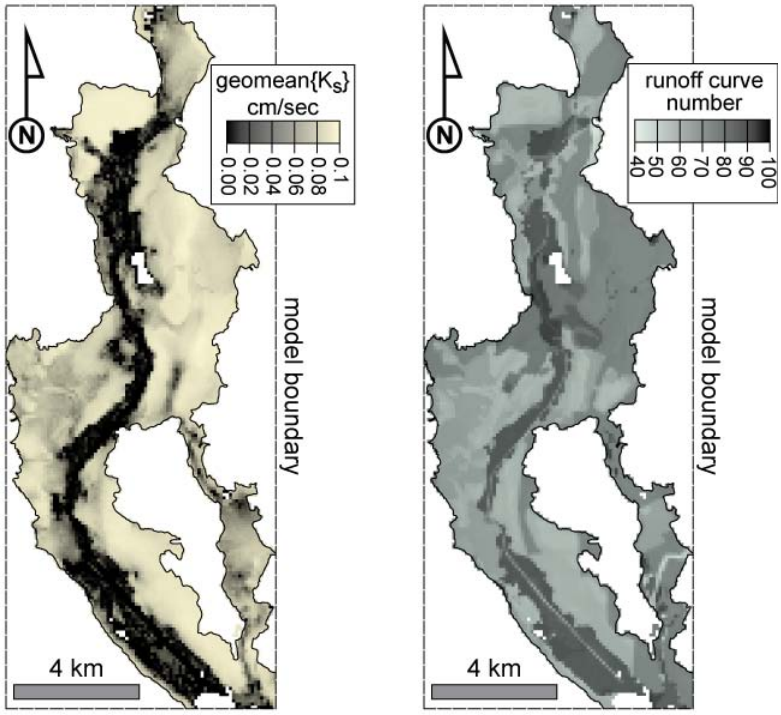

(a) Geometric mean of K_s **(b)** Runoff curve number

Figure 4.15 Soil and surface properties of the study area, as determined from from the soil GIS database and interpreted soil properties.

have a median of 45 mm/yr, with first and third quartiles of 15 and 60 mm/yr, respectively. These values are approximately 20% of the annual precipitation. The most sensitive parameters on recharge are the near-surface soil hydraulic properties, including K_s, and water retention parameters θ_{fc} and θ_{wp}. The sensitive control of K_s is apparent from the similarity between maps of annual recharge (Figure 4.16a) and geometric mean of K_s (Figure 4.15a).

Spatially distributed runoff (or infiltration excess; Figure 4.16b) is comparable to runoff curve numbers (Figure 4.15b). Runoff is computed by HELP to be a minor component of the annual water budget; however, this is possibly underestimated due to the limitations of runoff simulation using daily time step data (Scanlon et al., 2002).

Spatial monthly recharge rates are displayed both without irrigation in Figure 4.17a, and with irrigation in Figure 4.17b. Natural recharge arrives at the water table at different

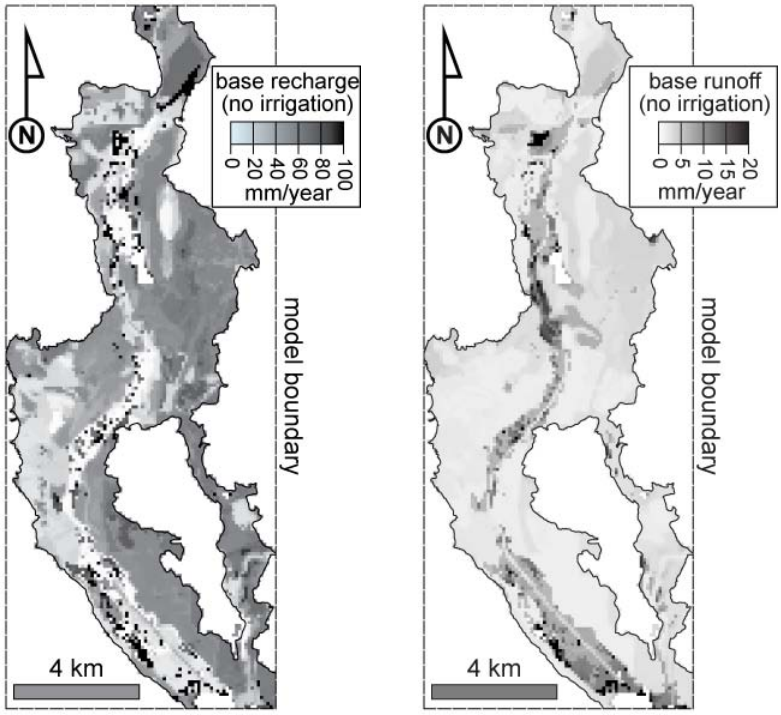

(a) Recharge **(b)** Runoff

Figure 4.16 Map of 'base' mean annual recharge and runoff, simulated without irrigation.

times of the year, which is influenced by the depth to water. This delay is due to the time of transport through the soil, which is proportional to the height of the soil column. If the soil is fully saturated ($\theta = \phi$), HELP simulates the flow of water through the soil column length, dl, with a unit hydraulic gradient ($dh/dl = 1$) and a delay, dt, of:

$$dt = \frac{dh\,\phi}{K_s}. \tag{4.9}$$

Simulations using irrigation have significant increases on net recharge in the irrigation districts. Zones 6 and 7 (identified in Figure 4.4f) have the lowest recharge of these zones, averaging 250 and 450 mm/yr, respectively. Irrigation zone 2, the most intensely irrigated district, has the highest net recharge of 1000 mm/yr.

Irrigation return flow is the ratio of annual recharge to irrigation plus precipitation. Results for the baseline synthetic climate are shown in Figure 4.18. Irrigation return flow is very dependant on the efficiency of irrigation (N_D), which was adjusted to meet the

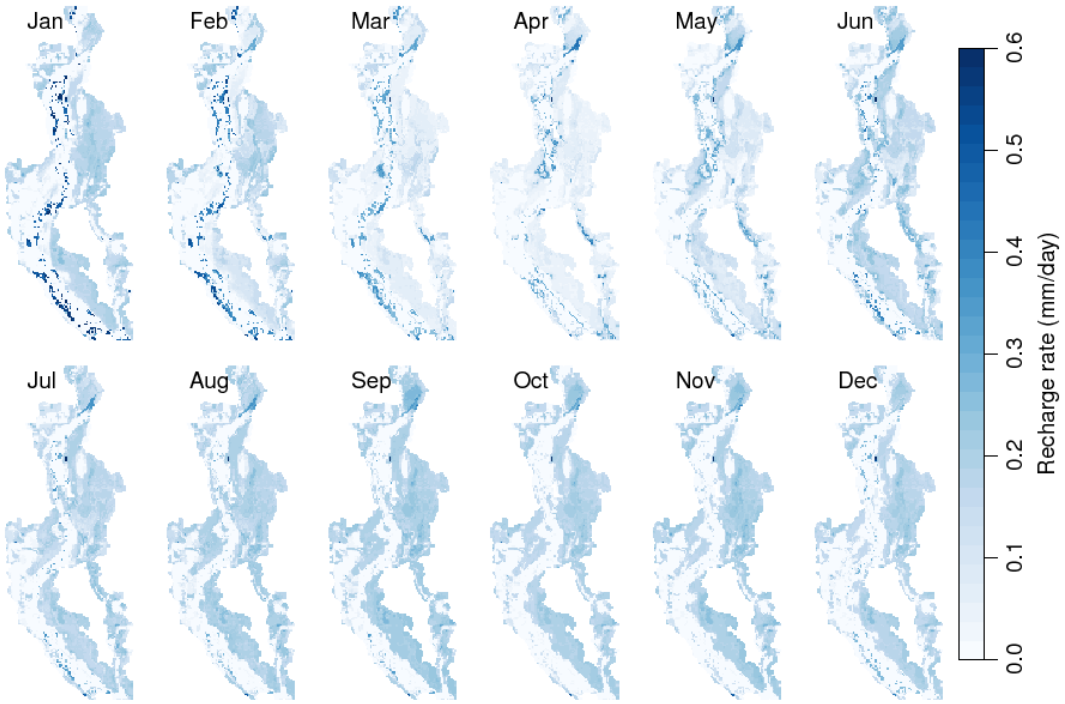

(a) Without irrigation

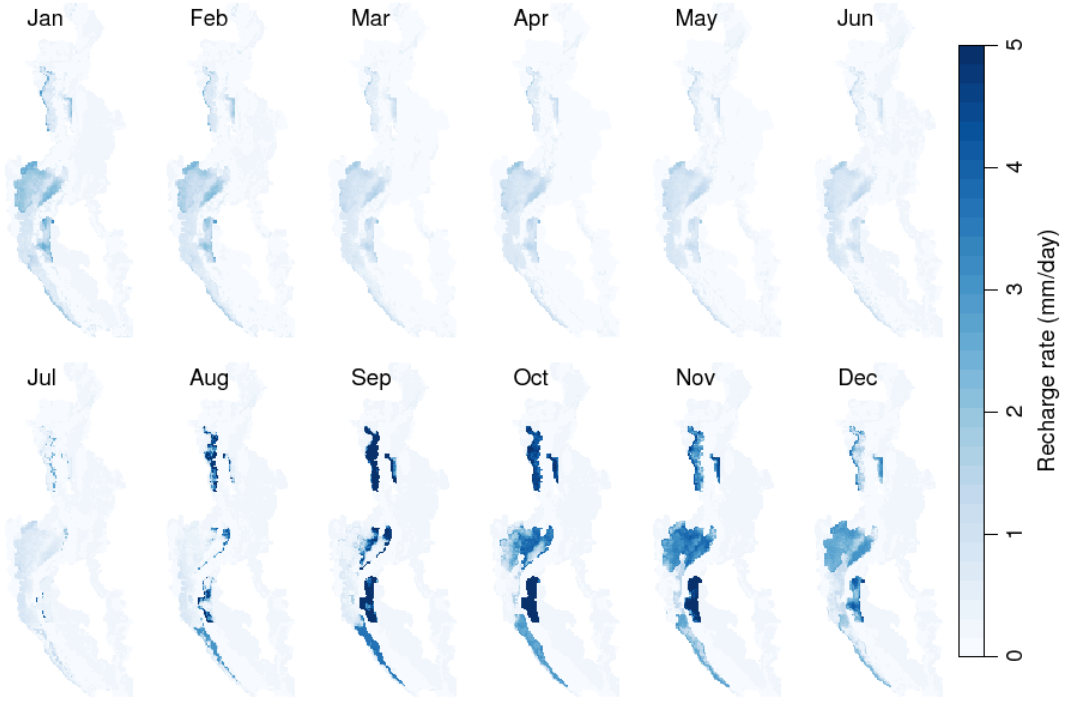

(b) With irrigation

Figure 4.17 Spatial monthly recharge rates in base climate (mm/day). Note changes in shading scales between (a) and (b).

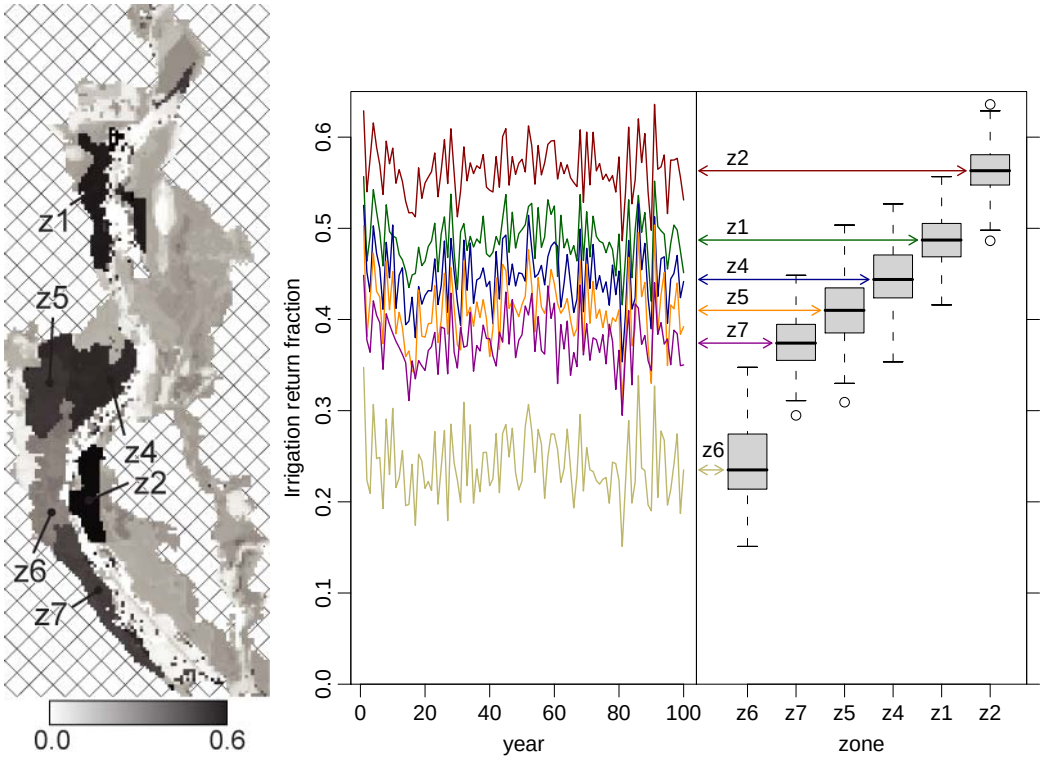

(a) Average return flow **(b)** Annual return flow fractions from locations in each irrigation district

Figure 4.18 Irrigation return flow (fraction of recharge relative to input precipitation and irrigation) in the base climate state.

observed application amounts. Where the N_D is close to 1.0 (perfect efficiency), irrigation return amounts are close to 0.2, while in less efficient districts this return fraction is nearly 0.6. From an irrigator's perspective, this loss is inefficient as it results in higher energy costs associated with unnecessary pumping of water.

4.4.3.1 Comparison of model results to observed data

Comparison of water levels in, and outside of irrigation districts are shown in Figure 4.19. Observation Well[4] No. 282 is located outside of the soil data extent (∼5 km north-west of the region) with no irrigation influence, and Obs. Well No. 332 is located within irrigation district 2 (Figure 4.19b).

[4]See http://www.env.gov.bc.ca/wsd/data_searches/obswell/wellindex.html

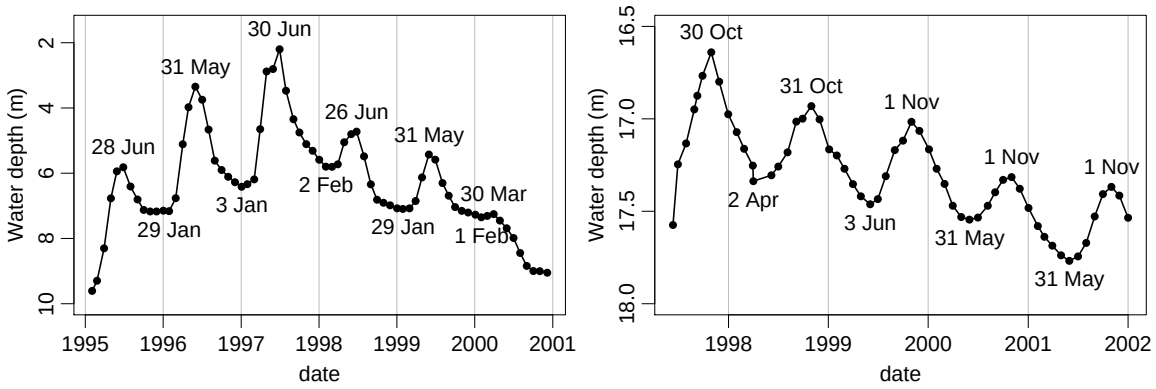

(a) Observation Well 282, located in a non-irrigated region

(b) Observation Well 332 in irrigation zone 2

Figure 4.19 Measured water levels in groundwater observation wells.

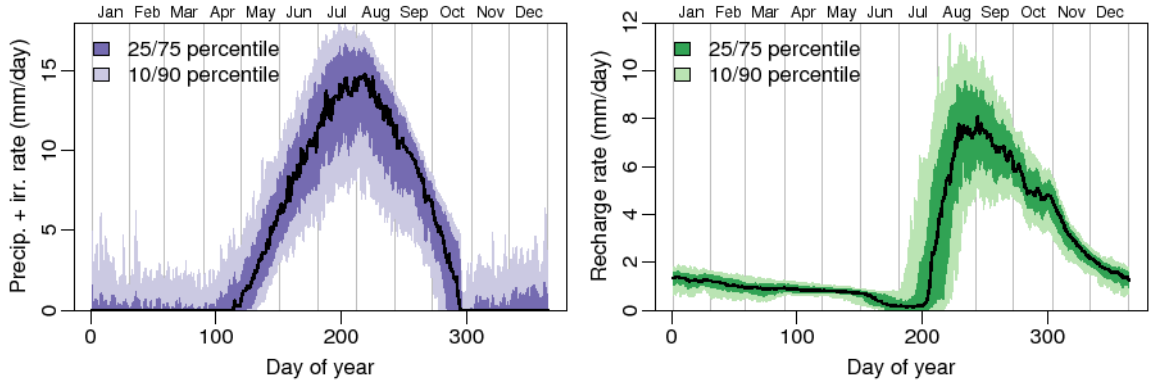

(a) Precipitation and irrigation rate

(b) Recharge rate

Figure 4.20 HELP simulation in an irrigation district 2 at the same location as Obs. Well 233 (Figure 4.19b).

Figure 4.20 shows seasonal irrigation (with precipitation) and recharge responses at the same location as Obs. Well No. 332 (Figure 4.19b). Although the water levels are influenced by nearby pumping water wells used primarily for irrigation, this comparison shows that both recharge rates and water levels are lowest in early summer, and increase sharply near the end of summer. Water levels in this irrigation district reach their peak in November, presumably after accumulation of recharge (i.e., integration of recharge rates in Figure 4.20b). In contrast, water levels outside of the irrigation district (Figure 4.19a) peak in spring during the freshet, and are at their lowest during winter.

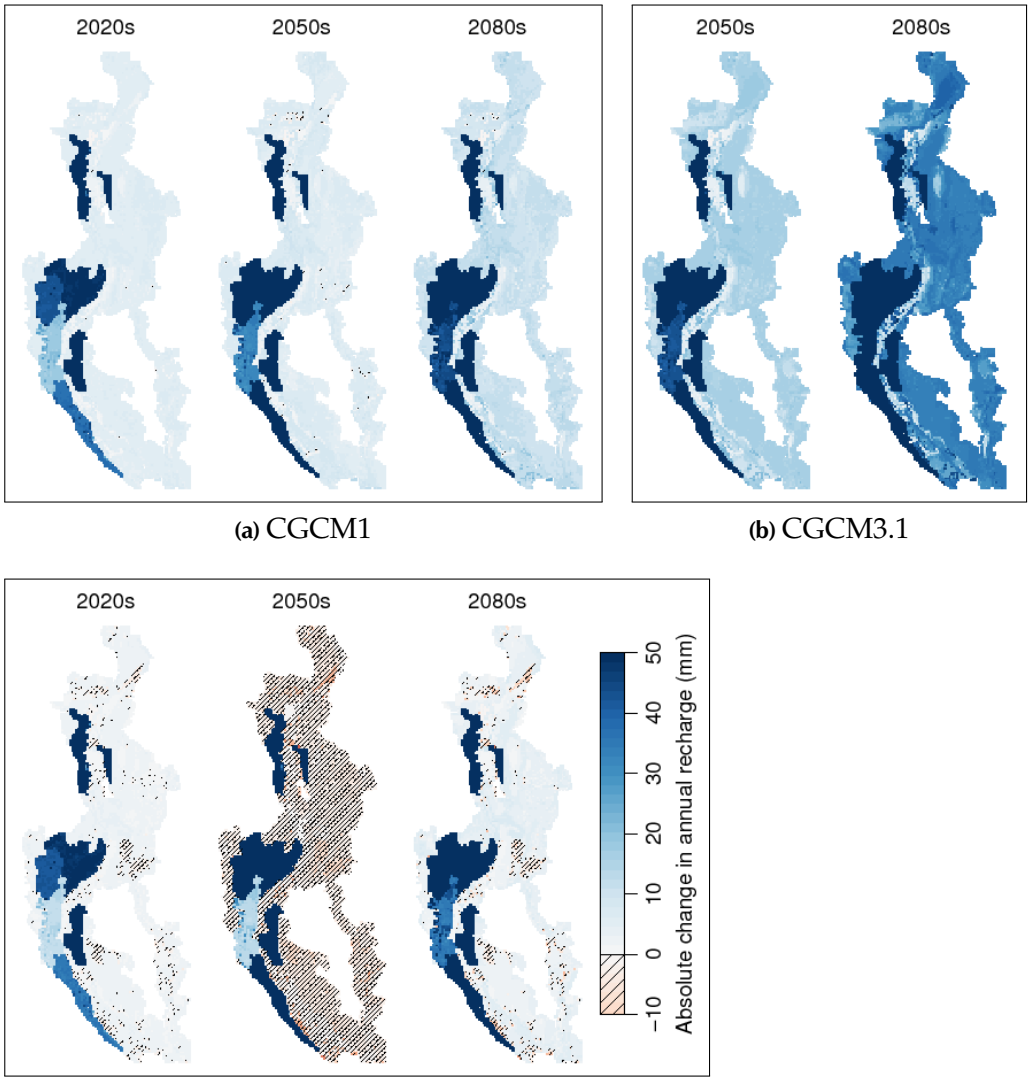

(a) CGCM1

(b) CGCM3.1

(c) HadCM3

Figure 4.21 Absolute changes to spatial recharge rates in future simulations.

4.4.4 Influences of climate change on recharge

Figure 4.21 shows the spatial absolute changes to mean annual recharge rates from the 'base' (or 'current') climate state to future conditions. Mean absolute changes in recharge rates for non-irrigated regions are shown in Figure 4.22, and for the most and least efficiently irrigated districts in Figures 4.24 and 4.23, respectively.

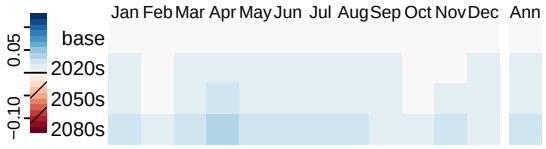

(a) CGCM1

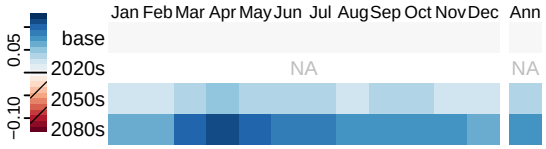

(b) CGCM3.1

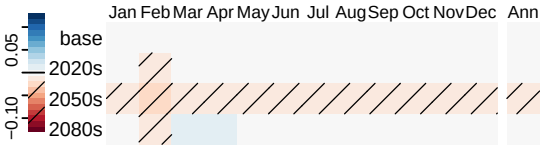

(c) HadCM3

Figure 4.22 Mean absolute changes in monthly recharge rates (mm/day) from non-irrigated regions.

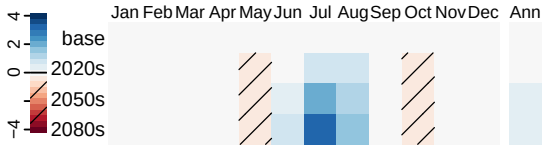

(a) CGCM1

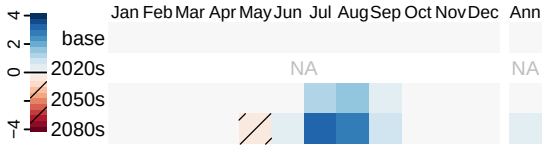

(b) CGCM3.1

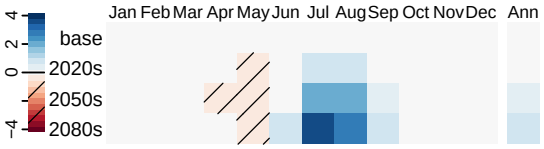

(c) HadCM3

Figure 4.23 Mean absolute changes in monthly recharge and irrigation return flow (mm/day) in zone #2, which has the least efficient use of irrigation (N_D=2.2).

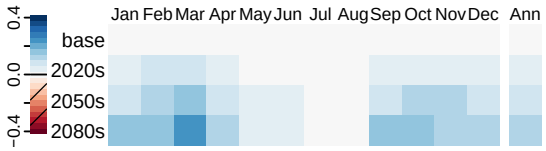

(a) CGCM1

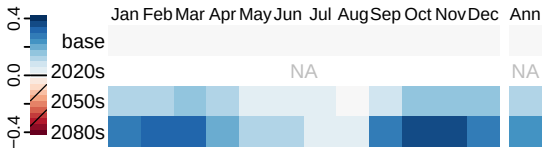

(b) CGCM3.1

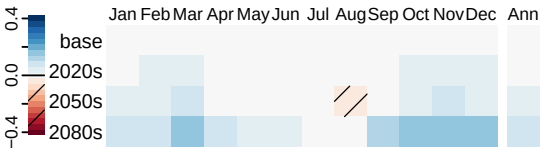

(c) HadCM3

Figure 4.24 Mean absolute changes in monthly recharge and irrigation return flow (mm/day) in zone #6, which has the most efficient use of irrigation (N_D=1.2).

The seasonal changes of recharge in non-irrigated regions (Figure 4.22) show that there is an increase in the earlier part of the year, indicating that the timing of recharge may shift earlier in the season. This may be expected, as warmer temperatures may initiate earlier snowmelt and ground thaw. Seasonal change of recharge in irrigated districts (Figures 4.23–4.24), show that the timing of changes may not be as predictable; however, irrigation use in these regions are strongly linked to the efficiency (i.e., N_D) of water resources used for the crop types.

Changes to recharge in future time periods for each GCM result in modest increases of recharge, but the magnitude of the change varies considerably between models. CGCM3.1 has the largest increases of recharge rates, CGCM1 has very minor increases, and HadCM3 is relatively stable (as indicated by the near-zero changes between climate states). The significant differences between these three models indicates that prediction of future recharge is highly dependent on the model selected. Thus, when undertaking recharge modelling studies for future climate change, it is important to consider a broader range of models.

4.5 Discussion

Present irrigation rates in this region are too high, which is not desirable for several reasons: (1) it is not efficient use of freshwater resources, as often this water needs to be pumped; (2) risk of accumulating salt or alkalis in the topsoil that may inhibit crop growth (e.g., Prendergast et al., 2004); and, (3) it may raise water tables above their natural levels (see Chapter 5). In this paper, irrigation efficiencies are estimated from present data and are held constant in future periods. However, irrigation technologies and practices may become more efficient with time—particularly if problems with water resources become directly apparent to the stakeholders.

4.6 Conclusion

All of the future climates predict increased warming during summer months. In particular, CGCM3.1 and HadCM3 predict high shifts during late summer months. All GCMs indicate potential reductions of precipitation during the summer at future time periods. CGCM1 and CGCM3.1 show increases in precipitation in late summer to winter. All scenarios show that the potential growing season will expand between 3–4 weeks due to increases in temperature.

Mean annual recharge rates have a median of 45 mm/yr, with first and third quartiles of 15 and 60 mm/yr, respectively. These values are approximately 20% of the annual precipitation. Recharge simulations using irrigation yield significant increases in net recharge in the irrigation districts, from 250 mm/yr to 1000 mm/yr. Changes to recharge in future time periods for each GCM result in modest increases of recharge, but the magnitude of the changes vary considerably between model, suggesting that recharge modeling studies for future predicted climate change should consider a range of models. In the "most efficient" irrigation district, an increase of irrigation return and recharge may be at most an 0.4 mm/day increase, while in the "least efficient" district, it may be up to an 4 mm/day increase.

Acknowledgments

The authors gratefully acknowledge R.J. Soffer for providing processed LAI data, and to Tom Mathews from Environment Canada for providing solar radiation data. Lastly, thanks to Terry Underwood from TRUE Consulting for providing irrigation use and geospatial data.

Chapter 5

Hydrogeology and Groundwater Flow Model of the Oliver Region

5.1 Introduction

A regional-scale groundwater model was developed for the southern Okanagan, which has a modelling domain in the valley-bottom that extends from the south end of Vaseux Lake to the north end of Osoyoos Lake. This numeric model is used to simulate the impacts of future predicted climate change on groundwater, by applying spatial and seasonal recharge rates, modelled deterministically using a separate hydrology model as discussed previously in Chapter 4.

The regional scale model was developed first as a steady-state model, calibrated to August conditions, which are regarded as low-flows for recharge and surface water flows. The model was then converted to a transient model, which has monthly stress periods[1] for two years. Recharge and stream flow were modified to for climate change assessment of the 2050s and 2080s time periods of the CGCM3.1 A2 scenario.

[1]MODFLOW and related numerical models use the term *stress period* to define time periods with specified boundary condition controls, which may vary from stress period to stress period.

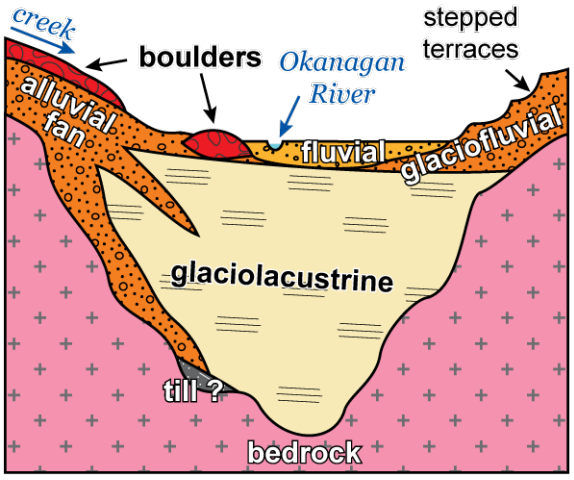

Figure 5.1 Generalized stratigraphy of the Oliver region, showing a west–east section across the valley.

5.2 Conceptual model

5.2.1 Hydrostratigraphy

The generalized valley bottom hydrostratigraphy, shown in Figure 5.1, consists of coarse sand, and gravel with boulders near the surface. Saturated sediments adjacent to Okanagan River and surrounding lakes form an unconfined aquifer. Sand and gravel sediments also extend along the valley margins; however, these are commonly unsaturated. The surface sediments are underlain by fine lacustrine silt and clay of limited permeability, which overlie bedrock that is assumed to be impermeable.

5.2.2 Aquifer hydraulic properties

Most of the high-producing water wells (BC MoE, 2006) in the Oliver region are completed in the upper sand and gravel aquifer, adjacent to (and vertically below) the Okanagan River. Table 5.1 shows the well names, and respective well tag numbers (WTN), their seasonal usage, and average pumping rate. The information on pumping rates was provided by Foley et al. (2005).

Table 5.1 Production water wells in the Oliver region, which are identified in BC using well tag numbers (WTN).

Well name	WTN	Seasonal usage	Aquifer type	Average pumping rate	
				(USgpm*)	(m^3/s)
Buchanan Rd.	21873	summer	unconf.	402	2191
Fairview	21867	year-round	unconf.	425	2317
Blacksage 1	49481	summer	unconf.	2000	10 902
Rockcliffe	82376	year-round	unconf.	1500	8176
Miller Rd.	84724	year-round	unconf.	1092	5952
Tugulnuit 2	83008	summer	unconf.	1200	6541
Town	29205	?	?	?	?
Lions Park	83010	year-round	unconf.	1230	6705
CPR	83011	year-round	unconf.	1000	5451
BCFGA 1	53199	summer	semi-conf.	300	1635
BCFGA 3	46717	summer	semi-conf.	550	2998
Deer Park Fire	82374	emergency	unconf.	1501	8182
Deer Park Dom.	82375	year-round	unconf.	108	589

*US gallon per minute; 1 USgpm $\approx 5.45\,m^3/day \approx 6.31\times10^{-5}\,m^3/s$

Pumping test data are available for some of these wells, which provide hydraulic property estimates for the sand and gravel aquifer, such as transmissivity, T, hydraulic conductivity, K_s, and specific yield, S_y (Table 5.2). The storage coefficient, S, is estimated to be about 5.7×10^{-5} (Hodge and Lowen, 1980).

Hydraulic conductivity, K_s, was calculated from T using an estimate of the saturated thickness, b, of the unconfined aquifer (using $T = K_s\,b$). The saturated thickness represents the difference in elevation between the silt contact and the water table. The geometric mean was used where multiple estimates of T were available. Figure 5.2 shows a probability distribution of the hydraulic conductivity values from the sand and gravel aquifer, which have a log-transformed mean of 2.4×10^{-3} m/s or 204 m/day.

No hydrogeological test data are available for the silt and clay aquitard, as it is a low-producing hydrogeological unit. Hydraulic conductivities in the silt and clay are estimated to be between 0.1 to 10 m/day, or 1.2×10^{-6} to 1.2×10^{-4} m/s, and specific yield values are estimated to be about 0.02 (e.g., Domenico and Schwartz, 1998).

Table 5.2 Hydraulic properties from pumping tests conducted at production wells: transmissivity, T, saturated aquifer thickness, b, hydraulic conductivity, K_s, specific yield, S_y, and aquifer test method(s).

Well name	T	b	K_s		S_y	Method*
	(m^2/day)	(m)	(m/day)	(m/s)		(Reference†)
Buchanan Rd.	9439	20.7	439	5.1×10^{-3}	0.16	TR (F)
Fairview	9546	26.5	359	4.2×10^{-3}	–	TR (F)
Blacksage 1	5200	24.8	210	2.4×10^{-3}	–	
Rockcliffe	15 310	25.3	605	7.0×10^{-3}	0.38	J, TR
Miller Rd.	1465	11.9	123	1.4×10^{-3}	0.18‡	TR (G1)
Tugulnuit 2	9500	11.9	800	9.3×10^{-3}	0.10	TR (G2)
Town	6495	8.8	737	8.5×10^{-3}	0.22‡	TR
BCFGA 1	204	4.6	45	5.1×10^{-4}	–	RD (H)
BCFGA 3	492	6.6	75	8.7×10^{-4}	–	RD (H)
Deer Park Fire	450	20.6	22	2.5×10^{-4}	–	RD (P)
Deer Park Dom.	5000	21.3	235	2.7×10^{-3}	–	RD (P)

*TD, Theis drawdown; TR, Theis recovery; J, Jacob; RD, residual drawdown

†F, (Foweraker, 1969); M, (Callan, 1971); H, (Hodge and Lowen, 1980); P, (Arengi and Badry, 1993); G1, (Allard, 2004); G2, (Foley et al., 2005)

‡Estimated from pumping well using the Neuman (curve matching) method—not reliable

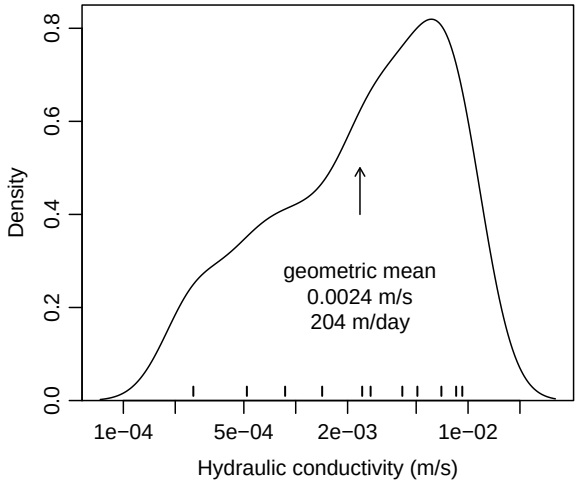

Figure 5.2 Probability distribution of the hydraulic conductivity of the sand and gravel aquifer from pumping test results in Table 5.2. This graph has a log-x scale, and shows the K_s values beneath the curve.

If the hydraulic property estimates are reasonable for the sand and gravel unconfined aquifer and the silt and clay aquitard, then there are approximately two-orders of magnitude difference in the hydraulic conductivity at the contact between the upper sand and gravel and lower silt and clay materials, so this contact may act as an impermeable (no-flow) boundary for simple models and analytical solutions of groundwater flow (Anderson and Woessner, 1992).

Similarly, the underlying bedrock is assumed to have very low bulk permeability, so it is considered impermeable. However, this assumption may be incorrect, as it is known that the bedrock is highly fractured (in outcrop exposures at high elevation), and water seepage has been observed along parts of the Okanagan Valley Fault system (Grasby and Hutcheon, 2001). Whether the bedrock fracturing extends to depth is uncertain, but nonetheless likely. Furthermore, a large hydraulic gradient exists between the uplands and the Okanagan Valley Fault system (shown in Figure 2.4), which has an elevation difference of 1100 m. However, as the fault system is beneath hundreds of metres of sediment, this flow cannot be verified nor easily quantified. Investigation of the bulk permeability of the bedrock and the contribution of groundwater flow through the bedrock surface is in progress (H. Voeckler, PhD candidate, University of British Columbia, in progress).

5.2.3 Direct recharge

Direct areal recharge to the aquifer occurs from infiltration of precipitation and irrigation return flow. Details of both the climate scenarios and direct recharge modelling were discussed previously in Chapter 4, but are summarized here.

Direct recharge was estimated using HELP version 3.80D (Berger, 2004), which is a revised and updated version from Schroeder et al. (1994). Spatially varying estimates of recharge were modelled at a 100 m grid resolution, based on an extensive soil database for the southern Okanagan (Wittneben, 1986), which was used to build soil profiles over the region. Recharge was modeled for each grid location, combining land use, leaf area index, water table depth and slope. Current and future predicted climate data were obtained for CGCM3.1 A2, which was developed by the Canadian Centre for Climate

Modelling and Analysis (Flato et al., 2000). Temperature data were downscaled (Wilby et al., 2002); however, changes in precipitation and solar radiation were calculated directly from the raw GCM data as these variables could not be reliably downscaled. Climate data were then synthetically generated using LARS-WG (Semenov and Barrow, 1997) for input to the recharge model. Three time periods are considered, which were selected from the availability of GCM data: base or 'current' (1961–2001), 2050s (2046–2065) and 2080s (2081–2100). Estimates of recharge, runoff and evapotranspiration were estimated.

5.2.4 Irrigation return flow

Irrigation return flow is the fraction of applied irrigation that contributes to recharge. Often, this is only approximated; for example Scibek and Allen (2006b) used 25% of irrigation. Details concerning irrigation input were discussed in Chapter 4, where irrigation was calculated from crop water demand coefficients, and daily time series of evapotranspiration and precipitation data. Irrigation return using this method is effectively calculated directly through the HELP model, rather than approximating the bulk range of irrigation return flow. Values in Figure 4.18, suggest that 20% is a reasonable minimum value; however, the simulated irrigation return is variable from year-to-year, and changes significantly between irrigation districts.

Irrigation districts are listed in Table 5.3, and their locations are shown over the groundwater model in Figure 5.10. Note that portions of the irrigation districts extend beyond the extent of the aquifer. The interpolation from the irrigation districts to the recharge model to the groundwater model have associated errors, which result in slight shifting in areas (described in more detail later). Irrigation application rates for current and future time periods are shown in Figure 5.3.

Total annual groundwater pumping volumes (described next section) account for 25.5% of the irrigation reported in Table 5.3,[2] which suggests that at least 74.5% of irrigation is

[2]This table estimates total irrigation using the area defined using the saturated groundwater model; the ratio of annual pumping to measured total irrigation from Table 4.4 is 24.6%

Table 5.3 Irrigation districts in relation to the groundwater model. The area indicated in this table is the interpolated area used in the groundwater model, which is not identical to the mapped extents of the irrigation districts. Irrigation totals in each district are mean annual rates, which were calculated using equation 4.5 in Section 4.3.3 with the last 100 years of daily synthetic climate data (of 200 generated years).

Name	No.	Area (m^2)	Area ratio to Ch. 4*	Irrigation (mm/year)		
				base	2050s	2080s
Mud Lake	1	3 185 779	1.117	1091	1233	1372
Blacksage	2	2 250 012	1.217	1343	1519	1690
Rockcliffe	4	4 193 850	0.862	965	1091	1214
Fairview	5	2 648 634	1.035	902	1020	1135
Hester Ck.	6	3 193 647	0.878	610	691	771
Mt. Kobau	7	2 463 621	0.866	840	950	1056

*See "Area" in Table 4.4, which is area of the mapped irrigation zones.

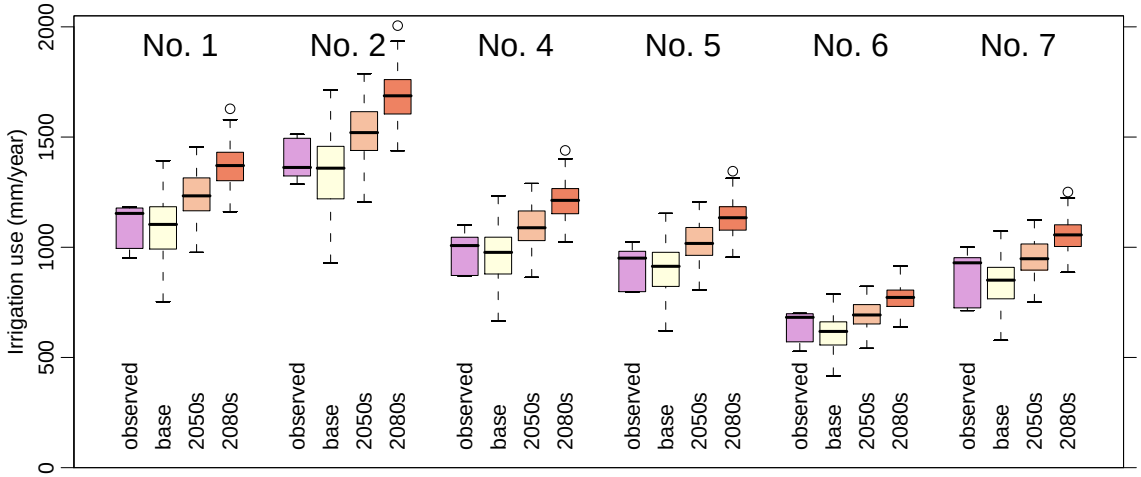

Figure 5.3 Boxplots of annual irrigation rates in each irrigation district showing the observed rates (between 2000–2005), and 100-years of calculated irrigation rates using synthetic base, 2050s and 2080s time periods. Relative changes from base to future periods for all irrigation zones are 1.14 and 1.26 to the 2050s and 2080s, respectively. Mean values for synthetic climate/irrigation data are in Table 5.3.

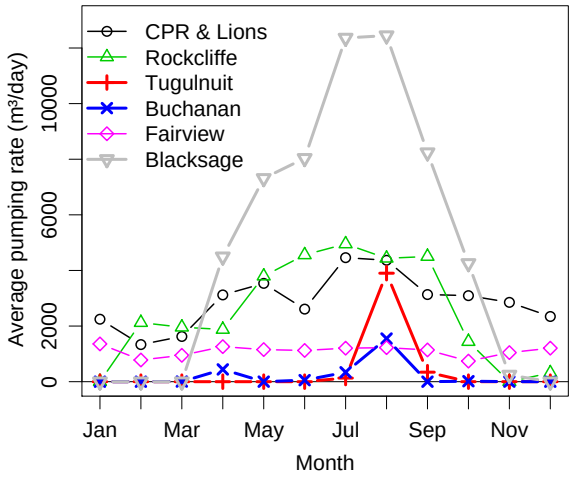

Figure 5.4 Well production rates for 2005, see Table 5.4.

supplied directly from Okanagan River; via the SOLID canal, which draws water from Okanagan River near McIntyre Dam.

5.2.5 Pumping wells

Monthly production rates were available for 2005 only (Table 5.4 and Figure 5.4), which were used in the transient model. Measurements were made at pumping stations near one or more production wells, so only one well was used to represent multiple wells; in particular: Lions Park was merged to CPR, Tugulnuit 2 was used to represent other Tugulnuit wells, and Blacksage 2 was used to represent Miller Road. It is expected that the pumping rates may increase in future time periods, due to large increases in crop water demands described in Chapter 4, and the dependence of some irrigation districts on groundwater sources. However, these pumping rates were not modified for future times, as it is uncertain how the pumping rates are presently influenced by irrigation demands, and how this influence may change in the future.

In future time periods, irrigation is expected to increase to meet the demands of irrigators, which is in due part to: (1) a longer growing season, and (2) higher evapotranspiration rates from increases in temperature. To meet these demand increases, water must be either extracted from Okanagan River (through the SOLID canal) or pumped from the

Table 5.4 Average well production rates for 2005, all units are m^3/day.

	CPR & Lions†	Rockcliffe domestic	Tugulnuit	Buchanan Road*	Fairview domestic*	Blacksage domestic*	Monthly totals
Jan	2247.1	1.3	0.0	0.0	1357.5	0.0	3605.9
Feb	1334.8	2124.0	0.0	0.0	779.9	0.0	4238.7
Mar	1626.0	1959.0	0.0	4.4	948.2	0.0	4537.6
Apr	3120.2	1877.7	0.0	441.3	1260.2	4493.5	11192.8
May	3535.3	3795.1	0.0	0.4	1153.6	7312.9	15797.3
Jun	2609.8	4558.8	0.0	54.8	1123.0	8034.8	16381.1
Jul	4459.8	4952.2	130.5	336.9	1204.6	12360.0	23444.0
Aug	4367.5	4437.7	3901.4	1550.7	1224.2	12447.2	27928.7
Sep	3133.4	4501.4	341.9	0.0	1141.4	8238.3	17356.5
Oct	3094.4	1441.6	0.0	17.0	740.1	4254.6	9547.7
Nov	2852.9	0.0	0.0	1.8	1045.4	241.7	4141.8
Dec	2344.9	316.4	0.0	0.0	1205.3	0.0	3866.6
Ann	2906.3	2497.6	370.5	203.1	1100.8	4816.1	11894.3

*Meter only read on a periodic basis
†Meter reported not to be accurate
Source: B. Hamilton, pers. comm. 2006

aquifer. Pumping rates were increased between April and October in all pumping wells by a factor of 1.2 for the 2050s, and 1.4 for the 2080s.[3] These increases account for and irrigation demand increases and a stronger reliability on groundwater resources.

5.2.6 Surface water hydrology

Hydrology data used in this analysis, including lake stages and flow rates in rivers and streams, are listed in Table 5.5.

5.2.6.1 Lakes

The primary control of hydrology in the region is from Vaseux Lake to the north, and Osoyoos Lake to the south; the two lakes are connected by Okanagan River. The stages for these lakes are controlled by McIntyre Dam for Vaseux Lake (Figure 5.5a) and by Zosel

[3]The increases to bulk annual pumping rates are 1.17 and 1.34 for the 2050s and 2080s, respectively.

Table 5.5 Hydrological gauging stations (HYDAT CD, Environment Canada, 2001).

Station name	ID	Location	Years
Lake stage elevations			
Vaseux Lake near the outlet	08NM243	49°16′25″N, 119°31′24″W	1991–*present*
Osoyoos Lake near Osoyoos	08NM113	49°01′43″N, 119°27′37″W	1946–*present*
River or creek flow rates			
Okanagan River near Oliver	08NM085	49°06′53″N, 119°33′50″W	1944–*present*
Vaseux Creek above Dutton Ck.	08NM015	49°15′44″N, 119°28′27″W	1919–1982
Vaseux Creek above Solco Ck.	08NM171	49°14′58″N, 119°19′16″W	1970–*present*
Inkaneep Creek, upper station	08NM082	49°07′10″N, 119°21′40″W	1941–1950
Inkaneep Creek, lower station	08NM012	49°07′00″N, 119°29′30″W	1919–1950
Testalinden Creek near Oliver	08NM130	49°07′13″N, 119°35′25″W	1965–1968
Testalinden Creek in canyon	08NM164	49°07′17″N, 119°35′53″W	1969–1986

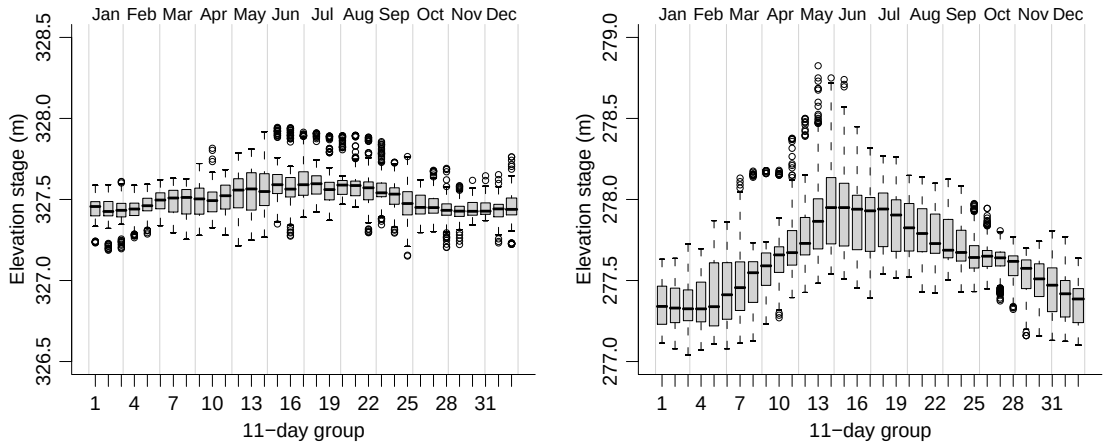

(a) Vaseux Lake (08NM243), 1991–2003 **(b)** Osoyoos Lake (08NM113), 1977–2003

Figure 5.5 Stages of lakes at both ends of Okanagan River in study area.

Dam at Osoyoos Lake in Oroville, Washington (represented by Figure 5.5b measured at Osoyoos, BC). Mean monthly deviations from annual mean lake elevations are shown in Table 5.6).

There are also many small ($\leq$ 1 km) lakes along the valley bottom and valley sides, such as Tugulnuit Lake,[4] Gallagher Lake, and Deadman Lake. These water bodies do not

[4]This is the official geographic name; however, *Tuc-el-Nuit Lake* is also very common

Table 5.6 Monthly median stages (m) for surface water bodies. Stages for Vaseux Lake and Osoyoos Lake are an elevation, while Okanagan River is a gauge height from an arbitrary datum.

	Vaseux Lake		Osoyoos Lake		Okanagan River	
	median	deviation	median	deviation	median	deviation
January	327.433	−0.063	277.331	−0.303	0.623	−0.116
February	327.450	−0.046	277.331	−0.303	0.656	−0.082
March	327.507	+0.011	277.500	−0.134	0.772	+0.034
April	327.503	+0.007	277.650	+0.016	0.841	+0.103
May	327.556	+0.060	277.833	+0.199	1.127	+0.388
June	327.576	+0.080	277.945	+0.311	1.051	+0.313
July	327.581	+0.085	277.920	+0.286	0.850	+0.112
August	327.582	+0.086	277.772	+0.138	0.791	+0.053
September	327.528	+0.032	277.671	+0.037	0.791	+0.053
October	327.444	−0.052	277.640	+0.006	0.721	−0.017
November	327.427	−0.069	277.550	−0.084	0.598	−0.140
December	327.439	−0.057	277.406	−0.228	0.587	−0.151
Annual	327.496		277.634		0.738	

have any major streams flowing in or out of their surface (with the exception of Tugulnuit Lake, which has a gravity-fed pipe down to Okanagan River). It is interpreted that all of these lakes are sustained through groundwater.

5.2.6.2 Rivers

Okanagan River is the main surface water body in the region (see Figure 2.1). The river is controlled by the *Okanagan Flood Control System*, which consists of channelized reaches and flow structures, and was constructed between 1950–1957 to reduce damages from seasonal flooding (Schubert, 1983). The river flow is controlled by McIntyre Dam, near the outlet of Vaseux Lake, where some of the flow is also diverted into the SOLID[5] irrigation channel. While the upper reach of Okanagan River is natural (unaltered channel; 5.6 km in length), the remaining 2/3 is channelized, from 1 km north of Oliver to Osoyoos Lake. The channelized portion was over-excavated, and river banks were constructed from emplaced

[5]Southern Okanagan Lands Irrigation District; formerly called SLOP or South Okanagan Lands Project

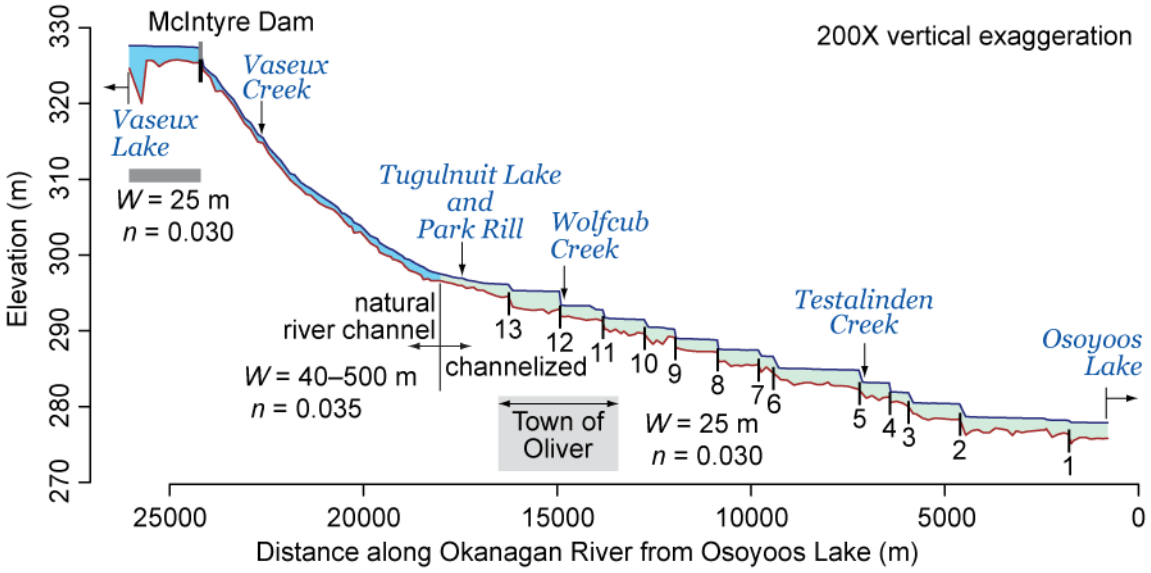

Figure 5.6 Elevation profile of Okanagan River, showing stage and river bottom, locations of numbered vertical drop structures and McIntyre Dam, approximate channel widths, W, and Manning's roughness coefficient, n; surveyed June 9–23, 1980 (Schubert, 1983; Nichols, 1993). Map of river is in Figure 2.1, page 14.

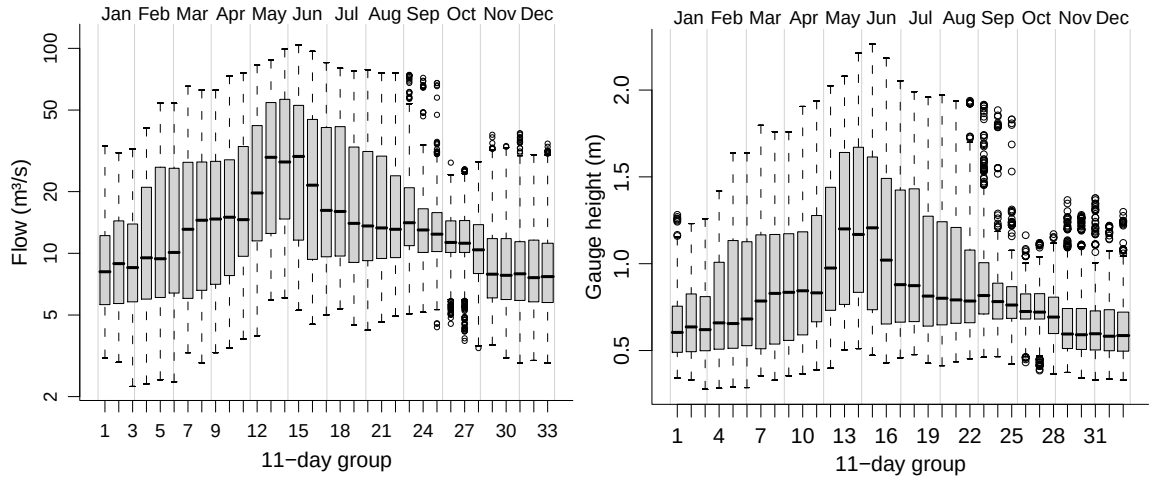

(a) Flow rate (log y scale) **(b)** Gauge height

Figure 5.7 Flow in Okanagan River at Oliver (ID: `08NM085`), 1957–2004.

local materials (Hodge, 1978). There are thirteen vertical drop structures[6] to slow the flow and control the grade (Figure 5.6), each with about 1 metre elevation drop.

[6]Located on the CD at `gisdata/ok_riv_struct.shp`

Historical flow data from a Water Survey of Canada station near Oliver are shown in Figure 5.7, which shows normals of both gauge height and flow rate. River stage and discharge are related using an empirical power-curve equation of the form (Kennedy, 1984):

$$Q_R = c\,(a + h_R)^b \tag{5.1}$$

where Q_R is the flow rate of Okanagan River (m^3/s), h_R is the river gauge height (m), and a, b and c are fitting parameters. Using stage–discharge calibration data from HYDAT ID `08NM085` in Okanagan River near Oliver (L. Campo, pers. comm. 2007), the nonlinear least squares (NLS) fit for the parameters in equation 5.1 is $a = 0.117$, $b = 2.134$ and $c = 16.321$. The NLS fit is excellent, with a maximum residual of 0.48 m^3/s. Equation 5.1 is rearranged to determine stage from flow rate:

$$h_R = \left(\frac{Q_R}{c}\right)^{\frac{1}{b}} - a \tag{5.2}$$

Seasonal fluctuations along Okanagan River were approximated using equation 5.2, and appear in Table 5.6. The upper reach of Okanagan River, from Vaseux Lake to McIntyre Bluff was adjusted using levels in Vaseux Lake.

Perhaps one of the most uncertain impacts of climate change on Okanagan Basin are to Okanagan River, and the lakes through which it passes. To account for climate change effects on these surface water boundaries would require simulation of the large portion of Okanagan Basin north of the study location ($\sim$7590 km^2 drainage area to Oliver, HYDAT ID `08NM085`, Environment Canada, 2001), which was outside the scope of this project. For this reason, it is assumed that both the lakes and Okanagan River stages have similar seasonal patterns and levels in future time periods. This is not an unreasonable assumption given that levels and flows are controlled.

5.2.6.3 Streams

The majority of the streams entering the Oliver region are ephemeral, and do not extend far down into the valley in available orthophotos. The stream catchments to the bedrock interface are shown in Figure 2.1. It is assumed that some of these small streams directly

recharge to groundwater at the bedrock–fill boundary, since they disappear partway down the valley over unconsolidated material.

The incoming annual flow from each stream, $\hat{Q}_{Ann}$, was approximated using an empirical correlation with the catchment area to the valley fill margin, A_B (Table 5.7; see Figure 2.1), and the median annual discharge. This estimate was further adjusted to incorporate the hypsometric curves (or distribution of elevations) unique to each catchment:

$$H_f = \sum_{z=1}^{n} h(z)\,[P_l(z - 275) + 1] \tag{5.3}$$

where H_f is the hypsometric factor for each stream catchment, $h(z)$ is a density histogram of the catchment elevations in 50 m increments (where $\sum h(z) = 1$), z is the mid-point of the elevation band, and P_l is the precipitation lapse rate relative to the valley bottom elevation (~275 m), which was determined in Appendix A.4, to be $6{\times}10^{-4}$ m^{-1} (or 60% increase in mean precipitation per 1 km rise in elevation). The quantity H_f considers the increased precipitation at higher elevations, and how this influences different catchments with different distributions of elevations. Higher values of H_f indicate that the streamflow is more influenced from increased precipitation at higher elevations.

Annual flow data from Water Survey gauges were determined using available data, which span over different time periods, and years with insufficient data were excluded from analysis. Summary statistics are listed in Table 5.8. Figure 5.8 shows boxplots of the annual flow data which are plotted against $A_g\,H_f$, or the area to the gauge adjusted by H_f. The zero-intercept best-fit line through the median values, weighted by counts is:

$$\hat{Q}_{Ann} = 92581 \frac{\mathrm{m}^3}{\mathrm{year}\cdot\mathrm{km}^2}\, A_B\, H_f \tag{5.4}$$

where $\hat{Q}_{Ann}$ is the annual estimate of flow (m^3/yr) from a stream catchment with area A_B (km^2), and hypsometric factor H_f. The inclusion of H_f in equation 5.4 improves the R^2 correlation statistic from 0.7987 to 0.8642. The line of best-fit, shown in Figure 5.8 passes through the range of historical annual flows, so it may be considered realistic. This correlation is an underestimate of total catchment flow, since hyporheic flow and other shallow groundwater bypasses stream gauges, which only consider surface water flow in

Table 5.7 Hydraulic parameters from stream catchments, shown in Figure 2.1; items are sorted by their hypsometric factor, H_f; A_B is the area of the basin to the bedrock margin; estimated annual flow, $\hat{Q}_{Ann}$, is described later.

Stream name	A_B (km^2)	H_f –	$A_B\,H_f$ (km^2)	$\hat{Q}_{Ann}$ (1×10^6 m^3/yr)
Vaseux	290.0	1.76	510.4	47.25
Inkaneep	160.7	1.62	260.8	24.14
Hester	9.2	1.60	14.6	1.35
Testalinden	12.3	1.58	19.6	1.81
Tinhorn	3.6	1.57	5.7	0.53
Reed	18.4	1.54	28.4	2.63
Wolfcub	54.1	1.49	80.8	7.48
Park Rill	83.0	1.48	123.2	11.41
Orofino	10.8	1.47	15.9	1.47
Togo	2.4	1.43	3.4	0.31
Victoria	13.1	1.42	18.5	1.72
Atsiklak	10.9	1.40	15.3	1.41
Burnell	8.1	1.35	10.9	1.01
Kearns	39.8	1.24	49.5	4.58

Table 5.8 Statistics from annual measured streamflow data; A_g is the area to each individual gauge; Q_1 and Q_3 are the first and third quartiles, respectively. Note that the time periods used for each gauge are different; statistics with more counts or valid years of analysis should be considered to be more approximate to true statistical values.

Short name	ID	A_g (km^2)	$A_g\,H_f$ (km^2)	Annual flow (1×10^6 m^3/yr) count	min	Q_1	median	Q_3	max
Tes1	08NM130	13.0	20.6	4	0.31	0.42	0.51	0.72	1.18
Tes2	08NM164	13.0	20.6	13	0.22	0.42	0.60	1.17	2.52
InkUp	08NM082	70.4	114.2	9	0.85	1.61	3.92	6.74	13.02
InkMid	08NM012	164.0	266.1	19	2.37	5.35	8.54	13.35	29.70
VasUp	08NM171	117.0	205.9	33	11.56	20.27	29.63	37.52	46.96
VasMid	08NM015	255.0	448.8	27	18.90	31.22	42.95	53.08	76.10

the creek channel. Estimates of $\hat{Q}_{Ann}$ for all catchments, Table 5.7, are calculated using equation 5.4.

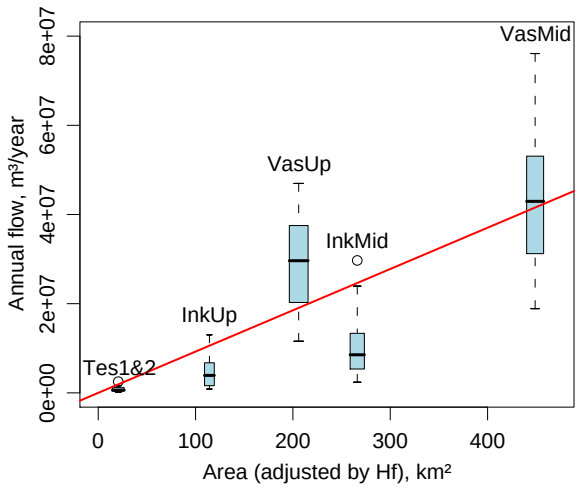

Figure 5.8 Analysis of annual stream flow data with catchment area, adjusted by H_f. Widths of boxplots are proportional to the square root of the count of annual flow values. The line of best-fit with median values (center of boxplot) is shown, which was used to calibrate equation 5.4.

It interesting to note that the correlations of basin flow with area are best using maximum values, and are poorest using minimum annual values (Table 5.8). This is perhaps because there are fewer losses of surface water in the catchment during high-flow years, and more variable losses of surface water in low-flow years.

The seasonal signal of creek flow was estimated using data from the Upper Vaseux Creek gauging station (ID `08NM171`), which was selected since it assumed that the creek bottom is close to bedrock, and would best represent total flow in the catchment. Other stations have very similar seasonal signals in both timing and shape. The seasonal signal was represented using a normalized seasonal distribution, D_t:

$$D_t = \frac{Q_t}{\sum (Q_t \, \Delta t)} \qquad \text{for all } t \text{ in a season} \tag{5.5}$$

where Q_t is the mean flow rate for time t in a season (such as in a 5-day period or a month), and Δt is the number of days in t. The normalized seasonal distribution curves are illustrated in Figure 5.9 for 5-day and monthly distributions. The normalized seasonal distribution is used to estimate seasonal flow at all creeks, given an annual flow (with units m^3/day):

$$\hat{Q}_t = \frac{\hat{Q}_{Ann} \, D_t}{365 \text{ days}} \tag{5.6}$$

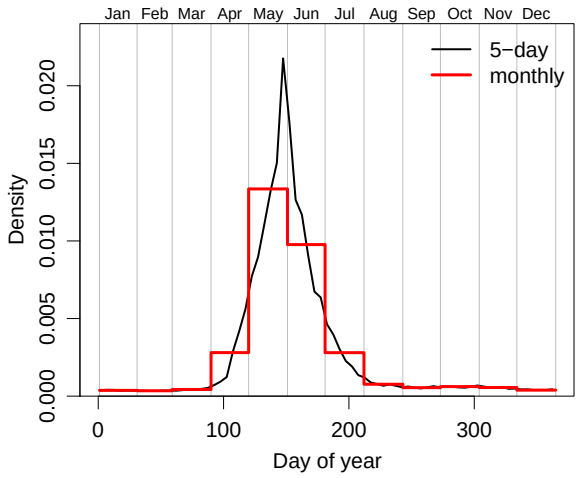

Figure 5.9 Normalized seasonal distribution of flow at Upper Vaseux Creek gauge, above Solco Ck., 1970–2003 (ID `08NM171`). Both 5-day and monthly curves represent a normalized seasonal distribution, D_t, which each integrate to 1 over a year.

In future climate periods, it is expected that peak flow of stream discharge will arrive earlier in the season due to earlier snowmelt (Cannon and Whitfield, 2002; Scibek et al., 2006). Differences in the start of the growing season (Table 4.7, page 95) were used to adjust the seasonal signal of creek flow, which then was re-interpolated to monthly values for each climate period. These shifts from the base period are 8 and 18 days for 2050s and 2080s, respectively. It is uncertain how annual flow volumes may change with future conditions. For this reason, $\hat{Q}_{Ann}$ was not modified for future periods. Values of D_t for each month are listed in Table 5.9.

Table 5.9 Monthly normalized distribution values, D_t (scaled 1×10^{-3} for display), for flow at Upper Vaseux Creek for current and future-predicted climate change periods for CGCM3.1. Each row adds to 1 when multiplied by the number of days in each month.

Case	Jan	Feb	Mar	Apr	May	Jun	Jul	Aug	Sep	Oct	Nov	Dec
base	0.371	0.345	0.429	2.804	13.350	9.764	2.802	0.766	0.547	0.615	0.555	0.386
2050s	0.339	0.333	0.543	4.616	15.184	7.292	1.881	0.614	0.484	0.564	0.484	0.373
2080s	0.343	0.354	1.160	8.104	14.555	4.704	1.086	0.556	0.489	0.578	0.431	0.376

5.3 Groundwater flow model

GMS version 6.0 (Owen et al., 1996; EMRL, 2005) was used for both the 3D stratigraphic construction and to simulate groundwater flow using MODFLOW-2000, version 1.15.00 (Harbaugh et al., 2000). GMS allows the user to define a groundwater model using a conceptual model approach, whereby properties and boundaries are defined spatially using vector-based arcs, polygons and points. These can represent, for example, aquifers, rivers, and wells, which contain specific boundary condition data, such as material properties, stage and pumping rates. The conceptual models are then translated to a finite-difference grid by the location of the vector elements on the grid, and boundary condition data are also translated to the respective MODFLOW modules.

Conceptual models for steady-state and transient boundary conditions were defined, which, respectively, represent low-flow conditions expected in mid-summer (represented by August) and for each month of a two year simulation (24 stress periods of 28 to 31 days). Two years with identical boundary conditions (stress periods) in each year were simulated to compare changes between each year. Four time steps were simulated in each stress period using a time step multiplier of 1.2, which total to 96 simulated time steps over 730 days.

5.3.1 Model domain and grid design

The finite difference grid, shown in Figure 5.10, has 256 rows, 98 columns (22.6 km by 7.758 km) and 9 layers. The horizontal grid spacings range between 50 to 100 m, with telescopic grid refinement focused around pumping wells. This resolution is sufficient to define cones of depression around the production wells, since the surrounding materials have high transmissivities. Many consulting reports indicate drawdowns in pumping wells on the order of tens of centimetres (e.g., Arengi and Badry, 1993), which may indicate that a fine-resolution grid is not required to properly discretized cones of depression around each well.

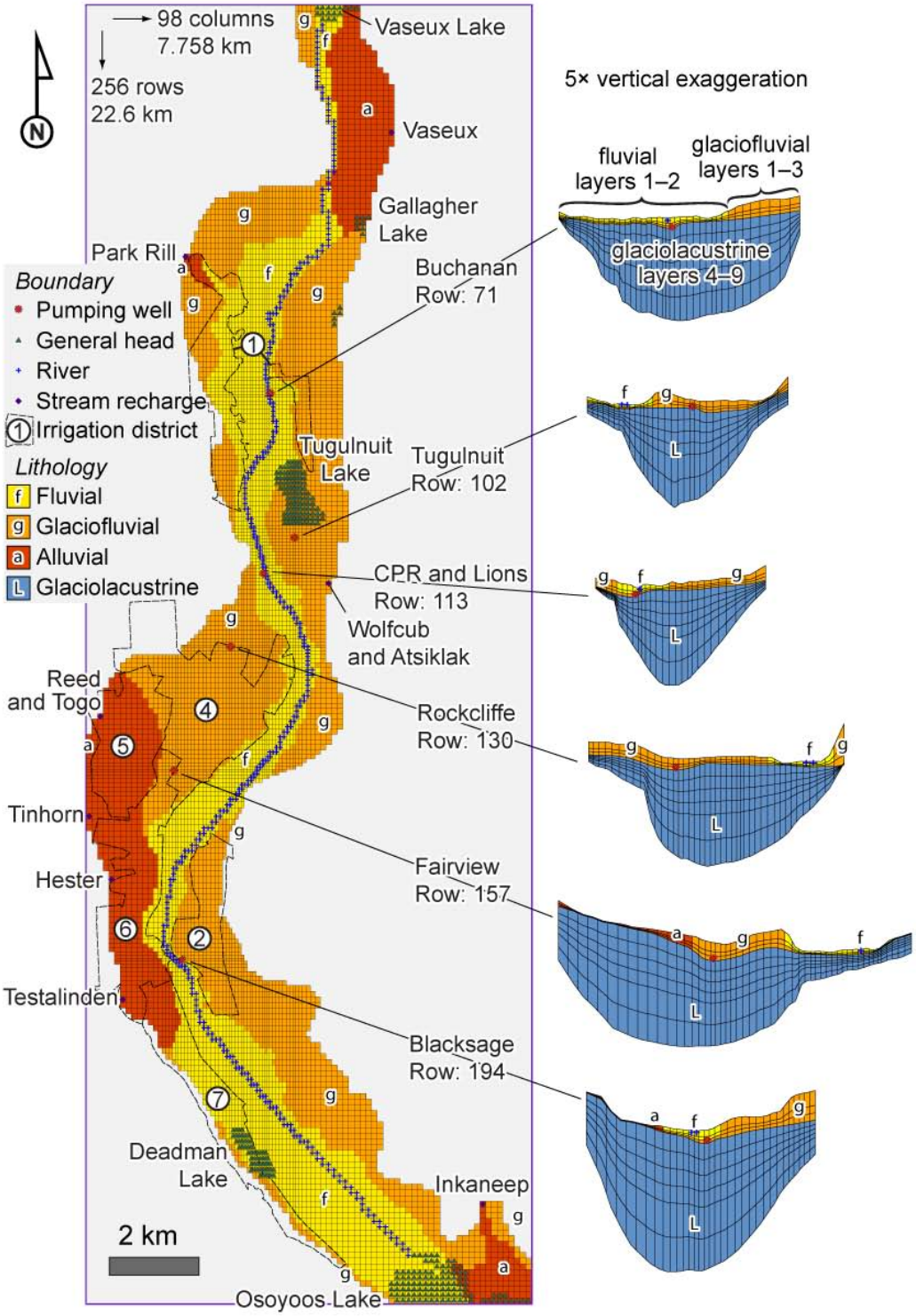

Figure 5.10 Regional model grid, materials and boundary conditions. The vertical profiles are shown at each pumping well, and have a slightly larger scale than the plan-view, and a vertical exaggeration of 5×. Locations of irrigation districts are also shown, which were used in the recharge analysis (Chapter 4).

The upper surface of the grid was interpolated from Level 1 digital elevation data (Natural Resources Canada, 2005); the top of layer 4 was interpolated using the silt top, described in Section 2.3.3.2, and is shown in Figure 2.10; the bottom of layer 9 was interpolated using the bedrock surface, described in Section 2.3.2, and is shown in Figure 2.6. The top three layers contain alluvial and glaciofluvial materials, and have vertical spacing fractions of 1/2, 1/4 and 1/4, from top to bottom. The uppermost layer is thicker than the others, since it is typically dry for most of the region above the flood plane, and it contains boundary data for the river and lakes, which require sufficient vertical space for the boundary bottoms.[7] The Okanagan River fluvial materials are in the top two layers only, and are usually underlain by glaciofluvial deposits for layer 3. Layers 4 to 9 are glaciolacustrine silt and clay materials, which have vertical spacing fractions of 1/8 for layers 4–7, and 1/4 for layers 8–9.

The bedrock is considered to be impermeable and was defined using the bottom and sides of the model domain, which are simulated as a no flow boundaries by MODFLOW. The aerial extent of the active model was defined such that the lowermost grid cells remained saturated under August steady-state conditions. MODFLOW cannot simulate processes that extended too far up along the raised benches, since the majority of this is unsaturated material. A more advanced code, such as FEFLOW (e.g., Diersch and Perrochet, 1999) would be better suited to simulate these regions and groundwater conditions.

5.3.1.1 Materials and flow package

The Layer Property Flow (LPF) Package was used to simulate groundwater flow in MODFLOW. The materials were defined using zones (array IDs), as shown in Figure 5.10. The package was configured to calculate interblock transmissivity using the harmonic mean, and all layers were set to be "convertible" (as opposed to "confined," where transmissivity is constant). Wetting was enabled for all layers, and is detailed later.

[7] The digital elevation data used for the upper surface does not always correlate with the hydrology boundaries from river surveys, and often the digital elevation data is influenced by tops of vegetation and buildings. For this reason, the digital elevation data are often overestimated, which consequently overestimate the bottom limits of the layer containing the bottom of river and lake boundaries.

Material properties were initially set to values indicated from aquifer tests (see Section 5.2.2). Horizontal hydraulic conductivity and vertical anisotropies were later adjusted during calibration using steady-state conditions with August model conditions, and are found later in Table 5.11. Horizontal anisotropy factors, K_x/K_y, for all materials were set to 1.0, since this anisotropy is not expected to change horizontally. Vertical anisotropy factors, K_h/K_z, were varied for each material. Vertical anisotropies for fluvial sediments are higher than surrounding materials, as suggested from other studies (e.g., Chen, 2000). Alluvial vertical anisotropy was also higher than other materials, since many of the material descriptions describe "hardpan" deposits (Section 2.3.3.5), which are interpreted to have come from mass transport flow deposits and, thus, likely have lower hydraulic conductivity. Also, a higher vertical anisotropy may help raise the water table along the benches, which is observed in some parts of the region.

5.3.2 Hydrological boundary conditions

Surface elevations for lakes were approximated from 0.75-arc second Level 1 digital elevation data (Natural Resources Canada, 2005), unless otherwise specified. Each type of surface water boundary was simulated using different MODFLOW packages, since each boundary condition has different mass-balance interactions with the aquifers. Park Rill was not simulated, as attempts using the Drain Package to remove near-surface water appeared unrealistic, and added to problems with simulation convergence.

5.3.2.1 Recharge and irrigation

Mean monthly recharge was applied to the upper layer in the model for each of the historic (current) and future climate periods. Monthly recharge results in Chapter 4 consisted of 100 years (1200 months) of gridded 100 m recharge rates, which were archived in multidimensional netCDF array files. These netCDF files were translated using a Python script[8] to a simple text file, which can be imported as a transient 2D scatter point file

[8]Located on the CD at `programs/monthlync2xys.py`

in GMS. The 2D transient points were then linearly interpolated to the irregular 2D grid with the same spacings as the MODFLOW model. This way, the interpolated grid can be used directly as an array for the Recharge (RCH) Package in MODFLOW. This package was configured to receive a recharge flux to the highest active cell. Three recharge arrays were prepared, which represent current conditions, the 2050s (2046–2065) and the 2080s (2081–2100), as predicted using CGCM3.1 A2.

Recharge fluxes used for this model also include considerable contribution from simulated irrigation return flow, as shown in Figure 4.17b. In this Figure, the irrigation zones do not directly overlay the aquifer—these regions outside of the model are considered to be unsaturated for part of the season, and cannot be simulated using MODFLOW. The differences of area (and annual irrigation application rates) used in recharge and irrigation return flow modelling and in saturated groundwater flow modelling is shown in Table 5.3.

5.3.2.2 River

Okanagan River has regulated flow from Vaseux Lake to Osoyoos Lake, which was modified using the monthly deviations of stage at Vaseux Lake (see Table 5.6). As this river flows year-round, it was simulated using the River Package (RIV). Boundary conditions were assigned to layer 1 of the model. River stage and bottom elevations of Okanagan River were defined from a detailed survey (Schubert, 1983). River stages were set to Osoyoos Lake levels if they were less than this lake. These adjustments were implemented in GMS using a Python script,[9] since the river stage was defined at 191 nodes from the survey data. Effects of climate change were not considered for the RIV boundary condition for Okanagan River.

The riverbed conductance was initially set to 10 $m^2d^{-1}m^{-1}$, which is lower than the surrounding hydraulic conductivities of the fluvial deposits. This value was adjusted during calibration.

[9]Located on the CD at `programs/gms_fixed2ts.py`

5.3.2.3 Streams

Development of the model initially used the Stream (STR) Package (Prudic, 1989); however, it was difficult to maintain a model that could converge with reasonable model error, and without significant oscillation in convergence. The STR package is limited in that fluxes cannot pass from the top layer, through upper dry cells to the highest active cell (if the highest active cell is several layers beneath the boundary), which is a likely scenario in the study region. The updated and much improved Streamflow-Routing Package (SFR2) (Niswonger and Prudic, 2005) could not be used, since it is unsupported in GMS. This MODFLOW package was redesigned to overcome some of the limitations described above, such as simulating unsaturated flow beneath streams.

As an alternate solution, stream flow rates were applied in the Recharge (RCH) Package, which applies a specified flux to the highest active cell. Flow rates from each stream, estimated in m^3/day, were converted to recharge fluxes using the area of a grid cell selected on the edge of the model nearest to the stream. Locations of the cells and the areas are listed in Table 5.10. A limitation of this method is that it is not possible to separate the contribution of flow from streams in the flow budget, since it is included with recharge. The fluxes were included in the 2D array of recharge using a Python script,[10] which uses the stream flow estimates in Table 5.7 with the seasonal response in Table 5.9 and the area of the grid cell in Table 5.10. Annual total stream flows were not modified for future time periods; only the seasonal timing.

5.3.2.4 Lakes

All the lakes in the region were simulated using the General Head Boundary (GHB) Package. The Lake (LAK) Package was not used, as this has more complex input requirements and posed more complications in attempts to construct a stable numerical model. Water levels, indicated in Table 5.6, were used for the transient stages. Effects of climate

[10] Located on the CD at `/programs/gms_addcreeksto2D.py`

Table 5.10 Application of streams to MODFLOW Recharge Package.

Creek name	Grid location		Area
	row	column	(m^2)
Vaseux	23	74	9789.76
Park Rill*	45	22	5413.70
Wolfcub†	116	63	6552.39
Reed‡	145	3	8799.79
Tinhorn	167	1	9769.76
Hester	178	5	9769.76
Testalinden	203	7	9668.22
Inkaneep	239	90	9834.56

*Plus tributaries: Burnell, Victoria, Orofino and Kearns
†Including Atsiklak Creek
‡Including Togo Creek

change were not considered for this boundary condition. The conductance for the polygon boundary was initially set to 10 $m^2d^{-1}m^{-2}$, which was adjusted during calibration.

5.3.2.5 Pumping wells

Pumping wells were simulated using the Well (WEL) Package, and the monthly pumping rates for 2005, Table 5.4. The depth range of screens for each well are detailed in Chapter 6, Table 6.3, which are translated and distributed along 1 to 3 cells in the upper layer of the MODFLOW grid. Effects of climate change were not considered for this boundary condition.

5.3.3 Solver and rewetting

Rewetting is a method used in MODFLOW where "dry" cells can be converted to "wet" or a variable head cell if the head in surrounding cells is high enough to trigger the rewetting (McDonald et al., 1991). This method is used since MODFLOW is a saturated-flow code, and considers "dry" cells as "no-flow" cells since it can not simulate complicated unsaturated groundwater flow. Cell rewetting was activated for all cells in the model—the model

must simulate flow with fluctuating water levels in a transient simulation. Rewetting also presents difficulties with convergence, since the convergence error used in solving the groundwater flow equation is prone to oscillation, as cells are converted between "wet" and "dry" within iterations of each time step. To avoid oscillation in the convergence, rewetting was enabled only from underlying cells (as opposed to neighbouring cells), and the head was calculated using the threshold of 12.0 with a wetting factor of 0.5, and an iteration interval of 3.

A wetting iteration interval was set to 3, since usually only 3 outer iterations are required to converge each time period; using higher intervals bypasses rewetting altogether. The threshold used in this model is considerably larger than used in other MODFLOW models (e.g., Scibek and Allen, 2004, page 62), which is possibly related to the short duration of wetting iteration interval. Attempts using smaller iteration intervals usually resulted in non-convergence, as the error would oscillate every third iteration. This model parameter is typically found through trial and error (Harbaugh et al., 2000), and larger threshold values increase stability of convergence. The drawback of using a high wetting threshold is that many cells would become "flooded", such that their head would extend beyond the top elevation of the cell. Flooding may even occur in cells that underlie dry cells—in these cases, the head has not exceeded the threshold required to re-wet the overlying dry cell. Although the water table is properly represented by using lower flooded cells, the three-dimensional flow might be misrepresented.

The geometric multigrid solver (GMG) was used (Wilson and Naff, 2004), which is an advanced MODFLOW-2000 solver based on the preconditioned conjugate gradient (PCG) algorithm. The solver was optimized for transient non-linear groundwater flow.[11] Optimal model solutions were achieved by setting the inner iteration residual convergence criterion to 0.001, the outer iteration head change convergence criterion to 0.01, a damping parameter of 0.51 with adaptive damping for remaining iterations, using ILU smoothing with semi-coarsening of the multigrid preconditioner along all dimensions.

[11] A groundwater model is considered *nonlinear* if it includes Cauchy boundary conditions or head dependant nodes, such as the MODFLOW River Package

Table 5.11 Hydrologic properties of materials used for regional model, determined through calibration (described later) of the August steady-state model to groundwater well heads.

Name	Materials	K_h (m/day)	$\frac{K_h}{K_z}$	S_s (1/m)	S_y	ϕ
Fluvial	Sand, some gravel	200.0	5.0	5×10^{-4}	0.25	0.3
Alluvial	Sand, gravel, clay	50.0	10.0	1×10^{-4}	0.2	0.3
Glaciofluvial	Sand and gravel	400.0	3.0	1×10^{-4}	0.2	0.3
Glaciolacustrine	Silt and clay	0.5	3.0	1×10^{-2}	0.1	0.3

5.3.4 Model calibration, material properties, and flow budget

Calibration was performed on a steady-state model (described next section) using approximations of hydraulic properties of the materials from results summarized in Section 5.2.2, and boundary conductances described previously. The model was calibrated iteratively by modifying independent hydraulic properties, and taking note of the model error between observed and simulated hydraulic heads from 430 water wells, and their locations within the modeling domain. A similar procedure was then used for modifying the conductances to the river and general head (lake) boundaries. Final calibrated values for hydraulic conductivities are listed in Table 5.11. Conductances of 10 $m^2d^{-1}m^{-1}$ and 20 $m^2d^{-1}m^{-2}$ provided the best-fit calibration for river arc and general head (lake) polygon boundaries, respectively.

The calibrated steady-state model is evaluated using residuals between computed and observed heads, where out of 430 wells, 243 have a negative residual (model underestimates observed) and 187 residuals are positive. The residual mean is 0.743 m, the absolute residual mean is 2.55 m, the root mean squared error (RMSE) is 3.64 m and the normalized RMSE is 6.4%. A plot of the residuals is shown in Figure 5.11. In this model, the hydraulic head is underestimated along the benches, while it is within reasonable error elsewhere. The flow budget for the steady-state model is summarized in Table 5.12.

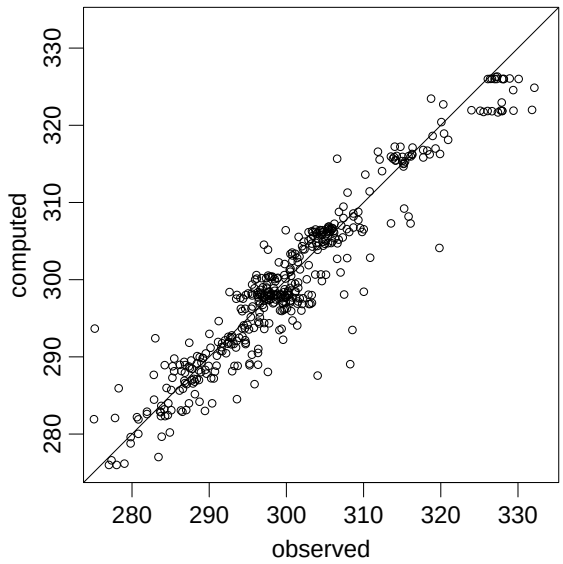

Figure 5.11 Steady-state calibration of regional model, showing a cross-plot of observed and computed heads from 430 wells. The normalized RMSE is 6.4%.

Table 5.12 Steady-state flow budget for regional groundwater model (all active cells). The difference between total in and out flow is -86.31 m^3, or -0.08%.

Source/sink	Flow in		Flow out	
	m^3	%	m^3	%
General heads	31074	28.79	−10447	9.88
Rivers	45029	41.73	−69406	64.26
Wells	0	0.	−27929	25.86
Recharge	31812	29.48	0	0.
$\sum$	107915	100.00	−108002	100.00

5.3.5 Transient simulations

Transient simulations were undertaken using the heads from the steady-state solution as an initial condition.[12] The two-year transient simulation was then repeated three times, using the heads of the previous simulation as the starting heads for the next. This looping

[12]Dry cells were removed and re-interpolated using neighbouring heads. In GMS, this was done by converting the heads from the last time step to 3D scatter points, then re-interpolating the points to the 3D grid using the inverse distance weighted (Shepard's) method with the nearest 8 points. This method replaces the dry head value, a dummy number -888.0, with realistic values of head (even if the head is below the cell bottom elevations).

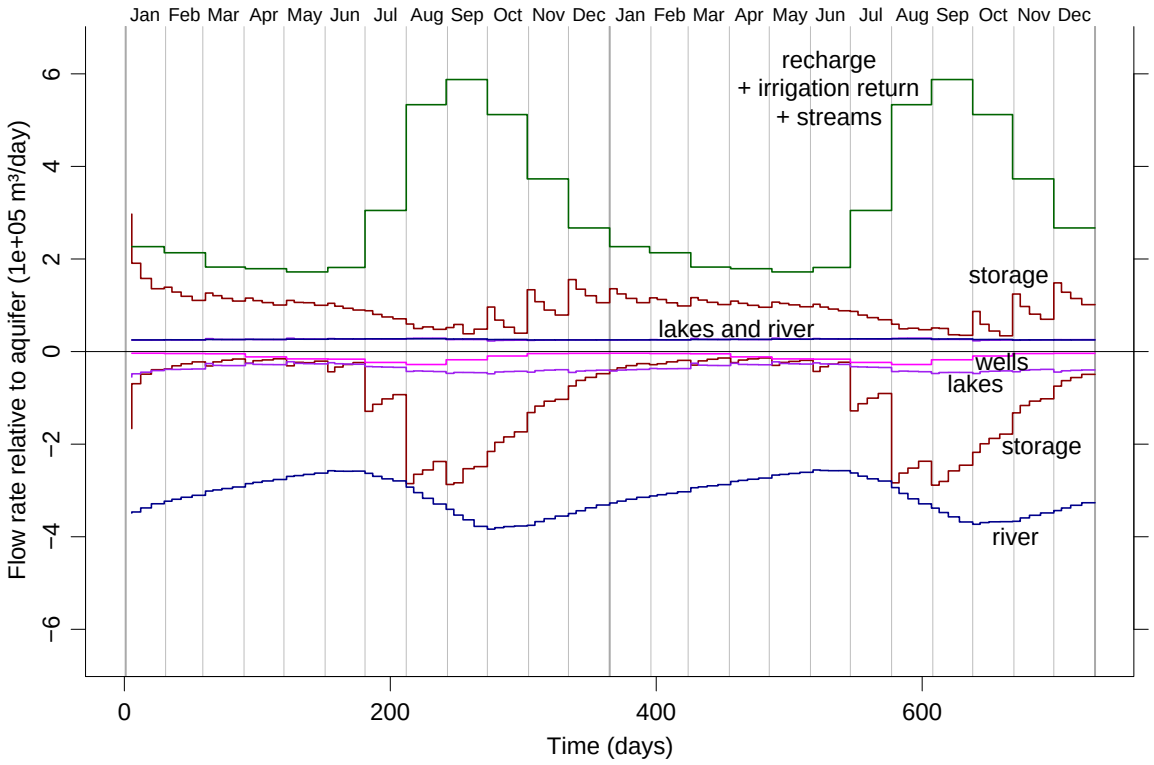

Figure 5.12 Transient flow budget for regional groundwater model using the base or "current" climate conditions for all active cells. Negative budgets indicate flow out of the aquifer, while positive budgets indicate flow into the aquifer.

of simulation allows the model to settle into a seasonal pattern, which has minor differences of head and flow rates from the first year to the second. In analysis, this could be regarded as a seasonal steady-state, since the difference of total in and out flows are nearly zero, specifically 50.03 m^3 or 0.0087%. This process was completed using the "current" or "base" recharge and stream flow conditions. The transient flow budget is shown in Figure 5.12.

The transient annual flow budget was calculated through integration of the second-year, using the trapezoid rule:

$$F \equiv \frac{f_1 + f_2}{2} dt_1 + \frac{f_2 + f_3}{2} dt_2 + \cdots + \frac{f_n + f_{n+1}}{2} dt_n \tag{5.7}$$

$$F = \sum_{i=48}^{95} \left[\frac{f_i + f_{i+1}}{2} \left(t_{i+1} - t_i \right) \right] \tag{5.8}$$

Table 5.13 Transient annual flow budget for current and future periods. The flow numbers represents the area under the curves in Figure 5.12, from January to December of the second year. Totals appear independently for flows of each climate condition. Relative changes to base conditions are listed only for future periods.

Source/sink	Flow in		Change	Flow out		Change
	1×10^6 m^3/yr	%	–	1×10^6 m^3/yr	%	–
Base						
Storage	32.536	19.66		−34.881	21.08	
General heads	9.619	5.81		−13.167	7.96	
Rivers	9.604	5.80		−113.115	68.35	
Wells	0.	0.		−4.341	2.62	
Recharge	113.746	68.73		0.	0.	
$\sum$	165.506	100.00		−165.504	100.00	
2050s						
Storage	34.629	18.39	1.064	−45.189	24.00	1.296
General heads	9.137	4.85	0.950	−14.676	7.79	1.115
Rivers	9.551	5.07	0.994	−124.110	65.91	1.097
Wells	0.	0.	–	−4.341	2.31	1.
Recharge	135.009	71.69	1.187	0.	0.	–
$\sum$	188.326	100.00	1.138	−188.317	100.00	1.138
2080s						
Storage	36.843	17.34	1.132	−55.801	26.26	1.600
General heads	8.552	4.03	0.889	−16.251	7.65	1.234
Rivers	9.472	4.46	0.986	−136.063	64.04	1.203
Wells	0.	0.	–	−4.341	2.04	1.
Recharge	157.600	74.18	1.386	0.	0.	–
$\sum$	212.467	100.00	1.284	−212.457	100.00	1.284

where F is the total annual flow in m^3/yr, dt is the time step duration in days, and f is the flow budget, in m^3/day. The indices 48 and $95+1$ select day 365 and 730, respectively. The transient annual flow budget is given in Table 5.13. The calculation from equation 5.8 is verified by comparing the annual total pumped in Table 5.4 with the flow budget from the wells; this calculation is less than 1 m^3/day.

The model water budget results for the base conditions show that recharge from precipitation and irrigation dominates the input to the aquifer (roughly 68% of the total water

budget). Water from lakes and rivers accounts for approximately 11% of the inflow to the aquifer. Water input to storage is 21%. The change in storage (inflow minus outflow) is roughly zero, as would be expected for such a seasonal steady-state simulation. Losses of groundwater to lakes and rivers accounts for a much higher percentage than the inflow (76%), while wells extract only 3% of the annual water budget.

The water table is defined using the head value from the highest active cell in the 3D finite difference grid, and was determined using a Python script.[13] The water table for the base conditions is shown in Figure 5.13. This figure shows the expected range of the modelled water table. The seasonal variation in Figure 5.13c shows that most of the variation occurs within irrigation districts—other areas have limited seasonal variations.

5.3.6 Climate impacts

Future predicted impacts of climate change on groundwater conditions were simulated by modifying the seasonal steady-state model boundary conditions with different recharge (and stream) fluxes for the 2050s and 2080s. In future time periods, the most noticeable change in the water budget is the increased contribution of recharge to the annual water budget (Table 5.13). As discussed earlier, this increase is related primarily to increases to irrigation return flow, which, in turn, is influenced by the irrigation efficiency of each district. However, because the well pumping rates were not increased in the future, this water budget does not give an accurate picture of the aquifer water balance. The added amount of water for irrigation return flow under future climate conditions must come from either the rivers, lakes or the aquifer (pumping). Thus, there would logically be more water extracted from the pumping wells. In the water budget results presented above, this excess recharge water is diverted to the lakes and river.

[13] Located on the CD at `programs/gms_2dTo3D_highest_active.py`. This feature is also available in GMS 6.0 (called 3D → 2D Grid, using highest active cell), however it incorrectly performed this calculation using transient grids.

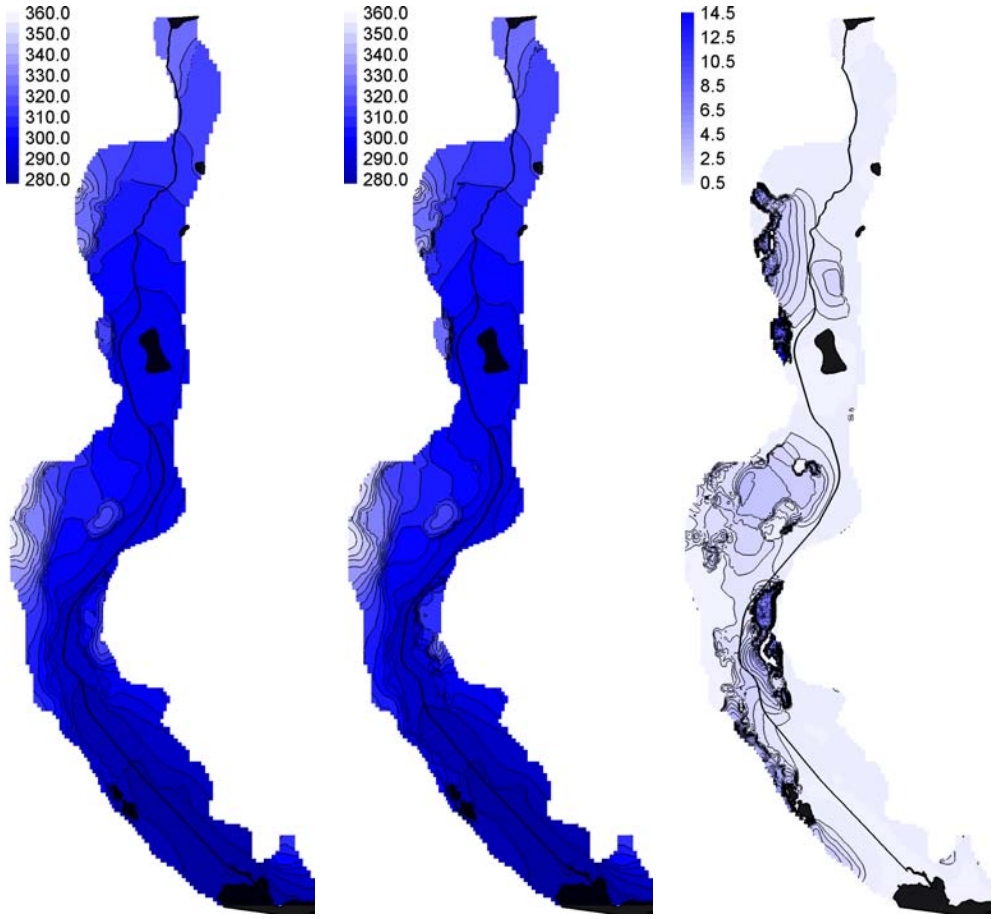

(a) Lowest levels; May 15 (day 135)

(b) Highest levels; October 29 (day 303)

(c) Difference between October and May levels

Figure 5.13 Water table for base conditions for base recharge conditions, all units are in metres. Black features on maps are Okanagan River and the Lakes.

Changes in groundwater levels, from base to future conditions, are shown in Figure 5.14, and summary statistics are given in Table 5.14. Increases in recharge and irrigation return flow will result in higher water tables with future climate conditions, particularly in the irrigation districts. It is clear that this influence is primarily from increases of irrigation return flow. Water level changes along river and general head boundaries in future time periods are minimal, as these boundaries were not adjusted for future conditions. Decreases in water level in Figure 5.14 are shown along the edges, and in

Table 5.14 Summary statistics for changes in water table in the second year of simulation for future conditions; note that there is a trend in the data, as the model would ideally require additional years to stabilize from the changed boundary conditions. All units are in metres.

Month	min	Q_1	median	mean	Q_3	max
Changes from base to 2050s						
Jan	−9.880	0.110	0.200	0.242	0.402	13.327
Feb	−8.079	0.109	0.186	0.240	0.374	13.286
Mar	−7.735	0.101	0.182	0.241	0.362	13.173
Apr	−7.018	0.089	0.173	0.233	0.359	12.936
May	−7.054	0.076	0.162	0.215	0.350	12.537
Jun	−7.996	0.079	0.180	0.220	0.358	12.154
Jul	−10.630	0.104	0.247	0.302	0.453	13.290
Aug	−14.642	0.128	0.309	0.414	0.596	15.343
Sep	−12.270	0.132	0.333	0.458	0.713	16.885
Oct	−13.123	0.126	0.315	0.419	0.625	16.771
Nov	−13.587	0.122	0.294	0.381	0.608	16.019
Dec	−12.135	0.123	0.274	0.354	0.573	14.886
Changes from base to 2080s						
Jan	−9.856	0.218	0.400	0.554	0.817	12.134
Feb	−8.835	0.226	0.390	0.555	0.787	12.213
Mar	−8.113	0.217	0.396	0.553	0.765	12.225
Apr	−7.456	0.197	0.391	0.533	0.759	12.145
May	−7.032	0.180	0.386	0.505	0.732	11.926
Jun	−7.707	0.201	0.443	0.549	0.801	11.827
Jul	−11.610	0.258	0.596	0.782	1.059	14.776
Aug	−12.178	0.300	0.708	0.974	1.385	14.076
Sep	−13.053	0.300	0.714	0.994	1.440	15.981
Oct	−12.676	0.273	0.644	0.873	1.294	16.407
Nov	−12.470	0.257	0.586	0.788	1.228	16.842
Dec	−10.577	0.262	0.561	0.745	1.158	16.761

other isolated regions within the modelling domain. These are possibly artifacts from the rewetting, as they are spatially isolated.

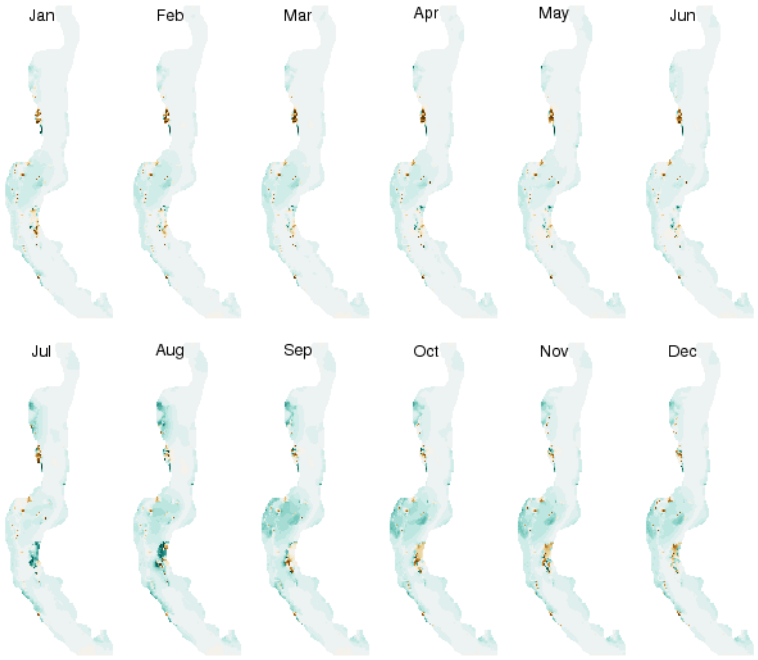

(a) Base to 2050s

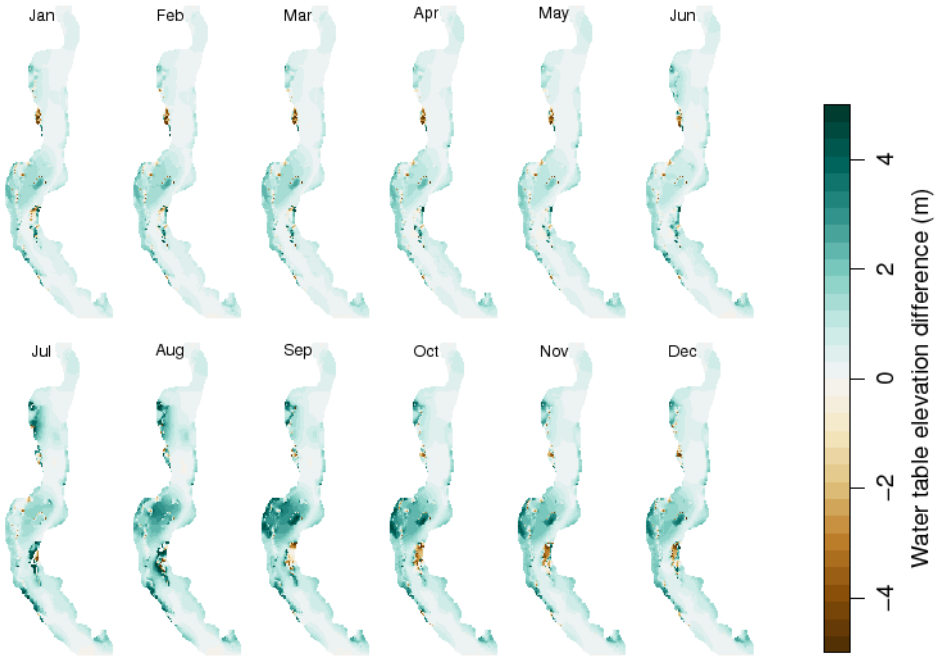

(b) Base to 2080s

Figure 5.14 Changes to groundwater levels in future simulations, relative to current or "base" conditions. These represent the differences in the water table for the second-year of transient simulations, where each month is represented by the last time step of each stress period. Described further in text; see summary statistics in Table 5.14.

5.4 Conclusions

Groundwater in the Oliver region is defined and maintained from the surface water bodies, Okanagan River and the bounding lakes in the valley. However, the largest contribution of groundwater to the aquifer system is from recharge and irrigation return flow. Most of the groundwater exits the aquifer system through Okanagan River. Groundwater extraction through wells along Okanagan River appear to have limited influences on the aquifer system, since pumping constitutes a small portion of the outflow from the aquifer flow budget.

Impacts of climate change using future-predicted recharge and stream boundary modifications, show that groundwater levels will increase. These increases, however, are mostly influenced by increasing irrigation application rates. As described in Chapter 4, these increases are highly coupled with the irrigation efficiency used in the districts.

Chapter 6

Well Capture Zone Analysis for Oliver, British Columbia

6.1 Introduction

A capture zone analysis was undertaken for the municipal groundwater wells in the Town of Oliver and the surrounding region. Capture zones completed from this study will be used for wellhead protection planning, as identified in the Concept Plan for Oliver.[1] These capture zones will offer an alternative to the calculated fixed radius (CFR) capture zones currently used in the land use allocation model (Foley et al., 2005).

A well capture zone is the spatial region surrounding a production water well, in which water will flow into the well within a period of time (Anderson and Woessner, 1992, Chapter 11). Essentially, the zone is based on a time of travel (TOT) calculation. There are a number of methods to determine TOT, including: (1) arbitrary or calculated fixed radius methods (US EPA, 1987); (2) analytical methods based on the parabolic shape of the capture zone when there is a measurable regional hydraulic gradient (e.g., Jacobson et al., 2002); and (3) numerical methods based on particle tracking simulations (e.g., Frind

[1] http://www.sgog.bc.ca/content.asp?contentID=156

et al., 2002). The most rigorous are the numerical methods, which rely on a calibrated groundwater flow model. In a numerical simulation, imaginary particles are released at the well screen, and tracked backwards within the model to determine their origin at specified times. The locus of the points of origin at any particular time defines the capture zone for that time. Typically, 1, 5 and 10-year captures zones are computed.

Defining the spatial extent of well capture zones can help land use management and land use planning in respect of designating land use activities within well capture zones that are effectively benign so as to avoid potential risks to the quality of groundwater produced from the well. For example, a land use decision may be explicitly based on trying to avoid placing a potentially high risk development, such as a gas station, within the capture zone of a well. For existing land use, the capture zones may aid in emergency response planning. For example, if a gasoline spill were to occur within the well capture zone area, the well could be shut down as an emergency response.

The spatial extent of a well capture zone is partially dependent on the heterogeneity of the hydraulic properties of the aquifer, which influence the groundwater flow directions. For example, gravel lenses can act as conduits where water can travel faster than in surrounding finer-grained materials, such as sand and silt. In contrast, clay plugs found in association with in-filled oxbow lakes in this study area may cause the flow to diverge towards nearby more permeable sediments. Consequently, zones with high conductivities are more susceptible to contamination since more water passes through these materials, and because transit times are faster. Thus, the spatial distribution of materials in the aquifer can lead to non-uniform capture zones that require a numerical model be constructed.

The most common method for model construction relies on defining layers, and assigning hydraulic properties to those layers as was done in the regional model discussed in the previous chapter. More sophisticated hydrostratigraphic models can effectively capture some spatial variability in the materials, such that lenses or changes in material type are incorporated into the different model layers (e.g., Abbotsford regional model

described by Scibek, 2005). This latter approach tends to capture some degree of heterogeneity at some spatial scale. In either case, the model and the computed capture zones are deterministic, which simply means that they are based on fixed model parameters defined for specific homogeneous or heterogeneous layers. When there is uncertainty in the distribution of materials, there is equal uncertainty in the computed capture zone. In this case, probabilistic capture zones are best computed.

In this particular study area, the upper aquifer consists dominantly of sand and gravel; however, other finer- and coarser-grained materials are also present. These materials represent glaciofluvial, alluvial and channel deposits. Silt and clay lenses are interpreted as in-filled oxbow lakes and over-bank deposits of the channel facies deposited by Okanagan River (see Figure 2.12, page 36). The variation and distribution of these materials contribute to the significant heterogeneity of the hydraulic conductivity in this aquifer. Furthermore, the materials in the upper aquifer are only known at sparse locations, from the borehole data, and not continuously throughout the aquifer. Thus, a geostatistical technique was used in this study to stochastically produce multiple realizations of continuous aquifer materials from statistical parameters derived from the existing borehole data. The multiple aquifer material realizations were then used to simulate groundwater flow, from which the probabilities of flow paths from each realization were analyzed to establish probabilistic capture zones around each well.

6.2 Groundwater model construction

A three-layer groundwater flow model was constructed in GMS 6.0 (Owen et al., 1996; EMRL, 2005). The upper two layers represent the upper aquifer, while the bottom layer represents the thick and regionally extensive silt and clay aquitard. Steady-state groundwater flow was simulated using MODFLOW 2000, Version 1.14.00 (Harbaugh et al., 2000). The heterogeneity of the aquifer materials in the upper two layers was stochastically generated using transition probabilities determined from the borehole data, using T-PROGS (Carle and Fogg, 1996, 1997; Carle, 1999), which is provided in GMS (Jones et al., 2005).

6.2.1 Transition probabilities and Markov chains

Transition probabilities are used in indicator geostatistics to quantify how one material change to another over spatial distances. These probabilities can be used with vertical (1-D) Markov chains, which are a stochastic process that is used to predict materials in 3-D. Both the transition probabilities and Markov chains are calibrated from classified soil materials in 438 boreholes (BC MoE, 2006) measured at 0.3 m vertical lag spacings to 10.8 m. The classifications were: (1) silt, (2) sand, (3) sand and gravel, and (4) gravel. Boulder deposits were classified as gravel, and clay deposits as silt. The decision to limit the number of classifications is based on a need to minimize the range of hydraulic conductivity values in the modelling domain.[2]

Vertical transition probabilities and fitted Markov chain model results are shown in Figure 6.1. The graphs are arranged in a matrix. Each graph shows the probability that material $\mathcal{R}$ will change to material $\mathcal{C}$ over different lag distances, where $\mathcal{R}$ is the material in the rows, and $\mathcal{C}$ is the material in the columns. A lag distance is simply a fixed spacing between two arbitrary points, at which the materials at each end are compared. The measured material proportions and fitted lens lengths are provided in Table 6.1, which have a best-fit with the observed transition probabilities. The fitted vertical embedded transition probabilities (e.g., Carle, 1999) are:

$$\mathbf{\Pi}_z = \begin{bmatrix} - & 0.35 & 0.40 & 0.25 \\ 0.20 & - & 0.60 & 0.20 \\ 0.25 & 0.55 & - & 0.20 \\ 0.20 & 0.50 & 0.30 & - \end{bmatrix} \quad \text{for silt, sand, sand \& gravel, and gravel}$$

In practice, horizontal Markov chains and transition probabilities are not determined, as the borehole data are too sparse along horizontal dimensions. Statistical parameters for the horizontal directions are thus assumed to be a scaled $\sim 10\times$ from the vertical (strike and dip values in Table 6.1), as it is expected the geological facies are more laterally

[2]MODFLOW models cannot converge if the range of hydraulic conductivity properties is too diverse; there are at least five or more orders of magnitude in K_s between clay and boulder deposits.

Table 6.1 Measured material proportions and fitted Markov chain models.

Material	Proportion	Lens length (m)	Lens ratios	
		Vertical (Z)	Strike (X)	Dip (Y)
Silt	0.0695	2.5	8.0	12.0
Sand	0.3017	6.0	10.0	10.0
Sand and gravel	0.3866	7.8	8.0	12.7
Gravel	0.2422	9.0	8.0	12.0
$\sum$	1.0			

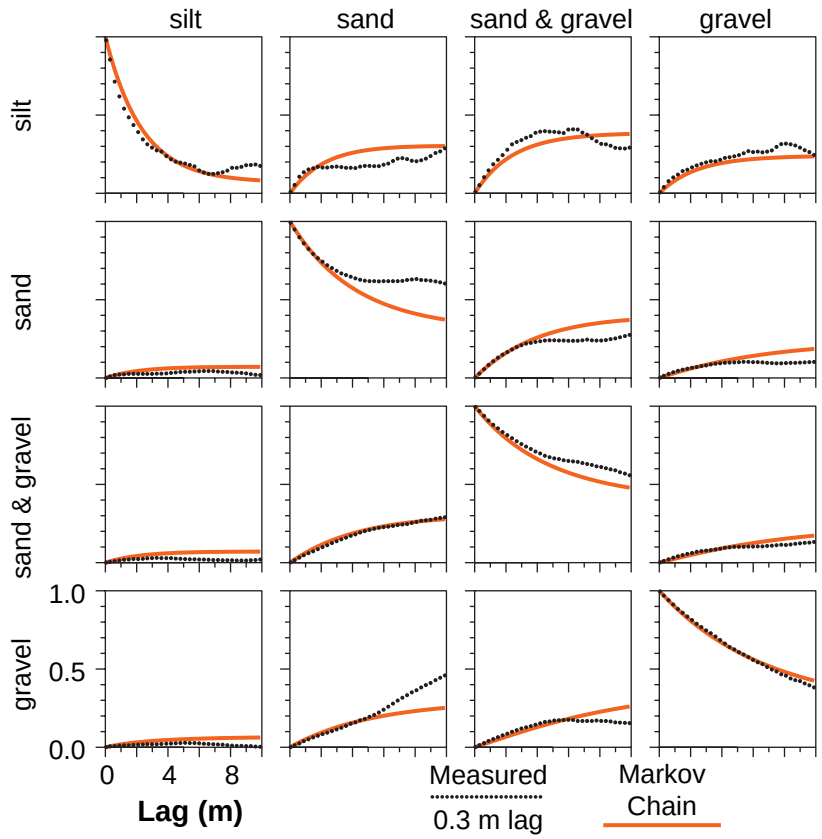

Figure 6.1 Vertical transition probabilities from the borehole data, and fitted transition probability models. To interpret this matrix of graphs: each graph shows the probability that material $\mathcal{R}$ will change to material $\mathcal{C}$ over different lag distances, where $\mathcal{R}$ is the material names in the rows, and $\mathcal{C}$ is the material names in the columns. A lag distance is simply a fixed spacing between two arbitrary points, at which the materials at each end are compared.

continuous in horizontal directions. The y-direction (north–south) lens ratios for silt and gravel are slightly larger than in the x-direction (east–west), since it is expected that these lenses are in the same general alignment with Okanagan River.

Thirty conditional simulations of aquifer materials were generated (see examples in Figure 6.2), through which groundwater flow was ultimately modelled. The conditional simulations were produced using TSIM, a subprogram of T-PROGS. The three-dimensional grids of aquifer material realizations are *conditional* in the sense that they honour both the transition probabilities and borehole data.

The default behaviour of TSIM is to create stochastic materials for the entire grid domain (all three layers), and materials cannot be modified within GMS. However, as it was desired to have the bottom layer of all aquifer realizations to be a silt and clay layer, the GMS file was modified using an external custom Python script.[3]

6.2.2 Grid design and material properties

The finite difference grid for the groundwater model (Figure 6.3a) has 313 rows, 119 columns (13 km by 4.1 km) and three layers. Horizontal grid spacing is 50 m and refines to 20 m near pumping wells. The upper two layers have equal thicknesses, which span through the upper aquifer. The top of the upper aquifer is defined from digital surface elevation data (Natural Resources Canada, 2005) to the silt top (see Figure 2.10, page 31). Layer 3 is represented by the thick silt, which extends down to the bedrock (see Figure 2.6, page 26).

The layer-property flow package (LPF) was used to represent the materials using convertible layer types. Vertical leakage correction was removed, and cell wetting parameters were disabled, as this allowed the model to converge. Material properties described in Table 6.2, were determined from bulk aquifer properties from aquifer tests (Section 5.2.2, page 106) and from published values for general material types (Domenico and Schwartz, 1998). Horizontal anisotropy for all materials is assumed to be homogeneous (1.0), despite

[3]Located on the CD at `/programs/tsimfix.py`

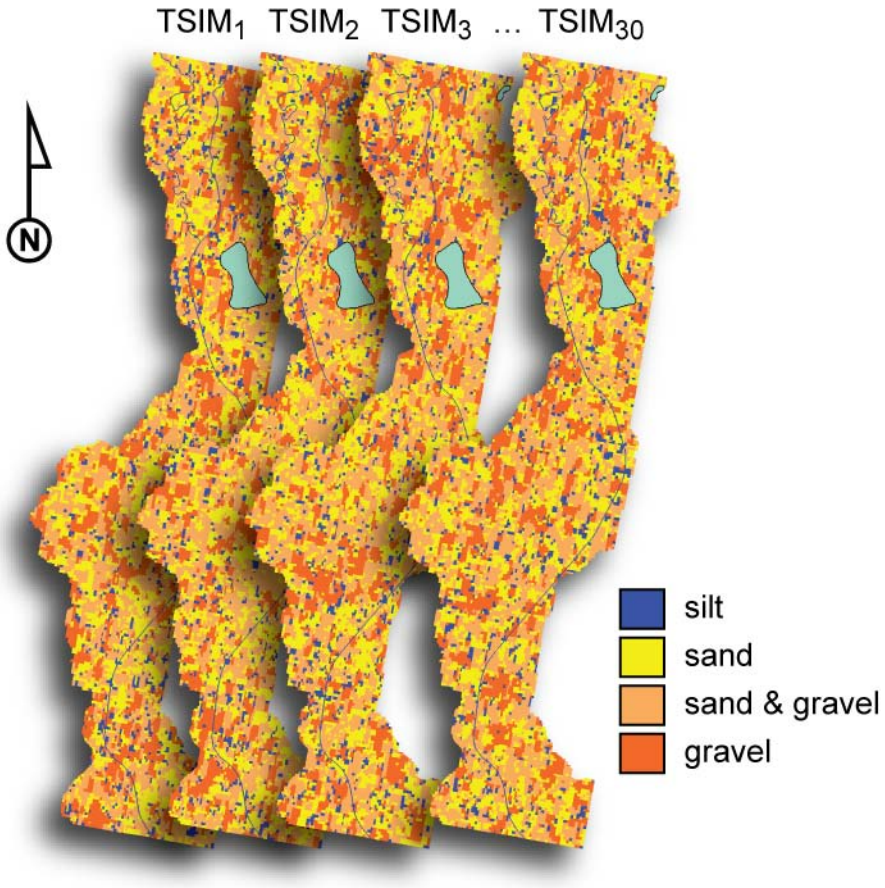

Figure 6.2 Realizations of aquifer materials from TSIM. These conditional simulations honour both transition probabilities and borehole data.

possible small-scale longitudinal imbrication of sedimentary materials along the length of Okanagan River. Vertical anisotropy for all materials was assumed to be 2.0, although other studies suggest that this values is an underestimate (e.g., Chen, 2000).

6.2.3 Boundary conditions

A recharge flux (RCH) was applied to the highest active cell (Figure 6.3b), and was obtained from the average annual recharge for current climate conditions with irrigation return flow, as described in Chapter 4. Influence of valley streams were not included to simplify the model. This omission is justified since most of the aquifer interactions with the pumping wells are nearby Okanagan River.

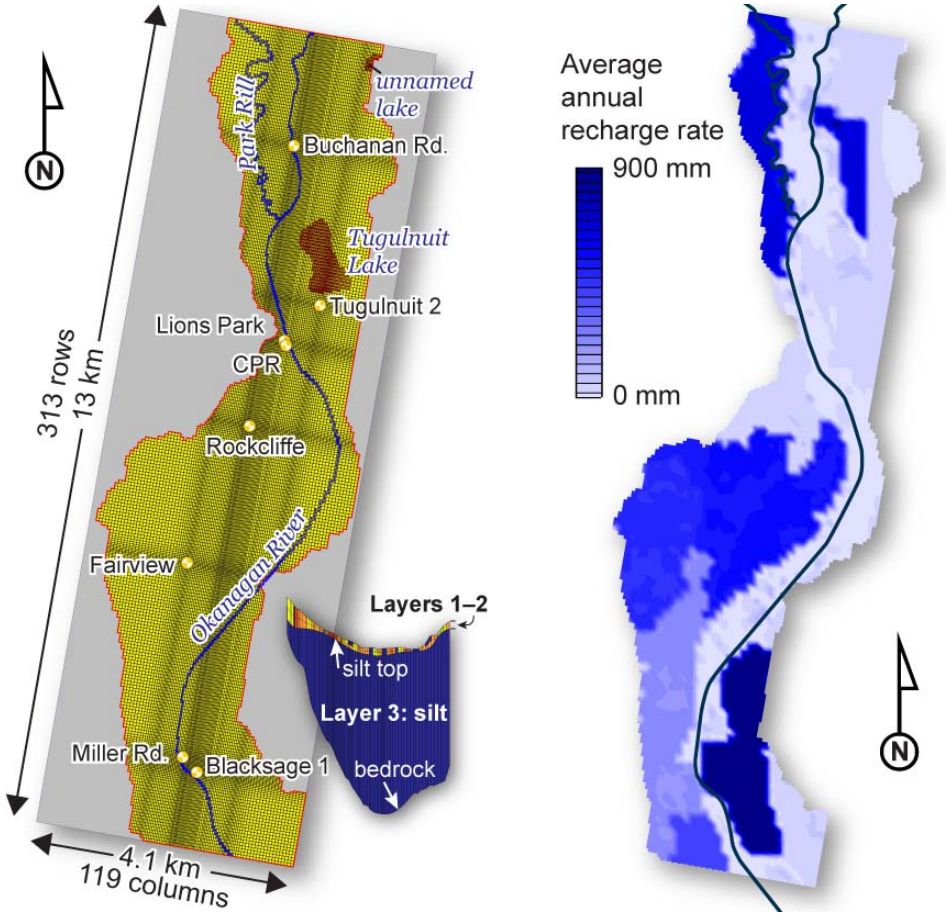

(a) Grid and boundary conditions **(b)** Annual recharge rate

Figure 6.3 Groundwater model boundary conditions.

Table 6.2 Hydrologic properties of materials used for capture zone analysis; horizontal hydraulic conductivity, K_h, and porosity, ϕ.

Material	K_h		ϕ
	(m/s)	(m/day)	
Silt	5.8×10^{-5}	5	0.2
Sand	5.8×10^{-4}	50	0.3
Sand and gravel	4.6×10^{-3}	400	0.3
Gravel	1.2×10^{-2}	1000	0.3

Table 6.3 Municipal production water wells used for the capture zone analysis, and their pumping rates.

Well name	WTN	Average pumping rate		Screen depth (m)	
		(USgpm)	(m^3/s)	from	to
Buchanan Rd.	21873	402	2.54×10^{-2}	17.4	22.1
Tugulnuit 2	83008	1200	7.57×10^{-2}	10.4	14.3
Lions Park	83010	1230	7.76×10^{-2}	18.3	23.2
CPR	83011	1000	6.31×10^{-2}	9.1	13.6
Rockcliffe	82376	1500	9.46×10^{-2}	15.0	24.4
Fairview	21867	425	2.68×10^{-2}	26.8	34.1
Miller Rd.	84724	1092	6.89×10^{-2}	14.8	18.0
Blacksage 1	49481	2000	1.26×10^{-1}	11.6	25.7

Okanagan River and Park Rill were simulated using the river package (RIV), while Tugulnuit Lake and a small unnamed lake were simulated using the general head boundary (GHB) (Figure 6.3a). The RIV and GHB boundary conditions were simulated in layer 1. River stage and bottom elevations of Okanagan River were defined from a detailed survey (Schubert, 1983). The river stage elevations for Park Rill were estimated from available digital elevation data, with a river depth estimate of 1 metre. Conductances were set to 400 $(m^2/day)/m$ and 20 $(m^2/day)/m^2$ for RIV and GHB, respectively, as these values are within the same order of magnitude of the aquifer materials (with correction for units) and allowed convergence of the model. A sensitivity analysis of river bed conductance parameters showed they have minimal influence on exchange of water through the RIV boundary condition.

Eight municipal production wells were simulated in layer 2 (and in layer 1, for some wells where the screen overlapped) using pumping rates from consulting reports and supplemented with well yield data from the WELLS database where needed (Table 6.3).

6.2.4 Simulation and probabilistic capture zones

The steady-state model was solved using the PGC2 solver, with both head change and residual volume criteria set to 0.01. Steady-state flow simulations were performed for

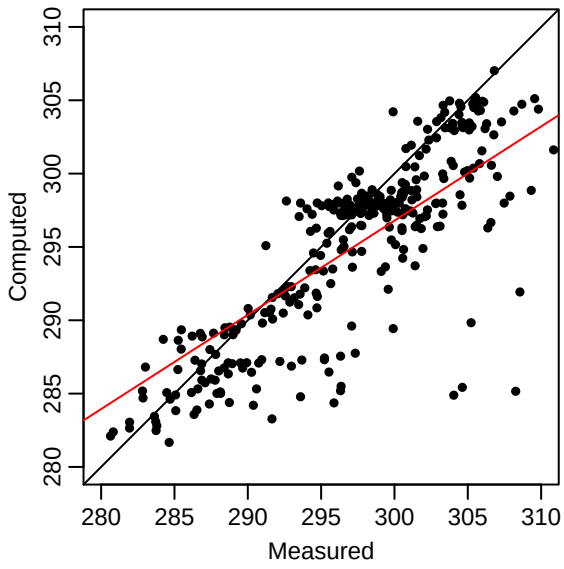

Figure 6.4 Observed vs. computed hydraulic heads (m), also showing 1:1 line and best-fit line with $R^2 = 0.57$; the normalized root mean squared error is 10.8%.

each aquifer material instance. Of the 30 groundwater simulations, four did not converge. River mass balances converge with minimal residual (sum of squared weighted residuals is 1.7×10^{-29}).

The model is reasonably calibrated with respect to observed water table points (Figure 6.4), with many observed points underestimated along the valley margins. The normalized root mean square error between observed and computed heads is 10.8%. The higher observed water table along the sides are difficult to simulate with this model, and would require: (1) additional boundary conditions (e.g., streams at valley sides) to raise their elevation; (2) higher recharge rates; or (3) lower hydraulic conductivities.

Probabilistic capture zones were determined in GMS using eight particles distributed within each cell, which were traced to each pumping well through MODPATH. Capture zones were determined for 60, 365 and 3650 days.

6.3 Results

Probabilistic capture zones for 60-days, 1-year and 10-years are shown in Figure 6.5. The contours that define the capture zones indicate the probability that water in the saturated

aquifer will reach the pumping well within the designated time. Time of travel above the water table (in the unsaturated zone) is not considered, although from recharge modelling this can range anywhere between a few weeks to a few months, depending on depth to water and hydraulic conductivities.

Details for each well are summarized as follows:

Buchanan Rd. (Figure 6.5a) this capture zone is influenced by nearby Okanagan River and by the higher water table to the east (influenced by the unnamed lake in this model). The forked geometry of the capture zone appears to be influenced by localized deposits of finer- and coarser-grained deposits, as found in the boreholes and simulated through T-PROGS.

Tugulnuit 2 (Figure 6.5b) this capture zone has overall lower probability values, as materials in this region of the upper aquifer are highly variable, resulting in a number of different material realizations from T-PROGS and dispersed flow path realizations. The 10-year capture zone is nearly identical to the 1-year capture zone.

Lions Park and CPR (Figures 6.5c and 6.5d) these capture zones are highly influenced by nearby Okanagan River, and also partially influenced by Lake Tugulnuit. The 10-year capture zones are elongated towards Lake Tugulnuit, which has a slightly higher hydraulic head than Okanagan River.

Rockcliffe (Figure 6.5e) this is the largest capture zone in the region, which is due in part to the high pumping rate and hydrostratigraphy. The geometry of this capture zone is mostly controlled by the silt top elevation, which appears to have a localized northward trench, interpreted to be a kettle hole that extends near Okanagan River. This well has the highest pumping rate of all wells and the surrounding aquifer has the highest measured transmissivity in the Oliver region. Boreholes 800 m northeast of this well (e.g., WTN 19573) indicate the presence of deeper coarse gravel and boulder deposits, which could be connected, to some degree, to Okanagan River.

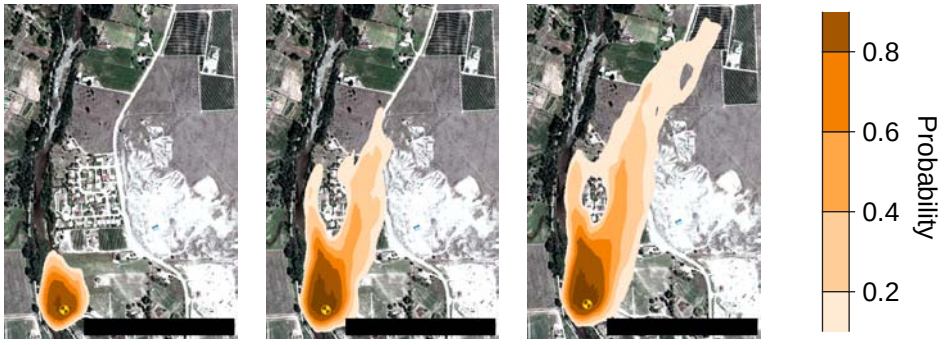

(a) Buchanan Rd.

(b) Tugulnuit 2

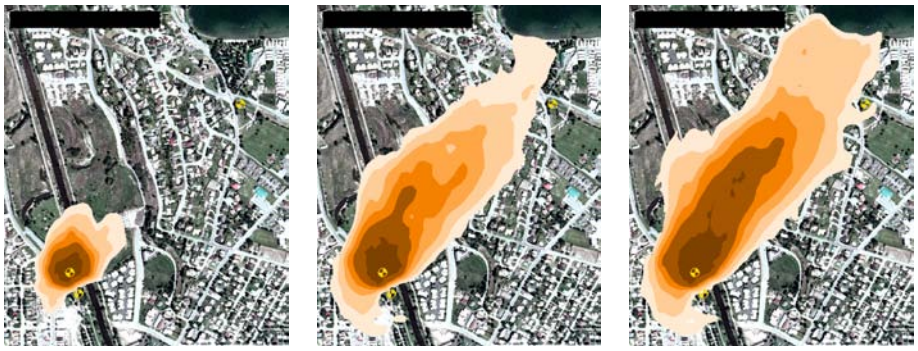

(c) Lions Park

(d) CPR

Figure 6.5 Probabilistic capture zones for each well, (left-to-right) for 60-days, 1-year and 10-years. Shaded contours indicate the probability that water in the aquifer will reach the pumping well within the simulation time. Scale bar width is 500 m.

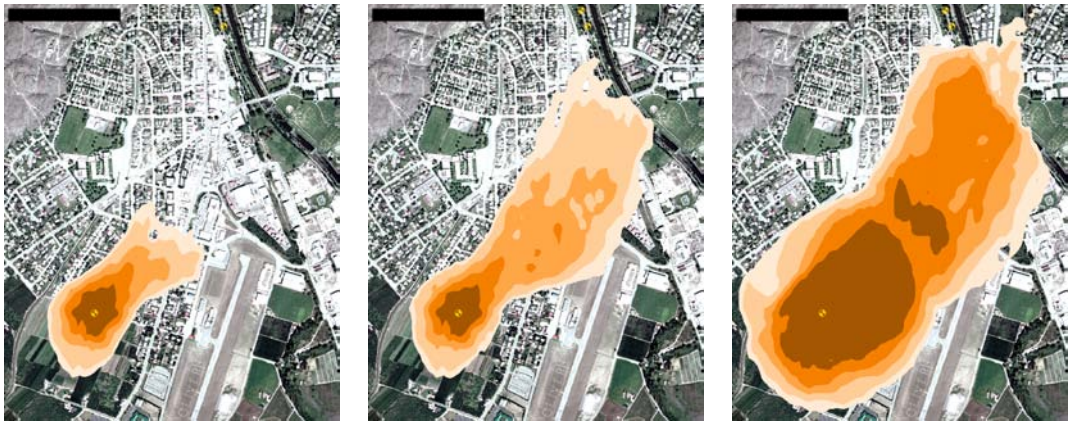

(e) Rockcliffe

(f) Fairview

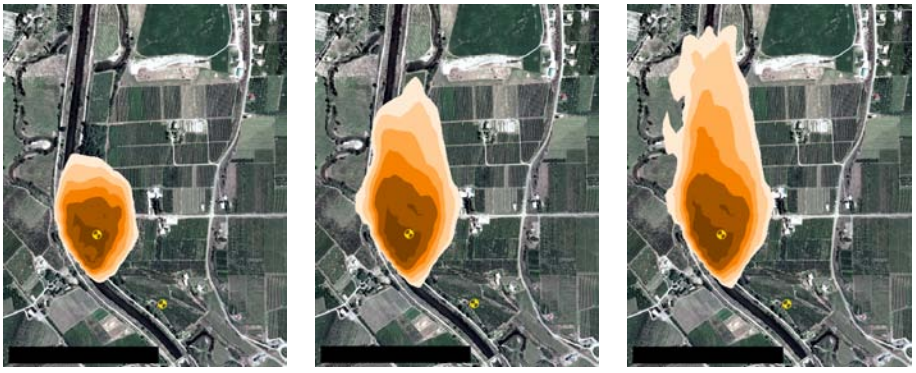

(g) Miller Rd.

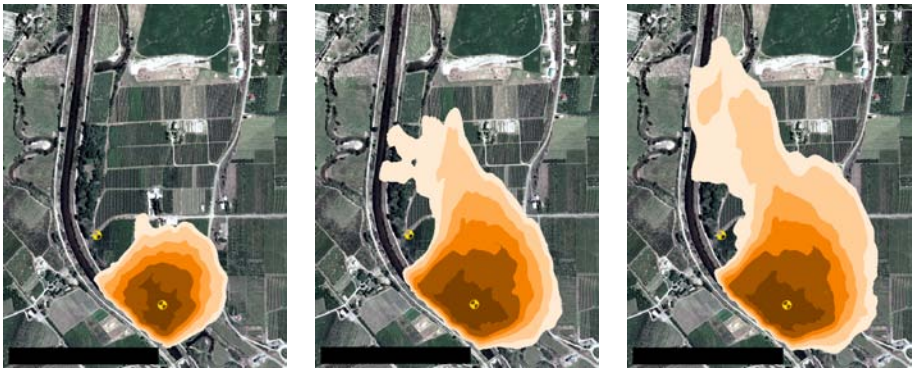

(h) Blacksage 1

Figure 6.5 . . . continued from previous page.

Fairview (Figure 6.5f) this well appears to obtain water through the underlying silt, thus having a capture zone with limited extent. The modeled capture zone is highly influenced by the silt top elevation, which is lower at this location. However, this well appears to also be in a region with boulder deposits, and may have a more complicated subsurface path that cannot be practically modeled without a more detailed survey.

Miller Rd. and Blacksage 1 (Figures 6.5g and 6.5h) these capture zones are highly influenced by nearby reaches of Okanagan River. The proximity of this boundary condition appears to constrain the capture zone, such that the differences between the 1 and 10-year capture zones are very minor.

6.4 Discussion

The capture zones determined in this study have a wide range of outcomes, which are influenced by unique hydrogeologic conditions surrounding each pumping well, such as the proximity to Okanagan River or Lake Tugulnuit, subsurface hydrogeology, or placement to other nearby wells. Circular capture zones, as determined using the CFR method by Foley et al. (2005), are comparable to several of the capture zones in this study. These similar capture zones include those around Fairview and Tugulnuit 2 pumping wells, and they also have similar dimensions to zones surrounding Blacksage 1 and Miller Rd. pumping wells. However, circular CFR capture zones are very different for the Rockcliffe, Lions Park and CPR pumping wells. These capture zones are elongated in the opposite direction to groundwater flow, with minimal capture zone exposure in the direction of groundwater flow.

The geometry and ranges of probability values in each capture zone are influenced by the heterogeneity of aquifer materials, as approximated from groundwater simulations through stochastic realizations of aquifer materials. Capture zones around Rockcliffe, and Tugulnuit wells are larger, and have less-defined probabilities overall due to the high variability of geologic materials found in the boreholes near these regions. In contrast, the

capture zone surrounding Buchanan Rd. is influenced by boreholes north of the pumping well with more continuous assemblages of materials.

Defining capture zones based on a probabilistic approach is particularly beneficial where there is a significant lateral groundwater flow, as this can have a large influence on the geometry of the zone. Also, probabilistic capture zones, by definition, convey more information on the spatial probabilities at which water will reach the well. These probabilities are influenced by the heterogeneity of the aquifer and surrounding boreholes. However, this method also requires a large number of boreholes, and the model can take considerable time to construct.

Chapter 7

Conclusions and Recommendations

7.1 Conclusions

The surficial geology of the Oliver region consists of fine-grained glaciolacustrine silt and clay, overlain by (1) alluvial sand and gravel near creeks, sometimes bound with clay; (2) isolated boulder deposits near the center of the valley; (3) glaciofluvial sand and gravel along the benches and above the flood plain; and (4) fluvial sand and gravels along Okanagan River, which are fluvially-reworked sediments from the region. With the exception of the glaciolacustrine sediments, all the materials have high hydraulic conductivities, generally over 50 m/day. Buried kettle holes identified in the subsurface may result in localized regions of thicker saturated deposits—and higher transmissivity and production rate potential from the unconsolidated aquifer adjacent to Okanagan River.

Daily precipitation time series were separated into regionally and locally derived sources using a simple cross-plot of values from two regions in Okanagan Valley. The local, regional and total precipitation components were independently simulated in the HELP hydrology model to evaluate the recharge response through multiple soil columns common to the region. These analyses show that recharge is influenced dominantly from

regional precipitation time series, whereas local precipitation has limited effect. The results of these tests suggest that recharge models are less influenced by summer precipitation, of which a large contribution is from locally-derived precipitation. The significance of the decreased sensitivity of recharge to summer precipitation is in the application of GCMs in recharge modelling. GCMs have coarse spatial resolution, and cannot realistically quantify mesoscale precipitation rates, which may result from localized and possibly high-intensity rainstorms. However, modeled recharge has very limited response from such precipitation.

Effects of climate change in the Oliver region may include: (1) increased temperatures, particularly through the summer months; (2) minor increase of precipitation in CCCma models and minor reduction with HadCM3; and (3) minor decreases of incoming solar radiation in CCCma models and minor increase with HadCM3. Impacts of these changes were investigated using a recharge model, which indicates increases of expected recharge with CGCM3.1, minor increases with CGCM1 and minor reductions of recharge with HadCM3. All models indicate an increased length of growing season, with increased potential evapotranspiration rates, which will result in significantly higher crop water demands. Irrigation return flow to the aquifer can range between 25% to 60%, which indicate that current irrigation practices are not optimized, as much of the water flows downward to groundwater rather than being utilized by the crops.

A regional transient groundwater model was constructed to simulate the flow of water. The MODFLOW model has river, general head (lakes) and recharge boundaries, which were created for present conditions, and for the 2050s and 2080s conditions, as predicted by CGCM3.1 A2. Results suggest that groundwater flow is impacted most significantly from irrigation return flow rates, which may result in the water table rising by 1–10 m in some heavily irrigated regions. Median water table changes from current to future conditions across the region are 17 cm and 35 cm for the 2050s and 2080s, respectively.

The water flow budget from the groundwater shows that the dominant source flowing into the groundwater is from recharge—much of which is irrigation return flow. Most of

the flow out of the groundwater system is to Okanagan River, and only a minor component of the outflow is from the simulated pumping wells.

Capture zones for municipal groundwater wells were determined using a local-scale groundwater model. These capture zones are similar to zones determined using the calculated fixed radius method. The capture zones determined using the numerical model are most effective where the groundwater flow rates are greatest, such as where there is a high hydraulic gradient and/or hydraulic conductivity.

7.2 Recommendations for research

There are several aspects of the analyses used in this study that could be improved. This analysis is very dependant on other model results, such as GCMs, or on codes that either simulate processes or analyze data. Other recharge simulation codes should be used to compare recharge results, since it has been shown through studies that compare recharge codes (e.g., Scanlon et al., 2002) that recharge can be significantly different depending on which code is used. Recharge simulations would only need to be performed on the primary soil types from the region, similar to Chapter 3. Irrigation use should ideally be coupled into a recharge code to apply recharge when soil moisture dropped below a threshold.

At the time of preparation, none of the available pedotransfer function programs (including ROSETTA) use coarse soil measurements as inputs to determine hydraulic properties. This limitation may underestimate K_s, and overestimate θ_{fc} and θ_{wp} for soils with a significant fraction of sediments $>$2 mm. These estimation errors may propagate to underestimate recharge, since coarser grained soils (e.g., gravel) drain water through the subsurface faster.

Constructing and calibrating a groundwater model for the Oliver region was challenging due to the highly variable elevation ranges, and the amount of unsaturated sediments

in the region. MODFLOW-2000 was used since it is a well established groundwater simulation code; however, it cannot simulate unsaturated groundwater flow, and the simulation is further complicated by cell re-wetting. Other groundwater codes that are capable of simulating variably saturated groundwater flow, such as HydroGeoSphere (Therrien et al., 2005) or FEFLOW (e.g., Diersch and Perrochet, 1999) may provide more realistic simulation capabilities for this region.

This study shows that present irrigation rates are too high, which may have several negative impacts, including: (1) inefficient use of fresh water resources, which may become less abundant in future times; (2) increased irrigation return flow, which may increase the accumulation of chemicals in the groundwater, including amounts of nitrates observed (T. Underwood, pers. comm. 2006); (3) possible buildup of salts in the topsoil from circulation and evaporation of groundwater (e.g., Prendergast et al., 2004). For these reasons, it is suggested that more field-based research be undertaken in the irrigated regions. This may include installing observation wells in the irrigated regions to monitor hydraulic head and groundwater chemistry.

Reference List

Allard, R., 2004. Well construction and capacity testing, new production well PW04-1 Oliver, British Columbia. Consulting report 04-1140-020, Golder Associates, Ltd., Kelowna, BC.

Allen, D. M., Mackie, D. C., Wei, M., 2004. Groundwater and climate change: a sensitivity analysis for the Grand Forks aquifer, southern British Columbia, Canada. Hydrogeology Journal 12, 270–290, doi:10.1007/s10040-003-0261-9.

Allen, R. G., Pereira, L. S., Raes, D., Smith, M., 1998. Crop evapotranspiration—guidelines for computing crop water requirements. FAO Irrigation and Drainage Paper 56, Food and Agriculture Organization of the United Nations, Rome, Italy, URL http://www.fao.org/docrep/X0490E/x0490e00.HTM.

Anderson, M. P., Woessner, W. W., 1992. Applied Groundwater Modeling: Simulation of Flow and Advective Transport. 2nd ed., Academic Press, San Diego, CA, USA, 381 pp.

Arengi, J. T., Badry, A., 1993. Performance and capacity evaluation of new community water well, Deer Park Mobile Home Park near Oliver, BC. Consulting report, Pacific Hydrology Consultants Ltd., Burnaby, BC.

Bauer, H. H., Vaccaro, J. J., 1987. Documentation of a deep percolation model for estimating ground-water recharge. Open-File Report 86-536, U.S. Geological Survey, Tacoma, WA, USA, URL http://pubs.er.usgs.gov/usgspubs/ofr/ofr86536.

BC MoE, 2006. WELLS: Water well database. Website, URL http://aardvark.gov.bc.ca/apps/wells/.

Bear, J., Cheng, A. H.-D., Sorek, S., Ouazar, D., Herra, I. (eds.), 1999. Seawater Intrusion in Coastal Aquifers: Concepts, Methods and Practices. Kluwer Academic Publisher, 625 pp.

Berardinucci, J., Ronneseth, K., 2002. Guide to using the BC aquifer classification maps for the protection and management of groundwater. BC Ministry of Water, Land and Air Protection, Victoria, BC, 54 pp., URL http://www.env.gov.bc.ca/wsd/plan_protect_sustain/groundwater/aquifers/.

Berger, K., 2004. The Hydrologic Evaluation of Landfill Performance (HELP) model: engineering documentation for HELP 3.80 D—enhancements compared to HELP 3.07. Tech. rep., Institute of Soil Science, University of Hamburg, URL http://www.geowiss.uni-hamburg.de/i-boden/suppengdochelp380d.pdf.

Brouyère, S., Carabin, G., Dassargues, A., 2004. Climate change impacts on groundwater resources: modelled deficits in a chalky aquifer, Geer Basin, Belgium. Hydrogeology Journal 12, 123–134, doi:10.1007/s10040-003-0293-1.

Callan, D. M., 1971. Groundwater development SOLID no. 3 system, Oliver, BC. File 0249723, Water Investigations Branch, BC Water Resources Service, Department of Lands, Forests, and Water Resources, Victoria, BC.

Canadian Institute for Climate Studies, 2005. Canadian climate impacts and scenarios. Website, URL http://www.cics.uvic.ca/scenarios/.

Cannon, A. J., Whitfield, P. H., 2002. Downscaling recent streamflow conditions in British Columbia, Canada using ensemble neural network models. Journal of Hydrology 259, 136–151, doi:10.1016/S0022-1694(01)00581-9.

Carle, S. F., 1999. T-PROGS: Transition probability geostatistical software, Version 2.1. University of California, Davis, CA, USA.

Carle, S. F., Fogg, G. E., 1996. Transition probability-based indicator geostatistics. Mathematical Geology 28 (4), 453–476, doi:10.1007/BF02083656.

Carle, S. F., Fogg, G. E., 1997. Modeling spatial variability with one and multidimensional continuous-lag Markov chains. Mathematical Geology 29 (7), 891–918, doi:10.1023/A:1022303706942.

Chen, X., 2000. Measurement of streambed hydraulic conductivity and its anisotropy. Environmental Geology 39 (12), 1317–1324, doi:10.1007/s002540000172.

Clague, J. J., 1991. Quaternary glaciation and sedimentation. In: Gabrielse, H., Yorath, C. J. (eds.), Geology of the Cordilleran Orogen in Canada, no. 4 in Geology of Canada, chap. 12, Geological Survey of Canada, pp. 419–434.

Cohen, S., Neilsen, D., Welbourn, R. (eds.), 2004. Expanding The Dialogue on Climate Change & Water Management in the Okanagan Basin, British Columbia. Environment Canada, Agriculture & AgriFood Canada and University of British Columbia, URL http://www.ires.ubc.ca/downloads/publications/layout_Okanagan_final.pdf, Final Report.

Collins, M., Tett, S. F. B., Cooper, C., 2001. The internal climate variability of HadCM3, a version of the Hadley Centre coupled model without flux adjustments. Climate Dynamics 17 (1), 61–81, doi:10.1007/s003820000094.

Croley, II, T. E., Luukkonen, C. L., 2003. Potential effects of climate change on ground water in Lansing, Michigan. Journal of the American Water Resources Association 39 (1), 149–163, doi:10.1111/j.1752-1688.2003.tb01568.x.

CSSC, 1978. The Canadian system of soil classification. Publication 1646, Canada Soil Survey Committee, Resource Branch, Canadian Department of Agriculture, Supply and Services Canada, Ottawa, ON.

Deutsch, C. V., Journel, A. G., 1997. GSLIB: Geostatistical Software Library and User's Guide. 2nd ed., Oxford University Press, New York, NY, USA, 380 pp.

Diersch, H.-J. G., Perrochet, P., 1999. On the primary variable switching technique for simulating unsaturated–saturated flows. Advances in Water Resources 23 (3), 271–301, doi:10.1016/S0309-1708(98)00057-8.

Dingman, S. L., 2002. Physical Hydrology. 2nd ed., Prentice-Hall, Upper Saddle River, NJ, USA, 646 pp.

Domenico, P. A., Schwartz, F. W., 1998. Physical and Chemical Hydrogeology. 2nd ed., John Wiley & Sons, Inc, New York, NY, USA, 506 pp.

EMRL, 2005. Groundwater Modeling System (GMS), Version 6.0. Environmental Modeling Research Laboratory, Brigham Young University, Provo, UT, USA.

Environment Canada, 2001. HYDAT CD-ROM user's manual. Water Survey of Canada, Downsview, ON, 2nd ed.

Environment Canada, 2002. Canadian Daily Climate Data on CD-ROM. Meteorological Service of Canada, Climate Products and Publications Division, Downsview, ON, URL http://www.climate.weatheroffice.ec.gc.ca/prods_servs/cdcd_iso_e.html, CDCD 2002—West.

Environment Canada, 2006. Canadian climate normals or averages 1971–2000. Website, URL http://climate.weatheroffice.ec.gc.ca/climate_normals/index_e.html.

ESRI, 1998. ESRI Shapefile technical description. White Paper, Environmental Systems Research Institute, Inc., Redlands, CA, USA, URL http://www.esri.com/library/whitepapers/pdfs/shapefile.pdf.

ESRI, 2005. ArcGIS 9.1 software and documentation. Environmental Systems Research Institute, Redlands, CA, USA.

Eyles, N., Mullins, H. T., 1991. The seismic stratigraphy of Okanagan Lake, British Columbia: a record of rapid deglaciation in a deep 'fiord-lake' basin. Sedimentary Geology 73, 13–41.

Eyles, N., Mullins, H. T., Hine, A. C., 1990. Thick and fast: Sedimentation in a Pleistocene fiord lake of British Columbia, Canada. Geology 18 (11), 1153–1157, doi:10.1130/0091-7613(1990)018<1153:TAFSIA>2.3.CO;2.

Fayer, M. J., 2000. UNSAT-H version 3.0: unsaturated soil water and heat flow model—theory, user manual, and examples. Tech. rep., Pacific Northwest National Laboratory.

Fernandes, R., 2003. Landsat-5 TM and Landsat-7 ETM+ based accuracy assessment of leaf area index products for Canada derived from SPOT-4 VEGETATION data. Canadian Journal of Remote Sensing 29 (2), 241–258.

Flato, G. M., Boer, G. J., Lee, W. G., McFarlane, N. A., Ramsden, D., Reader, M. C., Weaver, A. J., 2000. The Canadian Centre for Climate Modelling and Analysis global coupled model and its climate. Climate Dynamics 16, 451–467, doi:10.1007/s003820050339.

Fleming, S. W., Whitfield, P. H., Moore, R. D., Quilty, E. J., in press. Regime-dependent streamflow sensitivities to Pacific climate modes cross the Georgia–Puget transboundary ecoregion. Hydrological Processes doi:10.1002/hyp.6544.

Flerchinger, G. N., 2000. The Simultaneous Heat and Water (SHAW) model: technical documentation. Tech. rep., Northwest Watershed Research Center, USDA Agricultural Research Service, Boise, Idaho, URL ftp://ftp.nwrc.ars.usda.gov/download/shaw/ShawDocumentation.PDF.

Flint, R. F., 1935. "White-silt" deposits in the Okanagan Valley, British Columbia. Royal Society of Canada, Transactions 29, 107–114.

Foley, J., Allard, R., Sacre, J., 2005. Initial phases in the development of a groundwater protection plan—Town of Oliver. Consulting report 03-1440-057, Golder Associates, Ltd., Kelowna, BC.

Foweraker, J. C., 1969. Southern Okanagan Lands Irrigation District ARDA projects Nos. 10010 and 29041, construction and testing of domestic water supply test wells—Oliver area. Tech. rep., Groundwater Division, Water Investigations Branch, BC Ministry of Environment.

Frind, E. O., Muhammad, D. S., Molson, J. W., 2002. Delineation of three-dimensional well capture zones for complex multi-aquifer systems. Ground Water 40 (6), 586–598, doi:10.1111/j.1745-6584.2002.tb02545.x.

Fulton, R. J., 1965. Silt deposition in late-glacial lakes of southern British Columbia. American Journal of Science 263, 553–570.

Fulton, R. J., 1969. Glacial lake history, southern Interior Plateau, British Columbia. GSC Paper 69-37, Geological Survey of Canada.

Fulton, R. J., 1972. Stratigraphy of the unconsolidated fill and Quaternary development of north Okanagan Valley. GSC Paper 72-8, Part B, Geological Survey of Canada.

Fulton, R. J., 1991. A conceptual model for the growth and decay of the Cordilleran Ice Sheet. Géographie physique et Quaternaire 45 (3), 281–286.

Fulton, R. J., Smith, G. W., 1978. Late Pleistocene stratigraphy of south-central British Columbia. Canadian Journal of Earth Sciences 15, 971–980.

Gogolev, M. I., 2002. Assessing groundwater recharge with two unsaturated zone modeling technologies. Environmental Geology 42, 248–258, doi:10.1007/s00254-001-0494-7.

Gordon, C., Cooper, C., Senior, C. A., Banks, H., Gregory, J. M., Johns, T. C., Mitchell, J. F. B., Wood, R. A., 2000. The simulation of SST, sea ice extents and ocean heat transports in a version of the Hadley Centre coupled model without flux adjustments. Climate Dynamics 16 (2), 147–168, doi:10.1007/s003820050010.

Grasby, S. E., Hutcheon, I., 2001. Controls on the distribution of thermal springs in the southern Canadian Cordillera. Canadian Journal of Earth Sciences 38 (3), 427–440, doi:10.1139/cjes-38-3-427.

Green, T. R., Bates, B. C., Fleming, P. M., Charles, S. P., 1997. Simulated impacts of climate change on groundwater recharge in the subtropics of Queensland, Australia. In: Taniguchi, M. (ed.), Subsurface Hydrological Responses to Land Cover and Land Use Changes, Kluwer Academic, Boston, MA, USA, pp. 187–204.

Harbaugh, A. W., Banta, E. R., Hill, M. C., McDonald, M. G., 2000. MODFLOW-2000, the U.S. Geological Survey modular ground-water model—user guide to modularization concepts and the ground-water flow process. Open-File Report 00-92, U.S. Geological Survey, Reston, VA, USA, URL http://pubs.er.usgs.gov/usgspubs/ofr/ofr0092.

Hodge, W. S., 1978. A preliminary study on the possible effects of low river releases on groundwater levels—Okanagan River Valley. Tech. rep., Groundwater Section, Hydrology Division, BC Ministry of Environment.

Hodge, W. S., Lowen, D. A., 1980. Contract 71: Construction and testing of test production wells for the BC Fruit Grower's Association—Oliver, BC. Tech. rep., Groundwater Section, Water Management Branch, BC Ministry of Environment, EcoCat 6433.

Holman, I. P., 2006. Climate change impacts on groundwater recharge-uncertainty, shortcomings, and the way forward? Hydrogeology Journal 14 (5), 637–647, doi:10.1007/s10040-005-0467-0.

Houghton, J. T., Callander, B. A., Varney, S. K. (eds.), 1992. Climate Change 1992: The Supplementary Report to The IPCC Scientific Assessment. Cambridge University Press, Cambridge, UK.

Houghton, J. T., Ding, Y., Griggs, D. J., Noguer, M., van der Linden, P. J., Xiaosu, D. (eds.), 2001. Climate Change 2001: The Scientific Basis. Contribution of Working Group I to the Third Assessment Report of the Intergovernmental Panel on Climate Change, Cambridge University Press, Cambridge, UK, 944 pp., URL http://www.grida.no/climate/ipcc_tar/wg1/.

Jacobson, E., Andricevic, R., Morrice, J., 2002. Probabilistic capture zone delineation based on an analytic solution. Ground Water 40 (1), 85–95, doi:10.1111/j.1745-6584.2002.tb02494.x.

Jones, N. L., Walker, J. R., Carle, S. F., 2005. Hydrogeologic unit flow characterization using transition probability geostatistics. Ground Water 43 (2), 285–289, doi:10.1111/j.1745-6584.2005.0007.x.

Jyrkama, M. I., Sykes, J. F., 2005. Estimating groundwater recharge in response to potential future climate change: the importance of winter temperatures. In: American Geophysical Union, Fall Meeting 2005, vol. 86, San Francisco, CA, USA, pp. B1+, h52B-01.

Jyrkama, M. I., Sykes, J. F., 2007. The impact of climate change on spatially varying groundwater recharge in the Grand River watershed (Ontario). Journal of Hydrology 338, 237–250, doi:10.1016/j.jhydrol.2007.02.036.

Kalnay, E., Kanamitsu, M., Kistler, R., Collins, W., Deaven, D., Gandin, L., Iredell, M., Saha, S., White, G., Woollen, J., Zhu, Y., Leetmaa, A., Reynolds, B., Chelliah, M., Ebisuzaki, W.,

Higgins, W., Janowiak, J., Mo, K. C., Ropelewski, C., Wang, J., Jenne, R., Joseph, D., 1996. The NCEP/NCAR 40-year reanalysis project. Bulletin of the American Meteorological Society 77 (3), 437–471, doi:10.1175/1520-0477(1996)077<0437:TNYRP>2.0.CO;2.

Kalyn, D. J., 1983. Construction of observation well no. 282 Meyers Flat area. Contract 73, BC Ministry of Environment, Water Management Branch, Victoria, BC.

Kenk, E., Sondheim, M. W., 1987. CAPAMP: Data entry and validation procedures for soil, agriculture capability, surficial geology and the all purpose entity. MOEP Manual 10, Surveys & Resource Mapping Branch, BC Ministry of Environment and Parks, Victoria, BC.

Kennedy, E. J., 1984. Discharge ratings at gaging stations. Tech. rep., U.S. Geological Survey, Washington, DC, USA, URL `http://pubs.usgs.gov/twri/twri3-a10/`, Book 3, Chapter A10.

Kim, J.-W., Chang, J.-T., Baker, N. L., Wilks, D. S., Gates, W. L., 1984. The statistical problem of climate inversion: determination of the relationship between local and large-scale climate. Monthly Weather Review 112 (10), 2069–2077, doi:10.1175/1520-0493(1984)112<2069:TSPOCI>2.0.CO;2.

Leblanc, S. G., Chen, J. M., Fernandes, R., Deering, D. W., Conley, A., 2005. Methodology comparison for canopy structure parameters extraction from digital hemispherical photography in boreal forests. Agricultural and Forest Meteorology 129, 187–207, doi:10.1016/j.agrformet.2004.09.006.

Lesemann, J.-E., Brennand, T. A., 2007. Reconstructions of glacial lake paleohydrology in southern british columbia. In: GSA Abstracts with Programs, vol. 39 of Cordilleran section meeting, Bellingham, WA, USA, 4–6 May 2007.

Lesemann, J.-E., Brennand, T. A., Shaw, J., 2005. A revised conceptual model for growth and decay of the Cordilleran Ice Sheet in British Columbia, Canada, unpublished.

Liggett, J., Allen, D. M., Journeay, J. M., Denny, S., Talwar, S., Ivey, L., 2006. Intrinsic aquifer vulnerability maps in support of sustainable community planning, Okanagan Valley, BC. In: Sea to Sky Geotechnique 2006, Vancouver, BC, pp. 1329–1336.

Lutz, M., Ascher, D., 2004. Learning Python. 2nd ed., O'Reilly Media, Inc., Sebastopol, CA, USA, 591 pp.

MacAulay, H. A., Hobson, G. D., 1972. A seismic refraction survey of the north Okanagan and south Shuswap Valleys. GSC Paper 72-8, Part A, Geological Survey of Canada.

Mantua, N. J., Hare, S. R., 2002. The Pacific Decadal Oscillation. Journal of Oceanography 58, 35–44, doi:10.1023/A:1015820616384.

Massey, N. W. D., MacIntyre, D. G., Desjardins, P. J., Cooney, R. T., 2005. Digital geology map of British Columbia: whole province. Geofile 2005-1, Ministry of Energy and Mines.

McDonald, M. G., Harbaugh, A. W., Orr, B. R., Ackerman, D. J., 1991. A method of converting no-flow cells to variable-head cells for the U.S. Geological Survey modular finite-difference ground-water flow model. Open-File Report 91-536, U.S. Geological Survey, Reston, VA, USA, URL http://pubs.er.usgs.gov/usgspubs/ofr/ofr91536.

McFarlane, N. A., Boer, G. J., Blanchet, J.-P., Lazare, M., 1992. The Canadian Climate Centre second-generation general circulation model and its equilibrium climate. Journal of Climate 5, 1013–1044, doi:10.1175/1520-0442(1992)005<1013:TCCCSG>2.0.CO;2.

McGinley, J. A., Albers, S. C., Stamus, P. A., 1991. Validation of a composite convective index as defined by a real-time local analysis system. Weather and Forecasting 6 (3), 337–356, doi:10.1175/1520-0434(1991)006<0337:VOACCI>2.0.CO;2.

McNeely, R., Clague, J. J., 1996. Database of selected British Columbia radiocarbon dates. Open File 3259, Geological Survey of Canada.

Mearns, L. O., Hulme, M., Carter, T. R., Leemans, R., Lal, M., Whetton, P., 2001. Climate scenario development. In: Houghton, J. T., Ding, Y., Griggs, D. J., Nogeur, M., van der Linden, P. J., Dai, X., Maskell, K., Johnson, C. A. (eds.), Climate Change 2001: The Scientific Basis, vol. Contribution of Working Group I of IPCC Third Assessment Report, chap. 13, Cambridge University Press, pp. 739–768.

Meidinger, D., Pojar, J. (eds.), 1991. Ecosystems of British Columbia. No. 6 in Special Report Series, B.C. Ministry of Forests, Victoria, BC, 330 pp., URL http://www.for.gov.bc.ca/hfd/pubs/Docs/Srs/Srs06.htm.

Merritt, W. S., Alila, Y., Barton, M., Taylor, B., Cohen, S., Neilsen, D., 2006. Hydrologic response to scenarios of climate change in sub watersheds of the Okanagan basin, British Columbia. Journal of Hydrology 326, 79–108, doi:10.1016/j.jhydrol.2005.10.025.

Mullins, H. T., Eyles, N., Hinchey, E. J., 1990. Seismic reflection investigation of Kalamalka Lake: a "fiord lake" on the Interior Plateau of southern British Columbia. Canadian Journal of Earth Sciences 27, 1225–1235.

Nakicenovic, N., Swart, R. (eds.), 2000. Special Report on Emissions Scenarios. Special Report of the Intergovernmental Panel on Climate Change, Cambridge University Press, Cambridge, UK, 570 pp., URL http://www.grida.no/climate/ipcc/emission/.

Nasmith, H., 1962. Late glacial history and surficial deposits of the Okanagan Valley, British Columbia. Bulletin 46, BC Ministry of Energy, Mines and Petroleum Resources.

Natural Resources Canada, 2005. Canadian digital elevation data, Level 1, product specifications. Edition 2.1, Natural Resources Canada, Centre for Topographic Information, Sherbrooke, QC, URL http://www.geobase.ca.

NCAR, 2006. NCAR Command Language (NCL). Computational & Information Systems Laboratory at the National Center for Atmospheric Research, Boulder, CO, USA, URL http://www.ncl.ucar.edu/, Version 4.2.0.a034.

Neilsen, D., Koch, W., Smith, S., G., F., 2004. Crop water demand scenarios for the Okanagan Basin. In: Cohen, S., Neilsen, D., Welbourn, R. (eds.), Expanding the Dialogue on Climate Change & Water Management in the Okanagan Basin, British Columbia, chap. 8, Environment Canada, Agriculture & AgriFood Canada and University of British Columbia, pp. 89–119, Final Report.

Neilsen, D., Smith, C. A. S., Frank, G., Koch, W., Alila, Y., Merritt, W. S., Taylor, W. G., Barton, M., Hall, J. W., Cohen, S. J., 2006. Potential impacts of climate change on water availability for crops in the Okanagan Basin, British Columbia. Canadian Journal of Soil Science 86 (5), 921–935.

Nichols, R. W., 1993. A design brief on the floodplain mapping study, Okanagan River. File 35100-30/310-0000, Flood Hazard Identification Section, Lands and Parks Water Management Division; BC Ministry of Environment, Victoria, BC.

Niswonger, R. G., Prudic, D. E., 2005. Documentation of the Streamflow-Routing (SFR2) Package to include unsaturated flow beneath streams—a modification to SFR1 techniques. Techniques and Methods 6-A13, U.S. Geological Survey, Denver, CO, USA, URL http://pubs.usgs.gov/tm/2006/tm6A13/.

Owen, S. J., Jones, N. L., Holland, J. P., 1996. A comprehensive modeling environment for the simulation of groundwater flow and transport. Engineering with Computers 12, 235–242, doi:10.1007/BF01198737.

Päivänen, J., 1973. Hydraulic conductivity and water retention in peat soils. Acta Forestalia Fennica 129, 1–70.

Pojar, J., Klimka, K., Meidinger, D. V., 1987. Biogeoclimatic ecosystem classification in British Columbia. Forest Ecology and Management 22, 119–154.

Prendergast, J. B., Rose, C. W., Hogarth, W. L., 2004. A model for conjunctive use of groundwater and surface waters for control of irrigation salinity. Irrigation Science 14 (4), 167–175, doi:10.1007/BF00190188.

Prudic, D. E., 1989. Documentation of a computer program to simulate stream–aquifer relations using a modular, finite-difference, ground-water flow model. Open-File Report 88-729, U.S. Geological Survey, Carson City, NV, USA, URL http://pubs.er.usgs.gov/usgspubs/ofr/ofr88729.

Quick, M. C., 1995. The UBC watershed model. In: Singh, V. P. (ed.), Computer Models of Watershed Hydrology, chap. 8, Water Resources Publications, Highlands Ranch, CO, USA, pp. 233–280.

R Development Core Team, 2007. R: A language and environment for statistical computing. R Foundation for Statistical Computing, Vienna, Austria, URL http://www.R-project.org, ISBN 3-900051-07-0.

Rawls, W. J., Ahuja, L. R., Brakensiek, D. L., Shirmohammadi, A., 1993. Infiltration and soil water movement. In: Maidment, D. R. (ed.), Handbook of Hydrology, McGraw-Hill, pp. 5.1–5.51.

Richardson, C. W., Wright, D. A., 1984. WGEN: A model for generating daily weather variables. Ars-8, U.S. Department of Agriculture, Agricultural Research Service, Springfield, VA, USA.

Rück, A., Walker, I. R., Hebda, R., 1998. A palaeolimnological study of Tugulnuit Lake, British Columbia, Canada, with special emphasis on river influence as recorded by chironomids in the lake's sediment. Journal of Paleolimnology 19, 63–75, doi:10.1023/A:1007956901689.

Salathé, Jr., E. P., 2003. Comparison of various precipitation downscaling methods for the simulation of streamflow in a rainshadow river basin. International Journal of Climatology 23 (8), 887–901, doi:10.1002/joc.922.

Sampaio, Jr., J. H. B., 2006. An iterative procedure for perpendicular offsets linear least squares fitting with extension to multiple linear regression. Applied Mathematics and Computation 176 (1), 91–98, doi:10.1016/j.amc.2005.09.054.

Scanlon, B. R., Christman, M., Reedy, R. C., Porro, I., Simunek, J., Flerchinger, G. N., 2002. Intercode comparisons for simulating water balance of surficial sediments in semiarid regions. Water Resources Research 38, 1323–1339, doi:10.1029/2001WR001233.

Schaap, M. G., Leij, F. J., van Genuchten, M. T., 2001. ROSETTA: a computer program for estimating soil hydraulic parameters with hierarchical pedotransfer functions. Journal of Hydrology 251, 163–176, doi:10.1016/S0022-1694(01)00466-8.

Schroeder, P. R., Dozier, T. S., Zappi, P. A., McEnroe, B. M., Sjostrom, J. W., Peyton, R. L., 1994. The Hydrologic Evaluation of Landfill Performance (HELP) model: Engineering documentation for version 3. EPA/600/R-94/168b, United States Environmental Protection Agency, Office of Research and Development, Washington, DC, USA.

Schubert, B., 1983. Okanagan Flood Control System: plan, profile and cross-sections of Okanagan River 1980 survey. Survey Project No. 79-OBIP-2 (80), BC Ministry of Environment, Water Management Branch, Victoria, BC, Drawings A5221-1 to A5221-13.

Scibek, J., 2005. Modelling the impacts of climate change on groundwater: A comparative study of two unconfined aquifers in southern British Columbia and northern Washington state. Master's thesis, Simon Fraser University, 8888 University Drive, Burnaby, BC.

Scibek, J., Allen, D. M., 2004. Groundwater sensitivity to climate change (part III): Climate change modelling for the Grand Forks aquifer, southern British Columbia. Report, Department of Earth Sciences, Simon Fraser University, Burnaby, BC.

Scibek, J., Allen, D. M., 2006a. Comparing modelled responses of two high-permeability, unconfined aquifers to predicted climate change. Global and Planetary Change 50, 50–62, doi:10.1016/j.gloplacha.2005.10.002.

Scibek, J., Allen, D. M., 2006b. Modeled impacts of predicted climate change on recharge and groundwater levels. Water Resources Research 42 (11), W11405, doi:10.1029/2005WR004742.

Scibek, J., Allen, D. M., Cannon, A. J., Whitfield, P., 2006. Groundwater–surface water interaction under scenarios of climate change using a high-resolution transient groundwater model. Journal of Hydrology doi:10.1016/j.jhydrol.2006.08.005.

Semenov, M. A., Barrow, E. M., 1997. Use of a stochastic weather generator in the development of climate change scenarios. Climate Change 35, 397–414, doi:10.1023/A:1005342632279.

Shabbar, A., Bonsal, B., Khandekar, M., 1997. Canadian precipitation patterns associated with the Southern Oscillation. Journal of Climate 10 (12), 3016–3027, doi:10.1175/1520-0442(1997)010<3016:CPPAWT>2.0.CO;2.

Shaw, J., 1977. Sedimentation in an alpine lake during deglaciation, Okanagan Valley, British Columbia, Canada. Geografiska Annaler 59A (3-4), 221–240.

Shaw, J., Muro-Stasiuk, M., Sawyer, B., Beaney, C., Lesemann, J.-E., Musacchio, A., Rains, B., Young, R. R., 1999. The Channeled Scabland: back to Bretz? Geology 27 (7), 605–608, doi:10.1130/0091-7613(1999)027<0605:TCSBTB>2.3.CO;2.

Sibson, R., 1981. A brief description of natural neighbor interpolation. In: Barnett, V. (ed.), Interpreting Multivariate Data, chap. 2, John Wiley & Sons, New York, NY, USA, pp. 21–36.

Silins, U., Rothwell, R. L., 1998. Forest peatland drainage and subsidence affect soil water retention and transport properties in an Alberta peatland. Soil Science Society of America Journal 62 (4), 1048–1056.

Soffer, R. J., Fernandes, R. A., Beal, D., Khurshid, K. S., 2007. Leaf area index map of Okanagan Valley (BC), Canada 2006 at 30 m resolution. TIFF raster dataset.

Solomon, S., Qin, D., Manning, M., Chen, Z., Marquis, M., Averyt, K. B., Tignor, M., Miller, H. L. (eds.), 2007. Climate Change 2007: The Physical Science Basis. Contribution of Working Group I to the Fourth Assessment Report of the Intergovernmental Panel on Climate Change, Cambridge University Press, Cambridge, UK and New York, NY, USA, 966 pp.

Tempelman-Kluit, D., Parkinson, D., 1986. Extension across the Eocene Okanagan crustal shear in southern British Columbia. Geology 14 (4), 318–321, doi:10.1130/0091-7613(1986)14<318:EATEOC>2.0.CO;2.

Therrien, R., McLaren, R. G., Sudicky, E. A., Panday, S. M., 2005. HydroGeoSphere: a three-dimensional numerical model describing fully-integrated subsurface and surface flow and solute transport. Groundwater Simulations Group, Waterloo, ON.

Toews, M. W., Allen, D. M., 2006. Stochastic simulation of a sand-gravel aquifer to determine well capture zones. In: Connecting Water Resources 2006 Poster Abstracts, Canadian Water Network, Montreal, QC, p. 19, 20–23 November, 2006.

Toews, M. W., Allen, D. M., submitted. Aquifer characterization and numerical groundwater flow modeling in the Oliver area of the southern Okanagan, BC. Tech. rep., Simon Fraser University, Burnaby, BC, Report to the BC Ministry of Environment.

Toews, M. W., Whitfield, P. H., Allen, D. M., 2005. Modeling the effect of regional and local precipitation events on groundwater recharge. In: Abstracts with Programs, vol. 37, Annual Meeting and Exposition of the Geological Society of America, Salt Lake City, UT, USA, p. 359, 16–19 October 2005.

Toews, M. W., Whitfield, P. H., Allen, D. M., 2006. Sensitivity of spatially modelled recharge to climate change in the Okanagan Valley, British Columbia. In: Sea to Sky Geotechnique 2006 Conference Proceedings, T6-A Groundwater Protection and Sustainability III, International Association of Hydrogeologists, Vancouver, BC, pp. 1388–1394, 1–4 October 2006.

Toews, M. W., Whitfield, P. H., Allen, D. M., 2007. Seasonal statistics: the 'seas' package for R. Computers & Geosciences 33 (7), 944–951, doi:10.1016/j.cageo.2006.11.011.

Trenberth, K. E., 1997. The definition of El Niño. Bulletin of the American Meteorological Society 78 (12), 2771–2777, doi:10.1175/1520-0477(1997)078<2771:TDOENO>2.0.CO;2.

Tribe, S., 2005. Eocene paleo-physiography and drainage directions, southern Interior Plateau, British Columbia. Canadian Journal of Earth Sciences 42, 215–230, doi:10.1139/E04-062.

US EPA, 1987. Guidelines for delineation of wellhead protection areas. EPA 440/6-87-010, United States Environmental Protection Agency, Office of Ground-Water Protection, Washington, DC, USA.

USDA, 1986. Urban Hydrology for Small Watersheds. Technical Release 55, 2nd ed., United States Department of Agriculture, Natural Resources Conservation Service, Conservation Engineering Division.

USDA, 2007. National soil survey handbook. title 430-VI, U.S. Department of Agriculture, Natural Resources Conservation Service, URL `http://soils.usda.gov/technical/handbook/`.

USGS, 1997. Standards for digital elevation models. Part 1 (General), U.S. Geological Survey, National Mapping Division, URL `http://rockyweb.cr.usgs.gov/nmpstds/acrodocs/dem/1DEM0897.PDF`.

Vaccaro, J. J., 1992. Sensitivity of groundwater recharge estimates to climate variability and change, Columbia Plateau, Washington. Journal of Geophysical Research 97 (D3), 2821–2833.

van Genuchten, M. T., 1980. A closed-form equation for predicting the hydraulic conductivity of unsaturated soils. Soil Science Society of America Journal 44 (5), 892–898.

Vanderburgh, S., 1993. Basin architecture of the north Okanagan Valley fill, British Columbia. Ph.D. thesis, Simon Fraser University, 8888 University Drive, Burnaby, BC.

Vanderburgh, S., Roberts, M. C., 1996. Depositional systems and seismic stratigraphy of a Quaternary basin: north Okanagan Valley, British Columbia. Canadian Journal of Earth Sciences 33, 917–927.

Verseghy, D. L., McFarlane, N. A., Lazare, M., 1993. A Canadian Land Surface Scheme for GCMs: II, vegetation model and coupled runs. International Journal of Climatology 13, 347–370, doi:10.1002/joc.3370130402.

von Storch, H., Zwiers, F. W., 1999. Statistical Analysis in Climate Research. Cambridge University Press, 494 pp.

Wang, X., Jin, F. F., Wang, Y., 2003. A tropical ocean recharge mechanism for climate variability. Part II: a unified theory for decadal and ENSO modes. Journal of Climate 16 (22), 3599–3616, doi:10.1175/1520-0442(2003)016<3599:ATORMF>2.0.CO;2.

Washington, W. M., Parkinson, C. L., 2005. An Introduction to Three-Dimensional Climate Modeling. 2nd ed., University Science Books, Sausalito, CA, USA, 353 pp.

Wei, M., 1985. SOLID system study. Tech. rep., Groundwater Section, Water Management Branch, BC Ministry of Environment.

WHI, 2004. WHI UnSat Suite Plus. Waterloo Hydrogeologic Inc., Waterloo, ON, Version 2.2.0.3.

Whitfield, P. H., Cannon, A. J., 2000. Recent variations in climate and hydrology of Canada. Canadian Water Resources Journal 25 (1), 19–65.

Wilby, R. L., Dawson, C. W., 2004. Using SDSM Version 3.1—a decision support tool for the assessment of regional climate change impacts. Nottingham, UK.

Wilby, R. L., Dawson, C. W., Barrow, E. M., 2002. SDSM—a decision support tool for the assessment of regional climate change impacts. Environmental Modelling & Software 17 (2), 147–159, doi:10.1016/S1364-8152(01)00060-3.

Wilby, R. L., Wigley, T. M. L., 1997. Downscaling general circulation model output: a review of methods and limitations. Progress in Physical Geography 21 (4), 530–548, doi:10.1177/030913339702100403.

Wilby, R. L., Wigley, T. M. L., 2000. Precipitation predictors for downscaling: observed and general circulation model relationships. International Journal of Climatology 20 (6), 641–661, doi:10.1002/(SICI)1097-0088(200005)20:6<641::AID-JOC501>3.0.CO;2-1.

Wilson, J. D., Naff, R. L., 2004. MODFLOW-2000, The U.S. Geological Survey modular ground-water model—GMG linear equation solver package documentation. Open-File Report 2004-1261, U.S. Geological Survey, Denver, CO, USA, URL `http://pubs.usgs.gov/of/2004/1261/`.

Winter, T. C., 1983. The interaction of lakes with variably saturated porous media. Water Resources Research 19 (5), 1203–1218.

Winter, T. C., 2000. The vulnerability of wetlands to climate change: a hydrologic landscape perspective. Journal of the American Water Resources Association 36 (2), 305–311, doi:10.1111/j.1752-1688.2000.tb04269.x.

Wittneben, U., 1986. Soils of the Okanagan and Similkameen valleys. Report 52, British Columbia Soil Survey, BC Ministry of Environment, Victoria, BC.

Wolock, D. M., McCabe, G. J., Tasker, G. D., Moss, M. E., 1993. Effects of climate change on water resources in the Delaware River basin. Water Resources Bulletin 29 (3), 475–486, doi:10.1111/j.1752-1688.1993.tb03225.x.

Yazdani, R., Gray, M., Minty, D., 1992. Baseline thematic mapping present land use mapping at 1:250000. Shapefile dataset, URL http://aardvark.gov.bc.ca/apps/dwds/, version 1.

York, J. P., Person, M., Gutowski, W. J., Winter, T. C., 2002. Putting aquifers into atmospheric simulation models: an example from the Mill Creek Watershed, northeastern Kansas. Advances in Water Resources 25 (2), 221–238, doi:10.1016/S0309-1708(01)00021-5.

Zender, C. S., 2007. NCO user's guide. Department of Earth System Science, University of California, Irvine, CA, USA, URL http://nco.sourceforge.net/, NCO Version 3.1.8.

Appendices

Appendix A

Climate Data and Methods

A.1 Data sources for station data

All climate data were obtained from the Meteorological Service of Canada, and stations used are listed in Table A.1. Daily precipitation and temperature data were obtained from the 2002 Canadian Daily Climate Data CD-ROM (Environment Canada, 2002). A secondary station at both Oliver and Summerland was required to fill-in any missing data. RF1 global solar radiation data were available from Summerland CDA and Mt. Kobau Observatory stations only. Hourly relative humidity and wind velocity data were available from Osoyoos CS.

A.2 Differences in climatology between Summerland and Oliver

Climate data at Oliver were stochastically generated at Oliver using data from Summerland. This was primarily done since LARS-WG, the stochastic weather generator, could only be calibrated using the long record of valley bottom climate data, which includes RF1 global solar radiation. The climatology for Oliver is shown in Figure 4.2 and similar normals for Summerland are shown in Figure 3.2, which includes solar radiation.

Table A.1 Weather stations in Okanagan basin with available climate data.

Station name	ID	Location	Elev. (m)	Years
Oliver	1125760	49°10′ N, 119°34′ W	315	1938–*present*
Oliver 3	1125779	49°11′ N, 119°33′ W	280	1991–1995
Oliver East	1125765	49°11′ N, 119°32′ W	335	1962–1967
Oliver Monashee Vin.	11257FN	49°07′ N, 119°33′ W	375	1978
Oliver Rockcliffe	112N765	49°10′ N, 119°34′ W	332	1989
Oliver STP	1125766	49°11′ N, 119°33′ W	297	1924–2004
Mt Kobau Observatory	1125223	49°07′ N, 119°41′ W	1862	1966–1980
Osoyoos CS	1125852	49°02′ N, 119°26′ W	283	1990–*present*
Summerland CDA	1127800	49°34′ N, 119°39′ W	455	1916–1995
Summerland CS	112G8L1	49°34′ N, 119°39′ W	434	1990–*present*

Differences in climatology between Summerland and Oliver regions were determined from their relative and absolute mean monthly differences (Figure A.1 and Table A.2). Data sets were intersected before calculating normals, which was done so as to not let missing data from one station bias the differences. Differences in solar radiation between the two areas were determined using data from Mt. Kobau as representative of Oliver. Changes in wet and dry spells ($\delta\bar{P}_w$ and $\delta\bar{P}_d$, respectively) were determined by comparing the relative lengths of mean monthly interarrivals (e.g., von Storch and Zwiers, 1999) of daily precipitation using a threshold of 0.6 mm.

A.3 Validation of synthetic weather generation using LARS-WG

LARS-WG is capable of reproducing daily temperature (maximum and minimum), precipitation and solar radiation at Oliver using a weather generator calibrated for Summerland, as described using the transfer equations in Section 4.3.2.

Figure A.2 compares station measured precipitation, and the baseline precipitation for Oliver generated by LARS-WG. These figures show their 'images', as described in Toews et al. (2007). The lower-left panels of images, although created using 11-day bin

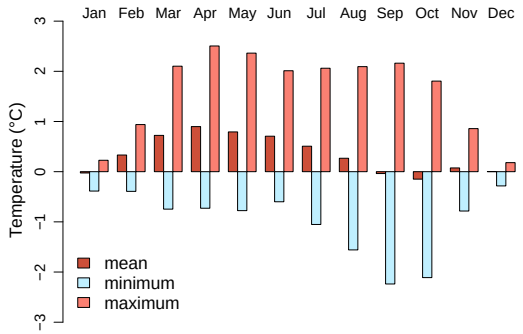

(a) Absolute changes in T_{mean}, T_{min} and T_{max}

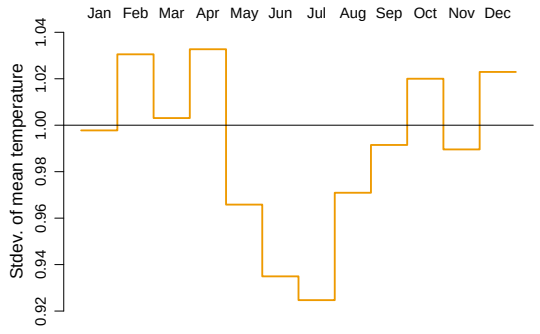

(b) Relative change in the standard deviation of T_{mean}

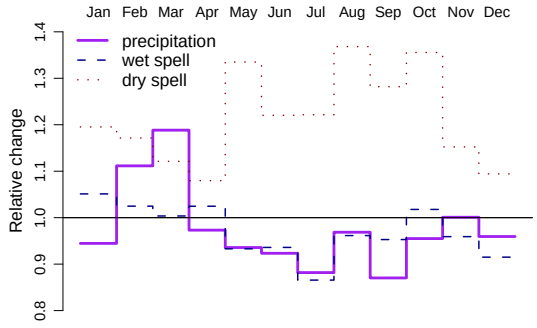

(c) Relative change in precipitation rates, wet spells and dry spells

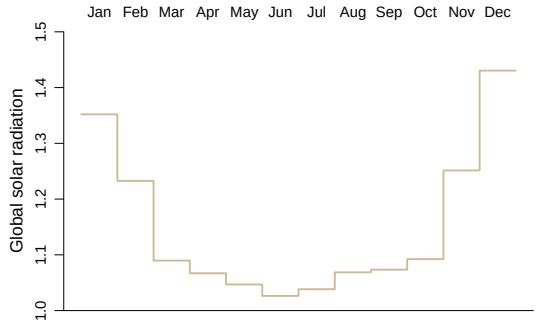

(d) Relative change in global solar radiation between Summerland and Mt. Kobau Observatory, using data from 1960–1994

Figure A.1 Differences in mean monthly normals between Summerland and Oliver regions. All data sets except (d) use data from years 1925–2004 (see Table A.2 for values).

widths,[1] compare well. However, the annual precipitation totals (in the upper right-hand panels) from the station measured data clearly have decadal-scale variations, which are not reproduced in the synthetic precipitation.

Figure A.3 shows the synthetic temperature and solar radiation data. An analysis between T_{min} and T_{max} between the measured Oliver data 1961–1990 and the base synthetic data have a mean and standard deviation of 0.0965 ± 0.465 and 0.0548 ± 0.450°C,

[1] LARS-WG considers variations on coarser monthly divisions

Table A.2 Differences in mean monthly normals between Summerland and Oliver regions. All data sets except ($\delta\bar{R}_s$) use data from years 1925–2004 (see Figure A.1 for plots).

	$\delta\bar{P}$	$\delta\bar{P}_w$	$\delta\bar{P}_d$	$\Delta\bar{T}_{\text{min}}$	$\Delta\bar{T}_{\text{max}}$	$\delta\,\text{stdev}\{\bar{T}\}$	$\delta\bar{R}_s$
Jan	0.945	1.051	1.195	−0.386	0.227	0.998	1.352
Feb	1.112	1.025	1.171	−0.393	0.939	1.031	1.233
Mar	1.188	1.004	1.121	−0.746	2.102	1.003	1.090
Apr	0.973	1.025	1.080	−0.728	2.505	1.033	1.067
May	0.936	0.933	1.335	−0.776	2.363	0.966	1.047
Jun	0.923	0.936	1.220	−0.600	2.011	0.935	1.026
Jul	0.882	0.866	1.221	−1.052	2.062	0.925	1.038
Aug	0.969	0.961	1.368	−1.559	2.093	0.971	1.069
Sep	0.870	0.953	1.282	−2.238	2.162	0.991	1.073
Oct	0.955	1.018	1.355	−2.111	1.805	1.020	1.092
Nov	1.001	0.959	1.152	−0.784	0.858	0.990	1.251
Dec	0.959	0.915	1.094	−0.284	0.180	1.023	1.430

respectively. These numbers show that the differences between the observed and stochastic values have a mean close to zero, with limited variability. One weakness of LARS-WG is the assumption that temperature data are normally distributed at any given time of the season. A rigorous analysis of temperature data at any month of the year reviles that the statistical distribution is not perfectly normally distributed, as there are usually few extreme values, and the distribution has a significant negative skew in the winter due to cold-spells. These differences are apparent between Figure 4.2a (measured) and Figure A.3a (synthetic).

A.4 Differences in precipitation amounts among stations near Oliver

Annual total precipitation amounts were compared between two stations in the Oliver region to determine how precipitation amounts are affected by elevation. Figure A.4 shows cross-plots between annual precipitation amounts between different stations in the study region, where each point represents a single year. The slope in the cross-plots, b,

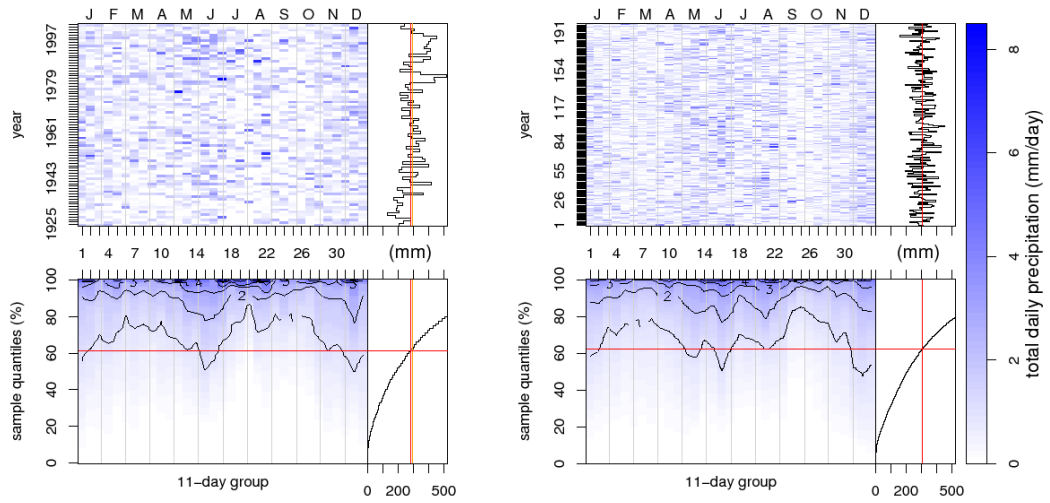

(a) Measured precipitation, 1925–2003

(b) Base synthetic precipitation, 200 years

Figure A.2 Comparison of measured and synthetic precipitation at Oliver.

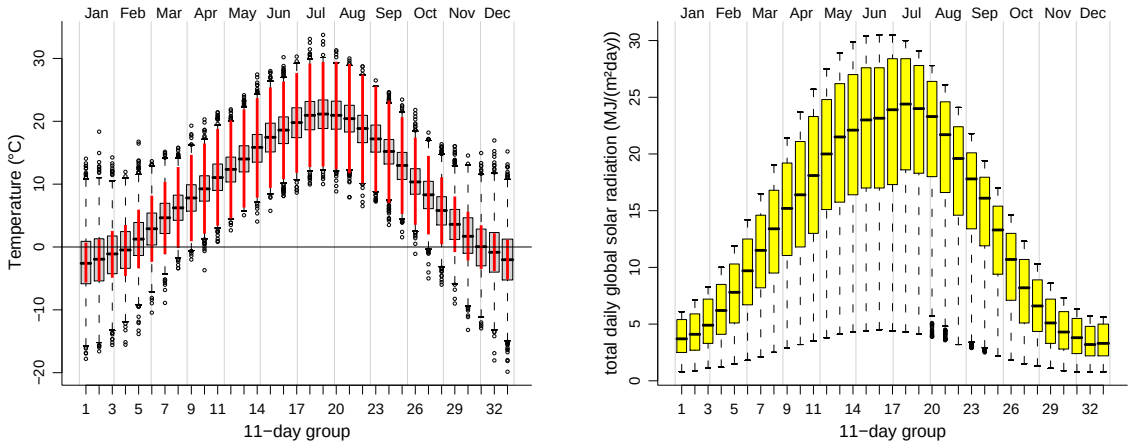

(a) Temperature

(b) Global solar radiation

Figure A.3 Base synthetic temperature and solar radiation at Oliver, 200 years.

was determined using perpendicular offsets, with a zero-intercept (derived from Sampaio, 2006):

$$B = \frac{1}{2}\frac{\sum x^2 - \sum y^2}{\sum xy} \tag{A.1}$$

$$b = -B + \sqrt{B^2 + 1} \tag{A.2}$$

A precipitation lapse rate can be established from the slope and elevation differences from Figure A.4, and is determined in Figure A.5. This lapse rate of $6{\times}10^{-4}$ m^{-1} (or 60% per 1 km rise in elevation) can be used to determine the mean precipitation at some elevation:

$$\bar{P}_{\mathcal{B}} = \bar{P}_{\mathcal{A}} \left(6{\times}10^{-4} \cdot dz + 1\right) \tag{A.3}$$

where $\bar{P}_{\mathcal{B}}$ and $\bar{P}_{\mathcal{A}}$ are the mean precipitation at locations $\mathcal{A}$ and $\mathcal{B}$, and dz is the elevation difference between the locations.

A.5 The seas package for R

This package was designed to visualize seasonal data, as well as import/export file formats used throughout the research project. It is written in the R programming language, and is capable of conveying descriptive statistics for any seasonal process. Documentation and examples are provided within the package, which can be downloaded from the Comprehensive R Archive Network.[2] A paper describing the seas package is published in *Computers & Geosciences* (Toews et al., 2007).

The package also contains many documented procedures for climate analysis, such as finding absolute and relative changes in climate states, as discussed in Chapter 4 and used in Figure A.1. In addition, several methods are available to read and/or write climate data formats for HELP, SDSM, and LARS-WG.

[2] http://cran.r-project.org/

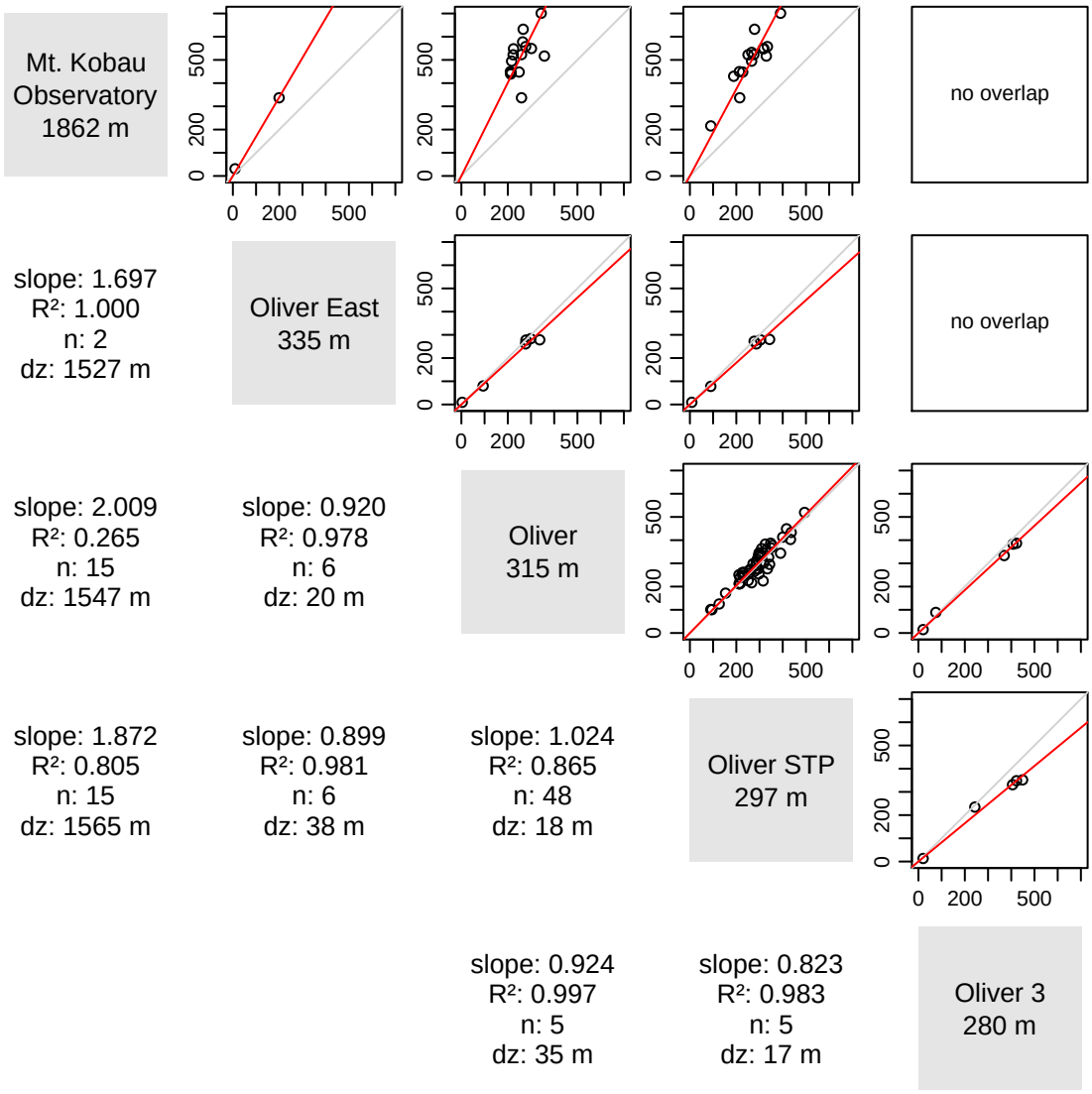

Figure A.4 Cross-plots of annual precipitation from stations in the Oliver region, in mm/year. Each point represents a single year, which is summed only where daily data from both stations overlap. Differences in elevation, dz, are also displayed for each cross-comparison.

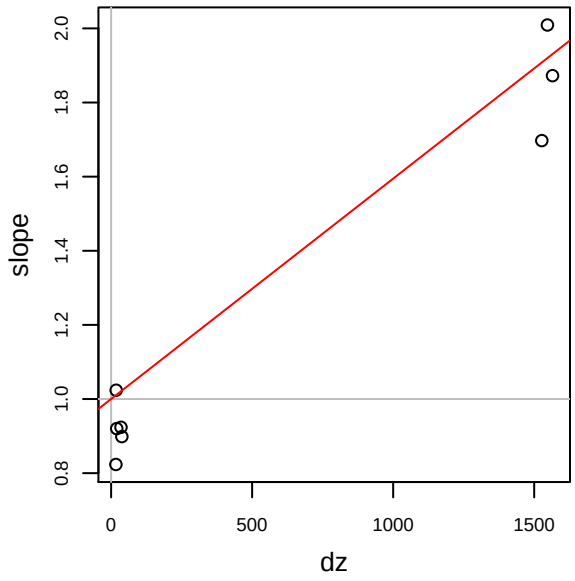

Figure A.5 Correlation between precipitation increase, determined from the slopes in the cross-plots in Figure A.4 (unitless), and elevation rise between the stations (m). The fitted slope is 5.95×10^{-4} m^{-1}, which was weighted by the number of observations in each cross-plot, and has a forced intercept of 1.

Appendix B

GCM Downscaling

B.1 Methods

B.1.1 Temperature downscaling using SDSM

The Canadian Institute for Climate Studies (Canadian Institute for Climate Studies, 2005) provided regridded NCEP/NCAR predictors and GCM data for CGCM1A and HadCM3. The files selected for the grid point nearest to southern Okanagan were `B0X_16X_11Y` for CGCM1/3.1 ($I_1 = 65$, $J_1 = 38$), and `B0X_65X_15Y` for HadCM3 ($I_1 = 65$, $J_1 = 57$). See Figure 4.3 for a map.

Downscaling predictors were selected (Table B.1) based on: (1) their correlation with monthly T_{mean} (Table B.2), (2) the seasonal signal of predictors, and how they shift in future-predicted time-slices. The unconditional monthly calibration results are shown in Table B.3.

B.1.1.1 Producing data for CGCM3.1

SDSM data for CGCM3.1 were not available at the time of writing, so they were created from the GCM data provided by CCCma.[1] The SDSM data files consist of raw GCM

[1]Data obtained from `http://www.cccma.bc.ec.gc.ca/`

Table B.1 Synoptic-scale predictors from GCMs used to downscale temperature data.

SDSM label	Description	CGCM1 / CGCM3.1	HadCM3
mslp	mean sea level pressure		
temp	mean temperature	✓	✓
rhum	relative humidity		
sphu	specific humidity		
p__f	geostrophic airflow velocity		
p__u	zonal velocity component		
p__v	meridional velocity component		
p__z	vorticity		
p_th	wind direction		
p_zh	divergence		
p850	850 hPa geopotential height	✓	✓
r850	850 hPa relative humidity		✓
s850	850 hPa specific humidity	✓	
p8_f	850 hPa geostrophic airflow velocity		
p8_u	850 hPa zonal velocity component		
p8_v	850 hPa meridional velocity component		
p8_z	850 hPa vorticity		
p8th	850 hPa wind direction		
p8zh	850 hPa divergence		
p500	500 hPa geopotential height		
r500	500 hPa relative humidity		
s500	500 hPa specific humidity		
p5_f	500 hPa geostrophic airflow velocity		
p5_u	500 hPa zonal velocity component		
p5_v	500 hPa meridional velocity component		
p5_z	500 hPa vorticity	✓	✓
p5th	500 hPa wind direction		
p5zh	500 hPa divergence		

values, which are normalized:

$$V = \frac{x - \bar{x}_b}{\sigma_b} \tag{B.1}$$

where V is the value in the SDSM file, x is the raw value from the GCM, $\bar{x}_b$ is the baseline mean of x, and σ_b is the standard deviation of baseline x. The baseline climate is defined

Table B.2 Unconditional monthly correlation coefficients (R^2; $\alpha = 0.05$) between T_{mean} from Oliver and the eight leading NCEP/NCAR predictors, 1961–2000.

Predictor	Jan.	Feb.	Mar.	Apr.	May	Jun.	Jul.	Aug.	Sep.	Oct.	Nov.	Dec.
	NCEP/NCAR predictors for CGCM1/CGCM3.1, at 50.1° N, 120.0° W											
mslp	0.156	0.138	0.025	0.005			0.004	0.005	0.035	0.094	0.175	0.134
p5_z	0.042	0.007	0.052	0.157	0.263	0.277	0.368	0.230	0.124	0.018	0.033	0.054
p500	0.069	0.036	0.173	0.406	**0.607**	**0.608**	**0.624**	0.550	0.303	0.100	0.061	0.078
p850	0.011	0.015	0.009	0.044	0.128	0.118	0.188	0.160	0.017		0.018	0.006
s500	0.159	0.119	0.159	0.235	0.085	0.043	0.016	0.006	0.075	0.139	0.186	0.124
s850	**0.566**	0.486	0.492	0.515	0.497	0.300	0.067	0.062	0.237	0.477	**0.630**	**0.560**
sphu	0.521	0.471	0.514	**0.530**	0.365	0.234	0.158	0.155	0.359	0.533	0.572	0.485
temp	0.555	**0.513**	**0.526**	0.504	0.372	0.280	0.602	**0.550**	**0.627**	**0.578**	0.625	0.544
	NCEP/NCAR predictors for HadCM3, at 50.0° N, 120.0° W											
mslp	0.149	0.133	0.024	0.005				0.004	0.036	0.093	0.170	0.129
p5_z	0.037	0.006	0.047	0.114	0.246	0.248	0.351	0.211	0.119	0.016	0.031	0.049
p500	0.071	0.037	0.174	0.406	**0.608**	**0.611**	**0.626**	0.551	0.305	0.101	0.062	0.079
p850	0.010	0.013	0.009	0.044	0.126	0.116	0.185	0.158	0.017		0.016	0.006
r500	0.079	0.063	0.034	0.006	0.067	0.072	0.092	0.070	0.018	0.017	0.117	0.060
r850	0.135	0.120	0.008	0.006	0.156	0.264	0.390	0.299	0.122		0.148	0.162
sphu	0.526	0.474	0.514	**0.549**	0.379	0.241	0.159	0.151	0.344	0.531	0.573	0.494
temp	**0.558**	**0.516**	**0.531**	0.529	0.387	0.294	0.612	**0.556**	**0.630**	**0.576**	**0.626**	**0.548**

Table B.3 SDSM unconditional calibration of temperature data for Oliver with the NCEP/NCAR predictors, 1961–2000.

	T_{mean}	T_{min}	T_{max}
	For CGCM1/CGCM3.1		
R^2	0.596	0.429	0.571
Std. Err.	2.440	3.234	3.034
	For HadCM3		
R^2	0.560	0.390	0.572
Std. Err.	2.539	3.334	3.028

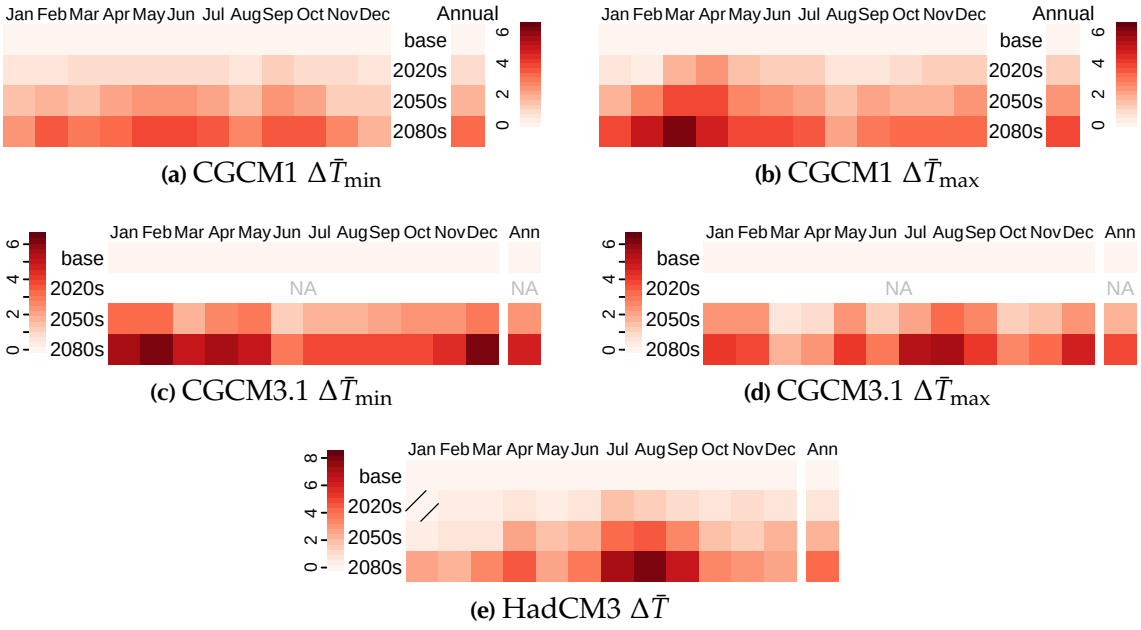

(a) CGCM1 $\Delta\bar{T}_{\min}$ (b) CGCM1 $\Delta\bar{T}_{\max}$

(c) CGCM3.1 $\Delta\bar{T}_{\min}$ (d) CGCM3.1 $\Delta\bar{T}_{\max}$

(e) HadCM3 $\Delta\bar{T}$

Figure B.1 Absolute changes in raw GCM data near Okanagan Basin.

Table B.4 Baseline mean and standard deviation from CGCM3.1/T47 run 1 SRES A2 near Okanagan Basin ($I_1 = 65$, $J_1 = 38$)

SDSM label	CCCma label	$\bar{x}_b$	σ_b	Units
`temp`	`tas`	272.4886	9.44099	K
`p850`	`zg`	1459.44143	76.20041	m
`s850`	`hus`	0.004111273	0.002176461	kg/kg
`p5_z`	NA	$-5.516\,94\times10^{-7}$	$2.914\,649\times10^{-5}$	—

for each GCM (or regridded NCEP/NCAR calibration data) between the years 1961–1990.[2] The baseline climate for the predictors from CGCM3.1 is in Table B.4.

Vorticity for CGCM3.1 are not provided through CCCma, since this is a derived model parameter. Vorticity was calculated from meridional and zonal wind components, which are available, using NCO commands (Zender, 2007) and an NCL script[3] (NCAR, 2006).

[2]This can be verified by analysing any SDSM data sets between 1961–1990, which have a mean and standard deviation of approximately 0 and 1, respectively

[3]Located on the CD at `programs/calcvort.ncl`

The predictor files for SDSM can be created in R (R Development Core Team, 2007) through extraction of the variable from the GCM near Okanagan Basin. For example, using a netCDF file[4] from CCCma describing global daily mean surface air temperature from the CGCM3.1/T47 SRES A2 experiment between 2046–2065:

```
> library(ncdf)
> nc <- open.ncdf("tas_a2_sresa2_1_cgcm3.1_t47_2046_2065.nc")
> tas <- get.var.ncdf(nc, "tas", c(65,38,1), c(1,1,-1))
> close(nc)
> temp <- (tas - 272.4886)/9.44099
> cat(sprintf("%9.3f",temp), file="c3gatempna.dat", sep="\n")
```

Downscaling of CGCM3.1 data can use the same regridded NCEP/NCAR "Calibration" data as distributed with SDSM files for CGCM1, since the two GCMs have the same spatial resolution.

B.2 Climate shift terms

Tables B.5–B.7 show the relative and absolute shift terms used between the base (or current) climate state to future states. These numbers were determined from either the raw GCM data near Okanagan Basin, or the 20 SDSM-downscaled temperature ensembles. The shift terms used in LARS-WG[5] are a combination of these values, and the values in Table A.2 (or Figure A.1), as described by equation 4.3.

B.3 Problems with screen temperature in CGCM1 and CGCM2

Figure B.2 shows the seasonal patterns of temperature data from CGCM1 at the GCM grid point near Okanagan Basin ($I_1 = 65$, $J_1 = 38$). Similar figures (not shown) were also prepared for CGCM2,[6] which appear similar. *All* daily temperature values in the winter from both GCMs appear to be at or near 0°C, which is unrealistic. Many of the non-zero values in these seasons are considered statistical outliers in the box plots, as they

[4]This is the most common file format for atmospheric data; it commonly has a `.nc` file extension

[5]Located on the CD at `data/LARSWG/`

[6]CGCM2 was not used in this study, but is presented here for completeness

Table B.5 Shift terms for CGCM1.

(a) $\Delta\bar{T}_{\min}$ (SDSM)

	2020s	2050s	2080s
Jan	0.536	1.472	3.073
Feb	0.420	1.518	3.411
Mar	0.819	2.017	3.842
Apr	1.363	2.337	3.713
May	0.733	1.327	2.674
Jun	0.655	1.188	2.352
Jul	0.906	1.397	2.756
Aug	0.878	1.542	2.703
Sep	1.427	2.202	3.930
Oct	0.737	1.798	2.784
Nov	1.112	1.421	3.158
Dec	0.999	1.882	2.682
Ann	0.883	1.675	3.086

(b) $\Delta\bar{T}_{\max}$ (SDSM)

	2020s	2050s	2080s
Jan	0.483	1.273	2.612
Feb	0.613	1.704	3.480
Mar	1.203	1.968	3.536
Apr	1.635	2.582	3.808
May	1.334	2.140	3.508
Jun	1.123	2.157	3.784
Jul	1.211	2.157	3.563
Aug	0.799	1.989	2.992
Sep	1.076	2.793	4.150
Oct	1.038	2.201	3.930
Nov	0.872	1.142	2.603
Dec	0.745	1.485	2.118
Ann	1.012	1.966	3.337

(c) $\delta\,\mathrm{stdev}\{\bar{T}\}$ (SDSM)

	2020s	2050s	2080s
Jan	1.035	1.010	1.105
Feb	1.031	1.100	1.092
Mar	1.065	1.181	1.196
Apr	0.978	0.975	0.995
May	1.063	1.010	1.169
Jun	0.981	0.979	1.037
Jul	0.970	0.969	0.987
Aug	1.012	0.973	0.970
Sep	1.050	1.024	1.029
Oct	1.014	1.023	1.131
Nov	1.037	1.015	1.101
Dec	1.014	1.026	1.127
Ann	1.015	1.018	1.026

(d) $\delta\bar{P}$ (GCM)

	2020s	2050s	2080s
Jan	1.010	0.963	1.110
Feb	0.943	0.938	0.976
Mar	0.891	1.004	1.024
Apr	0.964	0.968	1.062
May	0.794	0.785	0.756
Jun	0.895	0.903	0.821
Jul	0.879	0.973	1.115
Aug	1.186	0.997	1.228
Sep	1.398	1.188	1.287
Oct	1.066	1.241	1.304
Nov	1.096	1.104	1.280
Dec	1.198	1.248	1.196
Ann	1.031	1.047	1.118

(e) $\delta\bar{R}_s$ (GCM)

	2020s	2050s	2080s
Jan	1.020	0.996	0.974
Feb	1.054	1.050	1.007
Mar	1.046	1.022	0.992
Apr	1.024	1.005	0.971
May	1.057	1.039	1.058
Jun	1.014	1.017	1.008
Jul	1.025	0.969	0.953
Aug	0.950	1.002	0.915
Sep	0.930	0.953	0.913
Oct	0.973	0.949	0.926
Nov	0.948	0.981	0.891
Dec	0.936	0.924	0.953
Ann	1.004	0.998	0.971

seldom occur. In future time periods, values below 0°C seldom occur, as they appear to be truncated by the lower temperature limit. It is unknown why this behaviour is found in the model results; however, it is suspected that it is involved with the coupling with AGCM2, which both models share. NCEP/NCAR variables near the same grid point (not shown) appear similar to station measured seasonal temperatures, thus it is assumed this is a model error. Consequently, this same error in temperature data has propagated to the SDSM data files for CGCM1 and CGCM2, distributed and used by other researchers.

Table B.6 Shift terms for CGCM3.1.

(a) $\Delta\bar{T}_{\min}$ (SDSM)

	2050s	2080s
Jan	1.562	2.936
Feb	1.307	2.884
Mar	0.917	2.493
Apr	1.502	2.818
May	1.163	2.134
Jun	0.470	1.378
Jul	1.055	2.496
Aug	1.971	3.850
Sep	1.834	3.262
Oct	1.616	2.253
Nov	1.192	2.271
Dec	1.678	3.339
Ann	1.357	2.677

(b) $\Delta\bar{T}_{\max}$ (SDSM)

	2050s	2080s
Jan	1.344	2.508
Feb	1.728	3.092
Mar	0.892	2.351
Apr	0.984	2.283
May	1.531	2.685
Jun	0.841	2.186
Jul	1.296	3.010
Aug	2.294	3.878
Sep	2.144	3.398
Oct	1.156	2.439
Nov	1.200	2.246
Dec	1.367	2.732
Ann	1.397	2.733

(c) $\delta\,\mathrm{stdev}\{\bar{T}\}$ (SDSM)

	2050s	2080s
Jan	1.476	2.756
Feb	1.467	2.895
Mar	0.901	2.425
Apr	1.179	2.431
May	1.324	2.370
Jun	0.670	1.795
Jul	1.219	2.830
Aug	2.093	3.771
Sep	2.058	3.413
Oct	1.390	2.373
Nov	1.215	2.290
Dec	1.533	3.050
Ann	1.378	2.701

(d) $\delta\bar{P}$ (GCM)

	2050s	2080s
Jan	1.090	1.212
Feb	1.150	1.288
Mar	1.025	1.242
Apr	1.262	1.489
May	1.041	1.225
Jun	1.075	1.017
Jul	0.941	0.859
Aug	0.811	0.786
Sep	1.127	1.203
Oct	1.305	1.389
Nov	1.163	1.396
Dec	1.171	1.361
Ann	1.119	1.238

(e) $\delta\bar{R}_s$ (GCM)

	2050s	2080s
Jan	0.958	0.918
Feb	0.957	0.875
Mar	0.963	0.877
Apr	0.924	0.797
May	0.907	0.889
Jun	1.004	1.030
Jul	1.052	1.167
Aug	1.145	1.163
Sep	1.041	1.031
Oct	0.850	0.842
Nov	0.883	0.864
Dec	0.902	0.859
Ann	0.991	0.981

The model error identified in CGCM1 and CGCM2 has some influence in downscaled temperature data; however, it does not directly affect the downscaled output, since SDSM uses a multilinear approach using more than one predictor. This error may have also influenced a shortened winter duration (or an early spring), due to the anomalous lack of low temperatures modelled during this period. The mean of the data are realistic, however the variation is not, which is why the changes in standard deviation between scenarios were highly variable (e.g., Figure 4.9a).

Table B.7 Shift terms for HadCM3.

(a) $\Delta\bar{T}_{\min}$ (SDSM)

	2020s	2050s	2080s
Jan	0.020	0.725	2.323
Feb	0.422	0.864	1.833
Mar	0.461	0.623	2.344
Apr	0.831	1.908	3.402
May	0.271	0.845	1.199
Jun	0.124	0.418	0.792
Jul	1.107	2.095	3.560
Aug	1.317	3.240	5.706
Sep	0.700	2.445	4.801
Oct	0.411	0.850	1.890
Nov	0.554	0.988	1.760
Dec	0.751	1.715	2.263
Ann	0.581	1.395	2.662

(b) $\Delta\bar{T}_{\max}$ (SDSM)

	2020s	2050s	2080s
Jan	0.006	0.601	1.906
Feb	0.595	1.087	2.168
Mar	0.437	0.960	2.985
Apr	0.573	2.192	3.995
May	0.607	1.470	2.351
Jun	0.439	0.875	1.678
Jul	1.211	2.820	4.870
Aug	1.215	3.756	6.578
Sep	1.116	3.164	5.991
Oct	0.822	1.572	2.784
Nov	0.752	1.189	2.148
Dec	0.616	1.403	1.853
Ann	0.699	1.761	3.282

(c) $\delta\,\mathrm{stdev}\{\bar{T}\}$ (SDSM)

	2020s	2050s	2080s
Jan	1.061	1.032	0.987
Feb	1.007	0.993	0.981
Mar	1.001	1.041	1.071
Apr	0.987	1.024	1.028
May	1.021	1.032	1.060
Jun	1.011	1.023	1.037
Jul	1.006	1.041	1.071
Aug	0.999	1.018	1.040
Sep	1.017	1.047	1.092
Oct	1.026	1.053	1.069
Nov	0.987	0.980	1.005
Dec	0.964	0.929	0.923
Ann	1.016	1.045	1.073

(d) $\delta\bar{P}$ (GCM)

	2020s	2050s	2080s
Jan	0.984	0.976	1.096
Feb	0.949	0.908	1.150
Mar	1.114	1.090	1.209
Apr	1.173	1.144	1.279
May	0.964	0.969	0.938
Jun	0.817	0.835	0.742
Jul	0.847	0.455	0.358
Aug	0.946	0.485	0.277
Sep	0.787	0.734	0.651
Oct	1.137	0.963	1.130
Nov	1.013	0.993	1.009
Dec	1.079	1.111	1.060
Ann	1.004	0.949	0.997

(e) $\delta\bar{R}_s$ (GCM)

	2020s	2050s	2080s
Jan	1.014	0.956	0.856
Feb	1.017	0.986	0.865
Mar	0.943	0.957	0.841
Apr	0.951	0.954	0.893
May	1.016	0.988	1.028
Jun	1.094	1.083	1.106
Jul	1.076	1.154	1.188
Aug	1.027	1.092	1.115
Sep	1.075	1.102	1.121
Oct	0.965	0.983	0.927
Nov	0.953	0.942	0.859
Dec	0.968	0.876	0.893
Ann	1.026	1.043	1.035

The behaviour with screen temperature was checked in CGCM3.1 and, fortunately, seasonal patterns of data in this GCM appear realistic, and are comparable with NCEP/NCAR patterns. This improvement is perhaps due to the inclusion of AGCM3, which has significant improvements over previous atmospheric components used at CCCma.

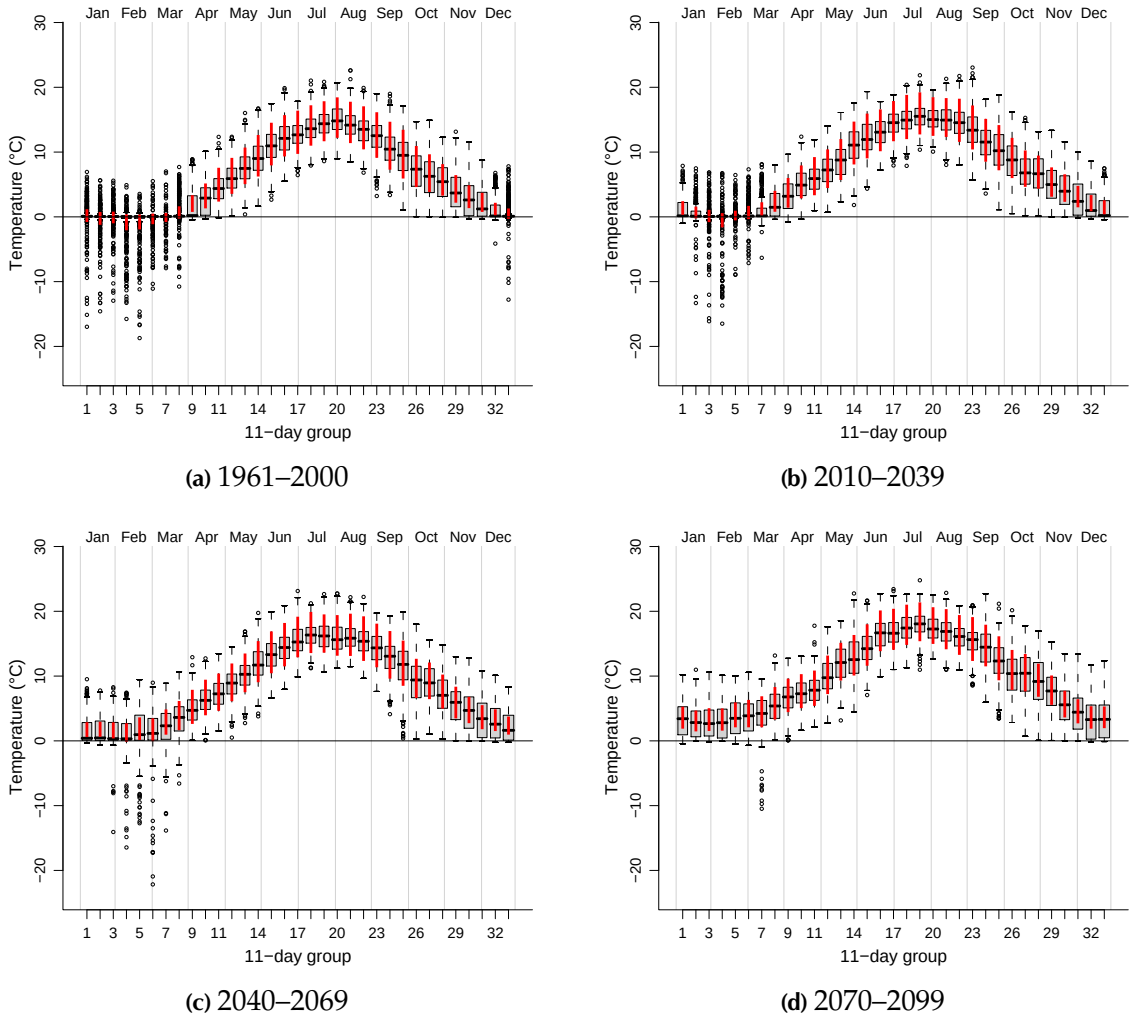

(a) 1961–2000

(b) 2010–2039

(c) 2040–2069

(d) 2070–2099

Figure B.2 Seasonal plots of raw CGCM1 screen temperature values near Okanagan Basin, at grid location $I_1 = 65$, $J_1 = 38$.

Appendix C

Recharge Modelling

C.1 Soil data

Soil data for the Okanagan are provided in an ArcInfo database, consisting of one polygon coverage, and three related dBase tables (Wittneben, 1986; Kenk and Sondheim, 1987). The soil types in the polygon coverage, `okdsok_p`, are described in the `SOIL1_NAME`, `SOIL2_NAME`, and `SOIL3_NAME` fields, which indicate the primary, secondary, and tertiary soil facies (where applicable). Relative proportions of each soil type in the polygon are described by `SOIL1_DEC`, `SOIL2_DEC`, `SOIL3_DEC`. The soil facies for each soil name are identified using a 1- to 3-letter database key. The general properties and description of the soil facies are contained in the `okdsok_p.soilcart` table.

Tables `okdsok_p.sc1` and `okdsok_p.sc2` contain layer data from each soil type, ordered from top–down using the `DEP_CODE` field. Each depth horizon indicates the mean thickness (`THICK_M`) and many other measured or interpreted soil properties, including: soil texture (`TEX_CSSC`), using the Canadian system of soil classification (CSSC, 1978); proportions of sand (`SAND_M`) and clay[1] (`CLAY_M`); bulk density (`BDEN_M`); and available soil water capacity[2] (`AWSC_M`) are also provided for each soil layer. These soil properties were

[1] Proportions of silt are not provided, but can be calculated from: %silt $= 100\% -$ %clay $-$ %sand

[2] From Dingman (2002, p.236): available soil water content, θ_a, is equivalent to $\theta_{fc} - \theta_{wp}$

Table C.1 CSSC drainage classes from the soil database are mapped to HELP soil texture numbers, T_n (see Schroeder et al., 1994, Table 1), which were designed to accommodate USDA soil classifications.

CSSC drainage class			
Descriptor	Code	T_n	USDA
rapidly drained	R	1	CoS
well drained	W	3	FS
moderately well drained	M	7	FSL
imperfectly drained	I	9	SiL
poorly drained	P	11	CL
very poorly drained	V	15	C

used in ROSETTA, and the hydrologic parameter estimates for all soil layers are shown in Figure C.1.

Each soil facies in the Okanagan soil database is designated a dominant and secondary drainage code (`DRAIN_D` and `DRAIN_U` in the `okdsok_p.soilcart` table); only the dominant is considered to define the surface soil texture in this study. This was mapped to a HELP soil texture class to determine the runoff curve number (Table C.1).

C.2 HELP and Python programming

Recharge was estimated through the use of the HELP 3.80D model (Berger, 2004). This program, however, does not have an application programming interface (API). The only user interface is through a DOS interface, which allows manual processing of a single soil profile and weather data set at a time.

The HELP program (all versions) consists of two primary components: (1) a non-interactive numerical modelling component, written in Fortran; and (2) an interface component, which imports data and produces formatted data files for the numerical modelling component. There are multiple interactive user interfaces available for DOS (Schroeder et al., 1994; Berger, 2004) and Microsoft Windows (WHI, 2004); however, these

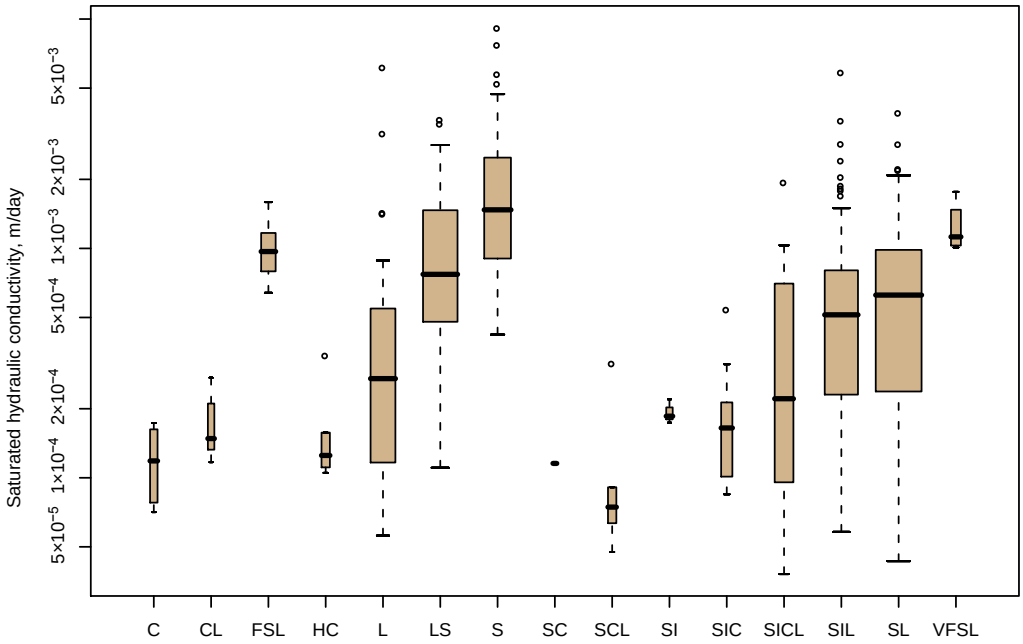

(a) Saturated hydraulic conductivities, K_s

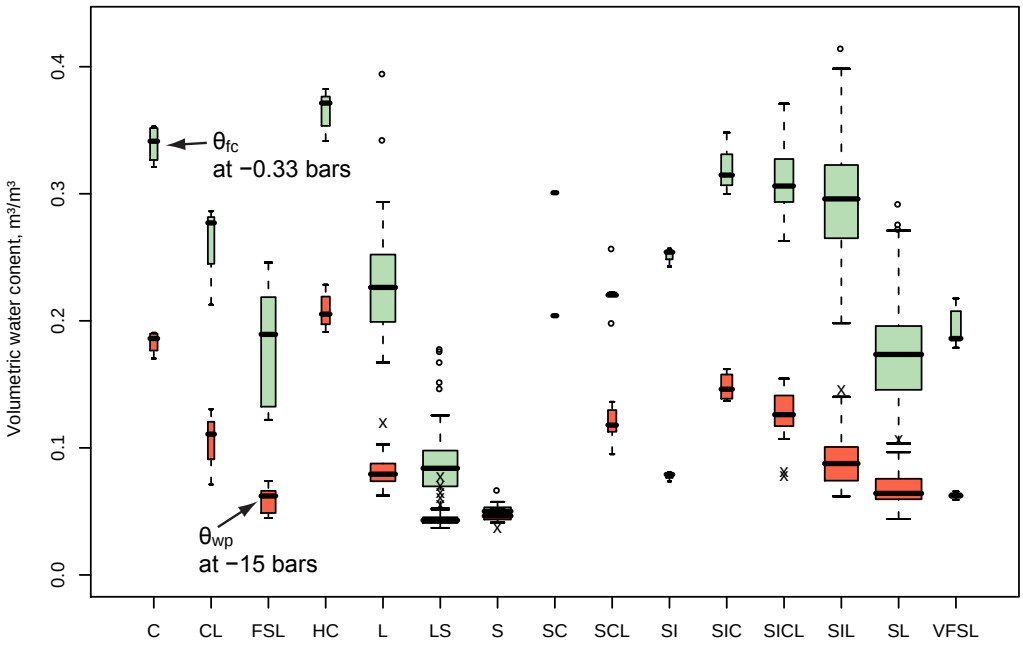

(b) Volumetric water retentions: field capacity, θ_{fc}, and wilting point, θ_{wp}

Figure C.1 Boxplots of soil property results from ROSETTA, grouped by CSSC soil texture.

interface methods limit the versatility of the model to a limited number of profile and simulation scenarios—all controlled manually by the user.

As part of this study, a program module was developed in Python (e.g., Lutz and Ascher, 2004) as a programming interface to the HELP model.[3] The programming interface can be adapted to any task through a script, particularly where the task is repetitive. This module uses the existing non-interactive numerical modelling component (called `HELP30.EXE`), which is part of HELP 3.80D. The module was used in a Python script[4] to effectively apply the HELP model spatially over a region. The script first reads all relevant geospatial and soil data from multiple resources, then evaluates available data at each grid location (described in detail next), runs the HELP numerical model, reads the model results, then finally stores the annual and monthly results in netCDF files (a time-varying raster format) for post-processing.

Each grid is evaluated using available data, specifically: (1) a precipitation file is selected, depending if the location is in a particular irrigation district, (2) land use is used to approximate a evaporative depth zone and vegetation cover (Table 4.6); (3) runoff curve number is calculated from vegetation cover, soil drainage properties, and surface slope; (4) a unique soil profile is constructed using the layer information from database, which extends down to the water table; and (5) evaporation and soil files for HELP are written, and HELP is simulated. From the output of HELP, recharge (leakage), runoff, and evapotranspiration are recorded.

C.2.1 Runoff curve number

The runoff curve number method (USDA, 1986) is used in HELP to estimate runoff excess (or infiltration). As the runoff curve number is an empirical value, there is no set methodology to determines its value. The method used here is similar to the "computed curve number", which is detailed in the BASIC source code for HELP 3.07[5] (Schroeder et al.,

[3] Located on the CD at `programs/HELP.py`

[4] Located on the CD at `programs/model_HELP.py`

[5] `http://el.erdc.usace.army.mil/products.cfm?Topic=model&Type=landfill`

Table C.2 Infiltration correlation coefficients, I_R, for different soil textures (USDA soil texture names and texture numbers, T_n); values are from lines 260–262 in `DESIGN.BAS` of the HELP 3.07 source code.

Texture	T_n	I_R	Texture	T_n	I_R
CoS	1	0.50	SiL	9	0.17
S	2	0.40	SCL	10	0.11
FS	3	0.39	CL	11	0.09
LS	4	0.38	SiCL	12	0.07
LFS	5	0.34	SC	13	0.06
SL	6	0.30	SiC	14	0.02
FSL	7	0.25	C	15	0.01
L	8	0.20			

1994). The normal antecedent moisture condition (AMC-II) runoff curve number on a flat surface, CN_{II_0}, is first calculated:

$$CN_{II_0} = C_0 + C_1\, I_R + C_2\, I_R^2 \tag{C.1}$$

where I_R is a infiltration correlation parameter for given soil textures numbers, T_n (Table C.2), which are linearly interpolated if T_n has a fraction component. Polynomial coefficients C_0, C_1, and C_2 are calculated from:

$$C_0 = 100.0 - 3.25\, V_n \tag{C.2a}$$

$$C_1 = -20.5 - 1.3\, V_n \tag{C.2b}$$

$$C_2 = -4.71 - 42.8\, V_n \tag{C.2c}$$

where V_n is an arbitrary value for vegetation cover used in HELP that ranges from 1.0 for bare ground to 5.0 for an "excellent cover of grass". These linear equations were determined from the original polynomial coefficients (Schroeder et al., 1994, Table 7), but are much smoother between the original five cover types and allow fractional values of V_n.

The slope adjusted AMC-II runoff curve, CN_{II}, is calculated by:

$$CN_{II} = 100 - (100 - CN_{II_0}) \left[\frac{(L/152.4)^2}{S/4} \right]^{CN_{II_0}^{-0.82}} \tag{C.3}$$

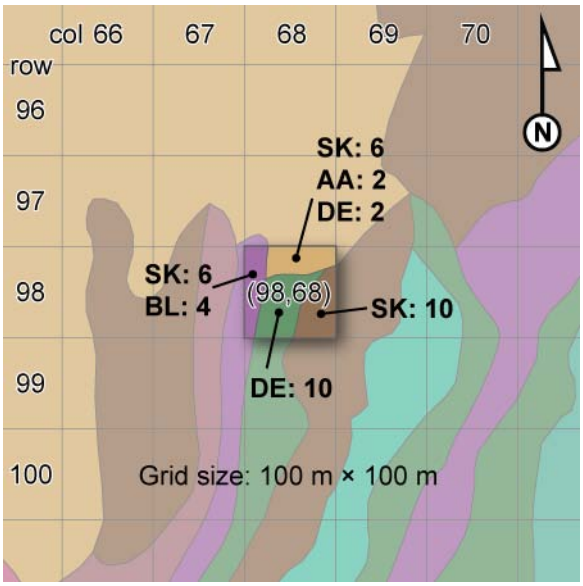

Figure C.2 Example of a grid cell from the soil database used for recharge estimation.

where L is the slope length (in metres), and S is the surface slope (in percent rise). This equation is from line 651 of `DESIGN.BAS`, which is slightly different (for unknown reason) than equation 34 documented in Schroeder et al. (1994). This routine in the Python module was verified to mimic the behaviour in the DOS versions of both HELP 3.07 and HELP 3.80D.

C.2.2 Application of HELP Python module

The `HELP.py` Python *module* is utilized by a Python *script*, `model_HELP.py`, which reads and interprets spatial data, creates soil profiles, and stores output in netCDF files. This allows the HELP model to be used to determine spatial recharge.

The `model_HELP.py` script first defines the directories of (a) HELP 3.80 (including `HELP30.EXE`, the Fortran-compiled executable), (b) input soil and slope data, and (c) output raster and netCDF data files. It then prepares soil profiles at each grid location, runs HELP and stores the results in a common netCDF file.

To illustrate this procedure, consider a single grid location at row 98, column 68, shown in Figure C.2. This coverage was created by using the `intersect` ArcInfo tool between the

soil coverage and a polygon mesh.[6] Soil data are exported from ArcGIS using a custom VBA script[7] into a simple ASCII file to be read and processed by `model_HELP.py`. The soil data for this example are in a text file `rc100_soil.txt` (showing tab characters):

```
98	68	3287.89309897966	0	DE	 	 	 	¶
98	68	2559.42989203828	0	SK	 	 	 	¶
98	68	2203.55881227394	6	SK	2	AA	2	DE¶
98	68	1949.11299240764	6	SK	4	BL	 	¶
```

These four lines describe the soil sub-polygons at grid location $R_1 = 98$, $C_1 = 68$ (from first two columns), where the grid origin is at upper-left. The areas of each sub-polygon are given in m^2, and are followed by 1 or more *decile*[8] and *soil name* data pairs for the primary, secondary and tertiary soil.

The area-weighted contributions of each soil type are considered for each grid location, and are stored in a Python dictionary structure:

```
>>> from model_HELP_util import *
>>> soil = readSoil('C:/oliver/soil/rc100_soil.txt')
>>> so = soil[(98,68)] # [row, column]
>>> print so
{'SK': 0.50510356035579296, 'AA': 0.044071199181455106,
'DE': 0.37286068019134649, 'BL': 0.077964560271405442}
>>> order = getorder(so)
>>> order
['SK', 'DE', 'BL', 'AA']
```

The contributions of each soil are out of 1. Here, the dominant soil type is `SK`, followed by `DE`, `BL` and `AA`. Next, soil profile class is created for `SK`, which then inherits the profile properties from the other soils, depending on their area contribution:

```
>>> soilProfile = AgCanSoil()
>>> soilProfile.readDB(order[0])
>>> for i in range(1,len(order)):
...     sec = AgCanSoil()
...     sec.readDB(order[i])
...     soilProfile.inheritSecondary(sec,weight=so[order[i]])
```

[6] FISHNET ArcScript by Robert Nicholas: http://arcscripts.esri.com/details.asp?dbid=12807

[7] Located on the CD at `programs/meshedFeatures.bas`

[8] The proportions are described using deciles, which are a fraction of 10; this database uses '0' to indicate 10 or 100%

```
...
>>> soilProfile.show()
 seq depth thick texNum poros    fc    wp       Ks   log_Ks
   0    12    12      6 0.426 0.239 0.070   0.0013    -2.89
   1    20     8      6 0.396 0.188 0.064  0.00091    -3.04
   2    28     8      5 0.371 0.149 0.055  0.00083    -3.08
   3    42    14      5 0.353 0.129 0.053  0.00083    -3.08
   4    48     6      4 0.332 0.113 0.050  0.00075    -3.12
   5    56     8      2 0.268 0.078 0.043  0.00039    -3.41
   6    74    18      1 0.258 0.057 0.044  0.00066    -3.18
   7   114    40      1 0.251 0.052 0.045  0.00082    -3.08
   8   135    21      3 0.312 0.058 0.042   0.0012    -2.94
   9   136     1      1 0.244 0.047 0.044  0.00095    -3.02
```

Other properties are then given to the soil profile, and the runoff curve number and geometric mean of K_s are calculated:

```
>>> soilProfile.slope = 15 # in percent
>>> soilProfile.slopelength = 152.4 # in metres
>>> soilProfile.vegetation = 3 # fair stand of grass
>>> soilProfile.texture = 9 # silty loam
>>> soilProfile.calcCNII() # calculate the runoff curve number
>>> print soilProfile.CNII
86.4286674137
>>> soilProfile.calcKsGeoMean() # calculate Ks geometric mean
>>> print soilProfile.KsGeoMean
0.000841587132125
```

Now the HELP model is initiated and run:

```
>>> import HELP
>>> HELP.climdir = 'C:/climatedata/LARSWG/HELP/'
>>> HELP.simdir = 'C:/oliver/HELP380/'
>>> HELP.simname = 'OLIVER'
>>> HELP.precipfile = 's2080.D4'
>>> HELP.tempfile = 's2080.D7'
>>> HELP.solarfile = 's2080.D13'
>>> HELP.etfile = 'DATA.D11'
>>> soilProfile.write() # write the D10 file
>>> HELP.run() # run the model, using os.system('HELP3O.EXE')
>>> mon = HELP.MON() # monthly recharge results
>>> mon.read()
>>> mon.show()
      date  precip  runoff     PET      ET    leak
2070-01-31    13.4     0.0    18.8    12.9    0.00
2070-02-28    30.8     0.0    23.7    18.3    0.01
```

```
2070-03-31    39.6     0.0    53.3    44.4    0.01
2070-04-30    24.1     0.0   100.5    23.7    0.01
2070-05-31    16.9     0.0   136.7    37.0    0.00
2070-06-30    25.3     0.0   157.4    20.4    0.00
2070-07-31    60.9     0.0   171.6    66.2    0.19
...
```

A similar procedure is repeated for each unique `(row, col)` key in the soil file, and results are archived in a netCDF file.

C.2.3 Computer software suggestions

Much of the processing for the spatial recharge methodology is computer intensive, and requires sufficient skills with both DOS and Cygwin[9] bash command-line shells. In short, some of the requirements include:

- ArcGIS 9.1, with standard extensions
- Microsoft Access database
- Python 2.4[10] – high-level programming language
  - GDAL and Python bindings[11] – geospatial data abstraction library, for reading, writing and converting GIS raster data
  - NetCDF library and Python bindings[12] – multidimensional raster data format for archiving HELP output, which has Easting, Northing and time dimensions
- Gridded input data from the study region, produced by ArcGIS
  - Rasters of slope (in percent), LAI, evaporative zone depth, etc.
  - Polygon shapefile of the grid over the region, with the same resolution as rasters; this can be created using an ArcGIS extension, and is called a 'fish-net' grid

[9] UNIX environment for Microsoft Windows: http://www.cygwin.com/
[10] http://www.python.org
[11] http://www.gdal.org/
[12] http://www.unidata.ucar.edu/software/netcdf/

  - Soil GIS database with linking tables for soil profile and property data

- Viewing and post-processing tools – most of these are UNIX-only, but work with Cygwin

  - NCO (Zender, 2007) – NetCDF Operators, for averaging and other calculations
  - ncview[13] – NetCDF viewer, animator and frame exporter
  - GraphicsMagick – image format tools for converting image frames into animations for other programs

C.2.4 Processing and viewing netCDF files

A netCDF file can be viewed using `ncview`, and frames can be extracted using the `-frames` option. The frames are in PPM-format, and can be converted to GIF (or other), for example:

```
$ gm convert frame.00000.ppm frame.00000.gif
```

the PPM frames can also be converted to an animated GIF, which can be used in Microsoft PowerPoint presentations:

```
$ gm convert -delay 10 -dispose 1 -loop 0 *.ppm output.gif
```

The dimensions of the netCDF files used in the study are ordered as `time` (unlimited), `ydim`, `xdim` and `bnds` (2-bounds). It can be inspected using:

```
$ ncdump -h file.nc
```

There are three possible unique time-scales of netCDF files produced using the recharge modelling methodology: annual, monthly and *n*-day (such as 11-days, to compress time). The variables contained in each netCDF file are based on the `*.YR`, `*.MON` and `*.DAY` output files from HELP 3.80D, which contain annual, monthly and daily output. Each column represents a time-dependant data variable (the columns are described in the `*.OUT` file).

Processing of netCDF files is accomplished using NCO (Zender, 2007), which is a command-line based suite of netCDF operators. A map showing the average values for

[13] http://meteora.ucsd.edu/~pierce/ncview_home_page.html

the `recharge` variable along the `time` dimension can be calculated:

```
$ ncwa -B "recharge < 5000" -v recharge annual.nc avgannualmap.nc
```

The resulting netCDF file can be converted to an ESRI ASCII grid:

```
$ gdal_translate -of AAIGrid NETCDF:"file.nc":recharge file.asc
```

which can converted and used in GMS and ArcGIS.

Monthly averages can be calculated by indexing the array, and can be assisted through for-loops, for example using a Bash shell:

```
for idx in {01..12}; do
  ncks -F -d time,${idx},,12 monthly.nc foo.${idx}
  ncwa -B "recharge < 5000" -a time foo.${idx} monthly_${idx}.nc
done
```

Monthly netCDF files of spatio-temporal recharge were ultimately used as a transient MODFLOW boundary by converting the file into an XY-series (time series) for GMS. The script `monthlync2xys.py`[14] determines the average for each month, and produces a transient 2D scatter file that can be opened in GMS.

[14] Located on the CD at `programs/monthlync2xys.py`

Appendix D

Supplementary CD Contents

D.1 `data/`

`oksoil.mdb` (3.8 MB): Soil database (non-GIS) for Okanagan and Similkameen regions (Wittneben, 1986; Kenk and Sondheim, 1987), with hydrological parameter estimates using ROSETTA (Schaap et al., 2001) and other methods. This Microsoft Access database can be viewed and used directly, or used through `AgCanSoil.py` with `HELP.py`.

D.1.1 `data/LARSWG/`

Climate data from LARS-WG (Semenov and Barrow, 1997) for Summerland and Oliver. LARS-WG specifies the metadata in `*.st` files, and stores data in `*.sr` or `*.dat` files with the same prefix. Missing data are specified with `-99.` values.

`Data/Summerland/` (2 files, 331 kB): Measured weather calibration data for Summerland, with daily T_{min}, T_{max}, precipitation and solar radiation measurements between 1960–1994. This dataset primarily consists of Summerland CDA (`1127800`) with missing values (except for solar radiation) supplied from Summerland CS (`112G8L1`).

Table D.1 Climate state file name prefixes used for LARS-WG and other programs.

File prefix	GCM	Time period
`base`	NA	1961–2000
`c1a2020`	CGCM1 GHG+A	2020s
`c1a2050`	CGCM1 GHG+A	2050s
`c1a2080`	CGCM1 GHG+A	2080s
`c3a2050`	CGCM3.1 A2	2050s
`c3a2080`	CGCM3.1 A2	2080s
`h3a2020`	HadCM3 A2	2020s
`h3a2050`	HadCM3 A2	2050s
`h3a2080`	HadCM3 A2	2080s

`Output/` (18 files, 32.6 MB): Synthetic weather for each climate state (see Table D.1) for 200 continuous years (73 000 days; no leap years). Climate variables include daily T_{min}, T_{max}, precipitation, solar radiation and potential evapotranspiration.

`Sitebase/` (13 files, 32.7 kB): Calibrated weather generator files for Summerland (defined in `Summerland.*` and `larswg.reg`), and generation configuration files (`*.sce`), which use equation 4.3 with Table A.2 and Tables B.5–B.7.

D.1.2 `data/SDSM/`

Temperature downscaling files used for SDSM (Wilby and Dawson, 2004). File names of climate variable data used by SDSM are 14-characters in length, and begin with a 4-character scenario identifier (`ncep` for NCEP/NCAR; `c1ga` for CGCM1 GHG+A; `c3ga` for CGCM3.1 A2; and, `h3a2` for HadCM3 A2), followed by a 4-character climate variable label (see Table 4.3), and ending with `na.dat`. All NCEP/NCAR calibration datasets are located in the `Calibration/` directories, which include regridded datasets and the calibrated downscaling parameter setup files (`*.PAR`) for T_{min}, T_{max} and T_{mean}. GCM data appear in the other directories. See Table 4.2 for the time ranges in each climate state.

CGCM1/ (23 files, 5 directories, 2.6 MB): CGCM1 GHG+A scenario files, provided by the Canadian Institute for Climate Studies (2005) from `BOX_16X_11Y` (or $I_1 = 65$, $J_1 = 38$, using global indices). NCEP/NCAR calibration data spans from 1961–2000.

CGCM3/ (12 files, 3 directories, 1.2 MB): CGCM3.1 A2 scenario files, described in Appendix B.1.1.1 for $I_1 = 65$, $J_1 = 38$. The calibration data and parameters used for this GCM scenario are identical to CGCM1, since the T47 Gaussian grid for CGCM3.1 has the same dimensions as the T32 grid used for CGCM1, and this calibration is *not* dependant on the GCM simulation.

HadCM3/ (11 files, 2 directories, 2.7 MB): HadCM3 A2 scenario files, provided by the Canadian Institute for Climate Studies (2005) from `BOX_65X_15Y` (or $I_1 = 65$, $J_1 = 57$, using global indices). NCEP/NCAR calibration data spans from 1961–2001, although the calibration used for downscaling is based on the same 1961–2000 time period as the CCCma models. The GCM data is continuous, from 1961 to 2099 (using 360-day years), so it needs to be split to match the time periods for CGCM1.

Observed/ (6 files, 942 kB): Daily observed T_{min}, T_{max} and T_{mean} climate for Oliver and Summerland (`OL_` and `SU_` prefixes, respectively), between 1961–2000.

D.2 gisdata/

GIS data that are in shapefile format (ESRI, 1998) have multiple files (e.g., `.shp`, `.shx`, `.dbf`, ...), although only the first is listed here with the file size representative of the file collection. Metadata are included with most of the geospatial data.

D.2.1 gisdata/boundaries/

bedrock_fill.shp (24.8 kB): Polygon boundary between bedrock exposure and Quaternary sediments (or valley fill). NAD83 BC Albers projection.

irrigation_districts.shp (79.9 kB): Irrigation district polygons near Oliver, based on a CAD coverage (T. Underwood, pers. comm. 2006). NAD83 BC Albers projection.

rc_clip.shp (2.22 kB): Polygon boundary for outer extent of recharge modelling around Oliver. NAD83 UTM Zone 10N projection.

rc_mesh.shp (3.22 kB): Polygon mesh for recharge modelling around Oliver, based on `rc_clip.shp`. Each 100 m by 100 m cell is identified using `col` and `row` indices (or attributes), which start at 1 in the upper-left corner.

rc_soil.shp (207 kB): Polygon boundary of outer extent of soil survey around Oliver. NAD83 UTM Zone 10N projection.

D.2.2 gisdata/capture_zones/

Capture zones are defined for eight wells near Oliver, as described in Chapter 6. The shapefile polygons were traced from the 0.2 probability contour. All projections for the capture zones are in NAD83 BC Albers.

ol_cz_0060.shp (28.7 kB): Polygons of 60-day capture zones.

ol_cz_0365.shp (40.8 kB): Polygons of 1-year capture zones.

ol_cz_3650.shp (49.2 kB): Polygons of 10-year capture zones.

D.2.3 gisdata/geology/

Polygons of mapped geological units or features in the Oliver region. All shapefiles have a NAD83 Zone 10N projection.

alluvial.shp (7.6 kB): Alluvial deposits along the valley sides. Shown in Figure 2.8.

boulders.shp (6.8 kB): Boulder deposits, as found on top of alluvial deposits, or within glaciofluvial deposits on the valley bottom. Shown in Figures 2.8 and 2.11.

fluvial.shp (10.4 kB): Fluvial deposits adjacent to Okanagan River. Shown in Figures 2.8 and 2.11.

glaciofluvial.shp (12.9 kB): Glaciofluvial deposits, as shown in Figure 2.8.

`kettle_holes.shp` (11.8 kB): Interpreted kettle holes interpreted from a DEM, shown in Figure 2.11.

`silt.shp` (38.0 kB): Polygon defining the extent of buried glaciolacustrine silt and clay, shown in Figure 2.10.

`terraces.shp` (24.1 kB): Interpreted terraces in the glaciofluvial deposits. The terraces are correlated across the valley and ranked (using the `Id` attribute) from highest elevation/oldest (1) to lowest/most recent (4), as indicated in Figure 2.11.

D.2.4 `gisdata/hydrology/`

`ok_riv_struct.shp` (14.9 kB): Point shapefile (14 points) of structures on Okanagan River with sill elevations, between Vaseux Lake and Osoyoos Lake (Schubert, 1983), shown in Figures 2.1 and 5.6. NAD27, Zone 11N projection.

`ok_riv_surv1980.shp` (33.1 kB): PointZ shapefile (191 points) of river profiles along Okanagan River, between Vaseux Lake and Osoyoos Lake, summarizing stage elevation (between June 9–23, 1980) and river bottom elevation (Schubert, 1983). NAD27 UTM Zone 11N projection.

`ol_snap_pour.shp` (3.8 kB): Snap-pour-points used to define valley-side stream catchments. The points were chosen as the intersection of the streams with the bedrock fill boundary. NAD83 UTM Zone 10N projection.

`ol_ws.shp` (104 kB): Polygons for each stream catchment along the valley sides, defined using snap-pour-points and other GIS rasters derived from a DEM. Used to determine catchment area and hypsometric parameters. NAD83 UTM Zone 10N projection.

D.2.5 gisdata/recharge_results/

Spatial recharge results for the Oliver region using the HELP model, represented using an ESRI ASCII grid format. All recharge results use the same 'base' climate state, representing 100 years of the 'current' climate conditions. The projection of the rasters is NAD83 UTM Zone 10N.

avg_annual_base_recharge.asc (254 kB): Average annual recharge and irrigation return flow. Units are mm/year.

avg_annual_noirr_recharge.asc (260 kB): Same as previous, except that irrigation is not simulated. This is the same data used in Figure 4.16a.

avg_monthly_base_recharge.zip (936 kB): Average monthly recharge and irrigation return flow, separated into 12 raster files for each month. Units are mm/month. This is the same data used in Figure 4.17b.

avg_monthly_noirr_recharge.zip (949 kB): Same as previous, except that irrigation is not simulated. This is the same data used in Figure 4.17a.

D.2.6 gisdata/wells/

awel_sok.shp (338 kB): Point shapefile of groundwater wells in the southern Okanagan, identified by their WTNs. NAD83 BC Albers projection.

wells_mt.mdb (114 MB): Microsoft Access 2003 database of the BC Ministry of Environment WELLS database (BC MoE, 2006); this version is a public-domain replication of the Ministry database; however, this particular version has many corrections and geologic interpretations.

D.3 print/

All published items listed here were not placed under copyright; thus, they inherit the same copyright terms as this thesis.

CWN06Montreal_poster.pdf (1.10 MB): Poster presented at the CWN Connecting Water Resources 2006 Conference, Montreal, QC (Toews and Allen, 2006).

CWNSpring06_field_trip_guide.pdf (1.46 MB): Field-trip guide for a cross-section of sand and gravel near Penticton.

GSA05_poster.pdf (1.85 MB): Poster presented at the Geological Society of America Annual Meeting and Exposition, 2005, Salt Lake City, UT (Toews et al., 2005).

recharge_IAH06.pdf (632 kB): Short paper presented at the International Association of Hydrogeologists' Sea to Sky Geotechnique 2006, Vancouver, BC (Toews et al., 2006).

D.4 programs/

Programs used in this thesis are listed below. These programs all consist of source code, as they are all based on interpreted programming languages (such as Python). As these programs are all text files, they can be opened in most text editors. Documentation for the programs are included in the source files themselves, and comments have been included throughout the code to help other people understand the algorithms. Often (although not always), examples are found near the top of each program code. Also, most programs listed here are executed through a command prompt; `cmd.exe` for Microsoft Windows, or any Unix-like shell on other systems. All programs have a General Public License, which allows anyone to use and modify them as they wish.

AgCanSoil.py (14.0 kB): Python module used to interface with soil database, which was reformatted into Microsoft Access 2000 format. This module is not used directly, but is used by `HELP.py` and `precip_sep.py`.

calcvort.ncl (2.36 kB): Calculate vorticity using netCDF files of zonal (u) and meridional (v) wind components using the NCAR Command Language (NCL; NCAR, 2006).

`gms.py` (7.25 kB): Python module for reading and writing files for GMS 6.0; present capabilities can read a solid file, and write a TIN.

`gms_2dTo3D_highest_active.py` (5.38 kB): Python script that extracts the highest active value from a 3D grid, and outputs a 2D array. Uses HDF5 array format, and is a workaround for a bug in GMS 6.0.

`gms_addcreeksto2D.py` (5.89 kB): Python script that adds recharge from creeks to a transient 2D HDF5 grid file from GMS.

`gms_fixed2ts.py` (5.25 kB): Python script that modified fixed nodes to time series nodes in a GPR file, by adding a constant for each time step. Specifically, this was used to modify river stage elevations.

`gmsborehole.py` (2.89 kB): Python module for reading and writing GMS 6.0 ASCII borehole files present capabilities can read a solid file, and write a TIN.

`gpl.txt` (17.5 kB): GNU General Public License v.2 for all programs listed here.

`h5remap.py` (1.64 kB): Python script used remap integers in HDF5 files, such as the primary format for GMS 6.0 (EMRL, 2005). This could be, for example, to remap an integer representing one material to another.

`HELP.py` (42.3 kB): Python module used to interface with HELP 3.80D. Examples are shown in Section C.2.2.

`meshedFeatures.bas` (5.73 kB): VBA code used in ArcGIS to export a simple text file of every polygon in a shapefile, showing the surface area, grid location and grid description; this was used and modified for soil and land use coverages.

`model_HELP.py` (23.7 kB), `model_HELP_util.py` (23.5 kB): Interactive Python script used to model recharge in the Oliver region and produce multiple files, including ASCII rasters of runoff curve numbers, geometric mean of K_s, and netCDF files of recharge.

`modflow.py` (50.5 kB): Python module used to interface with USGS MODFLOW-2000 files, and has been tested with files produced by both GMS and Visual MODFLOW (translated files). This module is capable of reading and writing file for several MODFLOW Packages, and is useful for manipulation of multidimensional data.

`monthlync2xys.py` (4.03 kB): Python script that reads monthly total recharge from a netCDF file, determines the mean of each month, and writes an XY-series file for GMS.

`nudgegrid.py` (2.73 kB): Python script that fixes a MODFLOW DIS grid to have non-zero thicknesses.

`precip_sep.py` (5.19 kB): Python module used to perform calculations on multiple precipitation scenarios with a standard set of soil columns; used for the precipitation separation paper (Chapter 3).

`read.hydat.R` (1.14 kB): R function to read CSV-formated daily flow and stage data from HYDAT CD-ROM (Environment Canada, 2001).

`trunch5.py` (5.54 kB): Python script used to truncate values from a TIN stored in a HDF5 file (with an `.h5` extension; exported from GMS) using either constant values or other TINs for upper and/or lower surfaces; extends the capabilities of the `trunc` function available in GMS.

`tsimfix.py` (2.92 kB): Overwrites values from TSIM aquifer material simulations within GMS 6.0 files (`.gpr` file extension); used to make bottom half of groundwater models have silt material, while upper half with stochastically generated materials.

`well2gms.py` (13.2 kB): Python script used to import well data using a WTN list from the MS Access WELLS database into an ASCII borehole file format recognized by GMS; the script may also remap soil IDs and combines identical adjacent soil layers.